University of Trento

DEPARTMENT OF PHYSICS

GENERATION, MANIPULATION AND DETECTION OF NIR AND MIR ENTANGLED PHOTON PAIRS

ALESSANDRO TRENTI

Tutor: prof. Lorenzo Pavesi

XXX PhD Cycle

Alessandro Trenti: *Generation, manipulation and detection of NIR and MIR entangled photon pairs.*
In partial fulfilment of the requirements for the degree of Doctor of Philosophy. © 20 April 2018

MEMBERS OF THE COMMITTEE

- Professor Daniele Bajoni, Universitá di Pavia, Italy;
- Professor Gregor Weihs, University of Innsbruck, Austria;
- Dr. Iacopo Carusotto, INO-CNR BEC Center and Universitá di Trento, Italy.

Trento, 20th April 2018

PUBLICATIONS

Some ideas and figures have appeared previously in the following publications:

- A. Trenti, M. Borghi, S. Biasi, M. Ghulynian, F. Ramiro-Manzano, G. Pucker and L. Pavesi, "Thermo-optic coefficient and nonlinear refractive index of silicon oxynitride waveguides", AIP Adv. 8, (2018).
- M. Borghi, C. Castellan, S. Signorini, A. Trenti and L. Pavesi, "Nonlinear silicon photonics", J. Opt. 19, (2017).
- M. Mancinelli, A. Trenti, S. Piccione, G. Fontana, J. S. Dam, P. Tidemand-Lichtenberg, C.Pedersen and L. Pavesi, "Mid-infrared coincidence measurements on twin photons at room temperature", Nat. Commun. 8, (2017).
- A. Trenti, M. Borghi, M. Mancinelli, H. M. Price, G. Fontana and L. Pavesi, "Quantum interference in an asymmetric Mach-Zehnder interferometer", J. Opt. 18, (2016).
- S. Piccione, M. Mancinelli, A. Trenti, G. Fontana, J. S. Dam, P. Tidemand- Lichtenberg, C.Pedersen and L. Pavesi, "Mid-infrared coincidence measurements based on intracavity frequency conversion", SPIE Photonics West 10516, (2018).
- C. Castellan, A. Trenti, M. Mancinelli, A. Marchesini, M. Ghulinyan, G. Pucker and L. Pavesi "From SHG to mid-infrared SPDC generation in strained silicon waveguides", SPIE Nanoscience + Engineering 2017 10358, (2017).
- A. Trenti, M. Borghi, M. Mancinelli, H. M. Price, G. Fontana and L. Pavesi, "One and two- photon quantum interference in a Mach-Zehnder interferometer", SPIE Photonics Europe 9894, (2016).
- F. Ramiro Manzano et al., "Microring Resonators and Silicon Photonics", MRS Advances (2016).
- M. Bernard et al, "Nonlinear Silicon Photonics", Frontiers in Optics FM1D-1, (2015).

CONTENTS

ACRONYMS

ASE Amplified Stimulated Emission

BAL Broad Area diode Laser

CAR Coincident-to-accidental ratio

CMOS Complementary Metal Oxide Semiconductor

CW Continuous Wave

DFG Difference Frequency Generation

DWDM Dense Wavelength Division Multiplexing

EFISH Electric Field Induced Second Harmonic

FBG Fiber Bragg Grating

FE Field Enhancement

FEM Finite Element Method

FWHM Full Width at Half Maximum

FWM Four Wave Mixing

FPC Fiber Polarization Controller

FPGA Field Programmable Gate Array

FSR Free Spectral Range

FTIR Fourier Transform Infrared

GVD Group Velocity Dispersion

HOM Hong-Ou-Mandel

JSI Joint Spectral Intensity

QE Quantum Efficiency

NEP Noise Equivalent Power

NIR Near-infrared

MIR Mid-infrared

MZI Mach-Zehnder interferometer

OPA Optical Parametric Amplifier

OSA Optical Spectrum Analyser

PIC Photonic Integrated Circuits

QI Quantum Information

QKD Quantum Key Distribution

QPM Quasi Phase Matching

PPLN Periodically Poled Lithium Niobate

SFG Sum Frequency Generation

SHG Second Harmonic Generation

SNR Signal to Noise Ratio

SNSPD Superconducting Nanowire Single Photon Detector

SPM Self Phase Modulation

SOI Silicon on Insulator

SPAD Single Photon Avalanche Diode

SPDC Spontaneous Parametric Down Conversion

TE Transverse Electric

TEC Temperature Controller

TM Transverse Magnetic

TOC Thermo Optic Coefficient

TPA Two Photon Absorption

UV Ultraviolet

1 INTRODUCTION

1.1 SILICON PHOTONICS

It is history now that silicon has driven the microelectronics revolution in the last century. The success of classical information processing owes much to advances in semiconductor technology, such as the ability to make devices in silicon in an integrated and scalable manner. Complementary metal-oxide semiconductor (CMOS) fabrication technology has allowed for cheap, fast and low-power implementation of densely-packed nanometer sized transistors.
The microelectronics roadmap was set by the famous *Moore's law*, stated by Gordon E. Moore in 1965, which predicts that the number of transistors on a microprocessor chip doubles approximately every two years, see Figure 1.

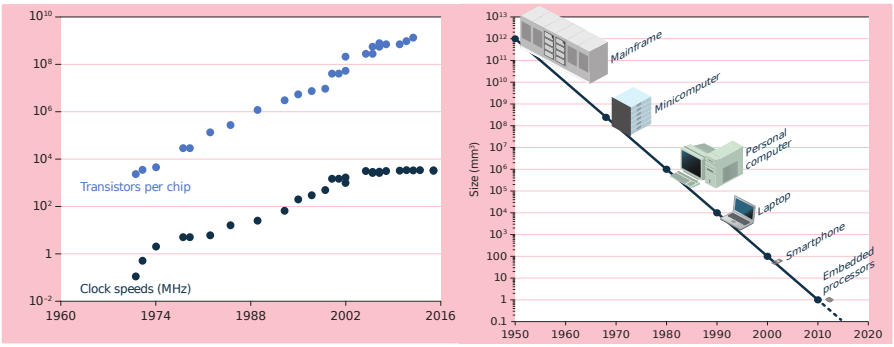

Figure 1: Moore's law road map. Image taken from [1].

Chipmakers deliberately have chosen to stay on the Moore's law track, which has evolved the first crude home computers of the 1970s to the nowadays available smartphones, tablets and also exhotic wearable technologies [2]. Nonetheless it is becoming increasingly evident that the Moore's law is about to hit a brick wall: transistors are reaching the size of $\sim$ 2-3 nm, where electronic transport is governed by quantum uncertainties that will make transistors hopelessly unreliable. The quest for a change of paradigm is becoming more and more urgent.

Photonics, i.e. the science of light, could be the solution for this outstanding issue of our modern information society. As a matter of fact, optical fibres have already started to replace copper wires all around the world. Indeed, fiber-optics communications guarantee transmission over longer distances and at higher bandwidths (data rates) than

wire cables. Moreover, optical fibres suffer less losses with respect to metal wires and they are also immune to electromagnetic interference. Nowadays optical fibres allow light to be guided through 1 km of glass fibre with a loss as low as $\sim 0.15\,\mathrm{dB}$ ($\sim 3.4\,\%$) at the wavelength of maximum transparency that is at $\lambda = 1.55\,\mu\mathrm{m}$ (third telecom window) [3].

On the other hand, optoelectronic and photonics technologies are becoming less costly and more integrated, leading the opportunity to increasingly miniaturize optical components. This is the framework where *silicon photonics* wants to play the the leading role in this scientific and technological challenge.

Despite the absolute dominion of silicon in the recent microelectronics revolution, we did not face at first, the same impetuous development in the field of Photonic Integrated Circuits (PIC). The main bottlenecks were the intrinsic indirect band-gap structure of silicon, which poses even today challenges to have active devices on chip; and also the lack of second order nonlinearity which prevents the development of modulators based on the electro-optic effect. For these reasons the first PICs were based upon III-V semiconductors, such as indium phosphide (InP), which allows the integration of various optically active (direct band-gap) and passive functions on the same chip. Nevertheless the vision of optoelectronics to have the integration of optics and electronics on the same chip, considerably pushed also the research towards the silicon photonics.

That was also the visionary idea of Soref which stated in 1993 [4]: "*The decade of the 1990's is an opportune time for scientists and engineers to create cost-effective silicon "superchips" that merge silicon photonics with advanced silicon electronics on a silicon substrate. We can expect significant electro-optical devices from Column IV materials (Si, Ge, C,and Sn) for a host of applications.*".

Soref envisaged a silicon-based *super-chip* which included low-loss coupling of optical components, plus low parasitic electrical connection of adjoining components.

Let us introduce the fundamental building blocks for the light manipulation on PIC: optical *waveguides* and *micro-resonators*. These can be thought as the optical counterpart of what transistor represents for microelectronics, see Figure 2.

Optical waveguides can be fabricated in different geometries, but are almost always characterized by the presence of a central core, surrounded by a cladding of lower refractive index, that confines light by means of *total internal reflection* (an exception to this scheme is represented by the Bragg-reflection waveguides [6]). Optical fibres are a particular type of waveguides, made of glass and with cylindrical geometry.

Silicon is characterized by a very high refractive index with respect to the ones of the typically used cladding materials. For example in

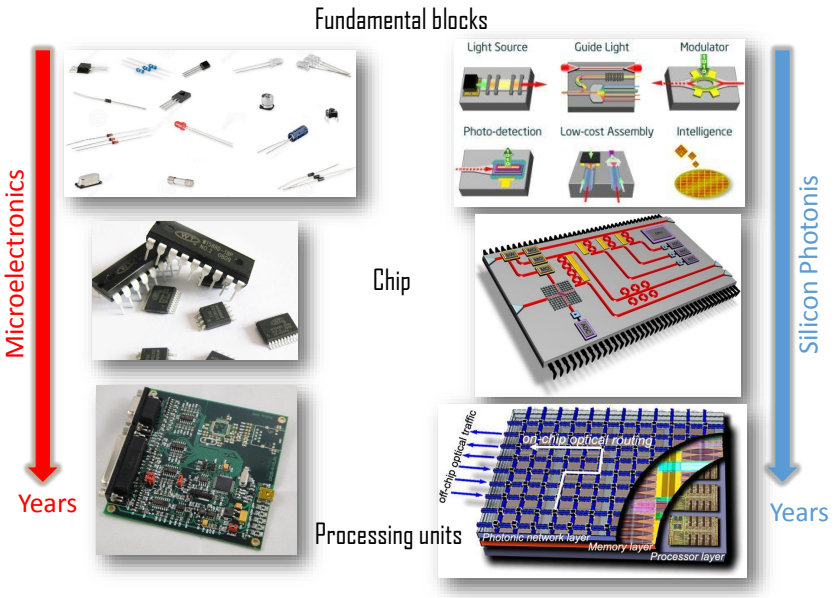

Figure 2: Silicon Photonics road map with respect to microelectronics during the years. From the basic building blocks, progressively more complex circuits have been realized by connecting together several components. Image taken from [5].

the case of the Silicon-on-Insulator (SOI) technology, at $\lambda = 1.55\,\mu m$ the refractive index of silicon is about 3.48, while the refractive index of silica which acts as the lower cladding material is about 1.44 [7, 8]. The strong refractive index contrast allows the manufacture of very compact photonic devices on a small footprint in a single chip. The record to date is more than thousands per cm^2 [9]. The typical cross-section dimensions for a rectangular single-mode SOI optical waveguide are $220 \times 450\,nm^2$. The small effective mode area of silicon optical waveguides, enhance light matter interaction. Silicon possesses a strong $\chi^{(3)}$ material nonlinearity, which can be effectively enhanced by the small cross-section of the device [10].

While for certain photonics applications, such as optical fiber communications or high power lasers [11], nonlinearities are detrimental to correct device operation, in other research areas they are actually highly sought for. As it will be discussed in detail in Section 1.2, material nonlinearities open a plethora of interesting phenomena: wavelength conversion, electro-optic modulation and generation of entangled photon pairs among the others [12].

Now, if one takes a waveguide and bends it on itself one obtains a planar microring resonator. Microring resonators are used in PIC for several applications: biomolecular sensing [13], routing of light [9] and for enhancing light matter interaction to trigger nonlinear effects [12].

A so called whispering-gallery-mode-resonator, is characterized by constructive light interference condition occuring at specific wavelengths. Interference effects are due to the wave nature of light. As a matter of fact, whispering-gallery waves were first explained within the St Paul's Cathedral in 1878 by Lord Rayleigh for the case of acoustic waves [14]. He realized that whispers could be heard across the dome but not at any intermediate position.
In the case of optical resonators, the resonance condition is given by the following relation:

$$m\lambda_m = 2\pi R\, n_{eff}(T) \tag{1}$$

where λ_m is the resonant wavelength and m is the mode number of the ring resonator. R is the radius of the ring resonator and $n_{eff}(T)$ is the effective refractive index experienced by the whispering-gallery wave which travels within the resonator. The strong thermo-optic coefficient in silicon allows a reconfigurable control of the microring resonator spectral characteristics, i. e. of the resonance wavelength in Equation 1. Again, the high refractive index contrast determines a strong modal confinement, leading to the possibility to fabricate bend radii below $5\,\mu m$ [15].
There is actually a vast literature of published works about the demonstration of waveguides and microring resonators circuits as building blocks for a photonic chip [12]. The most advanced effort towards a CMOS integrated architecture able to interface a light circuit with microelectronics, instead, was published at the end of 2015 in [16]. Here the authors reported an electronic–photonic system on a single chip, integrating over 70 million transistors and 850 photonic components that work together to provide logic, memory, and interconnect functions. Optical devices were fabricated using a standard microelectronics foundry process that is used for modern microprocessors. In particular, the chip was fabricated using a commercial high-performance $45\,nm$ CMOS silicon-on-insulator (SOI) process. The optical modulation capability was realized by means of a silicon microring resonator, with a radius of $5\,\mu m$, coupled to a waveguide. The light source used was a $1183\,nm$ laser, still not integrated on chip. Through a Field Programmable Gate Array (FPGA) control unit, successful execution of the *Hello world* basic functionality test and the STREAM memory benchmark, were demonstrated as examples of terminal-based programs [17].
Overall, this was an impressive demonstration of chip-scale electronic–photonic systems integration, with the ambitious aim of revolutionizing computing system architectures.

Things get even more interesting if instead of linear classical photonic circuits, quantum mechanical phenomena, such as superposition and entanglement, are exploited to process, transmit, and encode

information. This is the case for example of Quantum Information (QI) applications where the generation of nonclassical states of light by means of spontaneous nonlinear process has become a fervent research area in recent years.
It is in this context that quantum integrated photonics on a silicon based chip could provide a successful platform for the incoming quantum revolution.

1.2 NONLINEAR OPTICS

A nonlinear medium is characterized by a nonlinear relation between the polarization density $\mathbf{P}$ and the incident electric field vector $\mathbf{E}$. Generally this relationship is linear if $|\mathbf{E}|$ is small, but becomes nonlinear when $|\mathbf{E}|$ acquires values comparable to the inter-atomic electric fields, which are typically of the order $10^5 - 10^8 V/m$.
In the Drude-Lorentz model, one can think that the electric field of the incident light drives the dipole of the atoms or molecules causing them to oscillate like springs as it travels through the material. It is possible for an high intensity light to force these dipoles to the point that they oscillate with a nonlinear response such that the re-emitted light contains additional frequencies.
In an ideal linear optical material, the linear polarization vector $\mathbf{P}_0$ is related to the applied optical field $\mathbf{E}$ by [3, 18]

$$\mathbf{P}_0 = \varepsilon_0 \chi^{(1)} \cdot \mathbf{E} = \varepsilon_0 \sum_{ij} \chi^{(1)}_{ij} E_i \hat{\mathbf{u}}_j, \tag{2}$$

being ε_0 the vacuum permittivity, $\chi^{(1)}$ the first order susceptibility (which is a second rank tensor whose elements are labelled by $\chi^{(1)}_{ij}$), E_i the $i-$th component of the field $\mathbf{E}$, while $\hat{\mathbf{u}}_j$ is the unitary versor. Note that if the medium is isotropic, the susceptibility becomes simply a scalar coefficient. $\chi^{(1)}$ describes the refraction or dispersion characteristics of the incident wave, usually called *pump* wave, in the medium.
If $\mathbf{E}$ is strong enough, nonlinear optical effects start to be important in the medium, inducing a variation $\mathbf{P}_{NL}$ in the polarization vector. The polarization vector $\mathbf{P}$ can be written in general as:

$$\mathbf{P} = \mathbf{P}_0 + \mathbf{P}_{NL} \tag{3}$$

where $\mathbf{P}_{NL}$ is due to nonlinear optical effects and is defined as:

$$\mathbf{P}_{NL} = \mathbf{P}^{(2)} + \mathbf{P}^{(3)} + ... = \varepsilon_0 \left[\chi^{(2)} : \mathbf{E}^2 + \chi^{(3)} \vdots \mathbf{E}^3 + ... \right] =$$

$$= \varepsilon_0 \left[\sum_{ijk} \chi^{(2)}_{ijk} E_i E_j \hat{\mathbf{u}}_k + \sum_{ijkl} \chi^{(3)}_{ijkl} E_i E_j E_k \hat{\mathbf{u}}_l + ... \right] \tag{4}$$

being $\mathbf{P}^{(2)}$ and $\mathbf{P}^{(3)}$ the second and third order nonlinear polarization vectors, while $\chi^{(2)}$ and $\chi^{(3)}$ are the second and the third order susceptibilities. In general, the j−th order nonlinear susceptibility is a tensor of rank $(j+1)$: for isotropic or amorphous materials (such as silica-based optical fibers) it can be considered as a scalar quantity, while for crystalline structures (such as silicon) it must be considered in its tensorial form. Higher order susceptibility terms are smaller and smaller and they are effective only for large field intensities.

The propagation of light in a nonlinear medium is governed by the *wave equation*, which has the form [18]

$$\nabla^2 \mathbf{E} - \frac{n^2}{c_0^2} \frac{\partial^2 \mathbf{E}}{\partial t^2} = \frac{1}{\epsilon_0 c_0^2} \frac{\partial^2 \mathbf{P}_{NL}}{\partial t^2} \tag{5}$$

where n is the linear refractive index of the medium and c_0 is the speed of light in vacuum. It is thus evident from Equation 4-5 that the time-varying nonlinear polarization term $\mathbf{P}_{NL}$ plays the role of a source of new components for the electromegnetic field.

It is worthy to point out that *centrosymmetric media* have a vanishing $\chi^{(2)}$ coefficient in the electric-dipole approximation. Therefore, in these types of media the lowest order available nonlinearity is the third order. A remarkable example is silicon. A possible way to break the centrosymmetry, and thus induce a $\chi^{(2)}$ in silicon, can be obtained by stressing a silicon waveguide with a silicon nitride over-layer. This has been experimentally demonstrated in [19]. We will come back to this in Chapter 3, in which an experiment based on strained silicon waveguides is presented.

The second order effects can be evaluated by representing the propagating electric field $\mathbf{E}$ in the material as the superposition of two waves $\mathbf{E}_1$ and $\mathbf{E}_2$:

$$\mathbf{E}(\mathbf{r}, t) = \sum_{n=1}^{2} \left(\mathbf{E}_n(\mathbf{r}, \omega_n) e^{-i\omega_n t} + \text{c.c.} \right), \tag{6}$$

where c.c. stands for "complex conjugate". From Equation 4, the second order nonlinear polarization vector can be derived [18]:

$$\mathbf{P}^{(2)} = \varepsilon_0 \chi^{(2)} : \Big[\mathbf{E}_1^2 e^{-i2\omega_1 t} + \mathbf{E}_2^2 e^{-i2\omega_2 t} + 2\mathbf{E}_1 \mathbf{E}_2 e^{-i(\omega_1+\omega_2)t} +$$

$$+ 2\mathbf{E}_1 \mathbf{E}_2^* e^{-i(\omega_1-\omega_2)t} + \mathbf{E}_1 \mathbf{E}_1^* + \mathbf{E}_2 \mathbf{E}_2^* \Big] + \text{c.c.} \tag{7}$$

The first two terms in Equation 7 correspond to Second Harmonic Generation (SHG), a process where a photon at frequency 2ω is gener-

ated from two photons at frequency ω. The third and the fourth terms in Equation 7 correspond to Sum Frequency Generation (SFG) and to Difference Frequency Generation (DFG). In these processes a photon is generated (respectively) at frequencies $\omega_1 + \omega_2$ and $\omega_1 - \omega_2$. The last terms of Equation 7 give rise to the generation of a DC component of the polarization vector. This process is called optical rectification.
Another interesting $\chi^{(2)}$ process is called Spontaneous Parametric Down Conversion (SPDC). It can be viewed, at the first order, as the fission of a pump photon into two lower frequencies photons, typically called *signal* and *idler*. The classical framework fails to provide a full description of the SPDC process due to the fact that the process is of *spontaneous* nature: SPDC can not be derived from Equation 7. SPDC is stimulated by random vacuum fluctuations and it happens without the coupling of any additional weak field (as it is the case of the difference frequency generation DFG). Signal and idler photons are generally correlated in momentum, energy and time, where the degrees of correlation depends on the parameters of the pump, the medium and the collection optics [20].
Following the approach used for the second order case, the third order nonlinear polarization vector $\mathbf{P}^{(3)}$ can be written by expanding the total electric field as the sum of three waves [21]:

$$\begin{aligned}\mathbf{P}^{(3)} = \varepsilon_0 \chi^{(3)} \vdots \Big[&\mathbf{E}_1^3 e^{-i3\omega_1 t} + 3\mathbf{E}_1^2 \mathbf{E}_2 e^{-i(2\omega_1+\omega_2)t} + 3\mathbf{E}_1^2 \mathbf{E}_2^* e^{-i(2\omega_1-\omega_2)t} + \\ &6\mathbf{E}_1 \mathbf{E}_2 \mathbf{E}_3 e^{-i(\omega_1+\omega_2+\omega_3)t} + 6\mathbf{E}_1 \mathbf{E}_2 \mathbf{E}_3^* e^{-i(\omega_1+\omega_2-\omega_3)t} + \\ &3|\mathbf{E}_1|^2 \mathbf{E}_1 e^{-i\omega_1 t} + 6|\mathbf{E}_2|^2 \mathbf{E}_1 e^{-i\omega_1 t} \Big] + \text{c.c.} \end{aligned} \tag{8}$$

In this formula, for reasons of simplicity, all the possible permutations of the waves indices have been omitted. The first term in Equation 8 is related to Third Harmonic Generation (THG). In this process three photons with identical frequencies ω generate a photon at triple frequency 3ω. The second to fifth elements of the summation are responsible of Four Wave Mixing (FWM), where in general the interaction of three waves give rise to a fourth wave. The sixth term of the summation is responsible of both Self Phase Modulation (SPM) and Two Photon Absorption (TPA). SPM is related to the real part of the third order susceptibility $\chi^{(3)}$, while TPA is related to the imaginary part of $\chi^{(3)}$. In semiconductor materials, TPA refers to the absorption of two photons whose energies sum up to the energy required for the excitation of an electron from the valence to the conduction band [22].
The last term in the summation in Equation 8 is responsible for the cross Phase Modulation (XPM). XPM is still related to an intensity dependent refractive index, but here it is a signal at frequency ω_2 that influences the propagation of a signal at frequency ω_1.

Typically, in nonlinear wave-mixing processes the *energy* $\hbar\omega$ and *momentum* $\hbar\mathbf{k}$ must be conserved. Note that the fulfilment of the energy conservation does not imply the momentum conservation, since the nonlinear medium is in general dispersive. We will see in Chapter 2 that this phase mismatch actually inhibits constructing interference and therefore lowers the efficiency of the nonlinear process.
Spontaneous FWM can be viewed as the $\chi^{(3)}$ counterpart of the $\chi^{(2)}$-mediated SPDC. In particular, degenerate spontaneous FWM happens when two pump photons are spontaneously annihilated, generating a signal and idler photon, as it is sketched in Figure 3.

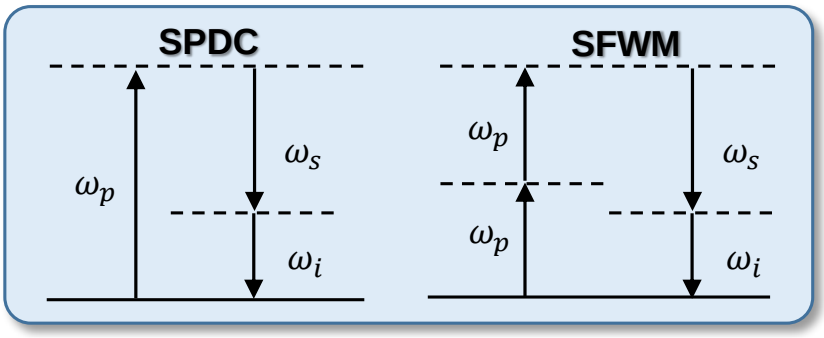

Figure 3: Energy diagram of the two nonlinear spontaneous parametric processes: SPDC and degenerate spontaneous FWM. Image taken from [12].

It can be shown that the state generated in spontaneous parametric processes can be in general written as [23]:

$$|\psi\rangle = \sum_{n=0}^{\infty} c_n |n\rangle_s |n\rangle_i \tag{9}$$

where n is an integer number and the subscript s,i stands for signal and idler respectively. The coefficient which appears in the sum is $c_n = \frac{[\tanh(s)]^n}{\cosh(s)}$, where s is the squeezing parameter that depends on the pump intensity [23].
In Equation 9 the *braket* notation was introduced, which is the standard notation used for describing quantum states in the linear algebra formalism [23]. The state $|\psi\rangle$ denotes a vector which belongs in general to an infinity-dimensional complex Hilbert space [24]. According to the Copenhagen interpretation of quantum mechanics, the probability to generate the state $|n\rangle_s |n\rangle_i$ in Equation 9 is given by $|c_n|^2$ [25].
The quantum state in Equation 9 expresses the fact that most of the time the generated state is $|\psi\rangle = |n\rangle_s |n\rangle_i = |vac\rangle$, i.e. there is no generation of photon pairs. The term with $n = 1$ in Equation 9 refers to the generation of a pair of photons, while terms with $n > 1$ are referred to multi-pair emission. If the pump field intensity is sufficiently

low, one can safely neglect higher order terms and approximate the state with the generation of only a signal and an idler photon, see Figure 3.

1.3 QUANTUM OPTICS

The increasing ability of exciting the spontaneous nonlinear parametric processes of SPDC and FWM, led to an impetuous development in the study of quantum states of light. The so called *second quantum revolution* is approaching and its importance is highlighted by the recent huge investment of the European Commission in the 1-billion-€-Flagship-scale initiative in quantum technology [26, 27]. In the first quantum revolution, the fundamental laws of the microscopic realm were discovered and the quantum mechanical formalism was developed [28, 29]. In recent years it has been realized that information storage, data transmission, and certain logic operations and algorithms can benefit when implemented using quantum-mechanical approaches [30]. Due to the strong interest and applications in quantum technologies, quantum devices started to move from the university laboratories to market applications. University start-up [31, 32] as well as large multinational companies, including Google, IBM, Intel, Microsoft and Toshiba, have started to heavily invest in quantum technologies [33]. This is the case, for example, of quantum computation, quantum cryptography, quantum lithography and quantum metrology.
The unit of quantum information is called *qubit*, or quantum bit, which can be thought as the quantum analogue of a classical bit. A qubit is a two-state quantum mechanical system, which can be in a superposition of both states at the same time as follows [30]:

$$|\psi\rangle = \alpha\,|0\rangle + \beta\,|1\rangle \tag{10}$$

where α and β are probability amplitudes, which are in general complex numbers. From a topological point of view, a qubit can be described with the Bloch sphere, represented in Figure 4.
The Bloch sphere is the geometrical representation of the $\mathbb{C}^2$ Hilbert space, which is the space vector where the quantum states in Equation 10 belongs to. The points on the surface of the sphere correspond to the pure states of the system, whereas the interior points correspond to the mixed states, i.e. statistical ensembles of pure states [30]. In spherical coordinates, the two-level quantum state in Equation 10 can be also written as:

$$|\psi\rangle = \alpha\,|0\rangle + \beta\,|1\rangle = \cos\left(\frac{\theta}{2}\right)|0\rangle + e^{i\phi}\sin\left(\frac{\theta}{2}\right)|1\rangle \tag{11}$$

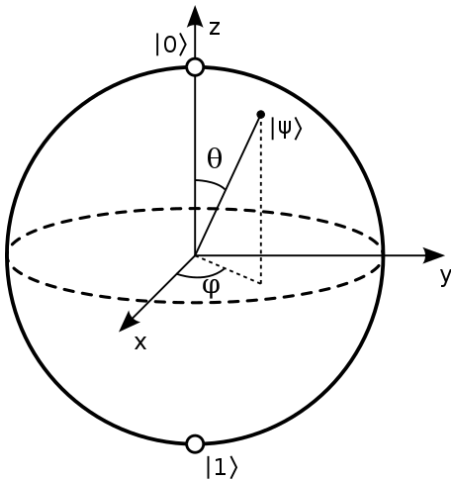

Figure 4: Bloch sphere.

where $0 \leqslant \theta \leqslant \pi$ and $0 \leqslant \phi \leqslant 2\pi$.
When we measure the qubit in the $|0\rangle, |1\rangle$ basis, the probability of outcome $|0\rangle$ is $|\alpha|^2$ and the probability of outcome $|1\rangle$ is $|\beta|^2$. Moreover we require the condition $|\alpha|^2 + |\beta|^2 = 1$, that is to say that the quantum state in Equation 10 is normalized to 1 for the total probability conservation.

An interesting way to encode a qubit is by using the polarization of a single photon: here the two states which appear in Equation 10 can be for example the vertical and horizontal polarization. Photons have the advantages to interact weakly with the environment over long distances and can be manipulated with linear optics. In 2001 a major breakthrough showed that scalable quantum computing is possible using only single photon sources and detectors, and simple (linear) optical circuits [34]. The whole Bloch sphere, sketched in Figure 4, is therefore accessible with linear optics operations: phase retardation, polarizing and non-polarizing beamsplitters in the case of polarization encoding. Together with university quantum centres, nowadays there are also companies which pursue all-optical architecture for quantum computing, exploiting the unique properties of photons as information carriers [35, 36].

Besides quantum computation, *quantum communication* is another hot topics which has faced amazing step further in recent years. In this field, *quantum cryptography* is one of the main interesting topic, due the strong interest in the protection of sensitive data from banks and national governments. The goal of cryptography is to enable two parties (commonly called Alice and Bob) to mask confidential messages such that the transmitted data are illegible to any unauthorized third party. Usually this is done by sharing secret keys, the most widely use for secure data transmission is the RSA cryptosys-

tem. RSA stands for Ron Rivest, Adi Shamir and Leonard Adleman, who first publicly described the algorithm in 1977 [37]. RSA is based on *factorization*, which is a one-way function: it is relatively easy to compute the product of two prime integers, but it is tedious and time consuming (especially with key lengths of 2048 or more bits) to factorize a number. No efficient algorithm for factorization has ever been disclosed, although there is no formal proof that such an algorithm does not exist [30].

The recent development of Quantum Key Distribution (QKD) can cover this major loophole of classical cryptography [38, 39]. It allows Alice and Bob to establish two completely secure keys by transmitting qubits along a quantum channel. The underlying principle of QKD is that nature prohibits to gain information on the state of a quantum system without disturbing it. The first QKD scheme and probable the most famous quantum cryptography protocol is named *BB84 protocol*. It was theoretically proposed by Bennett and Brassard in 1984 [40], and make use of a *single-photon* source. Other QKD protocols were also developed: B92 protocol [41], the six-state protocol [42], the SARG protocol [43] and the Ekert protocol (E91) [44]. For example the E91 scheme uses *entangled* photon pairs instead of single-photons, as it is the case of BB84.

An entangled state is defined as a quantum state in the composite system of two or more subsystems, which cannot be factored as a product of states of its local constituents [45]. An important consequence of this is that the measurement of the state of one particle in a two-particle entangled state defines the state of the second particle istantaneously, whereas neither particles possess their own well defined state before the measurement. If we consider two non interacting systems A and B with respective Hilbert spaces H_A and H_B, the Hilbert space of the composite system is defined as the tensor product $H_A \otimes H_B$ [46]. Given two basis vector $\{|0\rangle_A, |1\rangle_A\}$ of H_A and two basis vector $\{|0\rangle_B, |1\rangle_B\}$ of H_B the following is an example of an entangled state [46]:

$$|\psi\rangle_{AB} = \frac{1}{\sqrt{2}}\Big[|0\rangle_A \otimes |1\rangle_B - |1\rangle_A \otimes |0\rangle_B\Big] \tag{12}$$

If the composite system is in this state, it is impossible to attribute to either system A or system B a single state in the Hilbert space (*pure state*). The state which appears in Equation 12 is one of the four *Bell states*, which are specific maximally entangled quantum states of two qubits [47]. Entangled photon pairs with a quantum state as the one in Equation 12 can be produced through SPDC or spontaneous FWM in different degrees of freedom, such as: polarization, momentum, energy, time-bin and path-encoding [38, 48].

Now the question: does QKD protocols work in real-life applications?

The main problem in practical applications of QKD is the range limitations between the communications partners Alice and Bob. The span of current QKD systems is limited by the photon loss in the channel (optical fibers or terrestrial free space), which normally scales exponentially with the channel length. To the best of my knowledge, the record distance of QKD based provably secure cryptographic with low-loss optical fibres is 307 km [49]. One possible solution to increase the distance, is to set up a network of trusted nodes, with QKD repeaters [50]. A remarkable real-life example of QKD in a standard optical fiber network was demonstrated in Vienna in 2008 [51].
In order to go beyond trusted nodes, which restrict QKD to ground systems, the next option is to get rid of the optical fiber. It is possible to exchange keys using quantum cryptography in free space, between a terrestrial station and a low earth orbit satellite. As a matter of fact, China has recently launched a satellite with quantum communication devices [52]. A sketch of the Chinese quantum satellite is reported in Figure 5.

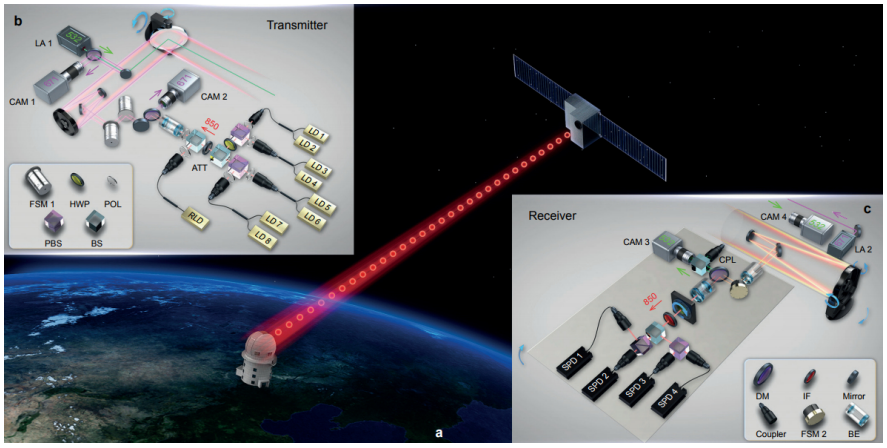

Figure 5: Sketch of the Chinese quantum satellite. The insets show the free space optical set-up for the transmitter and receiver stage.

The authors demonstrated satellite-based distribution of entangled photon pairs to two locations separated by 1203 km on the Earth. The separation between the orbiting satellite and these ground stations varies from 500 km to 2000 km. They observed two-photon entanglement and a violation of Bell inequality by $2.37 \pm 0.0.9$. The Bell inequality is a useful metric, used to determine the degree of entanglement of a quantum system [53, 54]. Bell measurement with photons are based on timing coincidence measurements, first demonstrated in 1970 by Burnham and Weinberg [55, 56]. With the transmission of entangled photons through the Earth's atmosphere in [52], it was possible to remarkably improve the maximum entanglement free-space

distribution separation previously reported of $\sim 100\,\mathrm{km}$ [57].

It is thus evident that the ability to generate, manipulate and detect quantum states of light is pivotal for the development of robust and scalable QKD and, more in general, for optical-based quantum technology. Many proof-of-concept quantum optical experiments have been reported so far with bulk nonlinear crystal, such as potassium titanyl phosphate KTP, lithium niobate $LiNbO_3$ and barium borate BBO [57–60]. However the quest of quantum technologies for integrated optical architecture becomes increasingly evident for improved performance, miniaturization and scalability [61, 62].
The first on-chip manipulation of entangled photon pairs was demonstrated by Politi et al. in the seminal work published in 2008 [63], which can be thought as the first successful demonstration of an integrated quantum photonic circuit. Still, the on-chip integration level was only attained at the manipulation stage. Indeed, that was *a-chip-in-a-lab*, while the general final goal of integrated quantum photonics is to have *a-lab-on-a-chip*.
In other terms, the vision of the integrated quantum photonics community is to have all the main building blocks of a quantum photonic circuit integrated on a chip:

- Integrated source of entangled or single-photons, depending on the applications. This refers both to the nonlinear photon-pair source, as well as to the on-chip integration of an active laser pump source;
- Reconfigurable on-chip manipulation;
- On-chip single-photon detection.

The two following questions naturally arise:

What is the right platform?
What is the current *lab-on-a-chip* state of the art?

Numerous integrated quantum photonics chips were demonstrated so far in the silica platform [63–70]. On the other hand, the silicon platform is particularly appealing due to the mature CMOS (Complementary Metal-Oxide-Semiconductor) fabrication technology, which had driven the micro-electronics revolution in the last century. We already commented in Section 1.2 that due to the centrosymmetric crystalline structure, silicon exhibits a vanishing $\chi^{(2)}$. Nonetheless, the exploitation of the $\chi^{(3)}$ spontaneous FWM effects, led to efficient generation of photon pairs both in waveguides and resonators geometries [71–76].
In particular in [71] the generation and manipulation of so called N00N states, or path-entangled states, in spiral waveguides was demonstrated on the silicon-on-insulator platform. These states are such that

N photons are in a superposition of all being in one location and all being in a second location. The on chip reconfigurable photon state manipulation was performed with thermal phase shifter placed on top of the silicon waveguides. Thanks to the relatively large silicon thermo-optic coefficient, it is indeed possible to efficiently tune the refractive index for inducing controllable phase shifts experienced by the photons travelling within the waveguides. A follow-up of this work was published in [77], where the path-entangled generation was achieved through spontaneous FWM within two microring resonators, as it is sketched in Figure 6.

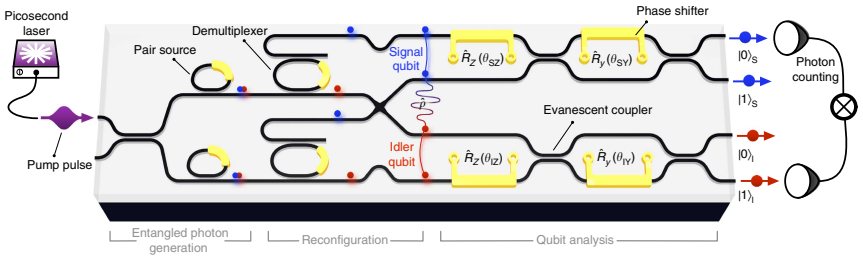

Figure 6: Sketch of the experimental layout for path-entanglement generation between ring resonator photon-pair sources on a silicon chip. Image taken from [78].

Very recently, a chip-based quantum key distribution was demonstrated in [78]. Here the authors adopted the III-V InP platform for the integration of an active electrically driven laser source and the silicon oxynitride (SiON) CMOS compatible platform for the demonstration of three QKD protocols: BB84, coherent one-way [79] and differential phase shift [80]. Clock rates up to 1.7 GHz, low quantum bit error rate (0.88%) and estimated secret key rates up to 568 kbps for an emulated 20 km fibre link were demonstrated.
However, even in this technologically state-of-the-art experimental demonstration of a chip-based QKD, the on-chip single-photon detector integration still lags behind. Despite worldwide global warming, the integrated quantum silicon photonics future will probably be extremely cold. This is because, at telecom wavelength, the best single-photon detectors which show performance close to an ideal detector, are based on superconducting technology, which requires cryogenic working temperature [81, 82]. Even though preliminary on-chip integrations of Superconducting Nanowire Single Photon Detector (SNSPD) have already been published [83], the real scalability of such architectures is inherently challenging.
Shifting the paradigm to the MIR could offer several advantages. Indeed, beyond 2.2 µm two-photon absorption (TPA) is not any more effective in silicon. This is an important point, as it is well known that TPA leads to a saturation in the photon pair generation rate at telecom wavelengths [12, 84]. The recent interest of the photonic commu-

nity to move to the MIR spectral region has driven the development of efficient sources [85–87]. However this effort was not followed by a corresponding MIR detector development. As a matter of fact, SNSPD are not as efficient in this spectral range as they are at telecom. Yet, we were recently able to demonstrate MIR coincidence measurements on twin photons at room temperature [88]. The detection method is based on efficient up-conversion of the MIR photon pairs into the visible, subsequently detected by a silicon-based SPAD. The experiment is based on a free-space configuration, but fully integrated devices can be conceived with the up-conversion mechanism. For example, up-conversion capability can be obtained by the exploitation of third order nonlinear effects in the CMOS compatible SiN or SiON alloy. Then up-converted visible photons can be efficiently detected by integrated silicon SPADs, with the control electronics eventually also integrated on chip.

An important omission that was not discussed so far, is that SPDC and spontaneous FWM intrinsically suffer from the fact to be *probabilistic* sources. An ideal single-photon source, instead, would be the one for which a single photon can be generated at any arbitrary time defined by the user (on-demand generation), with 100% probability and arbitrarily fast repetition rate. Examples of efficient deterministic source of single photons are: semiconductor quantum dots [89], single atoms [90] or molecules, ions [91] and color centers [92].
Needless to say, each platform has its own advantages and disadvantages. For example, in the case of semiconductor quantum dots, if from one side they are able to emit true, telecom, single-photons; on the other side they are typically forced to work at cryogenic temperature and the wavelength tunability is hard to attain. Only very recently, it was reported that by integrating strain–released InAs quantum dots on piezoelectric substrates, it was possible to achieve wavelength tunability, albeit with still limited performances [93, 94].

Finally, it is important to remark that SPDC and spontaneous FWM, are not true single-photon sources. In this processes photon pairs are emitted with a super-poissonian statistics and signal and idler beam individually exhibit thermal statistics [23, 95].
On the other hand, the fact that photons are emitted in pairs is particularly interesting, as it gives the possibility to exploit heralding schemes. A *heralded single-photon source* works as follows: if the exciting pump intensity is low enough to avoid multiple pair emission [96], the presence of a photon is revealed by the detection of the corresponding twin photon. Ideally one would have 100% heralding probability, i.e. 100% probability of measuring a signal photon once the heralding idler counterpart has been detected. In general, the heralding probability scales quadratically with the overall loss of the system from generation to detection, thus putting strict requirements to the system insertion loss and to the detector efficiency.

1.4 THE SIQURO PROJECT AND THESIS OUTLINE

The PhD thesis work here presented was carried out within the *SiQuro* project at the Nanoscience laboratory of the University of Trento. The project started in September 2013 and lasted four years. It was funded by the Provincia Autonoma di Trento (PAT) [97].
SiQuro's goal was to bring the quantum world into integrated photonics by using the silicon platform and, therefore, permitting the integration of quantum photonics with electronics. The vision was to have low cost and mass manufacturable integrated quantum photonic circuits for a variety of different applications in quantum computing and secure communications. It must be said that SiQuro was a challenging and ambitious project, nevertheless important achievements in the quantum photonics arena were reached.

My thesis is concentrated on the generation, manipulation and detection of quantum states of light. On one side, this was carried on in strained silicon waveguides, with the final goal to generate MIR entangled photon pairs via SPDC. Alongside, the generation and manipulation of correlated photon pair sources by means of spontaneous FWM in traditional silicon waveguides and microring resonators at telecom wavelength was also investigated. For the detection of MIR photon pairs, a suitable detection unit was developed as well. Moreover, even though the long-term goal of the project was the realization of a silicon quantum photonic circuit, I also implemented free-space quantum optical experiments. For this, I exploited a bulk nonlinear crystal, namely lithium niobate ($LiNbO_3$), which has a well-known sizeable $\chi^{(2)}$ nonlinearity.
The thesis is divided into seven *Chapters*, presented in three main *Parts*:

- Part I is dedicated to the discussion of $\chi^{(2)}$ sources of entangled photon pairs. In Chapter 2 the generation of NIR and MIR photon pairs from Periodically Poled Lithium Niobate (PPLN) is presented. The theoretical framework of quasi-phase matching is introduced and the experimental characterization of NIR SPDC photon pairs is presented. In Chapter 3 SHG measurements based on multimodal phase matching in strained silicon waveguides are presented and linked to the theoretical modelling. This is an ongoing experiment within the Nanoscience group, particularly interesting for the possibility to generate MIR entangled photon pairs in silicon via SPDC.
- Part II is dedicated to the discussion of $\chi^{(3)}$ sources of entangled photon pairs. In Chapter 4 the experimental investigation of the optical properties of a relatively high index silicon oxynitride SiON is presented. In particular, we estimated the thermo-optic coefficient of the material and its $\chi^{(3)}$ coefficient. The precise

knowledge of this parameters is needed for an effective design of quantum photonics circuit in this platform. In Chapter 5 the generation of NIR correlated photon pairs in silicon microring is presented. The occurrence of both stimulated and spontaneous FWM was investigated and linked to the theoretical expectation. A one-to-one comparison with the current state-of-the-art in silicon quantum integrated photonics is also addressed.

- Part III concerns the manipulation and detection of the correlated photon pairs presented in Part I and Part II. In Chapter 6 the theoretical and experimental analysis of an asymmetric Mach-Zehnder interferometer fed by NIR entangled photon pairs is presented. The situation of an amplitude unbalanced interferometer asymmetrically excited is considered, where differences in the arms imped perfect cancellation of otherwise closed quantum channels. In Chapter 7 the development of a novel MIR detector with single-photon detection capability is presented. By means of spectral translation, coincidence measurements on MIR twin photons at room temperatures are demonstrated. Finally, in Chapter 8 we demonstrate both theoretically and experimentally, how it is possible to control FWM in a photonic molecule made by two coupled silicon microring resonators. Only two parameters are required to set the internal state of the molecule: the inter-resonator phase and their relative eigenfrequency detuning. The same control can be applied in particular to spontaneous FWM, which therefore represent an intriguing possibility to engineer bright sources of correlated photon pairs in integrated resonators.

The thesis will end with Chapter 9, where concluding remarks and perspectives will be addressed.

Part I

$\chi^{(2)}$ SOURCES OF ENTANGLED PHOTON PAIRS

Part I is dedicated to discuss sources of entangled photon pairs based on $\chi^{(2)}$ optical nonlinearity. In particular in Chapter 2 the generation of correlated NIR and MIR pairs of photon from periodically poled nonlinear bulk material is presented.
In Chapter 3 the activation of a second order nonlinear effect in strained silicon waveguides is demonstrated and linked to the possibility to generate MIR entangled photon pairs in silicon.

2

SPONTANEOUS PARAMETRIC DOWN CONVERSION FROM THE NEAR INFRARED TO THE MID INFRARED

In this Chapter the generation of photon pairs by means of the $\chi^{(2)}$ process of Spontaneous Parametric Down Conversion (SPDC) is presented. In particular the discussion is focused on the generation from a domain engineered nonlinear crystal, known as Periodically Poled Lithium Niobate (PPLN). We will see that through the so-called *quasi phase matching*, it is actually possible to generate Near infrared (NIR) and (MIR) correlated photon pairs.
The experiment described in this Chapter was done in collaboration with Dr. Massimo Borghi and Dr. Mattia Mancinelli.

2.1 SPONTANEOUS PARAMETRIC DOWN CONVERSION

Spontaneous Parametric Down Conversion is a $\chi^{(2)}$ process which can occurs in non-centrosymmetric material. SPDC can be only fully described within the framework of second quantization as it is of spontaneous nature, stimulated by random vacuum fluctuations [98]. The essential feature of SPDC is that a single *pump* photon passing through a nonlinear optical material can decay into two daughter photons obeying energy and momentum conservation. For historic reasons, the two output waves are called *signal* and *idler*, where the output wave with higher frequency is the signal. An intuitive energy diagram sketch of SPDC is reported in Figure 7. These daughter photons are correlated in general in momentum, energy and time. Depending on the polarizations of the interacting fields, one distinguishes between type-0, type-I and type-II processes. Type-I and II processes involve orthogonally polarized fields, whereas in type-0 processes all photons are co-polarized.
The two photons are emitted simultaneously and are characterized, in the case of a non-domain-engineered material, such that the energy and momentum conservation holds [18]:

$$\omega_p = \omega_s + \omega_i \tag{13}$$

$$\mathbf{k}_p = \mathbf{k}_s + \mathbf{k}_i \tag{14}$$

The two-photon quantum mechanical state generated through SPDC is given by [99]:

$$\left|\psi_{gen}\right\rangle = e^{\beta C_{II}^{\dagger} - H.c.} \left|vac\right\rangle \tag{15}$$

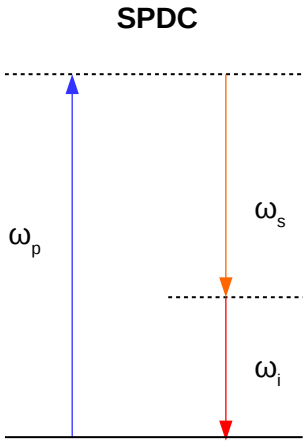

Figure 7: Sketch of the energy diagram for the $\chi^{(2)}$ process Spontaneous Parametric Down Conversion. The frequency of the pump photon is denoted as ω_p, while the frequency of the generated signal (idler) as ω_s (ω_i).

where $|\beta|^2$ is proportional to the average number of pump photons, H.c. stands for hermitian conjugate and

$$C_{II}^{\dagger} = \frac{1}{\sqrt{2}} \int d\omega_s d\omega_i \phi(\omega_s, \omega_i) \hat{a}_s^{\dagger} \hat{a}_i^{\dagger} \tag{16}$$

In Equation 16 we have introduced the function $\phi(\omega_s, \omega_i)$, which is known in literature as the *biphoton wavefunction*. The physical interpretation of the biphoton wavefunction is the following: its modulus square sets the probability to generate a photon pair with frequencies ω_s and ω_i.
In the limit of low pump power, $|\beta| \ll 1$, the quantum state in Equation 15 can be written as:

$$|\psi_{gen}\rangle \simeq |vac\rangle + \beta C_{II}^{\dagger} |vac\rangle \tag{17}$$

such that $C_{II}^{\dagger} |vac\rangle$ is a normalized two-photon state characterized by the biphoton wave function $\phi(\omega_s, \omega_i)$, which depends in general on the parameters of the nonlinear system under analysis, the pump pulse waveform and has to fulfil the energy and momentum conservation relations reported in Equation 13-14. The quantity $2|\beta|^2$ is the average number of generated photons per pump pulse.
In the case $|\beta| \ll 1$, it can be shown that the generated number of photons grows linearly as a function of the incident power [98]. The experimental verification of this power law is reported in Section 2.4.

2.2 THE PHASE MATCHING PROBLEM IN LITHIUM NIOBATE

In this Section, we consider explicitly the process of SPDC in a bulk crystal. The $\chi^{(2)}$ nonlinear bulk crystal medium used in the experiment described in Section 2.4 is lithium niobate ($LiNbO_3$). Lithium niobate is a nonlinear material which naturally exhibits a strong second order nonlinear $\chi^{(2)}$ coefficient. The second order nonlinear polarization can be written as [31]:

$$\begin{pmatrix} P_x^{(2)} \\ P_y^{(2)} \\ P_z^{(2)} \end{pmatrix} = 2\epsilon_0 \times \begin{pmatrix} 0 & 0 & 0 & 0 & d_{31} & -d_{22} \\ -d_{22} & d_{22} & 0 & d_{31} & 0 & 0 \\ d_{31} & d_{31} & d_{33} & 0 & 0 & 0 \end{pmatrix} \begin{pmatrix} E_x^2 \\ E_y^2 \\ E_z^2 \\ 2E_zE_y \\ 2E_zE_x \\ 2E_xE_y \end{pmatrix} \tag{18}$$

where the 2-D matrix in Equation 18 is the second-order nonlinear tensor. The highest coefficient is $d_{33} = 14\,pm/V$, which is the one that mediates type-o interaction, i.e. when all the fields are e-polarized (extraordinary polarized). With respect to the notation used in Equation 7, this corresponds to $\chi^{(2)}_{zzz} = 28\,pm/V$.
Type-o interactions is actually the one exploited throughout the PhD thesis with $LiNbO_3$ and it permits us to drop the tensor notation and consider the second second-order nonlinearity as a scalar quantity, which we call d_{eff}.
Spontaneous Parametric Down Conversion, as any other kind of nonlinear wave mixing process, has to satisfy both energy and momentum conservation laws. Mathematically these conservation laws are expressed by Equation 13-14. The momentum conservation expressed in Equation 14 ensures that a proper phase relationship between the interacting waves is maintained along the propagation direction inside the nonlinear medium. Only if that condition is fulfilled, amplitude contributions from different locations sum up constructively in phase at the end of the nonlinear crystal. Note that the accomplishment of the energy conservation (Equation 13) does not imply the momentum conservation (Equation 14), also called *phase matching condition*.
Considering for example the case of co-polarized collinear plane waves propagating in a material along the z axis, with $\mathbf{k} = k\,\hat{z}$, the momentum relation 14 becomes

$$k_p = k_i + k_s \implies \frac{1}{c_0} n(\omega_p)\,\omega_p = \frac{1}{c_0}\left[n(\omega_s)\,\omega_s + n(\omega_i)\,\omega_i\right] \tag{19}$$

where c_0 is the speed of light in vacuum and $n(\omega)$ is the index of refraction that depends on the frequency.
It is the frequency dependence of the index of refraction that makes phase-matching impossible in most frequency mixing processes, inhibiting constructing interference and therefore lowering the efficiency of the nonlinear process.
In addition to its intrinsic wavelength dependency, the refractive index also depends on temperature. It is phenomenologically described by the Sellmeier equation [100]:

$$n_e^2 = a_1 + b_1 f + \frac{a_2 + b_2 f}{\lambda^2 - (a_3 + b_3 f)^2} + \frac{a_4 + b_4 f}{\lambda^2 - a_5} - a_6 \lambda^2 \qquad (20)$$

where the parameters in Equation 20 depend on the material. In particular, a_3 and a_5 account for poles in the UV and IR wavelengths, with a_2 and a_4 weights respectively. The a_1 parameter accounts for contributions to the refractive index from plasmons in the far UV, whereas a_6 accounts for phonon absorptions in the far IR. Since the resonance frequencies of these effects are far from the spectral range of interest their terms have simplified expressions [100]. The b_i parameters account for thermal effects, involving the temperature dependent parameter f defined as $f = (T - 24.5)(T + 570.82)$, where T is the temperature expressed in °C.
In Figure 8 the magnesium doped lithium niobate (5%MgO:$LiNbO_3$) refractive index dispersion according to the Sellmeier equation at temperature (T =30 °C) is reported [101].

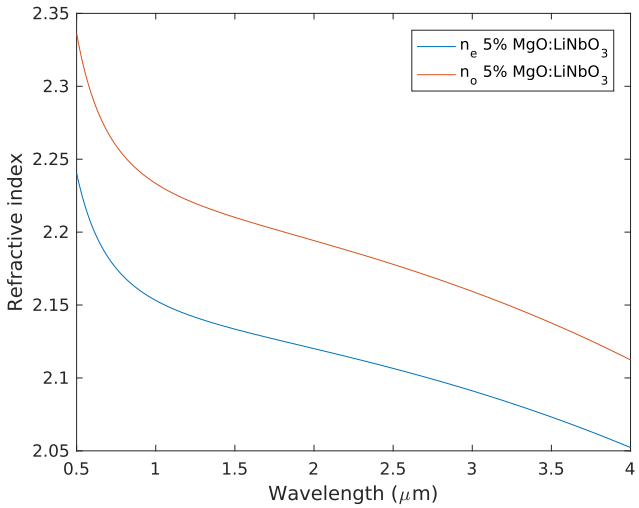

Figure 8: Room temperature extraordinary (blue curve) and ordinary (red curve) refractive index for 5%MgO:$LiNbO_3$. The Sellmeier parameters used are the ones reported in [101]. The refractive index is plotted for the transparency range of the material.

It is thus evident from Figure 8 that the refractive index is a monotonically decreasing function in wavelength, which forbids the momentum conservation explicitly reported in Equation 19. This gives rise to a phase-mismatch Δk.
In the following we are going to demonstrate that the higher the phase mismatch Δk, the lower the generation efficiency in the nonlinear process. To simplify the analysis, let us treat the problem in a classical framework, i.e. considering the stimulated counterpart of the SPDC process, namly Difference Frequency Generation (DFG). We point out that a similar derivation can be done for Second Harmonic Generation (SHG) as well, which will be analysed in Chapter 3 and for Sum Frequency Generation (SFG), which will be analysed in Chapter 7. This is also rather obvious, as SHG can be viewed as a special case of SFG, where the two incoming fields carry the same frequency.
In DFG, in addition to the pump field at ω_p, also the signal field with frequency ω_s is provided, triggering the generation of an idler field at $\omega_s = \omega_p - \omega_i$. Here we suppose DFG occurs in a lossless nonlinear optical medium, excited by collimated, monochromatic, e-polarized and continuous wave input beams. Furthermore let us suppose a normal incidence of the beam on the nonlinear medium, even if the treatment could be generalized (see Chapter 7).
Let us describe the pump and signal waves with wavevectors k_p and k_s so that their complex amplitudes are $E(\omega_p) = A_p e^{ik_p z}$ and $E(\omega_s) = A_s e^{ik_s z}$. Then, one can evaluate the amplitude of the nonlinear part of the polarization of Equation 7 as:

$$P^{(2)}_{DFG} = 4\epsilon_0 d_{eff} E(\omega_p) E^*(\omega_s) = 2\epsilon_0 \chi^{(2)} A_p A_s^* e^{i(k_p - k_s)z} \tag{21}$$

Let us now substitute Equation 21 into the wave equation Equation 5, and since the fields depend only on the z coordinate, we get

$$\frac{d^2 A_i}{dz^2} + 2ik_i \frac{dA_i}{dz} = -\frac{4 d_{eff} \omega_i^2}{c_0^2} A_p A_s^* e^{i\Delta k z} \tag{22}$$

Assuming that $\left|\frac{d^2 A_i}{dz^2}\right| \ll \left|k_i \frac{dA_i}{dz}\right|$, named slowly varying approximation, Equation 22 reduces to:

$$\frac{dA_i}{dz} = \frac{2i d_{eff} \omega_i^2}{k_i c_0^2} A_p A_s^* e^{i\Delta k z} \tag{23}$$

Equation 23 shows how the amplitude of the generated idler wave varies as a consequence of the coupling between the pump and signal waves. If we assume for simplicity A_p and A_s to be constant, known as *undepleted approximation*, by integrating Equation 23 over

the nonlinear medium length L, it is possible to obtain the amplitude of the idler generated field:

$$A_i(L) = \frac{2id_{eff}\omega_i^2}{k_i c_0^2} A_p A_s^* \int_0^L e^{i\Delta k z} dz = \frac{2id_{eff}\omega_i^2}{k_i c_0^2} A_p A_s^* \left[\frac{e^{i\Delta k L} - 1}{i\Delta k}\right] \tag{24}$$

It can be shown that the intensity of an optical field is given by the magnitude of the time-averaged Poynting vector [22], which is linked to the field amplitude by $I_j = 2n(\omega_j)\epsilon_0 c_0 |A_j|^2$ (for $j = p, s, i$).
The intensity of the generated idler is thus given by:

$$I_i = \frac{2d_{eff}\omega_i^2 I_p I_s}{n(\omega_p)n(\omega_s)n(\omega_i)\epsilon_0 c_0^3} L^2 \operatorname{sinc}^2\left(\frac{\Delta k L}{2}\right) \tag{25}$$

where $\operatorname{sinc}(x) = \sin(x)/x$.
As it is evident from Equation 25, the wavevector mismatch information appears only in the factor $\operatorname{sinc}^2(\Delta k L/2)$. This factor, which is known as the phase mismatch factor, is plotted in Figure 9.

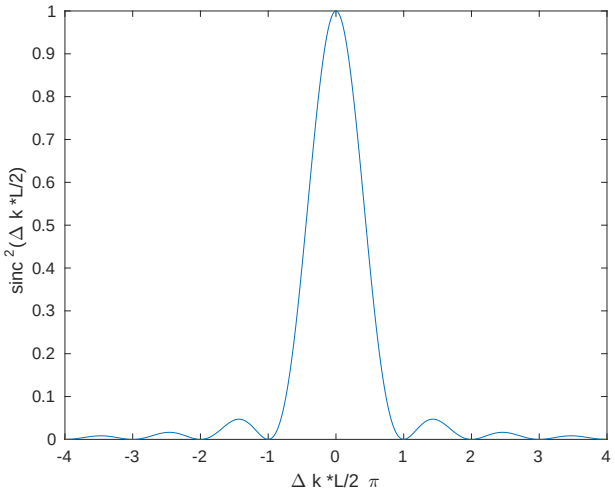

Figure 9: Effects of wavevector mismatch on the idler generated intensity in Equation 25. Here the maximum generated intensity has been normalized to one, i.e. only the phase mismatch factor quantity has been plotted.

The phase mismatch factor is unity for $\Delta k = 0$ and drops as Δk increases, vanishing when $|\Delta k| = \frac{2\pi}{L}$. Therefore for a given L, the larger the mismatch Δk the lower the efficiency. On the other hand, the phase-matching requirement becomes more stringent as L increase.
For a given mismatch Δk, we can define a length L_c that is called *co-*

herence length, which is a measure of the maximum length where the parametric interaction process is efficient

$$L_c = \frac{2\pi}{|\Delta k|} \tag{26}$$

There are various approaches to fullfill the phase matching requirement. A possibility is to use *birefringent* crystalline material, where the refractive index depends on the polarization and direction of the light that passes through it. Thus, the polarizations of the fields and the orientation of the crystal are chosen such that the phase matching condition is fulfilled. This phase matching technique is called angle tuning.
We will see in Chapter 3, that in a guided geometry which supports more than one mode, it is also possible to exploit another phase matching technique, which is called *modal phase matching*.
Another technique to make the nonlinear process efficient is called *quasi-phase matching* (QPM), which is the one exploited with $LiNbO_3$ nonlinear crystals throughout the PhD thesis.
In QPM, frequency conversion is enhanced via a periodicity in the nonlinear crystal. The poling is obtained by using electric fields applied through lithographically defined electrodes, for patterning of the domain structure of ferroelectrics along the crystal [102]. In what follows, we will refer to it as Periodically Poled Lithium Niobate (PPLN).

2.2.1 *Quasi Phase Matching*

Let us describe in the following how the quasi-phase matching technique works.
If the medium possesses a position dependent nonlinear coefficient $d(\mathbf{r})$, from Equation 23-24 we find:

$$I_i \propto \left| \int_V d(\mathbf{r})\, e^{-i\Delta\mathbf{k}\cdot\mathbf{r}}\, d\mathbf{r} \right|^2 \tag{27}$$

where we have generalized the problem to 3-D. Now if $d(\mathbf{r})$ is an harmonic function $d(\mathbf{r}) = d_0\, e^{i\mathbf{G}\cdot\mathbf{r}}$, with $\mathbf{G} = \Delta\mathbf{k}$ then the phase mismatch is fully compensated. The wavevector condition of Equation 14, in this case is replaced with

$$\mathbf{k}_p = \mathbf{k}_s + \mathbf{k}_i + \mathbf{G} \tag{28}$$

In reality it is rather difficult to fabricate a medium with a continuously varying harmonic nonlinear coefficient, as the one considered before. Anyhow, it is possible to fabricate simpler periodic structures, such as as media with nonlinear coefficients of costant magnitude but periodically reversed sign. This is the configuration exploited in the

PPLN crystals that are used in Chapters 2-6-7.
It is well known by Fourier analysis that a periodic function can be decomposed into a superposition of harmonic functions. The one-dimensional case of a periodically square wave modulation of the nonlinear coefficient, is expressed as:

$$d(z) = \sum_{m=-\infty}^{\infty} d_m e^{i\frac{2\pi m z}{\Lambda}} \tag{29}$$

where Λ is the period and $\{d_m\}$ are the Fourier coefficients.
Any of these components may be used for the phase matching. For example for the mth harmonic we have that $G = \frac{m2\pi}{\Lambda} = \Delta k$ and thus:

$$\Lambda = \frac{m2\pi}{\Delta k} = mL_c \tag{30}$$

so that the grating period equals an integer multiple of the coherence length $L_c = \frac{2\pi}{\Delta k}$.
Let us point out more quantitatively the improvement of the conversion efficiency attainable by QPM. As provided by the Fourier series theory in the case of a periodic square wave, $d_m = \frac{2}{m\pi} d_0$ for odd m and zero otherwise. If phase matching is obtained via the mth harmonic $\implies \Lambda = mL_c$, then the parametric conversion efficiency is proportional to $d_m^2 = \left(\frac{2}{\pi m}\right)^2 d_0^2$. On the other hand, a homogeneous medium with nonlinear coefficient d_0 and with the same length L but that suffers a wavevector mismatch Δk, has a conversion efficiency proportional to $\mathrm{sinc}^2\left(\frac{\Delta k L}{2\pi}\right)$ (equation 25). Now, with the formalism of the nonlinear coefficient it can be expressed as $d_0^2\ \mathrm{sinc}^2\left(\frac{\Delta k L}{2\pi}\right)$ which falls as $\left(\frac{d_0 L_c}{\pi L}\right)^2$ when $L \gg L_c$. By inserting $L_c = \frac{\Lambda}{m}$ in the last expression, it can be appreciated that the improvement of the conversion efficiency is a factor $4\left(\frac{L}{\Lambda}\right)^2$.
Thus it is clear that the use of a periodic medium can offer an improvement in the conversion efficiency which scales as L^2, where L is the nonlinear crystal length.

2.2.2 *PPLN for generation of NIR photon pairs at telecom wavelength*

In this PhD thesis work PPLN crystals are used for the generation of photon pairs in the NIR around 1.55 µm and in the MIR, to say around 3.1 µm. PPLN crystals have also been exploited to achieve SFG, in order to up-convert the generated MIR photon pairs into the visible. This is discussed in detail in Chapter 7. In this Chapter the PPLN characteristics for achieving SPDC are analyzed.
In Figure 10 the phase matching curves for the PPLN crystal used in the NIR generation are reported [31].

The curves are for normal incidence, and represent the fulfilment of Equation 28 for different nominal poling periods Λ as a function

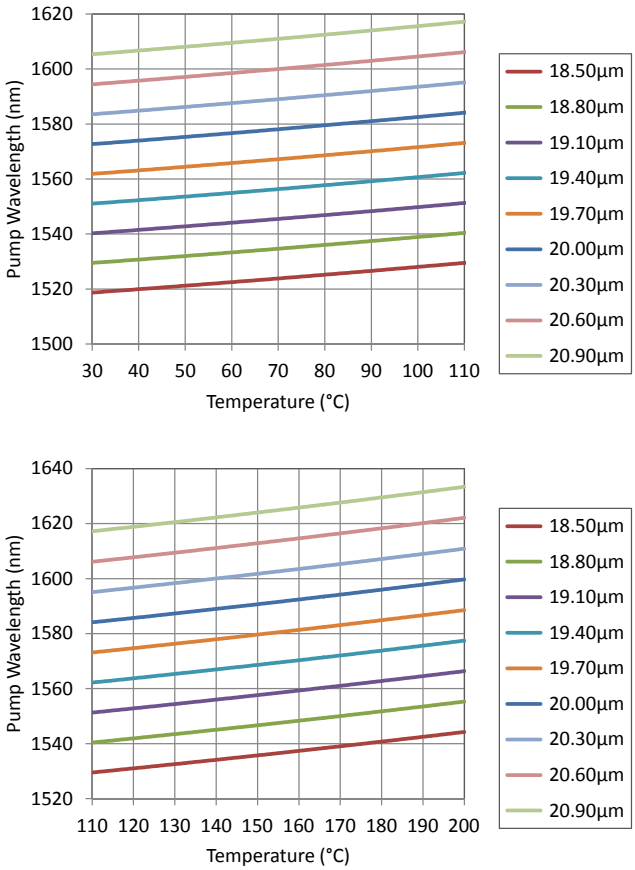

Figure 10: Second Harmonic Generation phase matching curves as function of temperature for 9 different poling periods. Image taken from datasheet [31].

of the crystal temperature. The fine tuning of the phase matching is performed by changing the temperature of the sample with an oven. Indeed, we have seen from the Sellmeier equation (Equation 20) that the $LiNbO_3$ refractive index does depend on the temperature and this actually provides a useful degree of freedom to tune the phase matching condition. Moreover, we will see in Chapter 7 in parametric stimulated processes, such as SFG or DFG, due to the vectorial nature of Equation 28, also the relative angle between two incoming fields upon the PPLN crystal can be exploited to tune the phase matching condition.

The phase matching curves in Figure 10 refer to SHG between 2 pump photons around $\lambda_p = 1550\,nm$, which are nonlinearly converted to a photon at a wavelength $\lambda_p/2$. This is exactly the inverse process of degenerate SPDC where a photon at $775\,nm$ is spontaneously split into two equal daughter photons at $1550\,nm$.

As we will see in Section 2.4, it is also possible to excite non-degenerate SPDC, i.e. with the signal and idler energies that are in general different and are fixed to satisfy Equation 13.

At the considered degenerate wavelength of 1550 nm, as can be seen from Figure 10, three of the available poling periods (18.80 µm, 19.10 µm, 19.40 µm) are able to phase match the process.
The PPLN crystal, shown in Figure 11(a), is sandwiched between a metal holder and an ITO coated glass. The poled regions have 500 µm × 500 µm cross section and are 1 mm long. Each poled grating is separated by 200 µm wide regions of unpoled material. Some poled regions are appreciable in Figure 11(b).

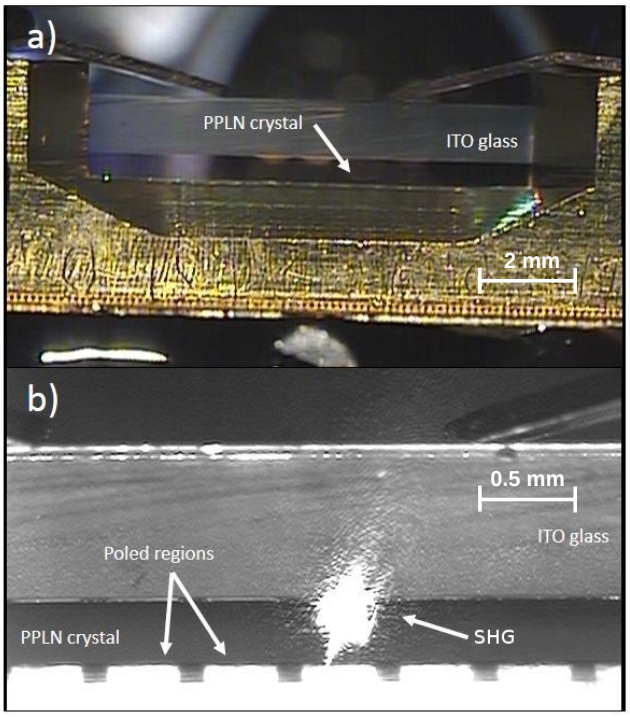

Figure 11: (a) Side view of the PPLN crystal. The crystal is completely transparent and is sandwiched between a conductive ITO glass and a metal holder.(b) Enlarged sideview of the PPLN crystal, showing the locations of the poled regions (actually a reflection on the metal holder) and the selective poling probing operated by the laser beam spot. The bright spot in the picture is due to SHG which generates an optical signal at 775 nm, when the nonlinear crystal is pumped at 1550 nm.

2.2.3 *PPLN for generation of MIR photon pairs*

The PPLN used for the generation of MIR correlated photon pairs at around $\lambda_{deg} = 3.1\,\mu m$ contains 16 poled regions and it is 10 mm long. The poling periods ranges from 24.06 µm to 36.95 µm with a 500 µm × 500 µm aperture. Each region is separated from the adjacent one by 50 µm of unpoled material. Considering SPDC process, with the pump photons at $\lambda_p = \lambda_{deg}/2 = 1.55\,\mu m$, the only available poling region which could achieve the quasi-phase matching condition has a nominal poling period equal to $\Lambda_{MIR}^{nom} = 34.48\,\mu m$.
We will see in Chapter 7, that we experimentally observe degenerate SPDC emission at $T_{deg}^{exp} = 135\,°C$. Compared to the theoretical expectation, this leads to a real poling period of $\Lambda_{MIR}^{real} = 34.68\,\mu m$.
In Figure 12 the simulated quasi-phase matched wavelength as a function of the crystal temperature is reported . The simulation is actually based on Equation 28 in the case of a collinear process, with the pump photons at 1.55 µm, 10 mm, long crystal with the estimated poling period of 34.68 µm. From Figure 12 it can be seen that at around a tem-

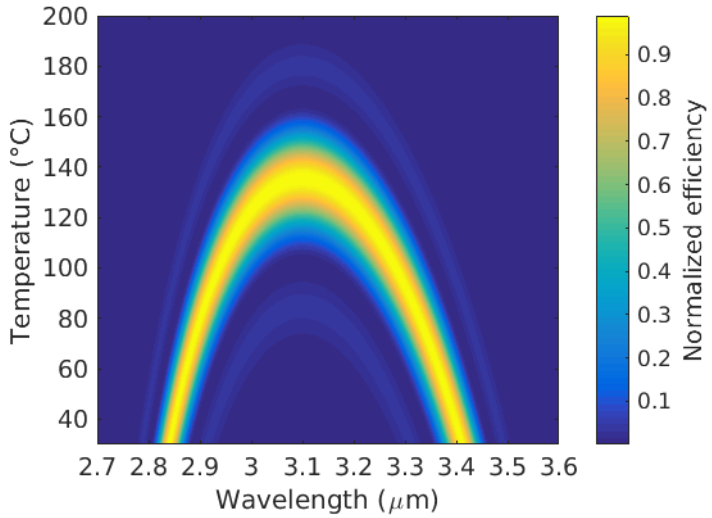

Figure 12: Simulated SPDC spectra as a function of the temperature. The simulation has been derived considering a collinear SPDC process, with the monochromatic pump photons at 1.55 µm and a 10 mm long crystal with a poling period equal to 34.48 µm.

perature of $T_{deg} = 135\,°C$ there is the generation of degenerate photon pairs at $\lambda_{deg}^{MIR} = 3.1\,\mu m$, with a bandwidth of 200 nm. For lower temperature SPDC occurs in a non-degenerate fashion, where the signal and idler frequencies are fixed by the conservation of energy and the process is efficient when the phase matching relation in Equation 28 is satisfied.

2.3 EXPERIMENTAL SET-UP NIR

In this Section the experimental set-up used to generate and detect SPDC generated photon pairs at telecom wavelength is presented. The experimental set-up used to generate and detect SPDC generated photon pairs at around 3.1 µm is discussed in detail in Chapter 7.
In Figure 13 the experimental set-up used to generate NIR correlated photon pairs is reported. The light source is a 775 nm Ti:Sapphire

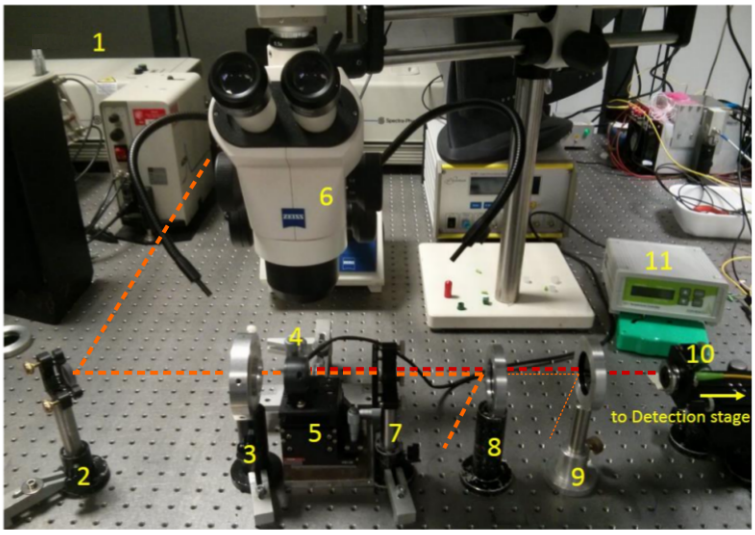

Figure 13: NIR photon pairs generation set-up. (1) 775 nm CW laser (2) Gold mirror (3) Input lens (4) Oven with PPLN crystal inside (5) Alignment stage (6) Microscope equipped with a visible camera (7) Output lens (8) 1500 nm long-wave pass filter (9) 1200 nm long-wave pass filter (10) Collimator (11) Temperature controller (TEC). The long-wave pass filter ordering is not important in the pump filtering operation.

laser equipped with an acousto-optic modulator that can switch the laser operation from a quasi-CW (not mode locked) to mode locked. The laser operates in the quasi-CW regime in our experiment. The output beam, of approximately 440 µm waist, has an average power of 1 *W*. Its power can be tuned using a variable optical attenuator. A gold mirror, directs the beam into the input converging lens, which has a focal length of 5 cm. The PPLN crystal is placed in the focal plane of the lens, where the beam waist is minimum and equal to 12 µm. The PPLN crystal used is shown in Figure 11. The crystal is 1 mm long and contains 9 different poled regions of 500 µm × 500 µm cross section and. As can be seen from Figure 10, it guarantees quasi phase matching in the range 760 nm - 820 nm of input wavelength. The fine tuning of the phase matching is performed by changing the temperature of the sample with an oven. This is accomplished using a temperature controller (TEC). The temperature can be tuned in the

range 30-200 °C, with a stability ±0.1 °C.
The SPDC photons and the 775 nm pump are collected and collimated by a lens of 8.5 cm focal length. Two long-wavelength pass filters (1200 nm and 1500 nm of cut-off wavelength respectively) allows to filter out the pump from the IR light, providing an isolation higher than 100 dB. Since the SPDC process is inherently inefficient, such a strong pump filter rejection stage is needed, in order to let only the generated photon pairs to reach the detector. Due to the one-octave frequency difference between the pump photons and the generated ones, this is typically easy to do with SPDC. We will see in Chapter 5 that the filtering operation becomes less trivial in the case of photon pairs generated by the $\chi^{(3)}$ based nonlinear process of spontaneous FWM.
Coming back to Figure 13, after the filtering stage, the IR beam is coupled into a single-mode fiber using a collimator. To maximize the coupling efficiency, the collimator can be tilted and translated in all the directions using a micrometric alignment stage. We estimated a total loss of 7.8 dB from the output facet of the sample to the SM fiber. The fiber is connected to a single photon counting module (ID Quantique id201) [32], a detecor based on a cooled InGaAs/InP avalanche photodiode (APD).

2.3.1 *Single-photon avalanche photodiode*

Spontaneous nonlinear parametric processes, such as SPDC or spontaneous FWM, typically leads to extremely low generation efficiency. Therefore, to detect the generated photon pairs one needs single-photon counting capability. In Section 2.4 we will see that the measured SPDC generation efficiency is $\eta \sim -100$ dB.
APD's are used to detect very low levels of light when it is needed to have a detector with a large gain factor. An APD is a highly sensitive semiconductor electronic device that exploits the photoelectric effect to convert light to electricity. It is basically a reversed-biased pn junction, with a strong electric field within the junction.
An APD can be used in *linear* (or proportional) mode by applying to the pn junction a reverse-bias voltage below the breakdown voltage V_{br}, or in geiger-mode with a voltage well above the breakdown voltage. The two operation modes are sketched in Figure 14.

Geiger-mode avalanche photodiode, also known as Single Photon Avalanche Diode (SPAD), works in the geiger-mode operation and can achieve single photon counting capability. In this mode, the absorption of a single photon triggers an avalanche breakdown within the semiconductor material, thereby creating a large current pulse that indicates the arrival of the photon. If the primary carrier is photo-generated, the leading edge of the pulse marks the arrival time of the detected photons. The generated current is self-sustaining until the

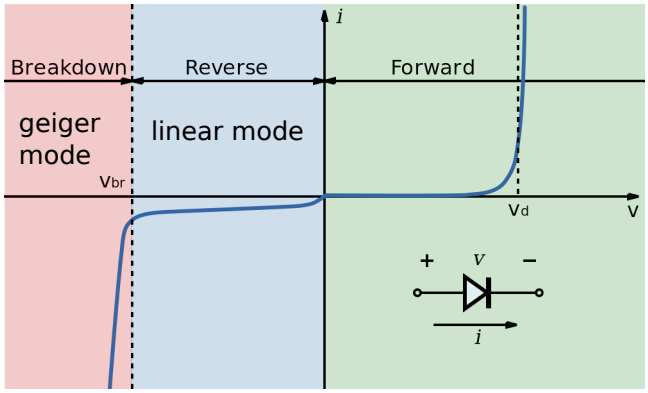

Figure 14: I-V characteristic of a pn junction. A detector works in the reverse-biased region. For $|V| < |V_{br}|$ the APD detection operation is in linear-mode, whereas for $|V| > |V_{br}|$ the operation regime is geiger-mode.

avalanche is quenched by lowering the bias voltage down to or below the breakdown voltage. At this point, the lower electric field in the junction is no longer able to accelerate carriers to excite other carriers, therefore the current ceases. Then, in order to be able to detect another photon, the bias voltage must be raised again above breakdown. There can be adopted several quenching mechanisms in single-photon counting units system. The one used in ID Quantique id201, is a gated quenching mechanism. With this method, the detector is periodically enabled ($|V| > |V_{br}|$) to detect photons with an adjustable frequency and duty cycle, which are optimised depending on the experimental characteristics.
Why don't we let the detector always on, to maximize the detection probability of detecting photons?
Well, this is due to the fact that in SPAD thermal effects can produce current pulses even in the absence of illumination. The resulting average number of counts per second is called *dark count* rate and is a key parameter in defining the detector noise. Dark pulses are due to electron-hole pairs thermally generated within the semiconductor. The dark count rate probability P_{DC} in a semiconductor APD generally follows a Boltzmann distribution, given by [103]:

$$P_{DC} \propto e^{-\frac{\Delta E}{k_B T}} \tag{31}$$

where ΔE is the semiconductor energy band-gap, k_B is the Boltzmann constant and T is the temperature. For a given material, i.e. fixing the band-gap ΔE, the higher the temperature, the more the dark counts. On the other hand, for the same working temperature, from Equation 31 one can see that, the lower the semiconductor energy band-gap, the higher the probability to thermally promote electron-hole pairs. This is the case for example of MIR detectors, which intrinsi-

cally have higher dark count rate with respect to visible detectors. In addition, MIR detectors are inherently sensitive to unwanted incident black-body radiation, which actually represents a non-negligible source of noise. Cooling the detector generally reduces these two noise sources, however these detectors still feature a lot of noise and often exhibit poor signal-to-noise ratios [104], which inhibit single-photon counting capability. We will see in Chapter 7, that a possible solution is to efficiently up-convert MIR photons into the visible domain, in order to exploit the high efficient and low noise silicon-based SPAD.

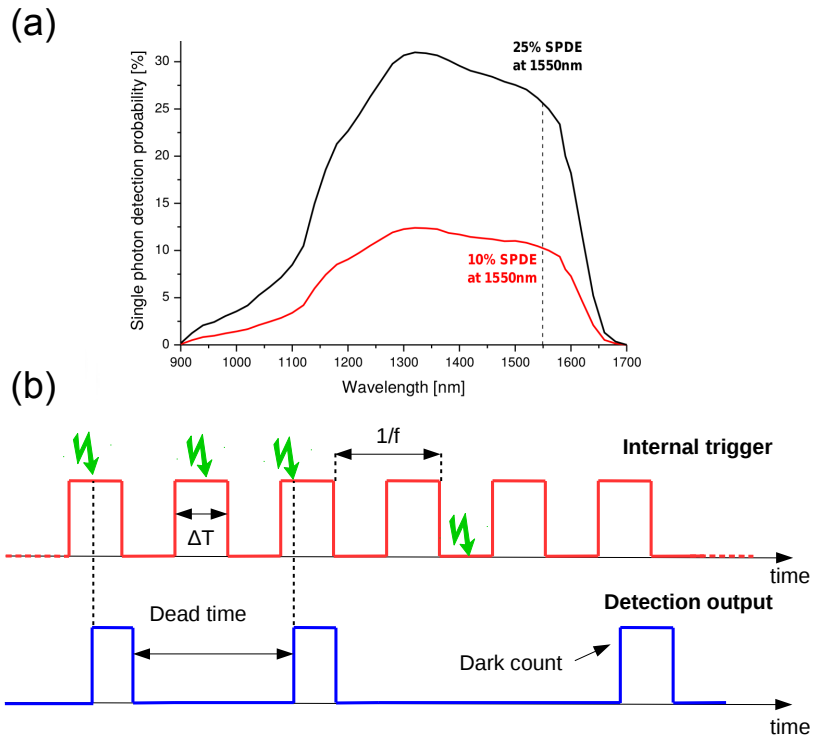

Figure 15: (a) Single photon detection probability versus wavelength. The red curve reports the 10% level setting at 1550 nm, while the 25% level at 1550 nm is reported in black. Image taken from [32]. (b) Sketch of the principle of operation of a gated APD, with a f gating frequency and a gate window ΔT.

The total dark count rate includes primary and secondary pulses. Secondary dark pulses are due to *after-pulsing* effects. The physical origin of after-pulse is the following: during an avalanche event some carriers are captured by deep levels in the junction and subsequently released with a statistically fluctuating delay; released carriers can re-trigger the avalanche, generating after-pulses correlated with a previous avalanche pulse. After-pulsing may strongly enhance the total dark count rate. Typically fast active quenching and a suitable *dead*

time, a tunable time interval which follows each detection in which the detector is off, strongly reduce the after-pulsing impact on the detector noise [105].

In the experimental measurements reported in Section 2.4, we used an InGaAs SPAD (ID Quantique id201) which shows sensitivity in the range $900-1700\,nm$. Its detection probability is reported in Figure 15(a). As it is sketched in Figure 15(b), the SPAD works in gated configuration, i.e. it measures for a time window of ΔT with a frequency f. If the device detects one photon (or a dark count), the detector is then blind for the dead time time window. The SPAD sensitivity has been set to 25 %, gating frequency $f = 10\,kHz$ and gating window $\Delta T = 100\,ns$. We experimentally checked that the 10 kHz gating frequency actually gives us the better signal to noise ratio. With this settings, the average dark count rate is $DCR = 100\,Hz$ and the maximum count rate is given by $CR = 10\,kHz$ (when no dead time is set).

2.3.2 *Home-made monochromator*

Since the power of the generated radiation through SPDC is too low to perform a spectrum with a standard Optical Spectrum Analyser (OSA) (lowest limit of detection $\sim -90\,dBm/nm$), a free space monochromator was built to acquire the spectrum of the down converted photons. A picture of the home-made monochromator is reported in Figure 16.

In order to be able to record the SPDC spectrum, after the collimator placed in position 10 in Figure 13, the IR radiation is guided through an optical fiber, coupled at its end to another collimator. To study the generated spectrum at wavelength lower than $1500\,nm$, the two long-pass filters in Figure 13 were substituted with a visible dichroic mirror and a silicon slab.

The SPDC photons are emitted in free space towards a reflection diffraction blazed grating mounted on a rotating platform (position 3 in Figure 16). The grating used is characterized by $600\,grooves/mm$ and a dispersion of $1.46\,nm/mrad$. To calibrate the grating, the oth-order reflection of a reference He-Ne laser beam (position 2 in Figure 16) was traced over a graduated system which follows the rotation of the grating (sketched as a ruler in the picture). A collimator was mounted over a micrometric alignment stage to let it translate and tilt. It was aligned to collect the 1st-order diffracted light coming from the grating. The position of the collimator is then fixed and the coupled 1st-order diffraction wavelengths is tuned as a function of the grating rotation. A CW, C-band, tunable infrared laser (Tunics T100-S HP from Yenista Optics) was used to calibrate the system: as a function of the incident wavelength, the grating was rotated to maximize the collected radiation and according to this rotation the oth-order re-

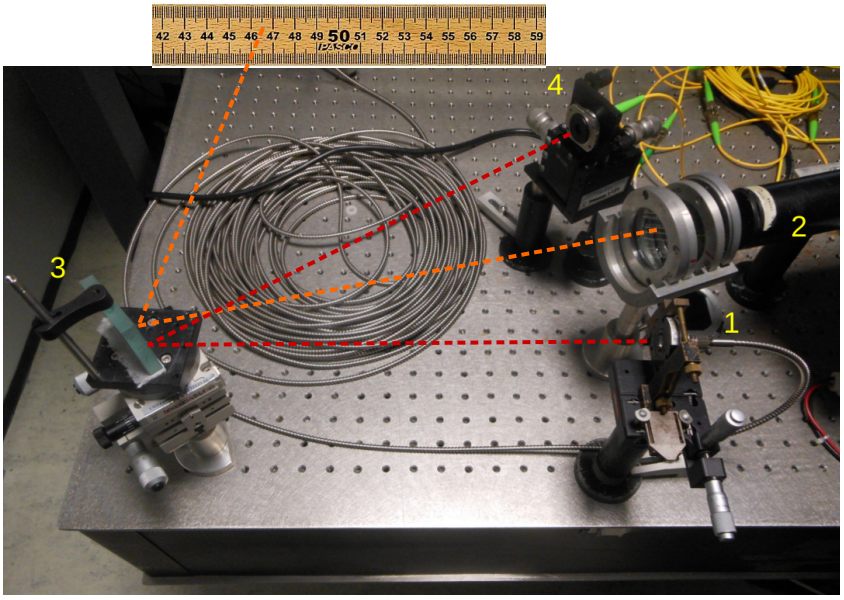

Figure 16: Free space home-made monochromator. (1) Optical fiber coming from the collimator placed in position 10 in Figure 13(a) (2) He-Ne laser at 632.8 nm (3) Grating (4) Collimator.

flected He-Ne beam that impinges on the graduates system has been recorded. Repeating this procedure for several wavelengths, it was actually possible to accurately calibrate the system. The spectral resolution of the instrument is about 0.5 nm. After the collimator, the collected signal is coupled into an optical fibre which is connected to the id201 SPAD.

2.4 EXPERIMENTAL MEASUREMENTS SPDC NIR

In this section, the experimental measurement to characterize the NIR SPDC process are presented.
First of all, we studied the quasi-phase-matched wavelengths as a function of the temperature of the crystal for different poling periods. Following the Covesion guidelines [31] (company from which we bought the crystals), we verified that the maximum rate of generated photons is found at the particular temperatures reported on the manufacturer datasheet (see Figure 10).
We started with a characterization of SHG, i.e. with the pump photons at 1550 nm which are frequency-doubled to 775 nm. The graph reported in Figure 17(a) is a tuning curve of the generated power at 775 nm as a function of the temperature for the poling period $\Lambda = 19.10\,\mu m$. In accordance with the data-sheet [31], the maximum

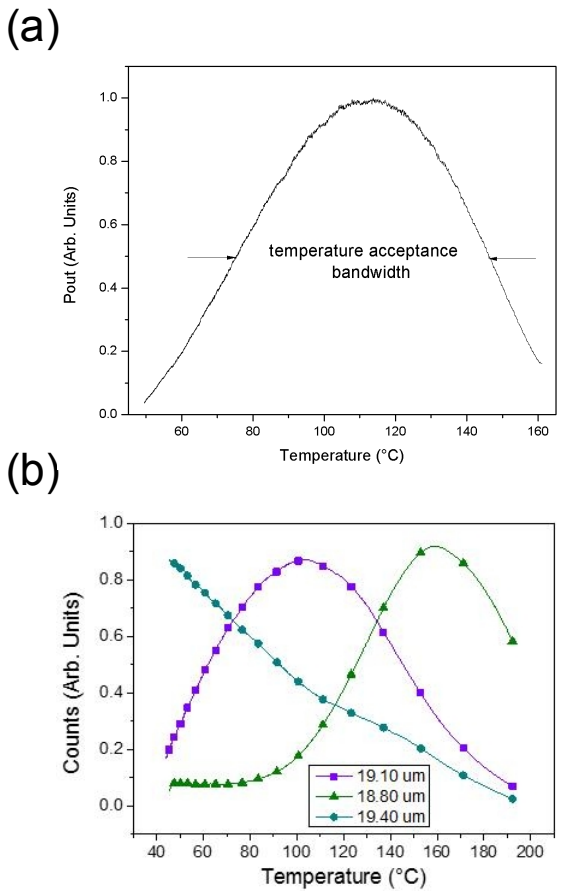

Figure 17: (a) SHG normalized power temperature dependence for a 1550 nm pump source for the poling period $\Lambda = 19.10\,\mu m$. (b) Normalized SPDC power temperature dependence tuning curves for 775 nm pump source, for poling periods 18.80 µm, 19.10 µm and 19.40 µm. The PPLN crystal length is 1 mm.

efficiency has been found at T = 110 °C. The temperature acceptance bandwidth, defined as the Full Width at Half Maximum (FWHM), is also compatible with the simulated one and it is found to be about 83 °C. Since the temperature acceptance bandwidth is quite large (generally the longer the crystal, the narrower and more sensitive the acceptance bandwidth), it is not possible to appreciate the side lobes of the $\mathrm{sinc}(x)$ of Equation 25 in the available temperature range. We also checked that the SHG generated radiation follows a quadratic relation as a function of the incident power.

After having preliminary characterized the SHG process, we proceeded with SPDC measurements. According to the SHG quasi-phase matching curves reported in Figure 10, around the degenerate wavelength of 1550 nm, only three poled regions can be exploited. The

three suitable poling periods are: 18.80 µm, 19.10 µm and 19.40 µm (respectively the green, violet and light blue curves).
In Figure 17(b) the experimental SPDC generated photons as a function of the $LiNbO_3$ crystal temperature are reported for the three poling periods. The experimental curves were obtained thanks to the experimental set-up reported in Figure 13. The fact that the three experimental curves depend on temperature and thus on the phase matching condition, Equation 28, is a clear sign of the occurrence of nonlinear parametric interaction. In particular the violet curve in Figure 17(b) resembles the one in Figure 17(a) for the SHG process.
For each studied poling period, the temperature at which the maximum generation efficiency is observed is consistent with what is expected from the curves reported in Figure 10.
However it is worthy to remark that SHG can be thought as the inverse process for SPDC, only if degenerate SPDC process is considered. For non-degenerate SPDC processes, the phase-matching relation of Equation 28 is in general different with respect to the one for SHG. Note that in Figure 17, the generated photons are integrated in the range 1500 −1650 nm. This bandwidth is defined by the higher wavelength long-pass interference filter, which has an abrupt decrease of the transmittance at 1500 nm, and by the roll-off of the detector efficiency, which occurs approximately at 1650 nm (see Figure 15(a)).
As a matter of fact, from Figure 17 we do not get a precise information about the spectrum of the generated photons.
The SPDC efficiency can be estimated knowing the pump power, the total losses from the PPLN nonlinear crystal to the detection stage and the measured count rate. The pump power incident on the PPLN crystal has been measured through a thermopile.
The generated power was measured with the single-photon coun-ter. A total loss of 7.8 dB from the output facet of the PPLN crystal to the SM fiber connected to the single-photon detector was estimated. Figure 18 reports the measured generated power as a function of pump power, for $\Lambda = 19.10\,\mu m$ at the maximum efficiency temperature T = 80 °C. As it is expected from the theory, at low pump power the SPDC power has a linear relation as a function of the incident pump power [98, 106]. This is experimentally confirmed by the linear fit in Figure 18. A conversion efficiency of (-99.6 ± 0.1) dB is estimated from the linear fit slope. The maximum generated photon flux is about 600 MHz.

Commercial similar PPLN crystals have a SPDC generation efficiency ∼−70 dB, [107] which is 30 dB higher then what we measured. A possible explanation of such a low generation rate could rely on the very poor quality of the poling of the crystal. Indeed, the microscope image shown in Figure 19 reveals that the poling is not perfectly periodic and suffers from several fabrication imperfections. While it is

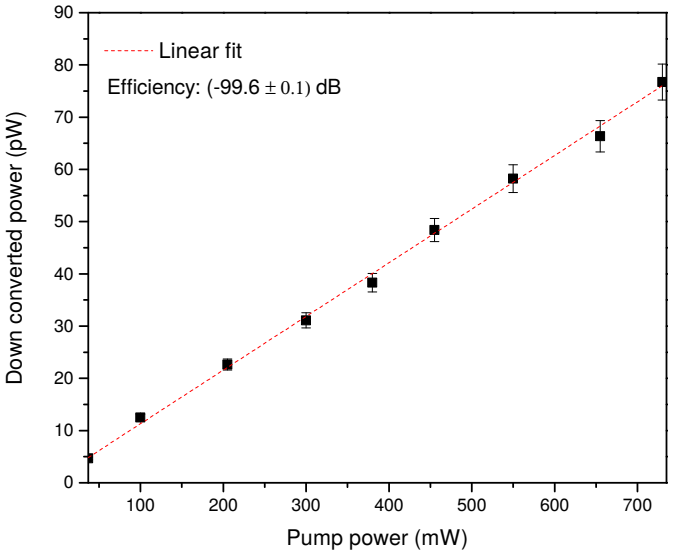

Figure 18: Generated SPDC power as a function of the pump power P_{in}. The red line is the linear fit while the scatters are experimental data.

not possible to directly see the ferroelectric patterned domain within PPLN with a visible camera, it is actually possible to see the reference crystal etching in correspondence of the poled gratings. However, such fabrication defects are likely to be effective defects also in the poling period.

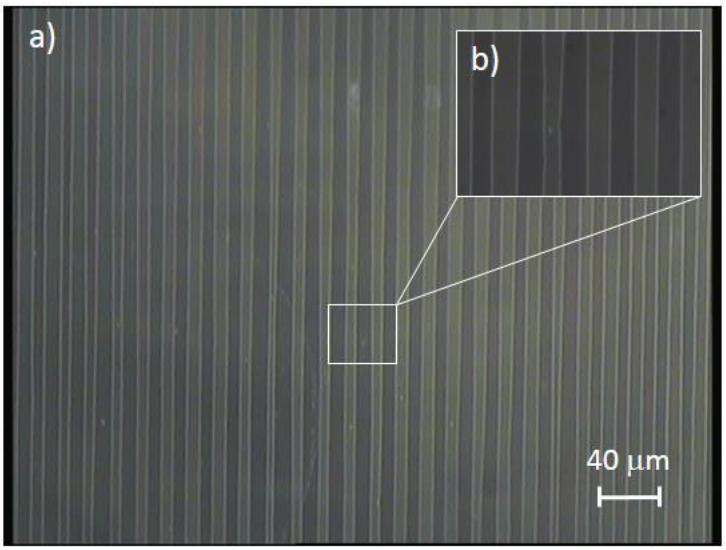

Figure 19: (a) Microscope image of the 19.1 µm poling period in our sample. (b) Details of the poling, revealing fabrication imperfections.

The effect of random imperfections is to lower the amplitudes of the spatial frequencies in the Fourier series in Equation 29, and, at

the same time, to add a background of new spatial frequencies (some of them can be phase matched with the input radiation, with the consequence that the spectral width of the generated radiation broadens). This effect is known as inhomogeneous broadening [22]. Since the generated power is proportional to the amplitude of these spatial frequencies, the overall efficiency of the process decreases.

Let us compare the experimentally observed conversion efficiency with the ones reported by various groups in literature. To do this, the typically used figure of merit for characterizing a photon pairs source is the *brightness*. The brightness indicates the rate of generated photons per unit of input power and bandwidth. A pair photon flux of about $\sim 10^6\,s^{-1}mW^{-1}nm^{-1}$ for a 10 mm long bulk crystal was reported in [108]. In our case, instead, the estimated brightness is about $\sim 6\times10^3\,s^{-1}mW^{-1}nm^{-1}$, which is more than two orders of magnitude lower. It must be considered, for a fair comparison, that our PPLN bulk crystal is 1 mm long and it is well known that SPDC efficiency grows linearly with the crystal length [109]. Still, considering also the length difference, our experienced brightness shows a limited brilliance, probably due to the detrimental random poling imperfections already pointed out.
Let us comment also that many works in literature deal with PPLN waveguide, rather than bulk PPLN. As a matter of fact, the use of a guiding structure permits the confinement of the pump, signal and idler beams over the entire length of the waveguide [110], which eventually results in a much more brilliant source. Bright narrowband photon pairs sources, particularly useful for long distance quantum communication experiments, of about $\sim 10^5\,s^{-1}mW^{-1}pm^{-1}$ were demonstrated so far by many groups [111, 112].

Let us come back to the experiment. The generated photon flux after the collimator stage N_c (position 10 in Figure 13) is given by:

$$7.8 = 10\log\left(\frac{N}{N_c}\right) \Longrightarrow\ N_c = N\,10^{-0.78} \simeq 100\,MHz \tag{32}$$

The corresponding generated power evaluated at $\lambda_{deg} = 1550\,nm$ is given by:

$$P = N_c\frac{hc_0}{\lambda_{deg}} \simeq 13\,pW \tag{33}$$

where h is Planck's constant. We checked experimentally that it was not possible to acquire a spectrum of the generated radiation with a standard OSA. This suggests that the generated power is actually broadband, symmetrically distributed around $\lambda_{deg} = 1550\,nm$. This is due to the energy conservation 13, thus if one photon of the pair is spectrally placed on the left of λ_{deg} the other photon must be placed symmetrically (in energy) with respect to λ_{deg} on the right.
In order to be able to perform spectra of the generated radiation

through SPDC, a free-space monochromator was built as it was explained in Section 2.3. To prevent spectra to be affected to both the fact that the grating may be not perfectly aligned with respect to the collimator for each wavelength, and also by the varying detector *responsivity* as a function of wavelength, a calibration was performed. The calibration was done by taking the spectrum of a broad band halogen lamp either with the OSA and with the free-space monochromator. The OSA responsivity is electronically compensated and therefore it is able to take a reference spectrum of the halogen lamp without been affected by spurious effects. The calibration curve was used to normalize the SPDC spectra, thus getting rid of spurious effects.
Spectra were taken for the three different poling periods able to achieve phase matching at the studied pump wavelength: 18.80 µm, 19.10 µm and 19.40 µm. In order to not be redundant in the description, only the analysis of the 19.10 µm poling period is reported in the following. The spectra reported in Figure 20(a) were taken with the single-photon detector connected through a GPIB cable in real time with a Labview software on a computer. Each experimental data was accumulated for 30 s.
Increasing the temperature, two peaks emerge and separate on the sides of λ_{deg}. In particular, this behaviour is clear for the peak at shorter wavelength, while the longer wavelength peak has a wavelength which lies beyond the spectral responsivity of our detector, see Figure 15(a). The experimental spectra are compatible with the simulation reported in Figure 20(b), which reports the simulated quasi-phase matched wavelength as a function of the crystal temperature. The simulation assumes a collinear process, with monochromatic pump photons at 775 nm and a 1 mm long crystal with a poling period of 19.10 µm. The experimental down-converted radiation bandwidth at T = 80 °C is $\gtrsim$ 400 nm, compatible with the simulated one.

In Chapter 6 coincidence measurements to assess the correlated nature of the NIR SPDC photon pairs will be presented. The photon pairs will be then injected into the same input port of an asymmetric free-space Mach-Zehnder interferometer (MZI). Two-photon quantum interference fringes are experimentally observed as a function or the relative time delay between the two MZI arms, which demonstrates the colour-entangled nature of the photon pairs.

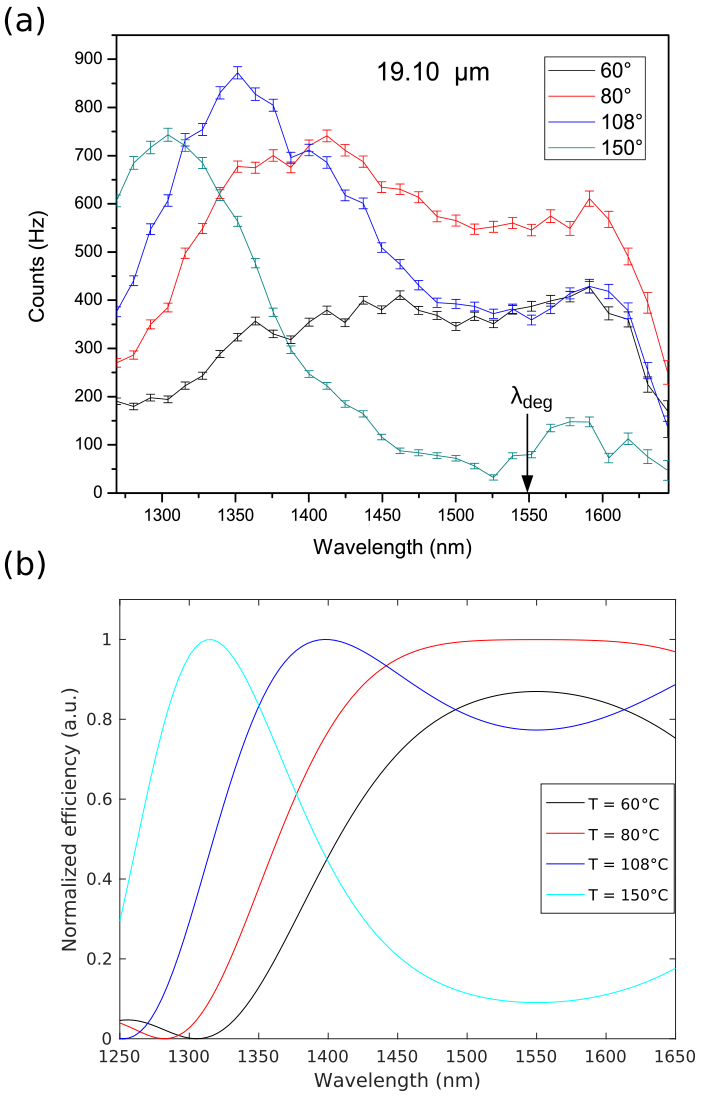

Figure 20: (a) Spectra of the generated radiation through SPDC as a function of $LiNbO_3$ temperature for the poling period 19.10 μm. The CW pump wavelength was fixed at 775 nm. (b) Simulated SPDC spectra as a function of the temperature. The simulation was derived by considering a collinear SPDC process, with the CW pump photons at 775 nm and a 1 mm long crystal with a poling period equal to 19.10 μm.

3

SECOND HARMONIC GENERATION IN STRAINED SILICON WAVEGUIDES

In this chapter the theoretical and experimental demonstration of Second Harmonic Generation (SHG) in strained silicon waveguides is presented.
Bulk silicon has a centrosymmetric crystalline structure that leads to a zero second order nonlinear $\chi^{(2)}$ coefficient in the dipole approximation. On the other hand, $\chi^{(2)}$ effects are highly sought in Si, for example for developing low power and fast electro-optic modulators. Recently, it has been reported that by stressing a Si waveguide with a silicon nitride over-layer, a sizeable $\chi^{(2)}$ is induced [113].
Moreover, in [114] SHG measurements were reported in large area strained silicon waveguides. However, the SHG data were affected by different contributions caused by the interfaces, the free carrier induced internal electric fields, the inhomogeneous strain and the uncontrolled modal structure of the waveguides.
In what follows, we present, instead, SHG in Silicon On Insulator (SOI) strained Si waveguides, designed by a nonlinear propagation model.
The experiment described in this Chapter was done with the collaboration of Mr. Alessandro Marchesini, Dr. Mattia Mancinelli and Mr. Claudio Castellan. Mr. Claudio Castellan also performed the waveguide simulation and the theoretical analysis reported in Section 3.2.2. The samples were fabricated by Dr. Mehr Ghulynian at the Bruno Kessler Foundation.

3.1 SECOND HARMONIC GENERATION IN SILICON

Second Harmonic Generation is a $\chi^{(2)}$ process in which two photons with the same frequency ω_p interacting with a nonlinear material are effectively converted into a photon with twice the energy.
The energy and momentum conservation laws for the SHG process are given by [18]:

$$2\omega_p = \omega_p + \omega_p \tag{34}$$

$$\frac{4\pi}{\lambda_p} n(\lambda_p/2) = \frac{4\pi}{\lambda_p} n(\lambda_p) \tag{35}$$

where $n(\lambda)$ is the refractive index of the material involved in the process. In Figure 21(a) the energy level scheme for the SHG process is reported.
In general for a dispersive material $n(\lambda_p/2) \neq n(\lambda_p)$, which intro-

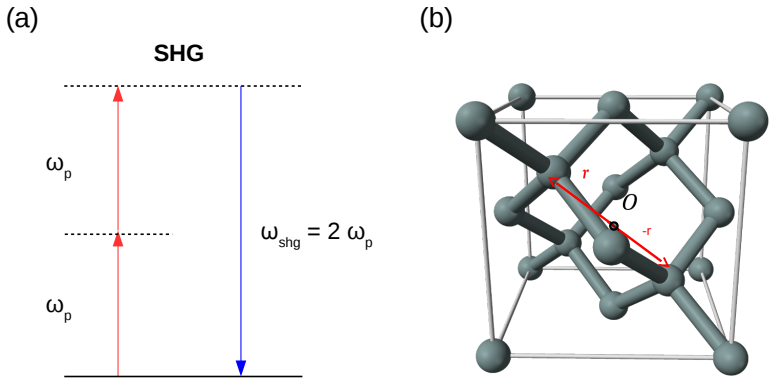

Figure 21: (a) Sketch of the energy diagram for the $\chi^{(2)}$ process of Second Harmonic Generation. The frequency of the pump photon is denoted as ω_p, while the frequency of the generated signal (idler) as ω_s (ω_i). (b) Bulk silicon crystalline structure.

duce a phase mismatch Δk in the momentum relation Equation 35.
It is not difficult to show, as we did for DFG in Equation 25, that this inhibits the conversion efficiency of the process, with a typical $\text{sinc}^2(\Delta kL/2)$ dependence, where L is the length of the considered nonlinear material. The larger the phase mismatch Δk, the lower the conversion efficiency.
Beside the phase matching issues, $\chi^{(2)}$ processes are also inhibited by the geometrical structure of the considered nonlinear material.
In particular, in the following we show that $\chi^{(2)}$ processes are not efficient in centrosymmetric material.
This is the case for example of bulk silicon, whose crystal structure is reported in Figure 21(b). As it is possible to see from the image, crystalline bulk silicon presents the diamond crystal structure, which can also be seen as a pair of intersecting face-centred cubic lattices, displaced by $1/4$ of the width of the unit cell in each dimension[115].
Indeed, let us suppose to consider a material with a centrosymmetric crystal lattice. Let us evaluate the result of a parity inversion transformation (a point reflection), that is to say to flip the sign of the spatial coordinates $\mathbf{r} \rightarrow -\mathbf{r}$ to the polarization vector, given in Equation 3. Under point reflection transformation, the electric field $\mathbf{E}$ flips, and the polarization vector results:

$$\mathbf{P}(-\mathbf{E}) = \varepsilon_0\left[-\chi^{(1)}\cdot\mathbf{E} + \chi^{(2)}:\mathbf{E}^2 - \chi^{(3)}\vdots\mathbf{E}^3 + ...\right] \tag{36}$$

However, due to the centrosymmetry, if the electric field flips, the polarization has to flip too. This leads to the condition $\mathbf{P}(-\mathbf{E}) = -\mathbf{P}(\mathbf{E})$,

which is only satisfied if $\chi^{(2)} = 0$.
Inducing second-order nonlinear effects in silicon waveguides requires the ability of destroying its centrosymmetric crystalline structure. In recent years, this has been achieved with the deposition of strain layers at the waveguide boundaries [116]. This idea led to the demonstration in (2006) of the Pockels effect [18] in silicon photonic crystal waveguides strained by a silicon nitride cladding [113]. In the experiment the authors realized a phase modulator by means of a Mach–Zehnder interferometer (MZI). By applying a DC electric field to one of the MZI arms, the effective refractive index of the propagating mode is altered by means of the Pockels effect. They estimated a $\chi^{(2)}_{\text{eff}} \sim 15\,\text{pm/V}$. Again, in (2014) a second order nonlinear coefficient as high as $\chi^{(2)}_{\text{eff}} \sim 340\,\text{pm/V}$ was reported [117].
However, recent experiments introduced some doubts on the interpretation of these measurements, attributing the measured electro-optic effect to the accumulation of free-carriers [118–121].
Also the SHG process was demonstrated in strained silicon waveguides, which estimated $\chi^{(2)}_{\text{eff}} = (40 \pm 30)\text{pm/V}$ [114]. These measurements were taken on a highly multimodal waveguide, without an accurate analysis of the modal structure of the interacting modes. In this scenario, the mode overlap between the optical modes and the tensor nature of the nonlinear susceptibility $\chi^{(2)}$ are completely ignored. In addition to the uncontrolled modal waveguide structure, the SHG data were affected by different contributions caused by the interfaces, the free carrier induced internal electric fields and the inhomogeneous strain [19]. In particular, the presence of trapped charges at the silicon/silicon nitride interface may result in the formation of a static field inside the waveguide, that can activate a field induced second order nonlinearity (EFISH) [122].

In what follows the modeling and the SHG measurement in Silicon On Insulator (SOI) strained Si waveguides is presented.
The design maximizes the SHG efficiency by a detailed simulation of the waveguide modal structure to achieve proper phase matching:

$$n_{\text{eff}}(\lambda_p/2) = n_{\text{eff}}(\lambda_p) \tag{37}$$

where n_{eff} refers to the effective refractive index experienced by the considered propagating mode within the waveguide. We will show the phase matching condition can be satisfied by different optical modes, condition known as *modal phase matching*.

This is actually a currently ongoing experiment within the NanoLab and at the end of the Chapter future perspectives and next actions on the topic will be addressed.

3.2 THEORETICAL MODELLING

In this section the theoretical modelling for the waveguides design is presented. First of all a brief introduction to the waveguide theory is given. Then the nonlinear propagation model to study SHG is introduced together with the design of the waveguide based on FEM simulation. Eventually the model is used to estimate the $\chi^{(2)}$ coefficient from the measured SHG efficiency.

3.2.1 *A brief introduction to the waveguide theory*

Index-guiding structures are based on *total internal reflection*. Total internal reflection occurs when a propagated wave strikes a medium boundary at an angle larger than a particular critical angle with respect to the normal to the surface. If the refractive index is lower on the other side of the boundary and the incident angle is greater than the critical angle, the wave is entirely reflected. To exploit the total internal reflection, an index-guiding structure is characterized by a *core* material with a higher refractive index with respect to the surrounding material, called *cladding*. Optical waveguides can be realized with different materials and with different geometries [22]. Throughout the thesis we will consider *channel waveguide*, in which the high refractive index material has a typical rectangular shape and it is surrounded by a lower refractive medium. A schematic of a typical channel waveguide is reported in Figure 22(a).

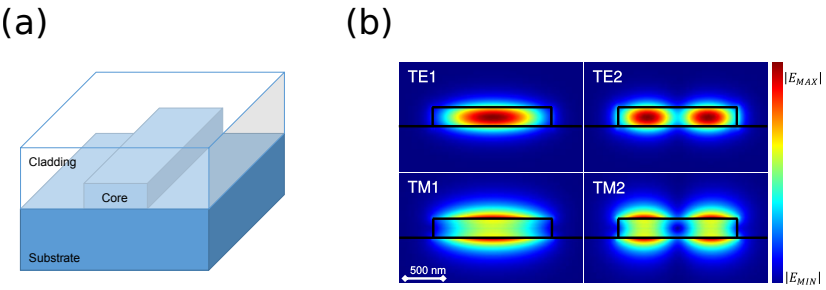

Figure 22: (a) Sketch of a rectangular waveguide fabricated on a Silicon on Insulator (SOI) wafer. (b) Modal profiles for the two lowest order TE and TM modes supported by a $(1.5 \times 0.25)\mu m^2$ silicon waveguide with a silica cladding. The profiles have been evaluated using a finite element simulation software for a wavelength of 1.55 µm. Image taken from [12].

In an optical waveguide, light travels in the form of discrete modes of electric field profiles $\mathbf{e}_m(x, y, \omega)$, which are solution of the Helmholtz equation[22]:

$$(\nabla^2_{(x,y)} + [\beta^{(m)}]^2)\mathbf{e}_m(x, y, \omega) = \frac{\omega^2}{c^2} n^2(x, y)\mathbf{e}_m(x, y, \omega) \qquad (38)$$

Due to the invariance of the refractive index distribution $n(x,y)$ along the propagation direction z, the dependence in this coordinate is of the form $e^{i\beta^{(m)}z}$, where $\beta^{(m)} = \frac{\omega}{c} n_{eff,m}$ is called the modal propagation constant and $n_{eff,m}$ the effective index.
In general, $n_{eff,m}$ is a complex quantity. As for plane waves, the real part is associated with propagation, the imaginary one with losses. The field intensity exponentially decreases along z as $e^{-\alpha z}$, where the attenuation coefficient is given by $\alpha = \frac{2\omega}{c} \operatorname{Im} n_{eff,m}$.
In Figure 22(b) the planar profiles of the first order modes supported by a rectangular waveguide with dimension $(1.5 \times 0.25)\mu m^2$ are shown. The core material is silicon, while the cladding is composed by silica. The corresponding refractive indexes are: $n_{Si} \sim 3.48$ and $n_{SiO_2} \sim 1.44$ at the wavelength $1550\,nm$ [8]. Silicon has a very high refractive index contrast with respect to silicon dioxide, which allows to achieve a strong modal confinement and eventually to manufacture very compact photonic devices [9].
In addition to the modal order m, optical modes are also classified on the basis of their polarization. In general, for waveguides of sub-wavelength dimension as the one in Figure 22(b), the electric and the magnetic fields are not transverse to the propagation direction and neither orthogonal to each other. The classification between Transverse Electric (TE) and Transverse Magnetic (TM) modes is done on the basis of their dominant electric feld component, which coincides with the direction parallel to the waveguide width in case of TE modes, and the direction parallel to the waveguide height for TM modes.
More formally the modal confinement factor for the $m-th$ mode is defined as:

$$\Gamma_m = \frac{\int_{wg} n^2(x,y)|\mathbf{e}_m(x,y)|^2 dxdy}{\int n^2(x,y)|\mathbf{e}_m(x,y)|^2 dxdy} \tag{39}$$

where the integral in the numerator is calculated over the waveguide area, while the integral in the denominator is calculated in all the xy plane. In general, the higher the modal order, the lower the confinement factor defined in Equation 39. As a consequence, the effective index monotonically decreases as the modal order increases, because the optical field senses less of the core refractive index.
Given the waveguide geometry, the maximum number of supported modes is limited. Apart from very simple geometries, as the slab one [123], no analytical expression exists for determining this number.
For the channel waveguides discussed within this thesis, a good rule of thumb is to consider the fact that light of wavelength λ can not be confined to features which are smaller than $\lambda/2$ due to the diffraction limit [22].

In general the propagation constant β (where we have dropped for simplicity the mode superscript) depends on the frequency, and it

can be expanded as a Taylor series around a central frequency ω_0 as follows:

$$\beta(\omega) = \sum_j \frac{\beta_j}{j!}(\omega - \omega_0)^j. \tag{40}$$

The first term of the expansion, β_1, is related to the group velocity of the mode v_g and to the group index of the mode n_g by the relation $v_g = 1/\beta_1 = c/n_g$. The second term of the expansion β_2 is called the Group Velocity Dispersion (GVD), while β_3 is the Third Order Dispersion (TOD), and so on. When $\beta_2 > 0$ the dispersion is said to be normal, while it is anomalous if $\beta_2 < 0$.
Especially for small structures, the values assumed by $\beta^{(m)}$ are dominated by the waveguide geometry, and can be tailored by suitable choice of the waveguide dimensions.

3.2.2 *Optical pulses in nonlinear waveguides*

In the following we want to describe the propagation of optical pulses in a waveguide under the effect of a nonlinear perturbation given by $\mathbf{P}_{NL}$, defined in Equation 4.
Let us consider $(\mathbf{E_0}, \mathbf{H_0})$ as the electromagnetic fields propagating in the unperturbed waveguide. Due to the nonlinear perturbation $\mathbf{P}_{NL}$, the electromagnetic fields are modified to $(\mathbf{E_1}, \mathbf{H_1})$. From Lorentz's reciprocity theorem, it follows that [124]:

$$\frac{\partial}{\partial z}\int_{A_\infty} (\mathbf{E_0^*} \times \mathbf{H_1} + \mathbf{E_1} \times \mathbf{H_0^*}) \cdot \hat{\mathbf{z}} \; dA = i\omega \int_{A_\infty} \mathbf{E_0^*} \cdot \mathbf{P}_{NL} \; dA. \tag{41}$$

Note that Equation 41 assumes that the variation of the index of refraction is small, and thus the modes of the perturbed and unperturbed waveguides are the same [125]. In both terms, the integration is carried over all the plane A_∞ transverse to the propagation direction $\hat{\mathbf{z}}$. If the electromagnetic field is linearly polarized, the perturbation can introduced as a modulation $u(z, \omega)$. The unperturbed and the perturbed fields can be then rewritten as:

$$\mathbf{E_0} = \frac{1}{2}\mathbf{e}(x, y, \omega_0)e^{i\beta_0 z} \qquad \mathbf{E_1} = \frac{1}{2}\mathbf{e}(x, y, \omega)u(z, \omega)e^{i\beta z}, \tag{42}$$

$$\mathbf{H_0} = \frac{1}{2}\mathbf{h}(x, y, \omega_0)e^{i\beta_0 z} \qquad \mathbf{H_1} = \frac{1}{2}\mathbf{h}(x, y, \omega)u(z, \omega)e^{i\beta z}. \tag{43}$$

Here ω_0 is the carrier frequency and $\beta_0 = \beta(\omega_0)$. The dimensionless quantities $\mathbf{e}(x, y, \omega)$ and $\mathbf{h}(x, y, \omega)$ express the field profile in the plane orthogonal to the main waveguide axis. They are assumed to be not modified by the perturbation, so that $\mathbf{e}(x, y, \omega) \sim \mathbf{e}(x, y, \omega_0)$ and

$\mathbf{h}(x, y, \omega) \sim \mathbf{h}(x, y, \omega_0)$. In this framework, the total optical power P_0 carried by the unperturbed electromagnetic field is given by:

$$P_0 = \frac{1}{4}\int_{A_\infty} (\mathbf{e} \times \mathbf{h}^* + \mathbf{e}^* \times \mathbf{h}) \cdot \hat{\mathbf{z}} \ \ dA, \tag{44}$$

while in the case of the perturbed field it is given by $P_0\,|u(z,\omega)|^2$. The definitions given in Equation 42, 43, and 44 can be inserted into Equation 41. It is then possible to derive the following partial differential equation describing the spatial evolution of the mode amplitude $u(z, \omega)$:

$$\frac{\partial u(z,\omega)}{\partial z} + i(\beta - \beta_0)u(z,\omega) = \frac{i\omega}{2P_0} e^{-i\beta z} \int_{A_\infty} \mathbf{e}^*(\omega) \cdot \mathbf{P}_{NL}(\mathbf{r}, \omega) \ \ dA \tag{45}$$

If different optical pulses with frequencies sufficiently spaced far apart are propagating in the same waveguide, it is necessary to write a separate equation of the form of Equation 45 for each of them. Otherwise, a single equation approach should be used.

Let us specialize Equation 45 to the nonlinear three-wave mixing process under analysis, which is SHG. Let us indicate with $u_p(z, \omega)$ and $u_g(z, \omega)$ the mode envelope of the pump and the generated SHG signal. By insering Equation 4 (considering $\mathbf{P_{NL}}$ up to the third order) into Equation 45 the temporal evolution for the generated SHG signal is given by [126]:

$$\begin{aligned}\frac{\partial u_g}{\partial z} + i(\beta_g - \beta_{g0})u_g = {} & i\frac{\omega_g \varepsilon_0}{8P_{g,0}} u_p^2 e^{i\Delta k z} \int \mathbf{e}^*_{g,0} \cdot \chi^{(2)} : \mathbf{e}_{p,0}\mathbf{e}_{p,0}\, dA + \\ & + i\frac{3\omega_g \varepsilon_0}{16P_{g,0}} |u_g|^2 u_g \int \mathbf{e}^*_{g,0} \cdot \chi^{(3)} \vdots \mathbf{e}^*_{g,0}\mathbf{e}_{g,0}\mathbf{e}_{g,0}\, dA + \\ & + i\frac{3\omega_g \varepsilon_0}{16P_{g,0}} |u_p|^2 u_g \int \mathbf{e}^*_{g,0} \cdot \chi^{(3)} \vdots \mathbf{e}^*_{p,0}\mathbf{e}_{p,0}\mathbf{e}_{g,0}\, dA\end{aligned} \tag{46}$$

and for the mode envelope of the pump:

$$\begin{aligned}\frac{\partial u_p}{\partial z} + i(\beta_p - \beta_{p0})u_g = {} & i\frac{\omega_p \varepsilon_0}{4P_{p,0}} u_g u_p^* e^{-i\Delta k z} \int \mathbf{e}^*_{p,0} \cdot \chi^{(2)} : \mathbf{e}_{g,0}\mathbf{e}^*_{p,0}\, dA + \\ & + i\frac{3\omega_p \varepsilon_0}{16P_{p,0}} |u_g|^2 u_p \int \mathbf{e}^*_{p,0} \cdot \chi^{(3)} \vdots \mathbf{e}^*_{g,0}\mathbf{e}_{g,0}\mathbf{e}_{p,0}\, dA + \\ & + i\frac{3\omega_p \varepsilon_0}{16P_{p,0}} |u_p|^2 u_p \int \mathbf{e}^*_{p,0} \cdot \chi^{(3)} \vdots \mathbf{e}^*_{p,0}\mathbf{e}_{p,0}\mathbf{e}_{p,0}\, dA\end{aligned} \tag{47}$$

whre $\beta_s = \frac{2\pi}{\lambda_s} n(\lambda_s)$ $(s = p, g)$ is the propagation constant and $\Delta k = 2\beta_p - \beta_g$ is the phase mismatch which arises from Equation 35. These equations represent the more general form of the coupled equations describing the nonlinear propagation of the pump and the SHG field in a waveguide, considering $\mathbf{P}_{NL}$ up to the third order. The sec-

ond term on the left hand side of Equation 46-47 takes into account pulse propagation dispersive effects, while the right hand side accounts for the nonlinear effects. Since $\chi^{(3)}$ is relatively strong in silicon, we have to take it into account in the coupled equations. In principle the $\chi^{(3)}$ coefficient should be also sensitive to the strain. However, as a first approximation we will consider the standard values of $\chi^{(3)}$ for non-strained silicon.
We will now introduce 4 different effective susceptibilities. Introducing the notation $W_{s,0}$ (s = g, p) for the energy density for unit length [125]:

$$W_{s,0} = \frac{\varepsilon_0}{2} \int n(x,y)^2 |\mathbf{e}_{s,0}(x,y)|^2 dA \tag{48}$$

the second order effective susceptibility is given by (in analogy with [124]):

$$\Gamma^{(2)} = \frac{\sqrt{A_0}\varepsilon_0^{3/2} \int \mathbf{e}^*_{p,0} \cdot \chi^{(2)} : \mathbf{e}_{g,0}\mathbf{e}^*_{p,0} dA}{W_{p,0}\sqrt{W_{g,0}}} \tag{49}$$

where A_0 is the waveguide core cross-section. Analogously, the three effective susceptibilities associated with third order nonlinearities can be defined as:

$$\begin{aligned}
\Gamma^{(3)}_{gg} &= \frac{A_0\varepsilon_0^2 \int \mathbf{e}^*_{g,0} \cdot \chi^{(3)} \vdots \mathbf{e}^*_{g,0}\mathbf{e}_{g,0}\mathbf{e}_{g,0} dA}{W^2_{g,0}} \\
\Gamma^{(3)}_{pp} &= \frac{A_0\varepsilon_0^2 \int \mathbf{e}^*_{p,0} \cdot \chi^{(3)} \vdots \mathbf{e}^*_{p,0}\mathbf{e}_{p,0}\mathbf{e}_{p,0} dA}{W^2_{p,0}} \\
\Gamma^{(3)}_{pg} &= \frac{A_0\varepsilon_0^2 \int \mathbf{e}^*_{p,0} \cdot \chi^{(3)} \vdots \mathbf{e}^*_{g,0}\mathbf{e}_{g,0}\mathbf{e}_{p,0} dA}{W_{p,0}W_{g,0}}
\end{aligned} \tag{50}$$

Using a FEM simulation procedure like the one described in [127, 128], it is actually possible to link the strain distribution inside the silicon waveguide to the induced $\chi^{(2)}$ tensor in Equation 49. As a matter of fact, this is really a non-trivial task and it is still a work in progress within the NanoLab group. Hereafter, we will rather consider, as a first approximation, an effective coefficient $\chi^{(2)}_{eff}$, which let us take $\chi^{(2)}$ out of the integral:

$$\Gamma^{(2)} = \chi^{(2)}_{eff,ppg}(\omega_p, \omega_g) \frac{\sqrt{A_0}\varepsilon_0^{3/2} \int (\mathbf{e}^*_{p,0}) \cdot (\mathbf{e}_{g,0} \cdot \mathbf{e}^*_{p,0}) dA}{W_{p,0}\sqrt{W_{g,0}}} \tag{51}$$

where $\chi^{(2)}_{eff,ppg}(\omega_p, \omega_g)$ is the effective element of the second order susceptibility tensor, evaluated at frequency (ω_p, ω_g).
Since $W_{g,0} \ll W_{p,0}$, it is likely that some terms can be neglected in

the third order contributions. Moreover, if we consider the extreme case of very small $\Gamma^{(2)}$, Equation 46-47 decouple and reduce to:

$$\frac{\partial u_g}{\partial z} + i(\beta_g - \beta_{g0})u_g = i\frac{\omega_g n_g^p \sqrt{n_g^g}}{8\sqrt{A_0\varepsilon_0}c_0^{3/2}} u_p^2 e^{i\Delta kz} \frac{P_{p,0}}{\sqrt{P_{g,0}}}\Gamma^{(2)*} + \\ + i\frac{3\omega_g}{16c_0^2 A_0 \varepsilon_0} n_g^p n_g^g |u_p|^2 u_g P_{p,0}\Gamma_{pg}^{(3)} - \frac{\alpha_g}{2}u_g \tag{52}$$

$$\frac{\partial u_p}{\partial z} + i(\beta_p - \beta_{p0})u_p = i\frac{3\omega_p}{16c_0^2 A_0 \varepsilon_0}(n_g^p)^2 u_p |u_p|^2 P_{p,0}\Gamma_{pp}^{(3)} - \frac{\alpha_p}{2}u_p \tag{53}$$

where α_g (α_p) is the loss coefficient per unit of length for the generated (pump) wave.
We will come back to Equation 52-53 in Section 3.3, where we will simulate the pulse propagation in the designed waveguides with the geometrical parameters obtained from FEM simulations.

3.3 DEVICE

We have seen that bulk silicon does not exhibit second order nonlinearities, due to its centrosymmetric crystalline structure.
In order to induce a non-vanishing $\chi^{(2)}$ coefficient one has to break the centrosymmetric structure. One of the possible techniques is depositing a layer of silicon nitride on top of the silicon. An overlayer of silicon nitride (Si_3N_4) on SOI waveguide generates a strain on the silicon waveguide core. The kind of strain depends on the stress induced by the overlayer [114]. Using a simulation procedure like the one described in [129], it is possible to determine the strain distribution inside the waveguide and eventually links the $\chi^{(2)}$ components to it, in any point of space in terms of the strain gradients in that same point.
As a first step, the resulting stress induced by the silicon nitride overlayer in the SOI wafer was determined by monitoring the change in the bending radius of unpatterned wafers, through both mechanical and optical profilometry. As a result, a 150 nm-thick Si_3N_4 layer, deposited at 780 °C using a low-pressure chemical vapour deposition technique, induces a 1.25 GPa tensile stress.

The design of the waveguides is performed by taking into account the phase matching conditions for achieving SHG, see Equation 37. First of all one has to set the range of the pump wavelength λ_p. To reduce the role of free carriers, Two Photon Absorption (TPA) has to be avoided. TPA competes with SHG, by limiting the maximum achievable pump peak power within the waveguide and by generating free carriers which causes losses both at the pump and SHG wavelengths. Since the silicon band-gap is $\Delta E = 1.11\,eV$, which corresponds to a wavelength of 1.1 µm, TPA can be strongly reduced by using a MIR

laser source with $\lambda_p > 2.2\,\mu m$. For this reason, the considered wavelength range for the simulation is [2.25;2.6] μm, where the upper limit is fixed by our available pump source, which will be discussed in Section 3.4.
The waveguide engineering is performed by varying the waveguide width and looking for multimodal phase matching in the range [2.25;2.6] μm. The cross section of the simulated waveguides is sketched in Figure 23. These are SOI waveguides with different widths around

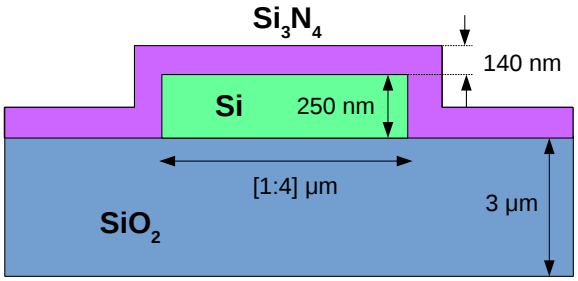

Figure 23: Cross section of the silicon channel waveguide with relative dimension. The width of the waveguide has been engineered in order to achieve SHG multimodal phase matching, while the other parameters are fixed.

2 μm, an height of 250 nm and a 140 nm-thick overlayer of silicon nitride and a 3 μm thick buried oxide layer. A parametric sweeps of the waveguide width and pump wavelength is performed with a FEM software to find the modal combinations for which:

$$n_{eff,m}(\lambda_p/2) = n_{eff,n}(\lambda_p) \tag{54}$$

where $n_{eff,m}$ refers to the effective refractive index for the $m-th$ mode. In particular, the FEM simulations find the set of waveguide parameters that have a modal structure which allows to pick up two modes whose effective refractive indexes best approximate Equation 54. For the ease of experimental input coupling, the pump beam has been fixed, as a first step, to be always in the first TE mode.
An illustrative representation of the simulation done is shown in Figure 24. Here the generated SHG signal propagates in the 7-th TM mode. As it is possible to see from Figure 24, considering the generated SHG signal to be in the 7-th TM mode, it is possible to fulfil the phase matching condition of Equation 54 for three different waveguide widths considering λ_p in the range [2.4;2.6] μm.
The simulated waveguide length is 2 cm, which determines a phase matching bandwidth of $\sim 0.5\,nm$. As it is possible to see from Figure 24(a), for the TE1-TM7 combination, the phase matched wave-

(a)

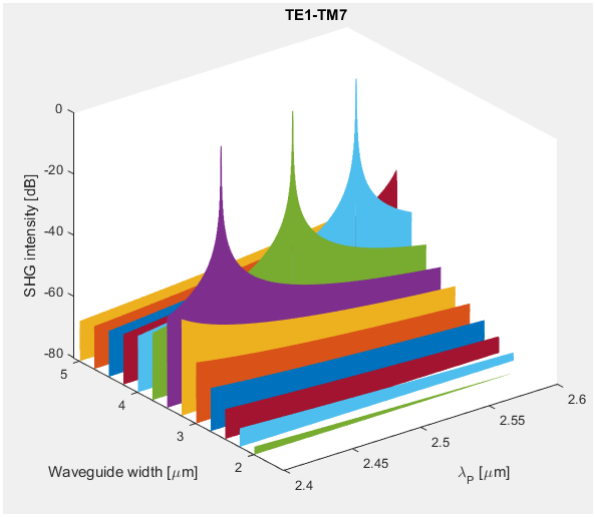

(b)

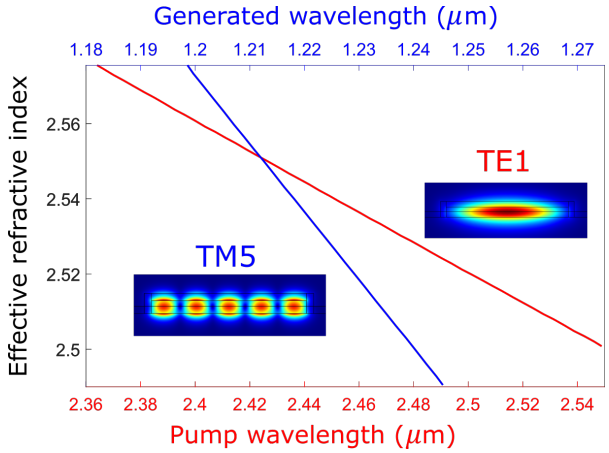

Figure 24: (a) Parametric sweep of pump wavelength λ_p and waveguide width in order to find the combination that maximizes the SHG efficiency. The pump beam is considered to be in the 1-st TE mode, while the SHG signals in the 7-th TM mode. (b) Effective refractive index as a function of wavelength for the 1-st TE mode and for the 5-th TM mode. For this simulation the waveguide width was set to 2.25 µm.

length is red-shifted by 50 nm, as the waveguide width is increased by 200 nm.

In Figure 24 is reported as an example the comparison of the effective refractive index as a function of the wavelength for different optical modes. Here we consider the effective refractive index dispersion for the fundamental Transverse Electric (TE) mode at wavelengths around 2.45 µm and the dispersion for the fifth order Transverse Magnetic (TM) mode at the corresponding halved wavelengths. For the

simulation reported in Figure 24, the waveguide width has been set to 2.25 µm. At $\lambda_p \sim 2.42$ µm the two effective indices assume the same value, and so the phase-matching condition is satisfied.

In the end, the optimal combinations lead to a fabrication of the sample which is an ensemble of 35 optical waveguides, divided in 5 sets. All the combinations implemented in the sample are listed in Table 1. The first column indicates the set of waveguides consid-

Set	SHG mode	$w_{min}(\mu m)$	$w_{max}(\mu m)$	$\lambda_{min}(\mu m)$	$\lambda_{max}(\mu m)$
1	TE5	1.55	1.6	2.471	2.551
2	TE7	2.25	2.4	2.4271	2.5863
3	TM3	0.9	1.2	2.294	2.5794
4	TM5	2.25	2.8	2.4044	2.5957
5	TM7	3.4	4.15	2.4124	2.5912

Table 1: List of the main parameters for the SHG waveguides.

ered. The second column represents the expected polarization and the mode order of the generated waves. The third and the fourth columns are respectively the minimum and maximum waveguide widths of that set. Note that in order to take into account the finite resolution of the fabrication and the accuracy in the simulation parameters with respect to the real parameters, a tolerance interval of suitable value has been designed, instead of a single nominal value. Finally, the last two columns represent the pump wavelength required to obtain phase matching condition, respectively, for the thinnest and the largest waveguide of the set, according to simulations.

3.3.1 *Simulation results*

In this part the nonlinear propagation model used to simulate the SHG generation is presented. The numerical simulation is based on the split-step Fourier method [3], which is a method to solve the pulse propagation problem in nonlinear dispersive media. The split-step Fourier method is an iterative algorithm, which relies on computing the solution in small steps, and treating the linear and the nonlinear steps separately. The equation which governs the pulse propagation, reported in Equation 52-53 can be further simplified and written in the form:

$$\frac{\partial u_g}{\partial z} + \beta_1^{(g)}\frac{\partial u_g}{\partial t} + i\frac{\beta_2^{(g)}}{2}\frac{\partial^2 u_g}{\partial t^2} = iK^*\chi^{(2)}_{eff,xxg}\frac{P_{p,0}}{\sqrt{P_{g,0}}}u_p^2 e^{i\Delta kz} - \frac{\alpha_g}{2}u_g \tag{55}$$

$$\frac{\partial u_p}{\partial z} + \beta_1^{(p)}\frac{\partial u_p}{\partial t} + i\frac{\beta_2^{(p)}}{2}\frac{\partial^2 u_p}{\partial t^2} = i\frac{3\omega_p}{16c_0^2 A_0 \varepsilon_0}(n_g^p)^2 P_{p,0}\Gamma^{(3)}_{pp}u_p|u_p|^2 - \frac{\alpha_p}{2}u_p \tag{56}$$

where the proportionality constant K, with reference to Equation 52, is given by:

$$K = \frac{\omega_g \varepsilon_0}{8} \frac{\int (\mathbf{e}^*_{p,0})_x \cdot (\mathbf{e}_{g,0} \cdot \mathbf{e}^*_{p,0}) dA}{P_{p,0} \sqrt{P_{g,0}}} \tag{57}$$

Here we have explicitly considered the pump beam to be in the 1-st TE mode. Equation 55-56 describe the propagation of an optical pulse in a nonlinear waveguide. The pump beam is described in the undepleted pump approximation and since it is expected that $P_g \ll P_p$ third order contributions have been neglected for the SHG field.
In Equation 55-56 the pulse envelopes move at the group velocity $v_g = 1/\beta_1$, while the effects of group-velocity dispersion (GVD) are governed by β_2 . The GVD parameter β_2 can be positive or negative.
In Figure 25(a) the temporal evolution of the pump (blue lines) and the generated signal (red lines) is represented. In particular, the time profiles for the two signals are shown for different positions along the propagation direction z in the waveguide. There are 10 time profiles for 2 mm step length from the left to the right.
The simulation assumes a conservative value of $\chi^{(2)} = 0.01\,pm/V$ and a temporal pump pulse width of $\Delta t = 1\,ps$, with a peak pump power $P_{peak} = 40\,W$. This leads to a simulated generated SHG power $\sim -90\,dB$ lower with respect to the pump power.
In Figure 25(b) the pump spectra evaluated at the same spatial step as Figure 25(a) are reported. It is evident that, for a peak power of $40\,W$, SPM induces a non-negligible spectral broadening of the pump pulse as the pump beam propagates along the waveguide. This is a detrimental effect since SPM actually enlarges the pump spectrum lowering the overlap with the SHG bandwidth, which in turn limits the SHG conversion efficiency.
Moreover we note from Figure 25(a) that the generation process could also be affected by a *walk-off* effect. Temporal walk-off effects arise when different wavelength components travel with different group velocity in a waveguide. If the temporal pump pulse width is too short, one could loose temporal overlap between the generated and the pump pulses, leading to significant decrease of the SHG signal. It is possible to define a walk-off length as [3]:

$$L_w = \frac{\Delta t}{|\beta_1^p - \beta_1^g|} \tag{58}$$

where Δt is the FWHM of the temporal pulse width.
From FEM simulation it is possible to estimate the group index n_g for the generated and pump wave, once the waveguide geometry is fixed in order to satisfy multimodal phase matching condition. The group index is linked to the β_1 parameter through the relation $n_g = c/v_g = c\beta_1$, where v_g is the group velocity. If we consider for example $n_g^p = 3.5$ and $n_g^g = 4.5$ and $\Delta t = 1\,ps$ (the case shown in Figure 25),

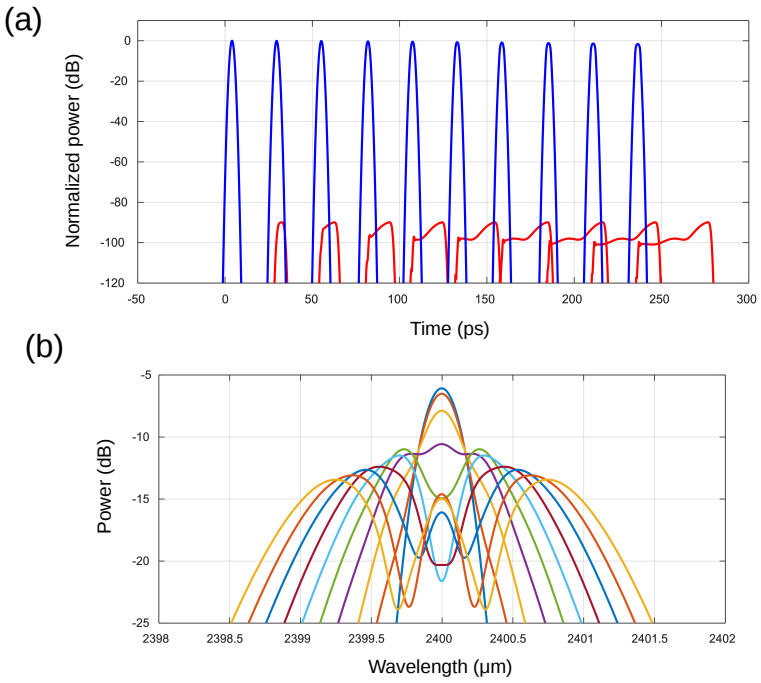

Figure 25: (a) Temporal evolution of the pump (blue lines) and the generated signal (red lines) shown for different position along the propagation in the waveguide (10 time profiles for 2 mm step length from the left to the right). The numerical simulation is based on Equation 55-56, assuming a temporal width $\Delta t = 1\,ps$, pump peak power $P_{p,0} = 40\,W$ and $\chi^{(2)}_{eff} = 0.01\,pm/V$. (b) Spectra of the pump signal during propagation along the waveguide evaluated at the same spatial step as in (a). A spectral broadening arises due to a non-negligible $\chi^{(3)}$ SPM effect.

we have $L_w = 0.3\,mm$. This means that after the pump pulse has travelled a distance of L_w, the SHG generated signal has acquired delay of Δt with respect to the pump. In the case of $\Delta t = 100\,ps$, the walk-off length results $L_w = 30\,mm$.
Since our waveguides were designed for a length L = 2 cm, a pulse width in the order of Δt = [10;70] ps is needed for avoiding temporal walk-off effects and optimize the SHG efficiency. This corresponds to a pump spectral width $\Delta\lambda \sim 1\,nm$. As a matter of fact, our source laser has a temporal time width $\Delta t = 35\,fs$, which poses the challenge to be able to significantly stretch it to avoid walk-off effects.

To summarize, the key pump requirements in order to be able to efficiently excite SHG in strained silicon waveguides are:

- The pump wavelength should be $\lambda_p > 2.2\,\mu m$, tunable in the range [2.25;2.6] μm to avoid TPA within the silicon waveguide,

which limits the maximum power which can effectively travel into the waveguide;

- the pulse time width Δt should be in the range $\Delta t = [10 : 70]ps$ to avoid temporal walk-off effects and to match the simulated phase matching bandwidth $\sim 0.5\,nm$;
- the pump power should be high enough to efficiently trigger SHG generation, but not too high to cause SPM which causes a spectral broadening of the pulse, eventually inhibiting the SHG phase matching.

In the end, the nonlinear propagation model here presented is used for estimating the $\chi^{(2)}$ parameter from the experimentally measured SHG efficiency.

3.4 EXPERIMENTAL SET-UP

In this Section the experimental set-up used to verify the occurrence of SHG in strained silicon waveguides is presented. A sketch of the optical set-up is reported in Figure 26.

It can be thought as divided in 3 main parts:

- The laser source;
- The home-made pulse shaper;
- The coupling stage and detection method.

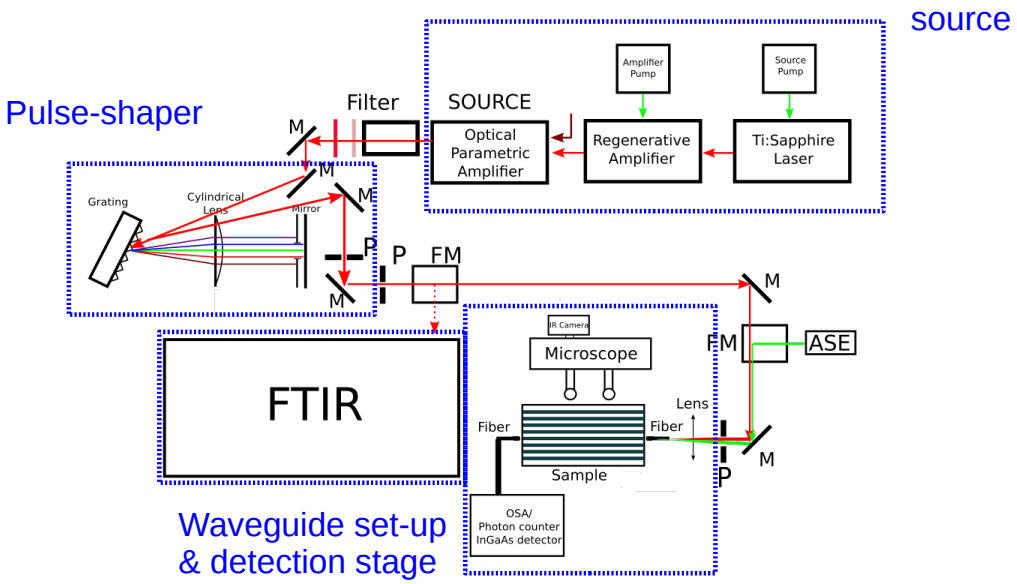

Figure 26: Sketch of the experimental setup used to study SHG in strained silicon waveguides. The red arrows represent the pump optical path. P: pinhole, FM: Flipping Mirror, ASE: Amplified Stimulated Emission broadband source, used to set the reference optical path. The pump travels in free space till right before the sample, where is coupled in fiber for the ease of the waveguide coupling handing.

3.4.1 *The laser source*

The laser source itself is composed by 3 different stages, as it is possible to see from Figure 27.
The generation of a coherent pulsed beam is given by a solid-state Ti:sapphire laser oscillator, optically pumped with a laser beam at 532 nm with an average power of 4.33 W. The laser can be operated in quasi CW or in mode-locked operation. Mode-locked operation is achieved thanks to an active acousto-optic modulator (AOM). The output pulsed beam has a center wavelength of 800 nm with a measured bandwidth of 70 nm, a pulse duration of $\Delta t = 35$ fs with a repetition rate r = 82 MHz. The output average power is 550 mW.
The seed laser is then amplified in a *regenerative amplifier* system (Newport Spectra-Physics SPITFIRE). Here the seed, i.e. the train of pulses coming from the Ti:sapphire laser, is amplified and a pulse selection is performed by means of a timing control unit. The Spitfire system is itself a laser cavity, where a pump at 527 nm, with average power 20 W and with a repetition rate of 1 kHz, generates population

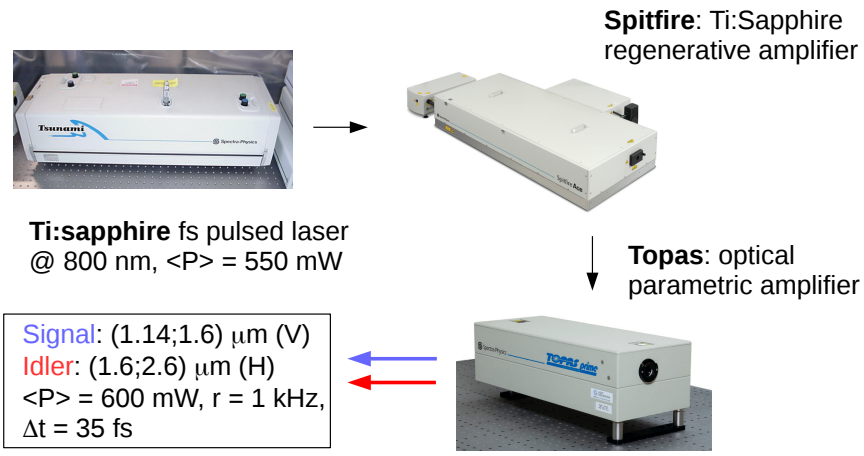

Figure 27: Sketch of the laser source used.

inversion in a Ti:sapphire rod and the selected seed pulses are amplified by the stimulated emission. In this way the repetition rate of the seed effectively passes from 82 MHz to 1 kHz. To reduce the pump peak power, before entering in the amplifier cavity, the seed pulses are enlarged by a strecher.
The pulse selection is achieved thanks to 2 Pockel cells, driven by 2 high voltage generators. When activated with a suitable voltage signal, the Pockel cells act as 1/4-wave plate, i.e. they rotate the polarization of a beam by 45°. When the cells are off, they have no effects on a beam. In this amplifier, the optical path is such that the seed experiences a double pass though the combination of the intra-cavity Pockel cell and a passive 1/4-wave plate. In this way, with the help of a polarizer, the seed pulses are effectively trapped in the cavity. A timing and delay generator provides the synchronization between the laser seed and Spitfire intra-cavity field. Since these optical beams have a different repetition rate, this leads to a selective choice of the amplified seed pulses. When the seed beam reaches a saturation regime in the amplification stage, it is released from the cavity and sent to a compressive stage, in order to compress the pulse time width back to a value of 35 fs. Eventually at the output of the regenerative amplifier the average power is boosted till 3.4 W at a repetition rate of 1 kHz.
The last stage is composed by an optical parametric amplifier (OPA) (TOPAS-C from Light Conversion). This is the nonlinear stage which acts as a tunable pump source in the MIR. Within the OPA the amplified pump field at 800 nm is split. The small part goes to a preamplification stage. Here the key optical element is a sapphire plate, which generates a supercontinuum signal in the range (1.14;1.6) μm.

This optical signal is then collinearly mixed with the remainder of the pump laser beam to parametrically trigger the generation of DFG of the idler beam in the range (1.6;2.6) µm.

In Figure 28, the spectrum measured directly at the output of the OPA is reported. Standard OSA for telecom wavelength are based on InGaAs detectors, which are not efficient in the whole spectral range of our pump source. Therefore, as it is shown in Figure 26, we used a Fourier Transform Infrared spectrometer (FTIR from Brucker optics) for the spectral analysis of the source. Our FTIR is equipped with a InSb detector, cooled with liquid nitrogen, which is sensitive in the range [1;5.5.5] µm. Basically in the experiment we exploited the FTIR as a spectrum analyzer, i.e. for studying the Fourier Transform of the interferogram of our optical signal.

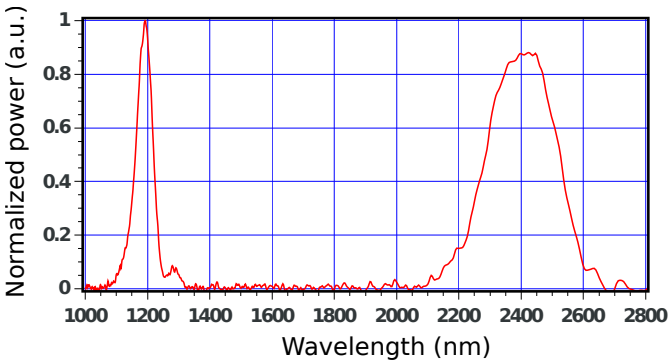

Figure 28: Spectum taken at the output of the OPA with a FTIR. The OPA was set to generate an idler centred at 2400 nm.

Signal and idler at the output of the OPA device are cross-polarized, so they can be easily separated with a polarizer.
The measured value of the average power at the output of OPA is <P> = 600 mW, when the instrument was set to generate a signal beam at $\lambda_s = 1200$ nm and correspondingly the idler at λ_i given by:

$$\lambda_i = (\lambda_s - \lambda_p)/(\lambda_s \lambda_p) = 2.4\,\mu m \tag{59}$$

where $\lambda_p = 800$ nm is the central wavelength of the pump beam at the output of the regenerative amplifier. The corresponding peak power can be calculated from the repetition rate r = 1 kHz and from the pulse temporal width $\Delta t = 35$ fs as follows:

$$P_{peak} = \frac{< P >}{r\Delta t} \sim 17\,GW \tag{60}$$

From Equation 60 one immediately realizes that the available power at the exit of the OPA is too high to be directly coupled into the waveguide. As a matter of fact, an incident power of the order of the one in Equation 60, is more than enough to burn the waveguide facet. Moreover, as it is possible to see in Figure 28, the idler beam has a

bandwidth of 253 nm, which is orders of magnitude larger with respect to the simulated phase-matching bandwidth which is ~ 0.5 nm (see Figure 24). This would also give rise to the so called walk-off effect [3], already discussed in Section 3.3.1.
We directly measured the temporal pulse width at the exit of the Spitfire with an interferometric autocorrelator (Newport PulseScout autocorrelator), which was $\Delta t = 35$ fs. With the help of an home-made pulse stretcher after the OPA, we were effectively able to enlarge the pulse width and at the same time considerably reduce the peak power to a feasible level.

Here a final remark on the presented laser source. Overall it is really powerful and is able to deliver a pulsed, linearly polarized, tunable optical signal from 1.1 µm to 2.6 µm. The main drawback is that the system is very sensitive to environmental fluctuations (in particular temperature and humidity) and to small misalignments which are amplified by the long optical lever. Therefore the laser source is not really "plug-and-play" and constitutes an active part of the experimental set-up, where daily small alignments are needed, in particular for the amplifier stage, to let the system work properly.

3.4.2 *Home-made pulse shaper*

Pulse shaping is needed to make the temporal pulse longer. In the following, a Fourier transform pulse shaper based on amplitude modulation is presented.
The basic idea to be able to reshape in the time domain an optical beam is to tailor its spectrum. More quantitatively, in the case of a transform-limited optical pulse (in the absence of frequency chirp), the spectral width of a Gaussian pulse is linked to its time width by the following Fourier relation [3]:

$$\Delta\omega\Delta t = 4 * \log 2 \tag{61}$$

As expected, expression Equation 61 indicates that, as the width of the pulse increases in the time domain, the spectral width decreases in the frequency domain and vice-versa.
A photograph of the pulse shaper is reported in Figure 29.
The pulse shaper is in the so called *4f* reflection configuration. After the OPA, first of all we separate the idler beam (red arrow) from the co-propagating signal beam (blue arrow). Since the two are linearly polarized with orthogonal polarization, this can be done with a polarizer. Alternatively, as it is shown in Figure 29, due to the large wavelength difference, they can be also separated with a 1500 nm long-wave pass filter which has a measured extinction ratio > 50 dB.
Then, the femtosecond idler pulse is first decomposed into its spectral components by a grating, which is mounted on a rotational stage.
The grating used is characterized by 600 grooves/mm and a disper-

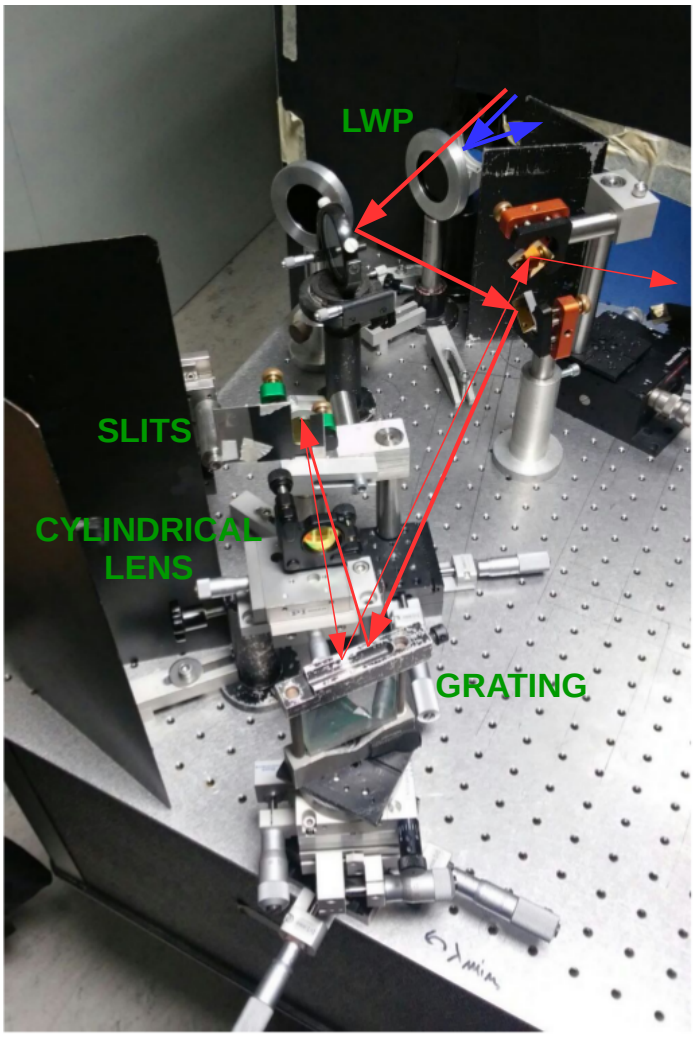

Figure 29: Photograph of the experimental pulse shaper. The red arrow represent the optical path of the idler beam at $\lambda_i \sim 2.4\,\mu m$. The angle between the incoming beam on the grating and the outgoing one is only for illustrative purposes. In the real set-up the beams are separated only along the z-direction, to let the shaped beam exit from the pulse shaper system. The blue arrow is the signal beam which comes also from the OPA and is filtered with a long wave pass filter 1500 nm.

sion of $1.46\,nm/mrad$. The angular dispersion generated by the gratings is transformed into spatial dispersion by a cylindrical lens with focal length $f = 10\,cm$. In the back focal plane of the lens, a tunable slit modulates the intensity of the different components. The spectral components are reflected back by a mirror and they pass again through the lens. The spectral components are then focused on the grating and recombined, creating a collimated reshaped pulse. If the

slits are absent, the 4f configuration forms a unit magnification telescope. Assuming a non-dispersive lens, this schematic is ideally free of frequency dispersion. A reflection geometry can be very convenient to achieve the dispersion-free condition. Only two focal planes are indeed present, instead of four as in the transmission configuration, simplifying the alignment of the setup.
The pulse shaper in Figure 29 is inherently a lossy system, which is exactly what we need to some extent. Indeed, we see from Equation 60, that we need to reduce the peak power by orders of magnitude, to have a $P_{peak} \sim 1\,W$ coupled into the waveguide. Therefore, from one side the enlarged temporal width helps to reduce the peak power, on the other side the reconfigurable slit system which filters out the spectrum, effectively reduces the optical power. As a matter of fact, even after the intrinsically lossy pulse shaper stage, additional neutral filters are needed to further reduce the optical power. Measurements of the achieved temporal pulse width as a function of the average pump power at the output of the pulse shaper are reported in Figure 30(a). The reported pulse time widths were estimated with Equation 61 from the bandwidth of the recorded spectra with the FTIR. We checked the accuracy of this method at telecom wavelength, by measuring the pump spectrum also with a standard OSA. In Figure 30(b), the idler spectrum is effectively cut to $\Delta\lambda = 14\,nm$. Experimentally the maximum achievable shaping was obtained reducing the spectral width till $\Delta\lambda = 0.5\,nm$, which corresponds to $\Delta t = 17\,ps$.
Note that in the particular case of the spectrum reported in Figure 28, it is actually crucial to effectively filter out the pump signal. Indeed, the signal at $1.2\,\mu m$ could be effectively diffracted into the second order by the grating collinearly to the first order of the idler, according to the grating equation [22]:

$$d\Big[\sin(\theta_i) + \sin(\theta_m)\Big] = m\lambda \tag{62}$$

where d is the distance between the lines of the grating, θ_i is the incident angle (experimentally chosen close to the grating blazed angle), θ_m is the diffracted angle, λ is the diffracted wavelength and m is the diffracted order. So this component will be transmitted from the pulse-shaper and it has to be suppressed, since it could be source of noise and could mislead the data analysis. As a matter of fact, with the idler wavelength set by the OPA at $2.4\,\mu m$, the corresponding signal wavelength lies exactly where we will look for the SHG generated signal. For this reason, at the output of the pulse-shaper we placed an AR-coated thick germanium window which provides an extinction ratio higher that 50 dB.
The manual system of grating rotation have been recently substitute with a mechanical automatic rotation system, remotely controlled, which can accurately and quickly tune the wavelength in the range

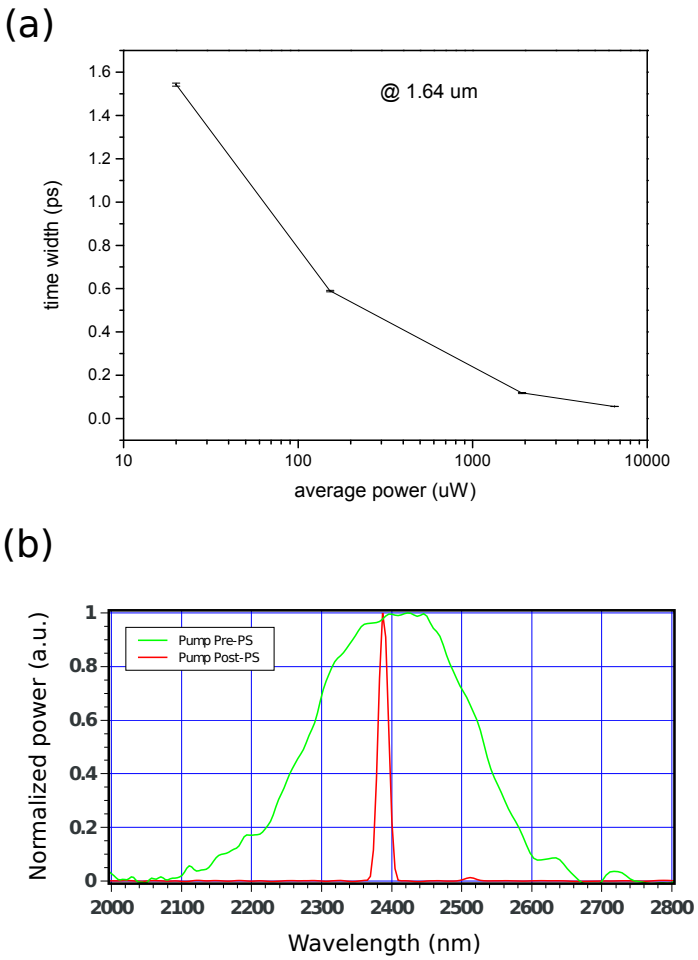

Figure 30: (a) Characterization of the temporal pulse width as a function of the average power at the output of the pulse shaper. (b) The idler spectrum at the input (green line) and at the output (red line) of the pulse shaper. The FWHM are respectively 253 nm and 14 nm.

[2.25;2.5] µm, once the slits have been fixed to have a minimum pulse bandwidth of $\Delta\lambda = 0.5$ nm.

3.4.3 *Coupling and detection method*

In this part we will discuss the coupling of the optical signal into the waveguide and the detection method. Hereafter, we will refer to the reshaped idler beam as the pump beam, which is ready to be inserted into the waveguides. Its average peak power at the output of the pulse shaper is less than 1 µW and it is not possible to trace it to the sample.
Moreover, we are also effectively blind in butt coupling a tapered fiber to the waveguide, since we do not have sensitive enough camera to check for pump signal scattering off the sample in the MIR. For this reason, as it is shown in Figure 26, we use a reference Amplified

Stimulated Emission (ASE) source at telecom wavelength. We make the pump and the ASE collinear and this allows us to use the reference to make the alignment and the coupling with a NIR-VIS camera (FIND-R-SCOPE, model 85700). Then, due to collinearity, the pump is almost aligned and the pump coupling can be maximized.
To measure the transmitted power through the sample and characterize the insertion losses, we use an extended InGaAs photodiode (Thorlabs FD05D), whose spectral range is [800;2600]nm. Its responsivity is shown in Figure 31(a). To improve the signal to noise ratio we use a lock-in amplifier, triggered with the 1 kHz repetition rate coming from the regenerative amplifier. With this system, with 1 s of integration time, the limit of detection is about 200 pA.

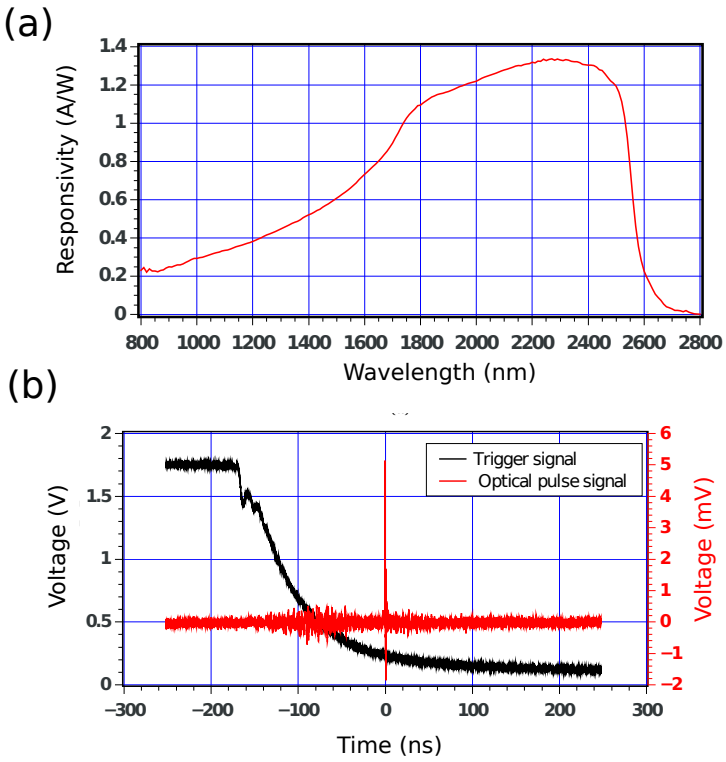

Figure 31: (a) Responsivity as a function of wavelength for the extended InGaAs photodetector used to measure the pump beam at $\lambda \sim 2.4\,\mu m$ and the reference power at $\lambda = 1.55\,\mu m$. (b) Voltage traces of the trigger electrical pulse from the regenerative amplifier and voltage signal at the output of the extended InGaAs, both measured with an oscilloscope. The trigger signal precedes the optical pulse by $\sim 180\,ns$. The trigger is in NIM logic, i.e. it has a low-level true. The correct timing down to the 2.5 ns gate width within the SPAD is performed thanks to a delay line.

Let us discuss the method to detect the SHG signal. We have seen from the simulations that with a conservative value for the second order coefficient of $\chi^{(2)} \sim 0.01\,pm/V$, the generation level is expected to be about -90 dB. Now, supposing to have 10 nW of average optical

power coupled within the waveguide (we will see in Section 3.5 this is the typical orders of magnitude for the pump power), the generated SHG signal is expected to be below the fW level. It is thus evident that we can not use a standard OSA for this task, since its limit of detection is $\sim 1\,pW$.
We used instead the id201 InGaAs single photon counter (SPAD), whose detection efficiency as function of wavelength is reported in Figure 15(a). The expected SHG generated at about $1.2\,\mu m$ actually lies within the spectral bandwidth of the SPAD. In order to reduce the non-negligible SPAD dark counts, the detector works in gated configuration, triggered by the $1\,kHz$ reference signal from the regenerative amplifier. Even though the pump wavelength lies well above the detector spectral responsivity upper limit, as a side effect we experienced that the pump power is effectively detected by means of TPA within the SPAD. We exploit this side effect for the timing fine tuning of the SPAD gating with respect to the incoming optical signal, see Figure 31(b).
Then, once the detection system is maximized, we simply filtered out the pump by bending the output tapered fiber. Indeed the $2.4\,\mu m$ is not really well guided by the telecom tapered fiber and it is enough to gently bend the fiber to induce huge bending losses and filter out the MIR signal, without inducing at the same time losses to the well confined SHG $1.2\,\mu m$ mode propagation. We set the gate window to the minimum possible time width of $2.5\,ns$, triggered with the repetition rate $r = 1\,kHz$, which determines the dark count rate to be $C_{DC} = 5\,Hz$.
Let us estimate the minimum optical power that can be measured by the detector. This is given by:

$$P = \frac{hc}{\lambda}\frac{C - C_{DC}}{DE} \tag{63}$$

where $DE = 23\%$ is the SPAD detection efficiency at $\lambda = 1.2\,\mu m$. If we suppose to set the minimum detectable value to have a signal-to-noise $SNR = 1$ for $1\,s$ of integration time, this results to be
$P \sim 0.004\,fW$, which is low enough to be able to detect a SHG signal from the strained silicon waveguide even in the worst case scenario of a second order coefficient of the order of $\chi^{(2)} \sim 0.01\,pm/V$. The more the integration time, the lower the deviation of the background noise, but, at the same time, the more time consuming the measurement. Generally, depending on the photon flux level, the most suitable integration time has to be set case by case.

3.5 EXPERIMENTAL MEASUREMENTS

In this section the experimental measurements of SHG in strained silicon waveguides are reported. The experimental measurements were

performed for the waveguide width of Set 3 and Set 4 with reference to Table 1, i.e. for the combination TE1-TM3 and TE1-TM5 respectively. In what follows only the measurement performed on Set 3 are reported, to avoid redundancy. For the third set, the coupling losses were estimated to (16 ± 1)dB with the cut-back technique and are most likely equally divided between input and output. The propagation losses were measured to be (5.1 ± 0.5)dB/cm. The coupling and propagation losses were characterized at 1550 nm. The total insertion loss measured at [2.25;2.5] µm is compatible with the telecom characterization.
We experimentally observed that we were not able to detect any kind of SHG signal from the designed sample length of L = 2 cm. Therefore, we decided to cut the sample to reduce the waveguide length. The waveguide length was reduced by a cutting procedure thanks to a diamond tip in the range [2;5] mm. This may seems counter-intuitive, as, following the theoretical derivation for the DFG generated power developed in Chapter 2, this can be straightforwardly generalized also for the SHG case, leading to [18]:

$$P_{SHG} \propto P_{pump}^2 L^2 \operatorname{sinc}^2\left(\frac{\Delta k L}{2}\right) \tag{64}$$

Therefore, the longer the sample the higher the generated power $\propto L^2$ and the smaller the bandwidth $\propto 1/L$.
While the pump beam was tailored to match the phase matching bandwidth with $\Delta\lambda \sim 0.5$ nm, still the temporal width of $\Delta t = 16$ ps may cause walkoff effects. As a matter of fact, the walkoff length defined in Equation 58, results $L_w = 5$ mm. Moreover, cutting the sample allows us to have a better signal to noise ratio in the passive characterization of the waveguides.

In Figure 32(a) the signal measured at the waveguide output by the InGaAs SPAD, as a function of the pump wavelength is reported. From the measurement the presence of a peak is evident at the pump wavelength $\lambda_p = (2265.9 \pm 0.1)$ nm with a phase matching bandwidth $\Delta\lambda = (1.17 \pm 0.02)$ nm, both of which were estimated from a Gaussian fit of the experimental data.

The measurement reported in Figure 32(a) was taken with a nominal waveguide width of w = 906 nm, with a waveguide length of L = 4 mm and a coupled peak pump power $P_p = 0.6\,W$, which is strong enough to excite a detectable SHG signal and at the same time low enough to avoid SPM within the waveguide, see Figure 25(b).
This corresponds to an incident average power upon the waveguide of <P> = 61.5 nW. The SHG bandwidth is larger than the simulated one of 0.5 nm due to the use of a shorter sample. Further measurements for nominally equal waveguide width as a function of the waveguide

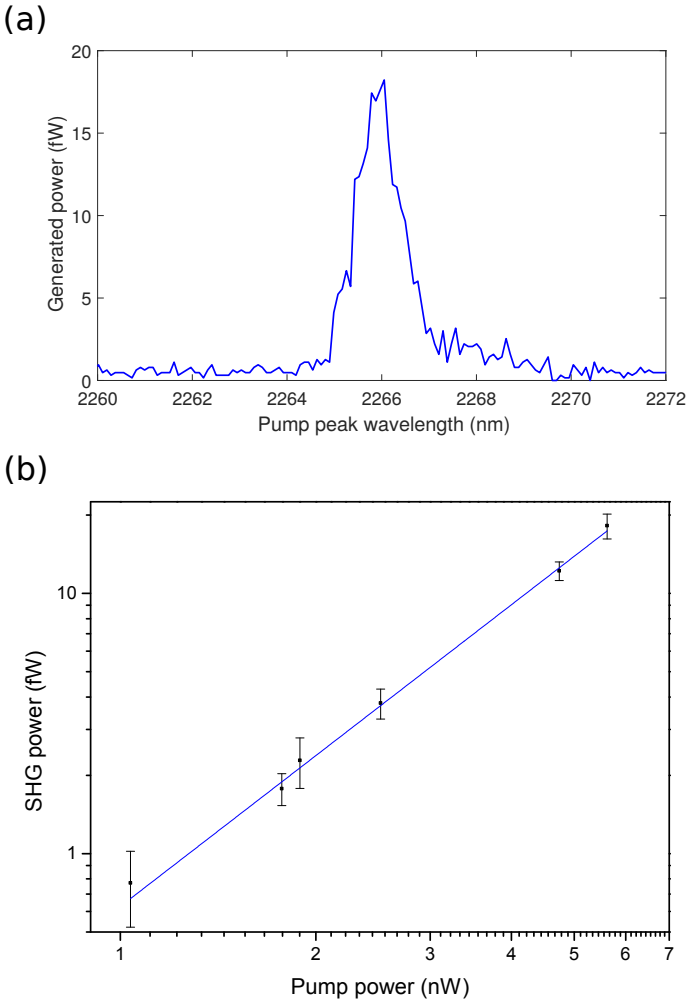

Figure 32: (a) Experimental measurement of the SHG signal as a function of the pump wavelength. The peak is at $\lambda_p = (2265.9 \pm 0.1)$ nm and the phase matching bandwidth is $\Delta\lambda = (1.17 \pm 0.02)$ nm. (b) Generated SHG power as a function of the average pump power. The data are reported in log-log scale and the blue line is a linear fit.

length are needed to better characterize the SHG bandwidth.
In Figure 32(b) the generated power dependence as a function of the average pump power within the waveguide is reported. The slope of the linear fit of the data, note that they are reported in log-log scale, is (1.93 ± 0.05). Theoretically it is expected to be 2, since the SHG generated power must increase quadratically with the pump power (see Equation 64). The close agreement between theory and experiment, constitutes an additional proof of the occurrence of SHG to the narrow-band phase matching feature reported in Figure 32(a).
We found the phase matched wavelength reported in Figure 32(a) compatible with the simulations. More in detail, in Figure 33 the dependence of the phase matched wavelength as a function of the

waveguide width is reported. The experimental data are reported as blue squares, while the black line represents the theoretical expectation from FEM simulations.

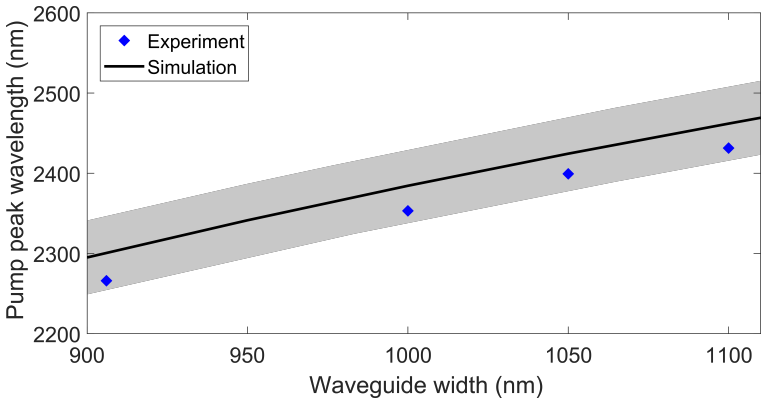

Figure 33: SHG peak wavelength as a function of the waveguide width. The blue symbols are experimental data, while the black line is the theoretical prediction from FEM simulation. The grey shaded area is the SHG peak wavelength theoretical uncertainty due to the photolithographic process tolerance $\pm 50\,nm$.

As it is possible to see from Figure 33, the trend of the experimental data follows the one predicted from the simulations. However, the two are slightly off-set. The physical explanation is that the real average width of the waveguide <w> is different from the nominal simulated one and this has the effect to overall shift the wavelength position of the SHG generated peak. An average deviation of $(35 \pm 1)nm$ is found between the nominal values of the waveguide widths and the fabricated ones, which is compatible with the tolerances of the photo-lithographic process ($\pm 50\,nm$) represented as the grey shaded area in Figure 33.
Finally, the experimental data are fed into the nonlinear pulse propagation model, in order to estimate the induced $\chi^{(2)}_{eff}$ coefficient.
Since the considered combinations are TE1-TM3 and TE1-TM5, the estimation regards mainly the tensor element $\chi^{(2)}_{eff,xxy}$. The estimated $\chi^{(2)}$ coefficients for the two combinations result $\chi^{(2)}_{set4} \sim 0.3\,pm/V$ and $\chi^{(2)}_{set3} \sim 1.5\,pm/V$. These are preliminary estimations, while for an accurate evaluation more statistics on nominally equal waveguides is needed. It is interesting to note that in the smaller waveguide, the measured $\chi^{(2)}$ is higher than the one in larger waveguide. This seems to endorse the fact that the SHG detected signal comes from the strain induced $\chi^{(2)}$, rather than surface effects. Indeed, in that case the $\chi^{(2)}$ is expected to have the same value. On the contrary, it makes sense from FEM simulations that smaller waveguides are more subjected to strain gradient effects, which eventually leads to higher induced $\chi^{(2)}$ coefficient.

Further investigations are needed in order to clearly demonstrate the origin of the measured SHG signal. In particular, the effect of strain has to be decoupled from other parasitic effects that could compete to the observed signal, such as the Electric Field Induced Second Harmonic Generation (EFISH) [19]. The presence of a positive charge surface density at the Si_3N_4-Si interface has been recently reported in different papers [19, 130]. As a net effect, the trapped positive charge attracts negative charges within the silicon, eventually forming permanent electric fields within the waveguide. The EFISH effect actually acts as a "dressed $\chi^{(2)}$", mediated by the relatively large $\chi^{(3)}$ coefficient of silicon as $\chi^{(2)}_{EFISH} \propto \chi^{(3)}\mathbf{E}_{DC}$, where $\mathbf{E}_{DC}$ is the static electric field generated by the positive charge surface density.

3.5.1 *Future perspectives*

The experimental measurements on strained silicon waveguides are still ongoing in the lab. In particular, a complete characterization as a function of the waveguide length and of the pump pulse bandwidth is still pending. Moreover, the graph reported in Figure 32(a) is not actually the SHG spectrum, as the signal is integrated over the InGaAs SPAD bandwidth, see Figure 15(a). We plan to take the SHG spectrum with a home-made spectrometer, like the one presented in Figure 16, which should be sensitive down to the single-photon level. It will be interesting to study the SHG bandwidth as a function of the waveguide length and of the tunable pump bandwidth with the pulse shaper directly from the measured SHG spectrum.

Besides the experimental characterization of the measured SHG signal, we also need to clarify the physical origin of the observed $\chi^{(2)}$. In particular, what we plan to do to disentangle the various contributions that may add up to the measured $\chi^{(2)}$, is to repeat the SHG experiment by using a screw equipped sample holder. This is reported in Figure 34(a), a tool that was already exploited in [119].
In this way, we have the freedom to externally introduce a tunable reconfigurable strain to the waveguide. By the evaluation of the variation of the generation efficiency as a function of the applied load, it will be possible to clarify the role of the strain on the observed $\chi^{(2)}$. It will be possible to find a relationship between the amount of $\chi^{(2)}$ induced by strain (that varies with the applied load) and the amount of $\chi^{(2)}$ that may be induced by other phenomena, such as the $\chi^{(2)}$ of the silicon nitride cladding or the trapped charges (that should be independent on the applied load).
Using a simulation procedure like the one described in Ref. [129], we will determine the strain distribution inside the waveguide. In Figure 34(b) is reported, as an example, the strain distribution inside the waveguide when the sample is stressed by means of the screw applying a displacement of 150 µm in the center of the sample. Fol-

lowing the work reported in [127], the comparison of this simulation with the experimental result, will give us the possibility to determine the relationship between the strain gradient tensor and the strain-induced second order nonlinearity, which are expected to be linearly proportional. For this goal, it would be useful to also experimentally evaluate the occurrence of SHG in Set 1 and Set 2 of Table 1, as they refer to a co-polarized TE multimodal combination. This will enable us to map another element of the $\chi^{(2)}$ tensor, specifically $\chi^{(2)}_{xxx}$, which will eventually let us cleanly link the the strain gradient tensor and the strain-induced second order nonlinearity [127].

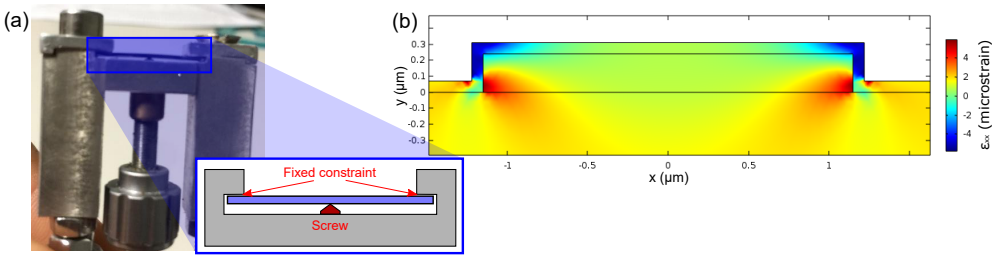

Figure 34: (a) Screw-equipped sample holder used to apply a tunable mechanical stress to the sample. (b) FEM simulation of the strain distribution in the waveguide placed in the center of the sample when the screw is applying a displacement of 150 µm.

Another strategy we are currently working on, is to study the effect of UV annealing passivation to the SHG signal in the strained silicon waveguides. Indeed, it is well known in literature that UV irradiation dramatically decreases the lifetime of the deep charge trapping centers at the silicon-nitride film interface [131]. If the SHG signal would be considerably decreased after the UV annealing, this would be a strong indication that charges by means of EFISH play a non negligible role in the observed experimental measurements. An interesting back-up option would be the deliberate exploitation of EFISH for inducing a sizeable $\chi^{(2)}$ into the silicon waveguide.
This idea takes inspiration from the recently published work by Timurdogan et. all [130], where the authors presented SHG measurements on silicon ridge waveguides, quasi-phase matched by DC electric field spatial distributions controlled with p-i-n junctions. They reported an induced $\chi^{(2)} = 41\,\mathrm{pm/V}$, which is actually comparable to the one of non-centrosymmetric media such as $LiNbO_3$, as discussed in Section 2.2.

Whatever eventually will be the successful strategy to induce the largest possible $\chi^{(2)}$ in silicon, a sizeable $\chi^{(2)}$ coefficient, besides enabling the highly sought electro-optic modulators, would also open the possibility to generate on-chip photon pairs via SPDC. Considering a pump at telecom wavelength, entangled photon pairs in the

MIR will be generated. This is an intriguing process, especially due to recent interest to the photonics community to the MIR spectral region [87].
However, while we have seen that the generation of nonlinear second order phenomena in silicon is not a trivial task, on the other side the single-photon detection in the MIR is really an issue. To this point, we will present in Chapter 7 that by means of spectral translation of MIR correlated photon pairs into the visible, we were able to demonstrate coincidence measurement at room temperature with relatively high CAR.

Part II

$\chi^{(3)}$ SOURCES OF ENTANGLED PHOTON PAIRS

Part II is dedicated to discuss sources of entangled photon pairs based on $\chi^{(3)}$ optical nonlinearity. In Chapter 4 the nonlinear and thermo-optical properties of SiON are presented. SiON is a material that is getting more and more appealing for photonics. Nonetheless the SiON optical properties have not yet been fully characterized. In particular, an accurate knowledge of the thermo-optic coefficient and of the nonlinear parameter n_2 is needed for the design of nonlinear and quantum integrated photonic circuits.
In Chapter 5 the generation of correlated photon pairs from silicon on insulator microring resonators is presented. The generation efficiency is characterized and linked to the theoretical expectations. A comparison with the obtained results with the current silicon integrated quantum photonics state of the art, is also addressed at the end of Part II.

4

STIMULATED FOUR WAVE MIXING IN SILICON OXYNITRIDE MICRORING RESONATOR

In this Chapter the optical properties of the silicon oxynitride material (SiON) are investigated by using racetrack resonators. SiON is appealing for photonics due to the fact that it is very transparent in a wide spectral range (it does not suffer multi-photon absorption losses), it shows minimal insertion losses and can be easily fabricated in a compatible way with respect to the well established CMOS technology. Nonetheless, the optical properties of SiON have not yet been fully characterized. We estimated in particular the thermo-optic coefficient of the material dn/dT and its $\chi^{(3)}$ coefficient, whose knowledge is essential for the design of nonlinear and quantum optical integrated photonic circuits, where thermal reconfiguration and nonlinear parameteric processes constitutes fundamental operations.
The work described in this Chapter was done in collaboration with Dr. Massimo Borghi. Dr. Fernando Ramiro Manzano designed the sample, which was fabricated by Dr. Mehr Ghulynian at the Bruno Kessler Foundation. Mr. Stefano Biasi also gave an important contribution with the interferometric measurement which fixes the microring excitation regime.

4.1 STIMULATED FOUR WAVE MIXING

In this Section, the theoretical framework to predict the generation efficiency of the $\chi^{(3)}$ nonlinear process named stimulated Four Wave Mixing (FWM) is presented. Stimulated FWM can be viewed as a fission process, where two pump photons are non-linearly mixed with a signal photon to generate and idler photon. In Figure 35 the FWM energy diagram is reported. As every nonlinear wave-mixing optical process, the energy and momentum conservation must be fulfilled in FWM. The energy and momentum relations are given by:

$$\omega_i = 2\omega_p - \omega_s \tag{65}$$

$$\mathbf{k}_i = 2\mathbf{k}_p - \mathbf{k}_s \tag{66}$$

where the *p*-subscript refers to the pump photons and the *s,i*-subscripts refer respectively to the signal and idler photons. Again, the fulfilment of the energy conservation (Equation 65) does not imply the momentum conservation (Equation 66), also called *phase matching condition* due to the frequency dependence of the refractive index.
In an optical resonator, all the waves involved in a parametric pro-

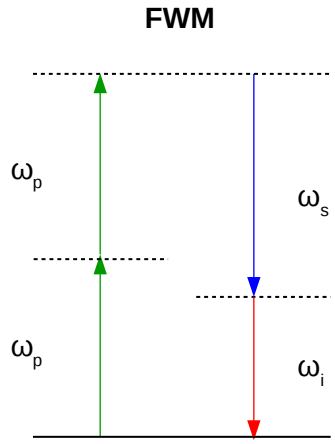

Figure 35: Sketch of the energy diagram for the $\chi^{(3)}$ process called Four Wave Mixing (FWM). In *stimulated* FWM, in addition to the pump photons with frequency ω_p, also an additional photon, say the signal at frequency ω_s is present, to trigger the generation of another photon, called idler at $\omega_i = 2\omega_p - \omega_s$. In spontaneous FWM two pump photons spontaneously decay into a signal and idler photon.

cess must be resonant within the cavity, otherwise they will undergo destructive interference. This implies that the frequency of the pump and of all the generated waves must be coincident with the eigen-frequencies of the resonator. For small detuning from the pump, the energy and phase matching condition are automatically met in a microring resonator.

4.2 MICRORESONATORS: THEORETICAL MODEL

In this Section the optical properties of a microring resonator are introduced. In planar integrated devices, light is coupled into the resonator by means of evanescent coupling with a bus waveguide. Only certain wavelengths are actually coupled into the resonator. The resonance condition is given by the following relation:

$$m\lambda_m = 2\pi R\, n_{eff}(T) \tag{67}$$

where λ_m is the resonant wavelength and m is the mode number of the ring resonator. R is the radius of the ring resonator and $n_{eff}(T)$ is the effective refractive index experienced by the whispering-gallery wave which travels within the resonator. It is worth to note that $n_{eff}(T)$ depends on the temperature through the thermo-optic coefficient of

the material, which will be analysed in detail in the final section of this chapter.
The simplest configuration of a ring resonator is obtained with a bus straight waveguide coupled to the ring resonator. This configuration is called *All-Pass* filter. A sketch of an All-Pass filter ring resonator is reported in Figure 36(a).

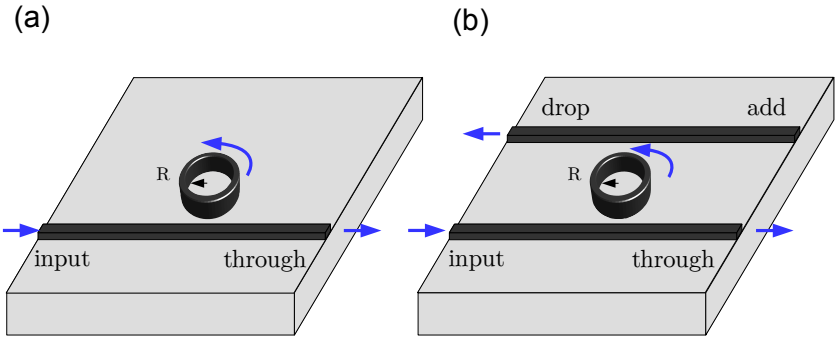

Figure 36: a) Sketch of an All-pass filter ring resonator. (b) Sketch of an Add-Drop filter ring resonator.

Whereas, as sketched in Figure 36(b), in the Add-Drop filter configuration two waveguides are coupled to the ring resonator. Through the *Transfer Matrix* formalism [132], it is possible to link the electric field amplitude at the input port, to the one scattered in the through port (and also in the drop port for the case of an Add-drop resonator).
In the following, the All-Pass transmission amplitude will be derived in a lossless point coupling approximation: that is to say, the exchange of energy is thought to happen in a point placed in the middle of the coupling region, where the gap is minimal.
With reference to Figure 37, the amplitudes of the electric field E_i (with i = 1,2,3,4) are related to each other in the coupling region by the following matrix relation:

$$\begin{bmatrix} E_4 \\ E_3 \end{bmatrix} = \begin{bmatrix} r & ik \\ ik & r \end{bmatrix} \begin{bmatrix} E_1 \\ E_2 \end{bmatrix} \tag{68}$$

Energy conservation at the coupling stage requires that the coupling coefficient k and the transmittance coefficient r satisfy: $k^2 + r^2 = 1$, where negligible coupling induced losses are considered.
In the free propagation region inside the ring resonator we find the following relation:

$$E_2 = E_3 e^{i(\beta + i\alpha)L} \tag{69}$$

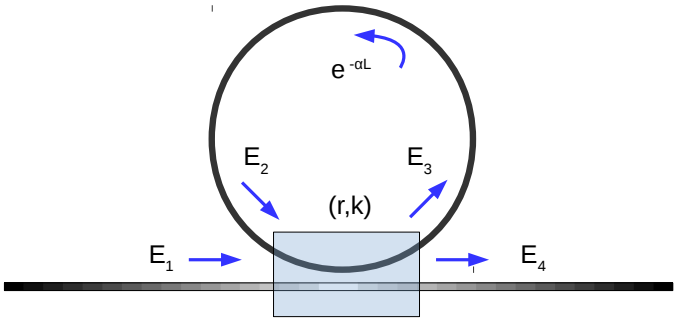

Figure 37: Sketch of the theoretical model of a coupled All-pass filter ring resonator. The coupling region is characterized by the transmission and coupling coefficients (r, k).

where $\beta(\lambda) = \frac{2\pi}{\lambda} n_{eff}(\lambda)$ is the propagation constant inside the ring, defined in Chapter 3, $L = 2\pi R$ is the perimeter of the ring and α is the loss coefficient.
Since only single-mode ring resonators will be analysed throughout the thesis, higher order modes inside the resonator will not be discussed. By inserting Equation 69 into Equation 68, the solution for the field amplitudes E_3 and E_4 in stationary conditions can be found. In particular, the normalized transmittance into the through port is given by:

$$T = \left|\frac{E_4}{E_1}\right|^2 = \left|\frac{r - \tau e^{i(\beta L)}}{1 - r\tau e^{i(\beta L)}}\right|^2 = \frac{r^2 + \tau^2 - 2r\tau\cos(\beta L)}{1 + r^2\tau^2 - 2r\tau\cos(\beta L)} \tag{70}$$

where $\tau = e^{-\alpha L}$ is the round-trip loss coefficient.
It can be shown, by expanding the exponential terms in Equation 70 to the first order in $(\lambda - \lambda_m)$, where λ_m is the m-th order resonance wavelength, that the peak is actually a lorentzian function [22]. In Figure 38 the transmittance response obtained from Equation 70 is reported. When $\Phi = \beta L = 2\pi$, typical Lorentzian-shaped transmittance dips are found at the ring's resonances. With respect to Figure 38, it is possible to distinguish three different regimes:

- *Under-coupling*: in this regime the losses induced by the coupling process (extrinsic losses) are lower with respect to the losses associated to light propagation inside the microresonator (intrinsic losses). In this excitation configuration, the transmittance shows narrow resonances (blue curve in Figure 38);

- *Over-coupling*: it is the opposite regime with respect to the under-coupling. Here the extrinsic losses are higher with respect to the intrinsic losses and the resonator is over-coupled. In over-

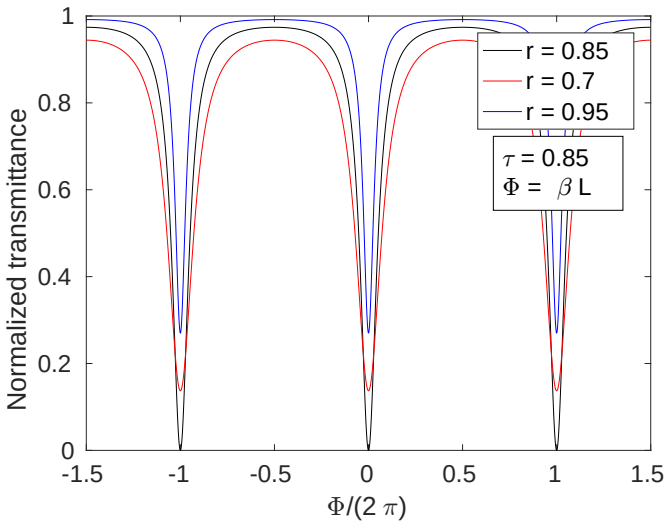

Figure 38: Transmittance spectra for an All-Pass filter single-mode ring resonator for three different values of the transmission coefficient r (r = 0.85, r = 0.7, r = 0.95). The intrinsic losses has been fixed arbitrarily to a value of $\tau = 0.85$

.

coupling, the transmittance shows broader resonances with respect to under-coupling configuration (red curve in Figure 38);

- *Critical coupling*: in this configuration the intrinsic losses balance the extrinsic losses. This gives rise to a complete destructive interference process at the coupling port of the resonator, which leads to a vanishing transmittance on resonance ($\Phi = m2\pi$, with m integer). The critical coupling configuration is the one which maximizes the field enhancement factor, defined as the ratio between the power circulating within the resonator with respect to the incoming power carried by the bus waveguide.

Let us discuss the main parameters which characterize a resonator.
It is not difficult to prove from Equation 67 that the spectral distance between two adjacent resonances, the so called *Free Spectral Range* is given by:

$$FSR_m = \frac{2\pi c}{n_g(\lambda_m)L} \tag{71}$$

where $n_g = \frac{1}{c}\left[n_{eff}(\lambda) - \lambda\frac{\partial n_{eff}(\lambda)}{\partial\lambda}\right]$ is the group index and the m-subscript denotes that FSR is evaluated with respect to the m-th resonance. From Equation 71 we see that the larger the resonator perimeter L, the smaller the FSR. Moreover, since n_g is wavelength-dependent, the FSR is not constant but depends on the resonance order m. As a consequence, resonances are not equidistant in frequency.

Another important parameter is the one related to the Full Width at Half Maximum (FWHM) of the resonances reported in Figure 38. The FWHM expressed in wavelength, evaluated for the m-th order, is given by:

$$\Delta\lambda_m = \frac{(1-r\tau)\lambda_m^2}{\pi n_g(\lambda_m)L\sqrt{r\tau}} \tag{72}$$

It is possible now to define the *quality factor* of the resonator, which is given by [22]:

$$Q = \frac{\lambda_m}{\Delta\lambda_m} \tag{73}$$

In general, the quality factor of a resonator is a dimensionless parameter which expresses how much an oscillator is under-damped. From Equation 72-73, we see that Q is related to the resonator's bandwidth relative to its centre frequency. High Q indicates a low rate of energy loss relative to the stored energy of the resonator. Typically, from the through port of a resonator one has direct access to the total quality factor Q_{tot}, which can be easily estimated by recording the transmittance power as a function of the input wavelength. The total quality factor is given by the following relation:

$$\frac{1}{Q_{tot}} = \frac{1}{Q_i} + \frac{1}{Q_e} \tag{74}$$

where Q_i is the intrinsic quality factor and Q_e is the extrinsic quality factor. The higher the quality factor magnitude, the lower the losses, which in turns let us interpret $1/Q$ as a quantity proportional to the resonator losses.
In particular, $1/Q_i$ takes into account the intrinsic losses, which are given by: material absorption, bending losses (also called radiation losses), scattering losses and surface absorption [133]. The extrinsic losses are instead given by the coupling losses, which can be tuned with the waveguide to resonator distance, to exploit different coupling regimes. As already pointed out, when the resonator is excited in critical coupling, this means that the intrinsic losses equals the extrinsic losses. In this particular case $Q_{tot} = Q_i/2$.
It is also possible to express the quality factor in terms of the photon lifetime τ_{tot}, which is related to the quality factor by $Q = \frac{\omega\tau_{tot}}{2}$. The physical interpretation is straightforward: the higher the quality factor, the lower the losses, the higher the photon lifetime, which is the time that a photon spends inside the cavity.
It is possible to show under weak coupling approximation ($k^2 \ll 1$)

and low intrinsic losses ($\alpha \ll 1$) that the photon lifetime τ_{tot} is related to the parameter (α, k) by the following relation [5, 134]:

$$\frac{1}{\tau_{tot}} = \frac{1}{\tau_i} + \frac{1}{\tau_e} \tag{75}$$

$$\frac{1}{\tau_i} = \alpha v_g \qquad \frac{1}{\tau_e} = \frac{k^2 v_g}{2L} \tag{76}$$

Another important parameter which characterizes a resonator is the *Field Enhancement* (FE) factor. FE represents the field gain occurring inside the resonator volume and can be expressed as $|FE|^2 = \frac{P_i}{P_e}$, which is the ratio between the circulating power inside the resonator, with respect to the incident power. By considering again the coupling equation Equation 68, the modulus square of the field enhancement is given by:

$$|FE|^2 = \frac{|E_3|^2}{|E_1|^2} = \left| \frac{ik}{1 - r\tau e^{i(\beta L)}} \right|^2 \tag{77}$$

In Figure 39, the $|FE|^2$ is plotted as a function of $\Phi = \beta L$ for the 3 different regimes (same parameters used in Figure 38).

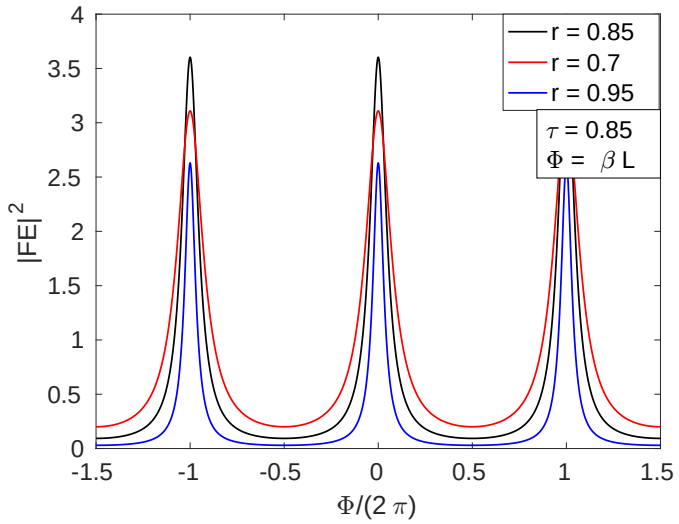

Figure 39: Modulus square of FE for an All-Pass filter single-mode ring resonator for three different values of the transmission coefficient r (r = 0.85, r = 0.7, r = 0.95). The intrinsic losses have been fixed arbitrarily to a value of $\tau = 0.85$.

As already stated, the field enhancement factor is maximum at the critical coupling condition, i.e. when $\tau = r$ (blue line in Figure 39). This result is also true for an Add-Drop Filter micro-ring resonator (see Chapter 8). FE can also be viewed as the resonator gain factor in steady state condition, with respect to the field propagation into

PARAMETERS	ALL-PASS	ADD-DROP
Q	$\frac{\pi n_g(\lambda_m)L\sqrt{r\tau}}{(1-r\tau)\lambda_m}$	$\frac{\pi n_g(\lambda_m)Lr\sqrt{\tau}}{(1-r^2\tau)\lambda_m}$
FSR	$\frac{2\pi c}{n_g(\lambda_m)L}$	$\frac{2\pi c}{n_g(\lambda_m)L}$
FE	$\frac{ik}{1-r\tau e^{i(\beta L)}}$	$\frac{ik}{1-r^2\tau e^{i(\beta L)}}$

Table 2: Main parameters which characterize the performances of a microring resonator in the All-Pass and Add-Drop filter configuration. They are expressed as a function of the coupler parameters (r, k), the total perimeter L, the m-th order resonant wavelength λ_m and the group index n_g.

a straight optical waveguide. The presence of a strong field inside a small volume is a peculiar property of micro-resonators, which makes them suitable elements for the observation of nonlinear effects at low input powers [72].
Similar results, with respect to the ones that have been achieved so far for an All-Pass filter resonator, can be obtained also for an Add-Drop filter micro-ring resonator with the transfer matrix formalism.
As it is sketched in Figure 36, the Add-Drop filter resonator presents two input ports, conventionally named input and add, and two output ones, named drop and through. In Table 2, the quality factor Q, the Free Spectral Range FSR and the Field Enhancement are reported together for the All-Pass filter and Add-Drop filter resonator. The same results obtained with the Transfer Matrix formalism of Equation 68 for the transmittance T (Equation 70) and for the FE (Equation 77) of a resonating device, can be obtained with a different approach, based on *Temporal Coupled Mode Theory* [135]. It can be shown that the dynamical equation that describes the evolution of the mode amplitude a for a single mode All-Pass resonator for a normalized to 1 excitation source, is given by [136]:

$$\frac{da}{dt} = i(\omega_m - \omega)a - \frac{1}{\tau_{tot}}a + i\sqrt{\frac{2}{\tau_e}} \tag{78}$$

where ω_m is the resonator eigenfrequency (in general for the m-th order) and τ_{tot} is the total lifetime, which satisfies the following relation $1/\tau_{tot} = 1/\tau_i + 1/\tau_e$. The temporal coupled mode theory formalism will be exploited in this chapter for the nonlinear refractive index estimation of the SiON.
It will also be extremely useful for studying a system composed by two indirectly coupled silicon micro-ring Add-Drop resonators in Chapter 8.

4.3 EXPERIMENTAL SET-UP

In this Section the optical set-up used to characterize the thermo-optic coefficient dn/dT and the nonlinear refractive index n_2 [12] of a relatively high ($n \sim 1.77$) SiON is presented. The refractive index of SiON can be tailored as a function of the relative amount of the gas mixture (SiH_4, NH_3 and N_2O) used in a parallel-plate plasma enhanced chemical vapour deposition (PECVD) [137].

4.3.1 *SiON All-pass racetrack resonator*

The device under test is a racetrack resonator in the All-Pass filter configuration [138]. The waveguide has a cross-section of $1.2 \times 0.55\,\mu m^2$, an internal bending radius of $R = 49.4\,\mu m$, while the coupling with the exciting waveguide is realized by means of a straight section of length $L_c = 20\,\mu m$ and a gap of $1.05\,\mu m$. An image taken from the design of the SiON mask is shown in Figure 40.

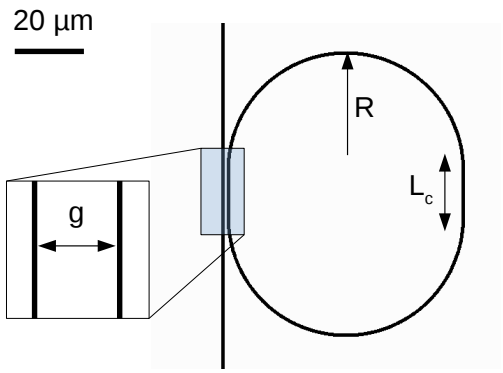

Figure 40: Design image for an All-Pass SiON racetrack resonator. The parameters are: $R = 49.4\,\mu m$, $L_c = 20\,\mu m$, $g = 1.05\,\mu m$.

The waveguide is single mode for both Transverse Electric (TE) and Transverse Magnetic (TM) polarizations at the probe wavelength at $1550\,nm$. The mode is confined between the lower $\sim 5\,\mu m$ thermal oxide cladding and an upper one, constituted by a double stack of 400 nm Borophosphosilicate glass (BPSG) and a $2\,\mu m$ thick PECVD SiO_x layer.
It is worth to note that the model developed in the previous section for an All-Pass micro-ring resonator, can also be applied in the case of a racetrack resonator. The main advantage of using a racetrack resonator is that it is easier to determine the coupling strength since it is controlled by two parameters: the length of the two straight coupling guides L_c and their separation gap (see Figure 40). Spacing tolerances are less critical for the coupling gaps in racetrack compared

to ring resonators, because if stronger couplings are needed only the coupling length has to be increased without decreasing the spacing between the input guide and the resonator. As a drawback, the total perimeter of a racetrack resonator is longer with respect to the one of a micro-ring with equal radius, which implies higher losses experienced by the mode inside the resonator. As we will see in this section, for the case of SiON this is not a big issue, due to the typical low intrinsic losses associated with the material.

With respect to the model developed for the micro-ring All-Pass resonator, there are only few differences to take into account: Equation 69 is now $E_2 = E_3 e^{-(\alpha_R L_R + \alpha_C 2L_C)} e^{i(\beta_R L_R + \beta_C 2L_C)}$, where two contributes are highlighted. One contribution comes from the straight propagation along the directional coupler (C-subscript) and the other one from the curved elements (R-subscript). L_C and $L_R = 2\pi R$ are the length of the directional coupler and the curved elements, respectively.

First of all, the device was passively characterized. With a pigtailed tunable C-band Continuous Wave (CW) laser (TUNICS T100S-HP, Yenista) the optical signal is edge-coupled into and out of the waveguides by means of tapered lensed fibres (OZ optics, spot diameter of $(2.5 \pm 0.3)\ \mu m$, working distance $(14 \pm 2)\ \mu m$), thanks to a micrometric positioning stage. The signal is measured with a commercial Ge photodetector (2033 - Newport Corporation), connected to a multimeter. From the voltage signal V read by the multimeter, the impinging power P on the instrument is given by the following relation:

$$P = \frac{V}{GR} \quad (W) \tag{79}$$

where G is the amplifier's trans impedance gain in V/A and $R = 0.8\ A/W$ is the detector responsivity at $\lambda = 1550\,nm$. The amplifier's trans impedance gain can be set to three values $(2 \times 10^3, 10^5, 2 \times 10^6) V/A$ with a resulting dynamical range that extends from few nW up to $5\,mW$. With the cut-back method, the total coupling losses have been measured to be (6 ± 0.5)dB, equally divided between input and output. The estimation uncertainty is due to statistic error, derived from repeated measurements. From the analysis of nominal equal waveguides but with different length, it was possible to estimate the propagation losses for TE and TM mode which result to be (2 ± 0.5)dB at a laser probe wavelength of $\lambda = 1550\,nm$.

With the help of a Labview programme which manages both the tunable laser and the multimeter, it has been possible to acquire both the transmittance spectra for the TE and TM mode. They are reported together in Figure 41. The decreased transmission at wavelengths around $1530\,nm$ is attributed to the presence of residual N–H bonds that could be minimized by additional annealing processes [139].

From a Lorentzian fit of the resonance dips in Figure 41, it is possible

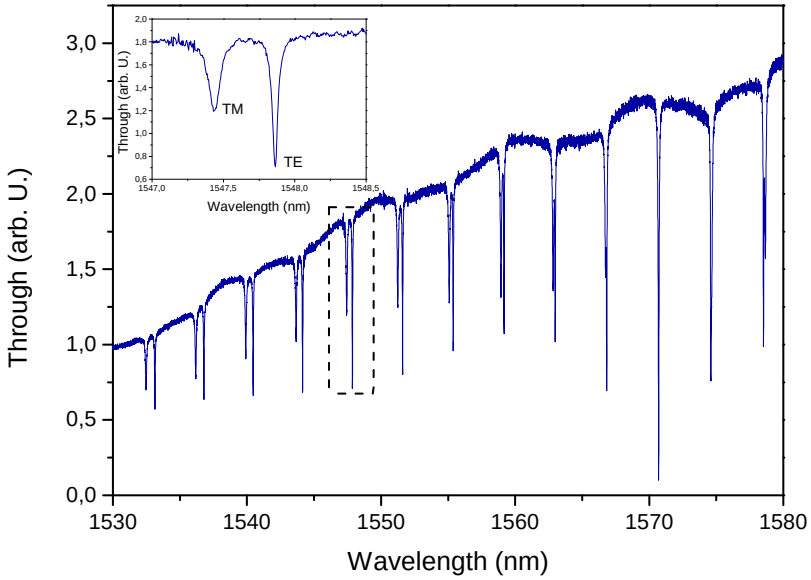

Figure 41: Transmittance spectra for both TE and TM mode for the racetrack resonator under test.

to estimate the total quality factor Q_{tot} (Equation 73) for the TE and TM polarization at the different resonance orders.
Actually, in order to be able to determine the nonlinear refractive index n_2 of the SiON, we also needed to know the external quality factor Q_e. A detailed analysis of the quality factor of the device is discussed in the Section 4.5 regarding the n_2 estimation.
Moreover, since the resonator is not excited in the critical coupling condition, for an accurate estimation of n_2 one also needs to know whether the micro-resonator is in under-coupling or over-coupling. This was fixed with an interferometric set-up, by simultaneously measuring the intensity and the phase of the light transmitted from the resonator as a function of wavelength. This was fixed by placing the sample into one arm of a free space Mach-Zehnder [140]. The Mach-Zehnder was set in a nearly balanced regime (both in amplitude and phase) by using a delay line and a variable optical attenuator placed in the free arm. Three output signals were recorded at the output of the interferometer, which are the light transmitted from the sample I_s (when the light in the free arm is blocked), the one coming from the free arm I_{ref} (when the light in the arm which contains the sample is blocked), and their interference I. The phase is than retrieved by the relation [140]:

$$\phi = \arccos\left[\frac{I - I_s - I_{ref}}{2\sqrt{I_s I_{ref}}}\right] \tag{80}$$

The racetrack resonator under study turned out to be under-coupled in the considered wavelength range around 1550 nm. More details about this interferometric experimental set-up are reported in [140, 141].
From a FEM simulation of the device reported in Figure 40, the group index n_g was estimated both for the TE and TM mode. From the fact that the group index is slightly larger for the TM mode, it is possible to recognize that in the inset of Figure 41, the shorter wavelength resonance is associated with the TM mode, while the other to TE mode. The group index is computed for both the straight and the bent waveguide (indicated as n_{gs} and n_{gb} respectively). The average group index is given by:

$$\langle n_g \rangle = (n_{gb} \times L_R + n_{gs} \times 2L_c)/(L_R + 2Lc)$$

The average group index $\langle n_g \rangle$ is indeed the quantity that we can compare with the experiment through the FSR relation (Equation 71).
From Figure 42 we see a good agreement between theory and experiment. The experimental group index, evaluated at a wavelength of 1550 nm, is $n_g^{TE} = (1.83 \pm 0.02)$ for the TE polarization and $n_g^{TM} = (1.80 \pm 0.02)$ for the TM polarization. The corresponding FSR, expressed in wavelength, from Equation 71 resulted to be $FSR^{TE} = (3.70 \pm 0.04)$nm and $FSR^{TM} = (3.76 \pm 0.04)$nm.

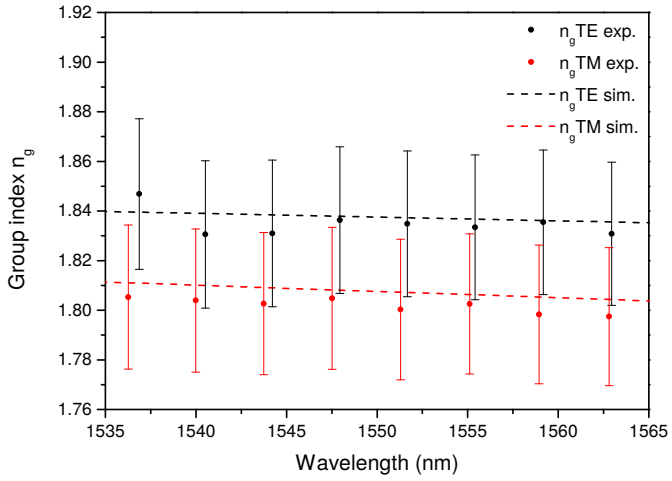

Figure 42: Measured (dots) and simulated (dashed lines) group index for the TE and TM polarizations.

4.3.2 *Waveguide set-up for SiON investigation*

Let us present the optical set-up that was used for the determination of the SiON thermo-optic coefficient dn/dT and the nonlinear coefficient n_2. The set-up is sketched in Figure 43.

As shown in Fig 43(a), the device is in thermal contact with a Peltier cell, whose temperature can be controlled by an external Temperature Controller (TEC) in the range of 25-75 °C, with an approximate accuracy of ± 1 °C. For the thermo-optic estimation the wavelength of one tunable C-band CW laser was swept around the TE resonance at 1540 nm and the resonance position was tracked for different Peltier temperatures.
In the case of the n_2 estimation, instead, we exploited the nonlinear effect of stimulated FWM. As it is shown in Figure 43(b), two CW tunable lasers are combined and injected into the input port of the resonator. Due to the low expected efficiency of the process (considering as a lower bound the relatively low n_2 of the silica [142]), a proper targeted filtering operation was performed. This increases the signal to noise ratio in the detection of the expected generated signal wavelength, which is determined by energy conservation in Equation 65.
For this purpose, both the injected lasers are cleaned from the background stimulated emission at the signal wavelength. In particular, the pump laser is cleaned with a free-space band-pass filter of central wavelength 1550 nm, a bandwidth of 5 nm and an extinction ratio higher than 50 dB. Similarly, the idler laser is filtered using a Fiber Bragg Grating with peak reflectance at 1567 nm, a bandwidth of 5 nm and an extinction ratio higher than 30 dB. After the filtering stage, the level of background radiation is found to be lower than 110 dBm.
The injected powers (expressed in dBm) right before the coupling with the waveguide are: $P_p = 4.26$ dBm and $P_i = 3.08$ dBm.
Light is collected at the output fibre and it is split: 1% goes to a germanium detector in order to monitor the level of the total transmitted signal to ensure that the pump and the idler wavelengths are set on resonance. The remaining is directed to an additional filtering stage. The generated signal is filtered from the co-propagating pump and idler beams by using two cascaded Dense Wavelength Division Multiplexing (DWDM) modules (~2.5 dB inserion loss), and directed to a photon counter (ID Quantique ID210) operating in Free Running mode, with a detection efficiency of 5% and a dead time of 40 µs. The DWMD modules achieve a signal isolation of more than 100 dB.

4.4 SILICON OXYNITRIDE THERMO-OPTIC COEFFICIENT ESTIMATION

It is possible to derive from Equation 67 that when the waveguide which forms the resonator experiences a variation in temperature ΔT, each resonance gets shifted from the original wavelength λ_0 by a quantity $\Delta\lambda$ which is given by:

$$\Delta\lambda(\Delta T) = \frac{\Delta n_{eff}(\Delta T)}{n_{eff}(\lambda_0)}\lambda_0 \tag{81}$$

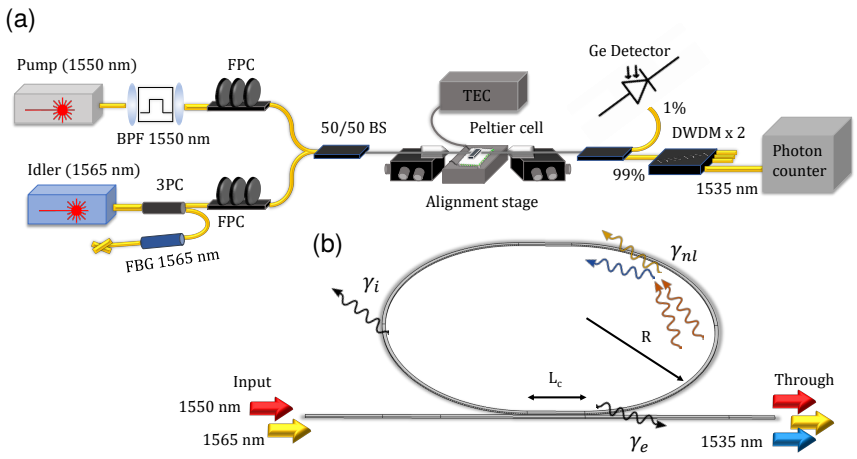

Figure 43: (a) Sketch of the experimental setup. FPC: Fiber Polarization Controller, FBG: Fiber Bragg Grating, 3PC: Three Port Circulator, TEC: Temperature Controller, DWDM: Dense Wavelength Division Multiplexing (b) Sketch of the resonator geometry, with indicated the main parameters. L_c : coupling length, R : (internal) bending radius, γ_i : intrinsic loss rate, γ_e: extrinsic loss rate, γ_{nl} : nonlinear coefficient. The device is excited from the input port by a pump and an idler laser at $\lambda_p \sim 1550\,nm$ and $\lambda_i \sim 1565\,nm$ respectively, while the generated signal at $\lambda_s \sim 1535\,nm$ is collected at the output of the through Port.

where Δn_{eff} is the effective index variation caused by the temperature variation ΔT.

As shown in Figure 44, the quantities $\Delta\lambda(\Delta T)$ and λ_0 (the cold resonance) can be easily extracted from the experiment. As it is possible to see from the spectra, the temperature increase causes a red-shift to the resonance dip, which indicates that the SiON thermo-optic coefficient is a positive quantity. In the investigated range of temperatures, the shift $\Delta\lambda$ is found to be linear as a function of the temperature (see inset of Figure 44).
For determining $\Delta n_{eff}(\Delta T)$, one also needs to know $n_{eff}(\lambda_0)$. Since the resonator has a small refractive index (FSR ~3.7 nm), it was shown that determining $n_{eff}(\lambda_0)$ is experimentally difficult [143]. This is due to the fact that it is difficult to estimate the correct modal order m in Equation 67 from the knowledge of the resonance wavelength and the resonator perimeter if the FSR is small.
Therefore, as it was already done for the group index n_g, the effective refractive index has been simulated by means of a FEM simulation. Due to the weak modal confinement, slight deviations of the waveguide geometry(due to fabrication errors with respect to the design dimensions) result in negligible variations in n_{eff}.

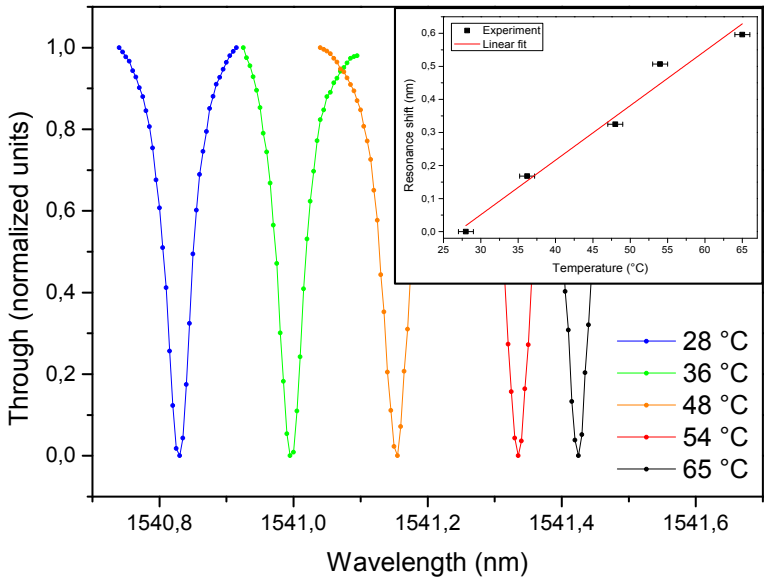

Figure 44: Transmittance spectra as a function of the Peltier temperature for the TE cold resonance (blue curve) at $\lambda = 1540.83\,nm$. In the inset the wavelength shift as a function of the temperature is reported.

In this way, it is possible to determine with Equation 81 the quantity $\Delta n_{eff}/\Delta T$ as a function of known parameters:

$$\left(\frac{\Delta n_{eff}}{\Delta T}\right)_{exp} = \frac{\Delta\lambda}{\Delta T}\,\frac{n_{eff}(\lambda_0)}{\lambda_0} \tag{82}$$

However, since the mode extends also into the cladding, the quantity $\Delta n_{eff}/\Delta T$ is not simply the thermo-optic coefficient of the waveguide core, but it contains informations about the thermo-optical properties of both the cladding and of the core materials.
In order to be able to decouple the two contributions, $\Delta n_{eff}/\Delta T$ is computed by FEM simulations by varying the thermo-optic coefficient of the core material. The best estimate of the the SiON thermo-optic coefficient will be the one which matches the experimental value of $\Delta n_{eff}/\Delta T$, reported in Equation 82. The refractive index of the oxide cladding n_{ox} is modelled as $n_{ox}(\Delta T) = n_{ox,o} + \Gamma_{ox}\Delta T$, where $n_{ox,o}$ is a reference refractive index at room temperature, and $\Gamma_{ox} = 0.95 \times 10^{-5}\ K^{-1}$ is the thermo-optic coefficient of the oxyde [144]. Likewise, the refractive index of the core is changed according to $n_{SiON} = n_{SiON,0} + \Gamma_{SiON}\Delta T$.
In Figure 45 the simulated slope of the relation $\Delta n_{eff}/\Delta T$ as a function of the thermo-optic coefficient of the core material is reported. The red dot shows the experimental value of the slope, which is found from the analysis of the shift of the resonance wavelength (see Figure 44). The experimental value of the slope $\left(\Delta n_{eff}/\Delta T\right)_{exp}$ matches the simulated $\Delta n_{eff}/\Delta T$ when the thermo-optic coefficient of the core

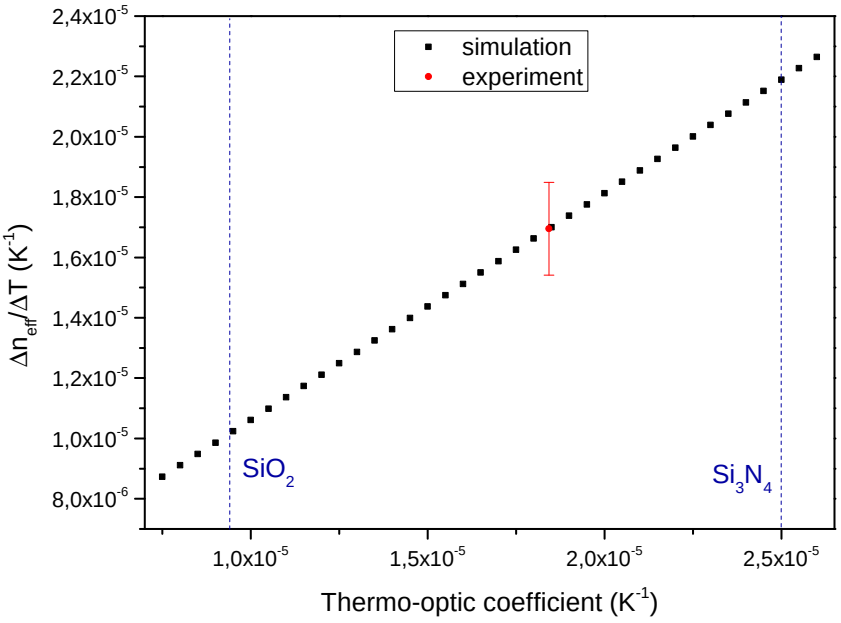

Figure 45: Simulated slope of the relation $\Delta n_{eff}/\Delta T$ as a function of the thermo-optic coefficient of the core material. The red dot shows the experimental value of the slope, which is found from the analysis of the shift of the resonance wavelength as a function of temperature shown in Figure 44. The vertical blue dashed lines are guidelines and indicate the values of the SiO_2 and Si_3N_4 thermo-optic coefficient [144].

material is $\Gamma_{SiON} = (1.84 \pm 0.17) \times 10^{-5}\,K^{-1}$. The uncertainty in the thermo-optic estimation comes from the error propagation of the linear fit, shown in the inset of Figure 44. As expected, the SiON thermo-optic coefficient lies in the range between the thermo-optic coefficient of the silica (SiO_2) $\Gamma_{SiO_2} = 0.95 \times 10^{-5}\,K^{-1}$ and the one of stoichiometric silicon nitride (Si_3N_4) $\Gamma_{Si_3N_4} = 2.5 \times 10^{-5}\,K^{-1}$. In particular, it is approximately the 74% of the latter [144].
Following the work of Bossi et. al. [145], from the measured refractive index at a wavelength of 850 nm $n_{SiON} = (1.839 \pm 0.001)$, we estimate a Si_3N_4 molar fraction of (73 ± 2)%, and a SiO_2 molar fraction of (27 ± 2)%. We point out, however, that the optical properties of SiON can not be thought simply as a linear combination of the ones of SiO_2 and of Si_3N_4. This is because the investigated SiON is not an "effective medium", in which SiO_2 and Si_3N_4 coexist in separate phases, but it is itself a new material with its own peculiar chemical bonds. As a support of this fact, the thermo-optic coefficient is about 70% of the one of Si_3N_4, while we will see that the nonlinear refractive index is only the 30% of the latter.
The simulation shown in Figure 45 does not determine the effective in-

dex shift by considering the thermo-optic coefficient as a weighted average between the two materials, but it is obtained solely by changing the value of the thermo-optic coefficient of the core material, without any additional assumption. The fact that the curve appears as a linear interpolation of the thermo-optic coefficients of SiO_2 and Si_3N_4 (by some coefficients which could wrongly be thought as their respective molar fraction) is only due to the linear relation between the change in the refractive index and the temperature variation. Moreover, the simulation does not take into account the impact of the photoelastic effective index shift due to the accumulated stress in the waveguide (called stress-optic effect), as a consequence of the temperature variation [146]. Indeed, by varying temperature to measure the thermo-optic coefficient, sometimes the measurement may not be accurate if the stress-optic effect is ignored. This is however a reasonable approximation in our case, as we estimated with a FEM simulation a maximum average stress (compressive and biaxial) of only 30 MPa in the waveguide core at 65 °C. By assuming as a first approximation the same stress-optical coefficients of Si_3N_4 for the silicon oxynitride core [147], this leads to a photoelastic effective index shift of $3.47 \times 10^{-7}\,K^{-}1$.
This value is actually two orders of magnitude lower than the one induced by the thermo-optic effect, and thus can be safely included within the error bar of our measurement.

4.5 SILICON OXYNITRIDE NONLINEAR REFRACTIVE INDEX ESTIMATION

In this Section, the method used to determine the nonlinear refractive index of the SiON is presented. Starting from Equation 78, it is possible to show that in a classical undepleted pump (and idler) approximation, the signal power generated P_s is given by [99]:

$$P_s = (\gamma_{nl} L P_p)^2 |FE(\omega_p)|^4 |FE(\omega_s)|^2 |FE(\omega_i)|^2 P_i \tag{83}$$

where FE is the field enhancement, P_p and P_i are the pump and idler power into the bus waveguide, L is the total perimeter and γ_{nl} is the nonlinear parameter. In particular, the nonlinear parameter is defined as:

$$\gamma_{nl} = \frac{\omega_p n_2 n_g^2}{c n_{SiON}^2 A_{eff}} \tag{84}$$

where A_{eff} is the effective area, defined in [12].
With reference to the optical set-up shown in Figure 43, a stimulated FWM experiment is performed for both the TE and TM polarization. The experiment is performed by tuning the pump and the idler laser frequencies ω_p and ω_i into two resonances and by monitoring the generated signal power at the frequency $\omega_s = 2\omega_p - \omega_i$. In Figure 46

the analysed resonance orders for both the TE and TM polarization are reported. Due to the non-negligible group-velocity dispersion at

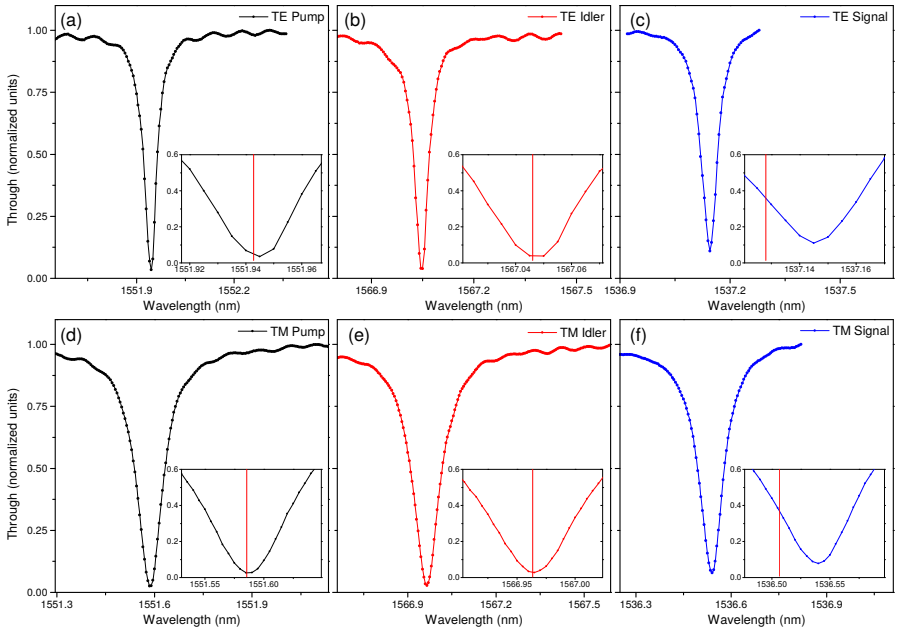

Figure 46: Panels from (a) to (c) report the spectral response of the through port of the resonator for the three TE resonances (pump, idler and signal resonances respectively) involved in the FWM process. Each inset shows a zoom of the resonance dip, with indicated the laser wavelength (solid red line) for the pump and the idler resonances. The solid red line in panel (c) is placed where the signal is generated, and follows directly from energy conservation. Panels from (d) to (f) are for TM polarization.

ω_p, the generated wavelength ω_s does not perfectly match the eigen-frequency of the resonator (see solid red lines in the insets of panels (c) and (f) of Figure 46).

Let us define a normalized detuning $\delta = \delta\omega/\omega_{0s}$, where ω_{0s} is the resonator signal eigen-frequency. It can be shown that the field enhancement as a function of a detuning δ is given by [148]:

$$|FE(\delta)|^2 = \frac{1}{(\omega_0 \tau_{rt} Q_{ext})} \frac{1}{\delta^2 + \left(\frac{1}{2Q_{tot}}\right)^2} \tag{85}$$

where $\tau_{rt} = L/v_g$ is the roundtrip time of light within the cavity and $v_g = c/n_g$ is the group velocity. While Q_{tot} can be extracted from the resonance linewidth (see Equation 73), the determination of the extrinsic quality factor requires an additional equation. This is provided by the (on resonance) normalized transmission T:

$$T = \left(\frac{Q_{ext} - 2Q_{tot}}{Q_{ext}}\right)^2 \tag{86}$$

from which one can extract Q_{ext} as:

$$Q_{ext} = \frac{2Q_{tot}}{1 \pm \sqrt{T}} \tag{87}$$

The sign at the denominator in Equation 87 depends on the regime under which the resonator operates.
In the under-coupled regime, $Q_{ext} > 2Q_{tot}$, which results in a minus sign in Equation 87. In contrast, in the over-coupled regime, one has to choose the plus sign. As already stated, from the measurements of the transmitted phase, the resonator is found to be under-coupled, so the minus sign was chosen. A summary of the main resonator parameters is reported in Table 3-4 for TE and TM polarization respectively.
In order to evaluate the generated flux of photons, it is important

Parameter	Pump resonance	Idler resonance	Signal resonance
λ_0 (nm)	(1551.940 ± 0.005)	(1567.045 ± 0.005)	(1537.145 ± 0.005)
Q_{tot}	$(3.43 \pm 0.04) \times 10^4$	$(3.17 \pm 0.4) \times 10^4$	$(2.90 \pm 0.4) \times 10^4$
T	$(3.15 \pm 0.06) \times 10^{-2}$	$(3.90 \pm 0.08) \times 10^{-2}$	$(11.3 \pm 0.3) \times 10^{-2}$
Q_{ext}	$(8.3 \pm 0.1) \times 10^4$	$(7.9 \pm 0.1) \times 10^4$	$(8.7 \pm 0.2) \times 10^4$
δ	~ 0	~ 0	(0.019 ± 0.001)
τ_{rt} (ps)		(2.14 ± 0.05)	
$\lvert FE \rvert^2$	(21.7 ± 0.7)	(19.7 ± 0.7)	(9.4 ± 0.5)

Table 3: Measured resonance wavelength λ_0, total quality factor Q_{tot}, on resonance transmittance T, extrinsic quality factor Q_{ext}, normalized detuning δ, roundtrip time τ_{rt} and field enhancement $|FE|$ relative to the pump, the idler and the signal TE resonances.

to evaluate the background radiation which reaches the SPAD after the output filtering stage. Indeed, the power measured in the signal channel of the DWDM, contains both the power generated by stimulated FWM inside the ring and the residual background radiation which is not suppressed by the filtering stages. To isolate only the FWM signal, the background level is evaluated in the adjacent channel of the DWDM (separated by 200 GHz from the signal channel), in which only the background noise is present. Here, we exploit the fact that the spontaneous emission of the laser is almost uniformly spread in wavelength, while the generated signal photons are suppressed in the adjacent channel by more than 30 dB). In order to evaluate the on chip power of the pump, the idler and the signal, coupling and propagation losses have been subtracted from the values measured out of the chip. Finally, Equation 83-85 have been used to estimate the value of n_2. In Table 5 a summary of the parameter used to estimate n_2 is reported. For the case of TE polarization, the result for the nonlinear coefficient is $n_2^{TE} = (6 \pm 1)\, 10^{-20}\, m^2 W^{-}1$. While in the case of TM polarization it results $n_2^{TM} = (8 \pm 1)\, 10^{-20}\, m^2 W^{-}1$. As expected, these

Parameter	Pump resonance	Idler resonance	Signal resonance
λ_0 (nm)	(1551.590 ± 0.005)	(1566.960 ± 0.005)	(1536.540 ± 0.005)
Q_{tot}	$(1.61 \pm 0.01) \times 10^4$	$(1.40 \pm 0.01) \times 10^4$	$(1.68 \pm 0.02) \times 10^4$
T	$(2.74 \pm 0.03) \times 10^{-2}$	$(3.80 \pm 0.04) \times 10^{-2}$	$(8.0 \pm 0.2) \times 10^{-2}$
Q_{ext}	$(3.86 \pm 0.02) \times 10^4$	$(3.48 \pm 0.02) \times 10^4$	$(4.7 \pm 0.09) \times 10^4$
δ	~ 0	~ 0	(0.019 ± 0.001)
τ_{rt} (ps)		(2.10 ± 0.05)	
$\lvert FE \rvert^2$	(10.5 ± 0.2)	(8.9 ± 0.2)	(6.3 ± 0.3)

Table 4: Measured resonance wavelength λ_0, total quality factor Q_{tot}, on resonance transmittance T, extrinsic quality factor Q_{ext}, normalized detuning δ, roundtrip time τ_{rt} and field enhancement $|FE|$ relative to the pump, the idler and the signal TM resonances.

Parameter	TE polarization	TM polarization
$P_{s,ext}$(dBm)	(-95.90 ± 0.03)	(-99.76 ± 0.08)
P_p (dBm)	(1.0 ± 0.2)	(4.0 ± 0.2)
P_i (dBm)	(-0.2 ± 0.2)	(0.51 ± 0.2)
Prop. loss ($dBcm^{-1}$)	(4 ± 0.5) (at λ_s) / (2.0 ± 0.5) (at λ_i, λ_p)	
Coupl. loss ($dBcm^{-1}$)	(3 ± 0.2)	(3 ± 0.2)
A_{eff} (μm^2)	0.99	1.58
$\gamma_{nl}(m^{-1}W^{-1})$	(0.26 ± 0.05)	(0.1 ± 0.04)
$n_2(m^2W^{-1})$	$(6 \pm 1) \times 10^{-20}$	$(8 \pm 1) \times 10^{-20}$
$\chi^{(3)}(m^2V^{-2})$	$(6 \pm 1) \times 10^{-22}$	$(9 \pm 1) \times 10^{-22}$

Table 5: List of the main parameters which appear in Equation 83 and Equation 85.

values are matched due to the isotropic nature of the material which comes from its amorphous structure. We can also define an average vale as $\langle n_2^{SiON} \rangle = (7 \pm 2)\, 10^{-20}\, m^2W^{-}1$. Note that in the estimation of n_2, we also considered the possible contribution in the observed FWM process from the silica cladding, since the mode extends also outside the waveguide core [12]. This is anyway a minor correction in the final estimation of the nonlinear propertied of SiON. The main source of error in the nonlinear parameters reported in Table 5, is the limited experimental resolution for an accurate determination of the detuning δ, which indicates the spectral distance from the signal resonance and the generated signal frequency ω_s (see Figure 46), which directly follows from energy conservation (Equation 65).

To conclude, as expected $\langle n_2^{SiON} \rangle$ lies between the nonlinear coefficient of SiO_2 and the one of Si_3N_4 [142, 149]. $\langle n_2^{SiON} \rangle$ exhibits almost three times the nonlinear index of silica. Therefore, in addition to the well known appealing properties of the SiON, such as low in-

sertion and propagation losses, wide transparency window from the visible to the infrared, lack of multi-photon absorption effects, CMOS compatibility and stress-free fabrication, here we evaluated a sizable thermo-optic coefficient and nonlinear refractive index.
With this work, we demonstrated that the characterized SiON platform has actually competing performances with respect to other CMOS-compatible platforms, such as silicon nitride and and high-index doped silica (trade-named Hydex) [150]. In these platforms, generation and manipulation of quantum states of light have been already reported so far in literature by many groups [67, 151, 152]. For what concerns silicon nitride, however, while it shows slightly superior performances in terms of n_2 and thermo-optic coefficient with respect to our SiON, it is worthy to point out that it may accumulates undesired stress at thicknesses over $200\,nm$, requiring thus specific design and processing solutions [153, 154].
Hence, I think that SiON is an excellent trade-off platform for the design of nonlinear and quantum optical integrated photonic circuits, in which thermal reconfiguration and nonlinear parameteric processes constitute fundamental operations.

5

SPONTANEOUS FOUR WAVE MIXING FROM SILICON-BASED MICRORING RESONATORS

In this Chapter the generation of correlated photon pairs in a silicon Add-Drop filter micro-ring resonator is discussed. The integration of sources of correlated photon pairs on a chip is a cornerstone for the scalability of the quantum technology revolution. In particular, the silicon-on-insulator platform offers scalable manufacture, integration, and it can relies on the mature CMOS technology which had established the microelectronics success.
A comparison with the obtained results with the current silicon integrated quantum photonics state of the art is addressed at the end of the Chapter.
The work described in this Chapter was done in collaboration with Dr. Massimo Borghi. Dr. Jean-Marc Fedeli of CEA-LETI fabricated the sample.

5.1 SPONTANEOUS FOUR WAVE MIXING

With reference to Figure 35, spontaneous FWM is a parametric $\chi^{(3)}$ process, which happens spontaneously and it is stimulated by random vacuum fluctuations. It can be viewed at the first order as a fission process, where two pump photons are converted into a higher energy photon, called *signal*, and into a lower energy photon, called *idler*. Since energy and momentum are conserved in the FWM process (see Equation 65-66), the signal and idler photons are typically correlated in momentum, energy and time. In general, the degree of correlation depends on the parameters of the pump, the nonlinear medium and the collection optics [20].
Using the temporal coupled mode theory introduced in Chapter 4 in Equation 78, it is possible to express the amplitude equations for the stimulated FWM process in an Add-Drop filter microring resonator. These are given by:

$$\begin{aligned}
\frac{da_p}{dt} &= i\left(\omega_p + \frac{i}{\tau_{tot}}\right)a_p + i\sqrt{\frac{2}{\tau_e}}\sqrt{P_p} \\
\frac{da_i}{dt} &= i\left(\omega_i + \frac{i}{\tau_{tot}}\right)a_i + i\sqrt{\frac{2}{\tau_e}}\sqrt{P_i} \\
\frac{da_s}{dt} &= i\left(\omega_s + \frac{i}{\tau_{tot}}\right)a_s + \Gamma a_p^2 a_i^*
\end{aligned} \tag{88}$$

where $1/\tau_{tot} = 2/\tau_e + 1/\tau_i$ is the relation which links the photon lifetimes in the case of a symmetric Add-Drop filter micro-ring resonator and $P_{p(i)}$ are the injected power into the waveguide for the pump wave and the idler one. With this formalism, $|\Gamma|^2$ is the rate of energy conversion into the signal wave. Note that in Equation 88, all the FWM terms have been neglected, except the one involved in signal generation. Also thermal and free carrier induced resonance shifts have not been taken into account. A more extended model can be found in [136, 155].
From a closer view to Equation 88, one immediately realizes that in the classical approximation it is not possible to describe the occurrence of spontaneous FWM, where correlated photon pairs are generated spontaneously from the annihilation of two pump photons. Indeed, if one removes the external excitation P_i, the idler mode amplitude a_i vanishes and therefore also a_s.
Dealing with spontaneous FWM in a microring resonator has two main key aspects with respect to a simple straight waveguide geometry (see Chapter 3):

- the advantageous *power enhancement* provided by the resonant structure. In particular, the enhacement factor with respect to a waveguide of the same length is given by $\left(|FE_p)|^4|FE_s|^2|FE_i|^2\right)$, where *FE* is the field enhancement factor (see Equation 83);
- all the waves involved in a parametric process must be resonant within the cavity, otherwise they will undergo destructive interference. This implies that the frequency of the pump and of all the generated waves must be coincident with the eigenfrequencies of the resonator. For small detuning from the pump, the energy and phase matching condition are automatically met in a resonator [12].

Within the framework of second quantization, the spontaneous FWM process can be described as the decay of two pump photons $\hat{a}_p^\dagger$, into a signal and idler photon mode $\hat{a}_s^\dagger$ and $\hat{a}_i^\dagger$. Similarly to what was done in Chapter 2 for the other spontaneous parametric process named SPDC, the two-photon quantum mechanical state generated through spontaneous FWM is given by [99]:

$$\left|\psi_{gen}\right\rangle = e^{\beta C_{II}^\dagger - H.c.}\left|vac\right\rangle \tag{89}$$

where $|\beta|^2$ is proportional to the average number of pump photons and H.c. stands for hermitian conjugate and

$$C_{II}^\dagger = \frac{1}{\sqrt{2}}\int d\omega_s d\omega_i \phi(\omega_s,\omega_i)\hat{a}_s^\dagger \hat{a}_i^\dagger \tag{90}$$

In Equation 90 we have introduced the function $\phi(\omega_s,\omega_i)$, which is known in literature as the *biphoton wavefunction* [20, 156]. The phys-

ical interpretation of the biphoton wavefunction is the following: its modulus square set the probability to generate a photon pair with frequencies ω_s and ω_i. In the limit of low pump power, $|\beta| \ll 1$, the quantum state in Equation 89 can be written as:

$$|\psi_{gen}\rangle \simeq |vac\rangle + \beta C_{II}^{\dagger} |vac\rangle \tag{91}$$

such that $C_{II}^{\dagger} |vac\rangle$ is a normalized two-photon state characterized by the biphoton wave function $\phi(\omega_s, \omega_i)$, which depends in general on the parameters of the nonlinear system under analysis, the pump pulse waveform and has to fulfil the energy and momentum conservation relations.
It turns out that the classical description of the stimulated FWM in a microring-resonator is useful to predict the behaviour in the quantum mechanical counterpart. In particular, it has been shown that the efficiency of spontaneous FWM can be estimated from the knowledge of the efficiency of the corresponding stimulated process and from the enhancement factor (FE) of the device [157]. The first can be obtained by injecting in the device a signal seed together with the pump, and by monitoring the power of the generated idler. The second can be obtained from the spectral response of the device.

5.2 SILICON BASED ADD-DROP MICRORING RESONATOR

The device under test is an Add-Drop filter micro-ring resonator, whose geometry is shown in Figure 47. It has an internal bending radius $R = 6.5\,\mu m$, fabricated using 193 nm Deep UltraViolet photolithography.

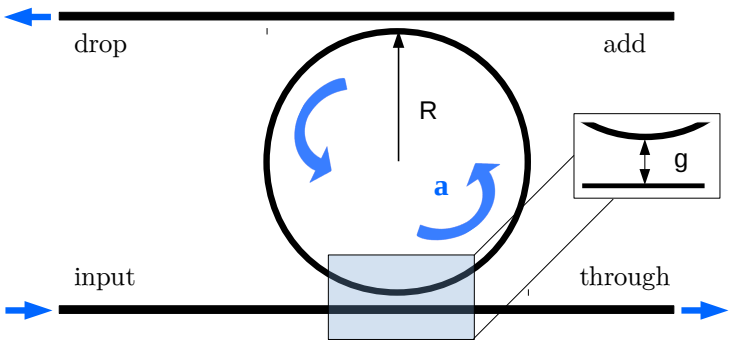

Figure 47: Sketch of the symmetric Add-Drop filter micro-resonator under test. The internal bending radius is $R = 6.5\,\mu m$ and the gap distance between the bus waveguide and the micro-resonator is $g = 160\,nm$.

The cross-section of the waveguide is $500 \times 220\,nm^2$, the thickness of the Buried Oxide Layer is $2\,\mu m$, while the one of the top cladding is

745 nm. The waveguide is single-mode for the TE and TM polarization at the probe wavelength around $\lambda = 1550\,nm$. The resonator is evanescently coupled to the bus waveguides through a 160 nm gap. We estimated a coupling coefficient of $k^2 \sim 2\%$ at a wavelength of 1550 nm from FEM modelling. The total photon lifetime is given by:

$$\frac{1}{\tau_{tot}} = \frac{1}{\tau_i} + \frac{2}{\tau_e} \tag{92}$$

From the symmetrical coupling configuration we can say that the resonator is in an under-coupling regime. Indeed, by calling τ the round-trip losses and the coupling parameters (r, k) introduced in Chapter 4, we have the general relation for the critical coupling condition for an Add-Drop filter micro-ring resonator given by $r_2\tau = r_1$. Now, since we are dealing with a symmetrical coupling condition we have that $r_2 = r_1$, which implies that for a lossy micro-resonator $\tau = e^{-\alpha L} < 1$ (where α is the absorption coefficient and L the resonator perimeter) the ring resonator cannot be excited in a critical coupling regime.
In particular, in analogy with the All-pass microring resonator treatment, if one defines from Equation 92 an effective intrinsic photon lifetime which takes into account the coupling losses induced by the upper bus waveguide $1/\tau_i^{eff} = 1/\tau_i + 1/\tau_e$, this quantity will be in general, for the lossy case, always lower than $1/\tau_e$, which fixes the under-coupling regime.
As shown in Figure 47, the device has an input port, which is used to excite the micro-resonator and a drop and a through port, which are used to collect the resonantly coupled and the transmitted signal respectively. We used a tunable C-band laser, fibre coupled to a tapered lensed fibre, to inject light into the input port. A micrometric XYZ positioning stage is used to minimize the total insertion loss. We estimated 7 dB of coupling losses per facet and $3\,dB cm^{-1}$ of linear propagation loss. The sample is 0.5 cm long, which accounts for ~ 15.5 dB of total insertion losses. A fiber polarization controller allows setting the polarization before entering into the chip. A tapered lensed fiber is used to collect light at the output of the device, and the power is measured with a Ge photodetector. The device spectrum, taken at the drop port of the micro-ring resonator is shown in Figure 49.
In Figure 49 the polarization has been set to maximize the propagation of the TE mode. The TM mode is not well guided through the resonator, as it experiences huge losses due to the presence of a metallic heater on top of the resonator used to tune the resonance wavelengths [158]. From this spectrum, we extracted a Free Spectral Range of $FSR = (13.2 \pm 0.2)nm$, and a total quality factor which decreases from (15800 ± 800) at $\lambda = 1538.6\,nm$ to (11300 ± 400) at $\lambda = 1565.2\,nm$. The main source of error in the total quality factor estimation comes from the strong Fabry-Perot oscillations due to waveguide end facets reflections, which are superimposed on the micro-ring spectral response,

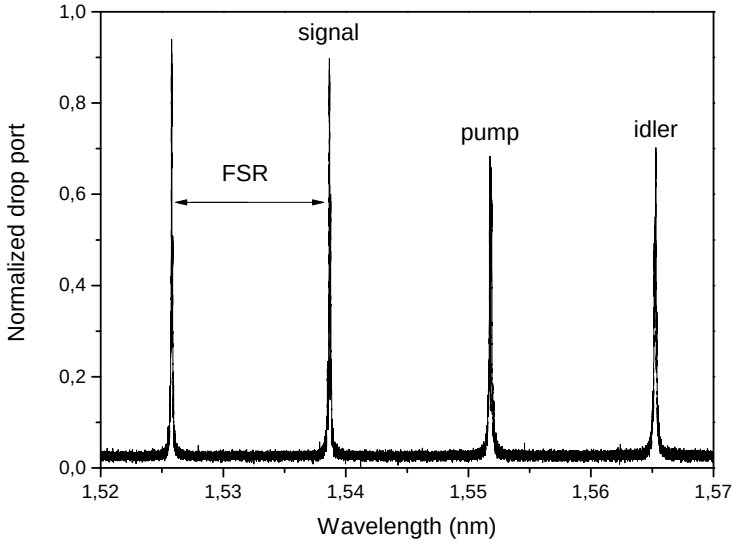

Figure 48: Normalized spectral response of the device taken at the drop port of the micro-resonator. The labels on the spectrum refer to the resonances selected for the FWM experiment.

as it can be seen from Figure 49. From the total quality quality factor and from the measurement of the propagation losses we extracted a coupling coefficient between 2% and 3%, in good agreement with FEM simulations. The fact that the total quality factor decreases as the wavelength gets longer can be understood from the following qualitative argument: as the wavelength increases, the optical modes get effectively less confined within the waveguide core. Therefore, the extrinsic quality factor decreases as a consequence of the fact that the waveguide-resonator coupling increases and also the intrinsic losses increases as the optical mode feels more the roughness of the waveguide side walls.
The power enhancement factor $|FE|^2$, defined in Table 2 in the case of a symmetric Add-Drop filter resonator is given by:

$$|FE|^2 = \left| \frac{ik}{1 - r^2 \tau e^{i(\beta L)}} \right|^2 \tag{93}$$

where τ is the roundtrip loss ($\tau \sim 0.992$ in our case). From this value it results that $|FE|^2 \sim 28$ at 1568.6 nm, $|FE|^2 \sim 32$ at 1551.8 nm and $|FE|^2 \sim 40$ at 1538.6 nm.

5.3 EXPERIMENTAL SET-UP

In this section the experimental set-up used to perform coincidence measurement on the correlated photon pairs generated within the silicon micro-ring resonator is presented.
As a general remark, comparing to the $\chi^{(2)}$-based SPDC process, spontaneous FWM is more difficult to deal with, since one has to filter out the strong pump signal which is spectrally placed in the middle of the generated photon pairs. Moreover, spontaneous FWM is an inherent poor efficiency parametric processes, making the filtering of the pump photons a non trivial task. As a matter of fact, we spent a lot of effort in optimizing the filtering capability of our set-up, trying to reduce as much as possible the associated insertion losses. The losses problem is particular crucial after the on-chip generation stage, as for coincidence measurement the losses scale in a quadratic fashion rather than in a common linear way: it is enough to loose one photon of the pair to loose the coincidence event at the correlator stage.
Let us start describing the microring resonance wavelength tuning. The ability of tuning the resonant wavelength of the silicon microresonator relies on the relatively large thermo-optic coefficient of the silicon $\frac{dn}{dT}^{Si} = 1.86 \times 10^{-4}\,K^{-1}$ [159].
By letting flow an electrical current into the metallic heater placed on top of the resonator, heat is dissipated by Joule effect with the quadratic relation in current $P = RI^2$, where R is the metallic heater resistance and I is the electrical current flowing through the circuit. Now, since the resonant wavelength condition reported in Equation 67 does depend on temperature ($n_{eff} = n_{eff}(T)$), a temperature change is spectrally reflected into a resonant wavelength shift.
As it is shown in Figure 49, it is enough to inject a current of 2.5 mA, to induce almost a spectral shift of 8 nm. The metallic heater resistance is $R = 10\,k\Omega$ and we use a stabilized voltage generator as a voltage source. As expected, the relative wavelength shift follows a quadratic law as a function of the injected electrical current.
The wavelength resonance tuning capability allows us to match the pump laser wavelength within the spectral bandwidth of the filtering stage. In Figure 50 the set-up used to perform coincidence measurement is reported. It can be thought as composed by different stages:

- pump source, input spectral filtering and polarization stage;
- microresonator device with thermal tuning of the resonant wavelength. On-chip generation of correlated photon pairs;
- output filtering rejection of the pump source and selection of the signal and idler wavelengths by means of a free-space homemade monochromator;

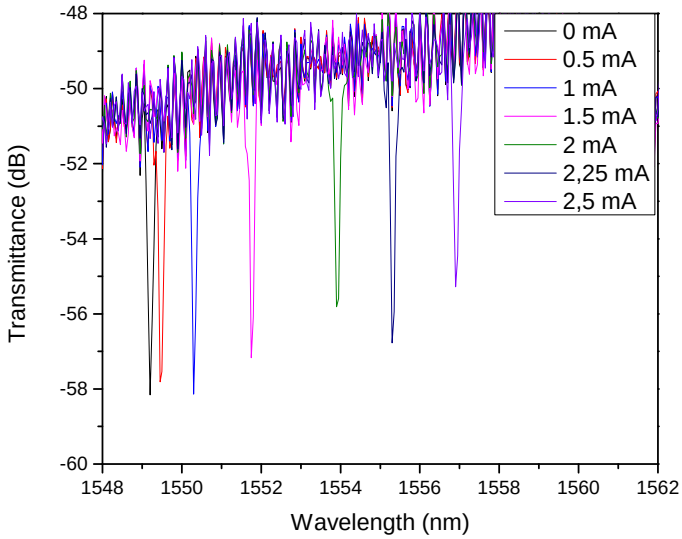

Figure 49: Transmittance spectrum taken in the through port as a function of the applied electrical current through the metallic heater placed on top of the resonator.

- detection stage consisting of two single-photon counter InGaAs detectors and coincidence circuit based on a FPGA logic.

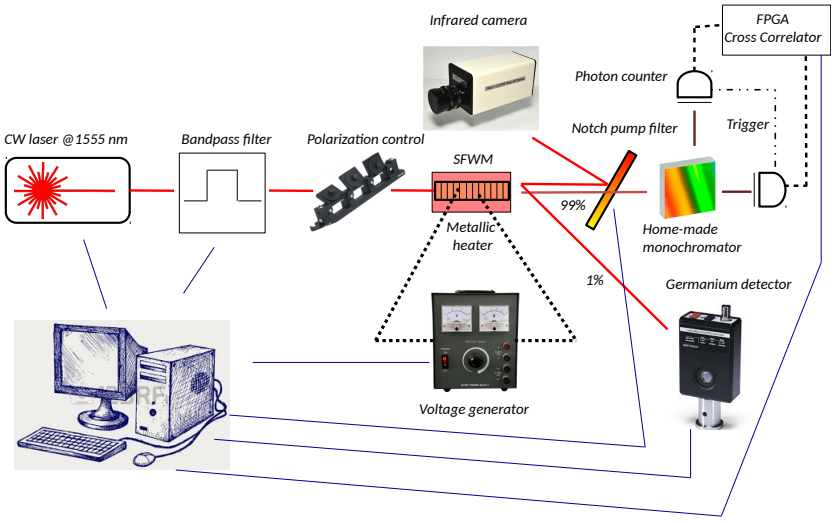

Figure 50: Sketch of the experimental set-up used to perform coincidence measurement on the correlated photon pairs, generated through spontaneous FWM within the silicon micro-ring resonator.

5.3.1 *Filtering stages*

Let us start describing the first stage of the optical set-up reported in Figure 50. The pump source is a C-band tunable laser (Pure Photonics PPCL300) with a narrow linewidth of about 10 kHz and a maximum output power equal to 18 dBm. A typical spectrum of the input laser excitation used is reported in Figure 51(a) (black curve), where the laser source was directly fibre coupled to an Optical Spectrum Analyser OSA (Anritsu MS2850A) and the laser power was set to 0 dBm. It is crucial for the experiment to suppress the ASE level (~ −60 dBm) at the wavelengths where the signal and the idler photons are expected to be generated. The laser is filtered from the associated ASE with the

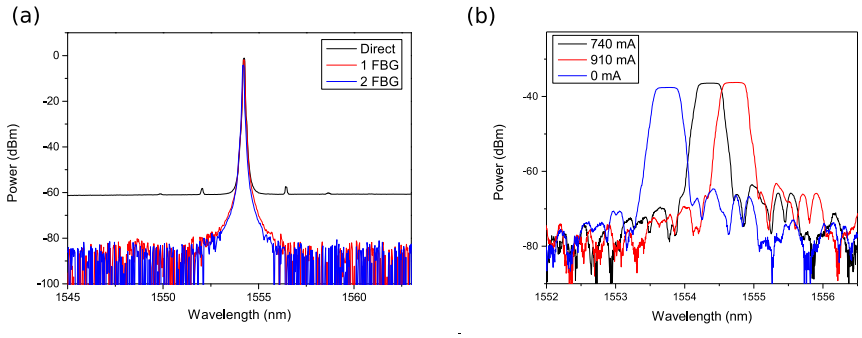

Figure 51: (a) Pump input spectrum with and without the input filtering stage in order to reduce the unwanted amplified stimulated emission signal associated to the laser source. (b) Spectral response of the bandpass input optical filters used in the experiment to clean the laser pump source. (b) Tuning of one of the FBG input filter as a function of the current.

help of two Fibre Bragg Gratings (FBG) (from AOS, Advanced Optical Solutions GmbH), which act as in-fibre narrow band-pass filters. In particular, in the input filtering stage they are used in reflection with the help of a 4-port circulator.
As it is possible to see from Figure 51(a), the FBG single filter rejection rate is about 35 dB. In this way the pump laser initial ASE with 1 mA pump power is reduced from an initial value of −60 dBm to almost −130 dBm when two FBG are used. With the dynamic range of our OSA, limited to about −90 dBm, in Figure 51(b) it is not actually possible to appreciate the effect of the second FBG after the preliminary filtering operation of the first one.
The overall insertion loss associated with this stage was estimated to be 2 dB. Moreover, each FBG was placed within a home-made oven heated by a high power dissipative resistor, in order to tune the spectral response as a function of the applied electrical current. As one can see from Figure 51(b), it is possible to red-shift the FBG bandpass spectral characteristic as a function of the applied electrical current.

This further degree of freedom was exploited to spectrally align in the FBG filters at the desired wavelengths. With this method it is possible to effectively shift the pass-band central wavelength by almost 5 nm, without deteriorating the spectral response of the device.
After the input laser radiation is cleaned, light is TE polarized and injected into the input port of the Add-Drop filter microring resonator, as shown in Figure 47. The microring resonator characteristics were already discussed in Section 5.2, so let us continue with the discussion of the output filtering stage. This is composed of a pump rejection stage and a signal and idler targeted filter in the form of a home-made monochromator. Following the scheme in Figure 50, the light collected at the output fibre is split: 1% goes to a germanium detector in order to monitor the level of the total transmitted signal and so to ensure the laser is set to a resonance. The remaining 99% is directed to a pump rejection stage. This is composed of 3 FBG and 3 fibre pigtailed optical isolators. They are placed "in series", alternating one optical isolator with one FBG. The FBG filters used in this stage are the same as the input stage, but in this case they are exploited as notch filters in transmission in order to reject the pump laser. Optical isolators are needed to reduce back reflections in optical fibres and backscattering of light to the sample and eventually to the the laser source.
As it is possible to see from Figure 52, the transmittance FBGs spectra are similar to the ones discussed earlier for reflection operation. Also in this case each FBG was placed in a home-made oven heated by a high power resistor, in order to tune the spectral response as a function of the applied electrical current.

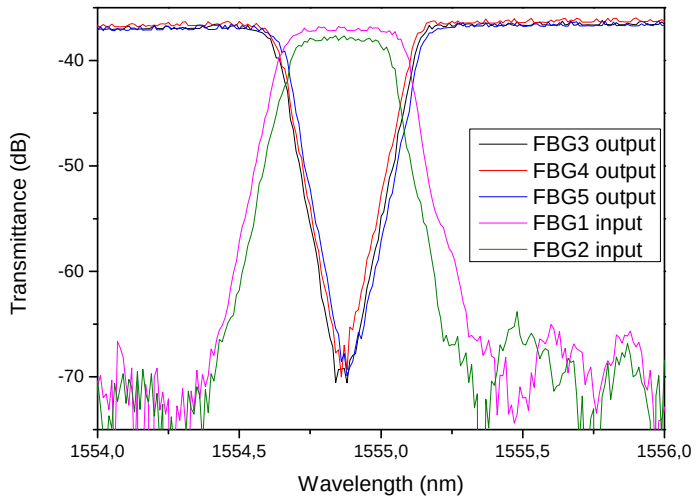

Figure 52: Spectral response of the optical filters used in the experiment.

In Figure 52 it is shown that it is actually possible to tune the FBG filters, such that the transmission and rejection bands spectrally overlap. The control as a function of the applied electrical current is performed by two data acquisition devices (Measurement Computing) powered by a stabilized voltage source, all of which are controlled with a Labview program. The overall insertion loss of this stage is 3 dB, with a pump rejection rate of −105 dB.
After this stage, we need to further filter the remaining optical signal at the wavelengths where we expect to generate the signal and idler photons. This is actually needed, because even though the pump has been strongly filtered, there is still a non negligible level of background radiation. The main source of noise is due to the remaining ASE, which is effectively integrated over all the non-vanishing responsivity of the InGaAs single-photon detector (see Figure 15), which goes from 800 nm to 1650 nm. For this reason a double-pass homemade free-space monochromator was built to select the generated signal and idler wavelength. As it is possible to see from Figure 53, it has two separated optical lines, one for the signal (blue dashed line) and the other for the idler (red dashed line). A fibre port collimator is used to launch collimated radiation into a polarizing free space stage to maximize the grating first order diffraction response. This is composed by a quarter and half waveplate, able to set the light polarization perpendicular and linearly polarized before the grating. After the two waveplates, a telescope composed by one diverging lens and one converging lens (focal length 5 cm) is used to increase the collimated beam waist and so to maximize the probed grating surface.

It is well known that by increasing the number of grating lines seen by the optical signal, the resolving power of the grating is increased [160]. Each beam experiences a single-pass on two reflective gratings close to the blaze angle, in order to reduce as much as possible the monochromator insertion losses. Signal and idler photons pass through two separate telescopes to reduce the beam waist and finally are coupled in fiber by means of two fibre port collimators.
We measured a total insertion loss for the monochromator stage of −4.5 dB for the idler line and −5 dB for the signal one. The monochromator not only filters the signal and idler photons from the remaining pump ASE, but also suppresses the remaining pump photons. Finally, the idler photons are further cleaned with a FBG centered at 1565 nm used in reflection with the help of a 3-port circulator. The total insertion loss of this final stage is 1.5 dB.

5.3.2 *Detection stage*

The correlated photon pair detection is performed by two InGaAs single-photon counting detectors (ID Quantique Id210 and ID Quan-

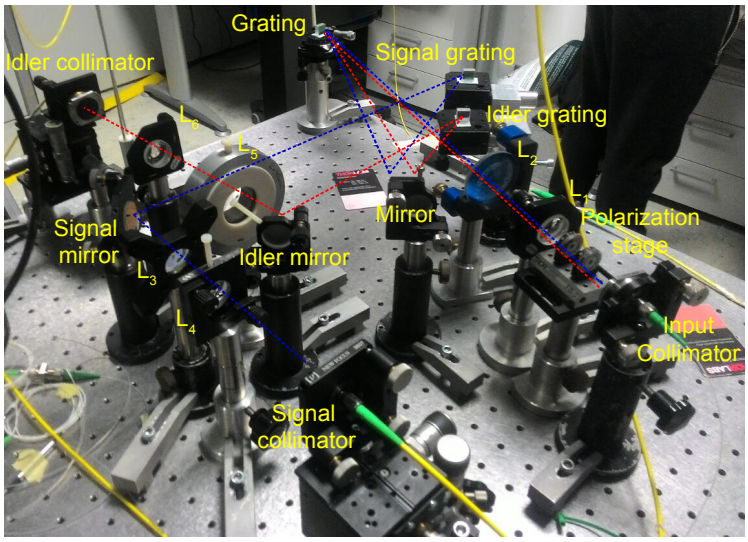

Figure 53: Photograph of the home-made free space monochromator, used to separate the initially collinear signal and idler photons. The blue line follows the signal optical path, while the red line follows the idler optical path. L_i (i =1-6) are optical lenses.

tique Id201). Id210 is operated in the so called free-running mode. In this operation mode the detector is always allowed to detect a photon, except for the dead time interval which follows each detection. The dead time is an important parameter, which determines the SPAD dark count rate. The best compromise in terms of signal to noise ration after a preliminary characterization, was achieved with 5% of detection efficiency and 40 µs of dead-time.
With these parameters, the simulated minimum detectable signal, Poissonian distribution of photon arrival times, is $\sim -120\,\mathrm{dBm}$ (with one second of integration time), which well matches the experimental observation reported in the photon counter characterization in Figure 54. The maximum count rate per second is given by $1/40(\mu s) = 25\,\mathrm{kHz}$. It is possible to see from Figure 54 that by approaching the maximum count rate, the detector counts tend to saturate as the impinging power is increased. The physical interpretation is the following: the more the incident flux of photons, the more the detection events and associated dead-time, the more the detections lost. In Figure 54 it is also reported a polynomial fit of the experimental data, which is used to derive the impinging photon flux on the detector from the read count rate. The two main causes of photon detection loss are:

- In general a single-photon detector is not able to resolve the number of impinging photons. The absorption of a photon is enough to trigger an avalanche breakdown, thereby creating a

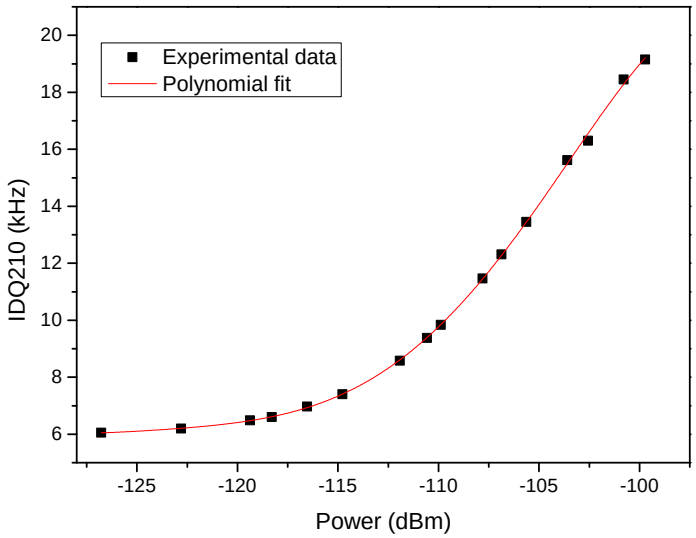

Figure 54: Experimental characterization of the response of the InGaAS id210 single-photon detector as a function of the incident power (expressed in dBm) for a detection efficiency of 5% and a dead-time of 40 µs.

large current pulse that indicates the arrival of the photon. If there are two or more photons incident on the active area of the detector at the same time, if the detector is enabled at that time, the detector will count only one photon;

- After a detection event, which could be due to a dark count or the absorption of a photon, the generated avalanche current within the detector is is quenched by lowering the bias voltage down to or below the breakdown voltage. Within this time window the detector is blind and if a photon arrives on the detector, it will not be counted.

The saturation trend implies that the detector response is not linear as a function of the incident photon flux. Therefore the calibration curve in Figure 54 is crucial for a correct estimation of the incident photon flux on the detector from the count rate. In general, the higher the dead-time, the lower the dark counts but the blinder the detector. Note that in CW excitation, photon pairs are emitted simultaneously at random times, therefore it is crucial to have the device enabled as long as possible to avoid losing detection events. Ideally the best case would be the one where the detector is always ready to detect a photon, but this increases considerably the dark count rate. Also, the higher the detection efficiency, the higher the probability to detect a photon, but at the same time, the higher the dark counts. The best

trade-off has been found by choosing 5% of detection efficiency and 40 µs of dead-time.
Let us discuss the detection scheme used in the coincidence measurement. A sketch is reported in Figure 55. Signal and idler photons after the monocromator (see Figure 53) are separately coupled to fibres and detected by the two InGaAs single-photon counters (Id210 and Id201). Id210 works in free running mode (40 µs of dead-time) and has the task to detect the idler photon. Id201 is triggered by Id210 and is enabled for a gate width of 100 ns with 25% of detection efficiency. Therefore the signal photons are heralded by the detection of the idler ones. In this way Id201 is enabled only when the signal photons are expected, which reduces the dark count rate. Also a dark count can trigger Id201, which will open as well a gate width of 100 ns where there will be the probabilistic chance to detect a dark count, background radiation, or nothing.
Triggering Id201 accumulates an amount of electronic delay from the initial idler detection event in Id210. We measured an electronic delay of ~ 60 ns. Therefore the arrival of the signal photons have to be delayed with respect the idler ones. For this purpose, a compensation signal delay line composed by 18 m of single-mode patch optical fibre is placed before Id201. Since the time delay during the propagation within the fibre is roughly ~ 5 ns per meter, this is enough to match the electronic gate signal coming from Id201. After the detection, the two SPAD output voltage traces are fed into a home-made field programmable gate array (FPGA) digital correlator that provides the coincidence rate. The coincidence window is 1.33 ns.

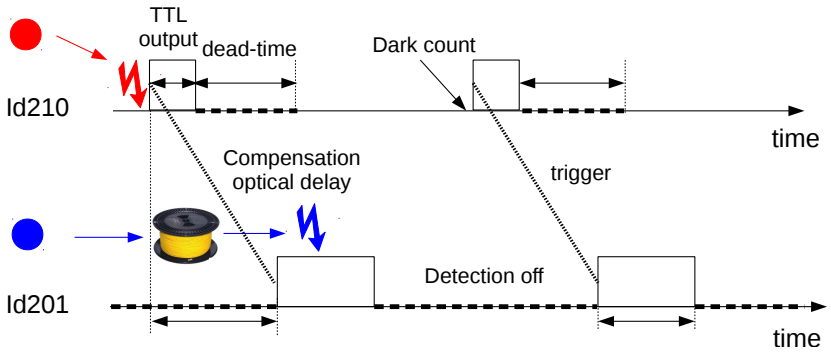

Figure 55: Sketch of the detection scheme used to perform coincidence measurement. The blue circle represents the signal photon, while the idler photon is sketched with a red circle. Detector Id210 works in free-running mode and is always enabled apart from the dead-time. Detector Id201 is enabled by the TTL output voltage signal coming from the Id210, where the high level logic can be either due to the absorption of a photon or a dark count event.

5.4 EXPERIMENTAL MEASUREMENT

In this Section, coincidence measurements performed on correlated photon pairs generated by spontaneous FWM in integrated SOI microring resonators is discussed. First of all stimulated FWM is investigated to characterize the generation efficiency. Then coincidence measurements on the generated photon pairs are performed, which actually demonstrates the time-correlated nature of the photon pair.

5.4.1 *Stimulated FWM*

As stated at the beginning of the chapter, the efficiency of spontaneous FWM can be estimated from the knowledge of the efficiency of the corresponding stimulated process and from the enhancement factor of the microring resonator [157]. This has been done with the help of an additional seed laser, which plays the role of the idler beam. In a set-up similar to the one shown in Figure 43, the idler laser is combined using a 50/50 fibre splitter with the pump laser. Light from the Drop port is then monitored with an OSA, providing a spectral resolution of 1 nm. An example of spectra of the transmitted light is shown in Figure 56. Here, we can identify two main peaks, corresponding to the idler and to the pump laser, and two minor side peaks, whose wavelengths $\lambda_{s1} = (1536.5 \pm 0.2)$nm and $\lambda_{s2} = (1570.0 \pm 0.2)$nm, are centred at the neighbouring resonances of the microring. Note that the dispersion β_2 is quite flat and close to zero ($\beta_2 = -0.01\,ps^2/cm$ at 1550 nm) in the investigated spectral interval, which ensures that the considered wavelength resonances closely follow the energy conservation [12].

These peaks are attributed to stimulated FWM, and follow the energy conservation relations $\omega_{s1} = 2\omega_p - \omega_i$ and $\omega_{s2} = 2\omega_{s1} - \omega_p$. The signal peak at λ_{s2} has a lower power with respect to the one at λ_{s1} since the enhancement factor of the corresponding resonance order is lower than the one at λ_{s1}.

In order to assess if the signal peaks are due to stimulated FWM, we characterized their power dependence as a function of the power of the pump and the idler lasers. The results are shown in Figure 57(a-b) for the peak at $\lambda_{s1} = 1536.5$ nm.

The slopes of the linear fit of the data (note that both the x and the y axis are expressed in dBm) are (2.00 ± 0.02) in Figure 56(b) and (0.98 ± 0.04) in Figure 56(c).

From the theory of stimulated FWM, these are expected to be respectively equal to 2 and 1, since the generated signal must grow quadratically with the pump power and linearly with the idler power. The close agreement between theory and experiment confirms that the

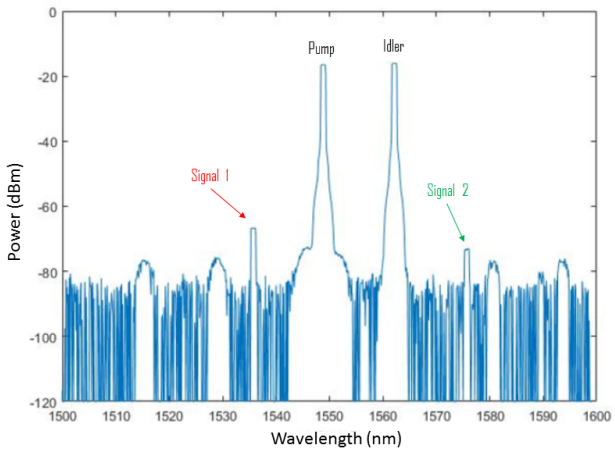

Figure 56: (a) Transmission spectra recorded at the drop port of the microring resonator when the pump and the idler laser are coupled into two different resonance orders. Two minor side peaks, corresponding to stimulated FWM occurring between the pump and the idler, can be observed into the neighbouring resonance orders at $\lambda_{s1} = (1536.5 \pm 0.2)nm$ and and $\lambda_{s2} = (1570.0 \pm 0.2)nm$. The broader peaks at $-75\,dBm$ are due to the pump laser non uniform ASE, and occur independently of the idler.

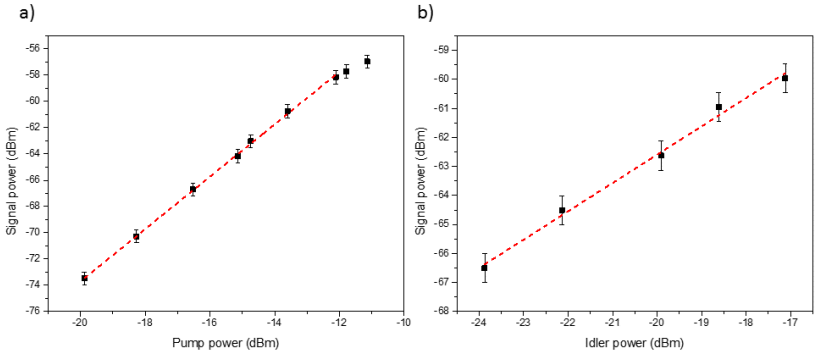

Figure 57: (a) Signal power at λ_{s1} as a function of the power of the pump (both values are referred at the output of the sample). The idler power is kept constant to $-16\,dBm$. The red dashed line is a linear fit of the data. (b) Signal power at λ_{s1} as a function of the power of the idler (both values are referred at the output of the sample). The pump power is kept constant to $-16\,dBm$. The red dashed line is a linear fit of the data.

signal peaks are attributed to SFWM. From Figure 56(c), the efficiency η of the conversion process, defined as:

$$\eta(P_p) = 10\log\left[\frac{P_s}{P_i}\right] \tag{94}$$

results $\eta = (-42.6 \pm 0.2)dB$ for a pump power of $\sim 1\,mW$ in the exciting waveguide. This is one order of magnitude lower than the

simulated efficiency, which can be calculated with the temporal coupled mode equation, reported in Equation 88.
The disagreement can be attributed to the fact that the field enhancement factor can be actually lower than the simulated one, due to Fabry-Perot reflections at the end facets of the sample. Fabry-Perot oscillations are actually visible in the transmission spectrum reported in Figure 49. This may slightly offset the involved waves in FWM from a perfect on resonance excitation, thus lowering the corresponding field enhancement factor (see Equation 85). We did not investigate this further in detail, since the experimental conversion efficiency can be used as a lower limit for calculating the efficiency of the spontaneous process.

5.4.2 *Coincidence measurement*

Following Ref. [157], the power of the generated signal/idler photon pairs can be derived from the stimulated FWM as follows:

$$P_{sp}(dBm) = \eta + 10 * \log\left[\frac{\hbar\omega v_g}{2L|FE|^2}\right] \tag{95}$$

where $L = 2\pi R$ is the resonator perimeter and v_g is the group velocity (assumed to be non-dispersive). Using $v_g = 0.75 \times 10^8\, m\, s^{-1}$ (from FEM simulations) and $|FE|^2 \sim 30$ (experimentally extracted from the spectral response), we obtain $P_{sp} \sim -97\, dBm$. This power refers to the one propagating on chip, which means that the one coupled off-chip is about $-104\, dBm$ (here we have used $\sim -7\, dB$ of coupling losses).
In Figure 58 the result of a coincidence measurement performed is shown. The pump laser was tuned into the resonance order at $\lambda_p = 1554.75\, nm$, aligned with respect the FBG filters in Figure 52. The pump power in the input waveguide was $\sim 2\, mW$. Only a photon pair can generate an avalanche at the same time in both the single-photon detectors, giving rise to a coincidence event. However, also the dark counts of the detectors contribute to generate spurious coincidences. The coincidence background is the rate of coincidences that does not result from the detection of both photons from a pair. The counts resulting in background coincidences are uncorrelated.
In Figure 58 a clear coincidence peak appears at zero time delay over an almost constant background, constituted by the accidental counts (after 100 s of integration time). The peak is a manifestation of the fact that signal and idler photons are emitted at the same time, so they give rise to a coincidence in the photodetection. The maximum observed coincidence rate was $(9.8 \pm 0.5)Hz$. When the input pump power is set to $2\, mW$ the on-chip generation rate is $\rho_g = 3.5\, MHz$, which is $-94\, dBm$, in close agreement with the theoretical prediction.

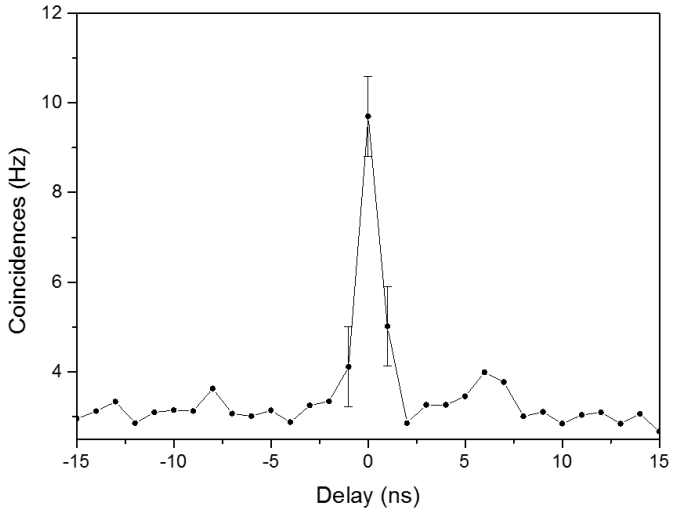

Figure 58: Coincidence rate (Hz) after 100 s of integration time. The pump power in the input waveguide is $\sim 2\,mW$.

Starting from the generation rate, the expected coincidence rate can be calculated as [72]:

$$\rho = \rho_g * 10^{(L_s+L_i)/10} \tag{96}$$

where $L_{s(i)}$ are the losses (expressed in dB) associated to the signal (idler) from the on-chip generation to the final detection. The expected coincidence rate results to be $\rho \sim 17\,Hz$ which is close to the experimental value shown in Figure 58.
In the theoretical estimation the losses associated to the detection efficiency, the dark counts, the dead-time and gate width of the photon counters, have also to be taken into account. For the model Id210, the detection efficiency was evaluated directly from the calibration curve reported in Figure 54. It is consistent with the simulated one through numerical simulations, in which photons are assumed to strike the photodetectors following a Poissonian statistics.
The efficiency of the triggered photon-counter Id201 was taken simply directly from the 25% of detection efficiency. This is because in the triggered operated mode, it is actually affected by low dark count ($\sim 0.1\,\sqrt{Hz}^{-1}$) and we also checked the detector responses in a linear fashion in this regime.
In Table 8 the losses associated with each stage are reported. The total loss associated to the idler line is (-31 ± 3)dB, while the one associated to the signal line is (-22 ± 1)dB.
We then proceed to investigate the rate of coincidences and the Coincidence to Accidental Ratio (CAR), as a function of the pump power. The CAR is the typical figure of merit used to quantify the performance of a coincidence measurement. CAR is defined as the ratio between the coincidence events in the main peak at zero delay and the

Stage	Idler loss (dB)	Signal loss(dB)
Off-chip coupling	(8 ± 1)	(8 ± 1)
Pump filter	(3 ± 0.1)	(3 ± 0.1)
Monochromator	(6.0 ± 0.1)	(5.0 ± 0.1)
Detection	(13.6 ± 1.5)	6
Total	(31 ± 3)	(22 ± 1)

Table 6: Losses experienced by the signal and the idler photons after that they are generated in the microring resonator and coupled into the drop waveguide.

mean value of the background outside this central peak. A high value of the CAR indicates that the system is characterized by low loss and low noise associated to both dark counts and to stray light, which comes from the residual of the pump laser or from the unfiltered ASE at the signal/idler wavelengths. Note that in our configuration we are far from the ideal situation where the CAR is only limited by multi-pair effects (usually the case for SPDC based clean photon pair sources) [161]. The results are shown in Figure 59.

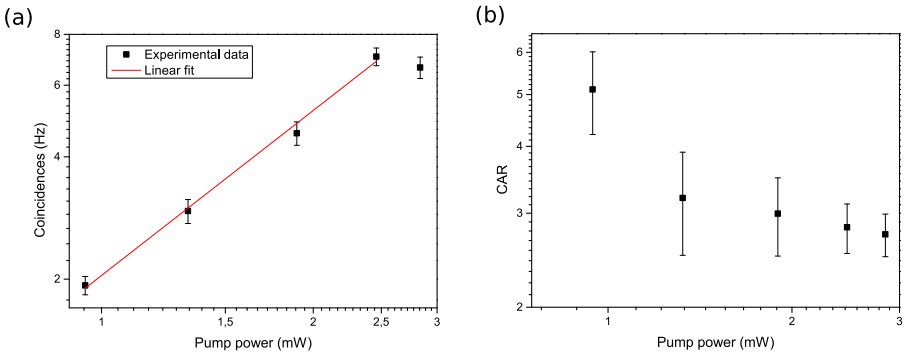

Figure 59: (a) Coincidence events as a function of the pump power coupled into the input waveguide. The red dashed line is a quadratic fit of the data (except the last point). (b) Coincidence to Accidental Ratio (CAR) as a function of the pump power coupled into the waveguide. Both the two graphs are plotted in log-log scale.

The slope of the linear fit of the data (note that both the x and the y axis are expressed log scale) is (1.35 ± 0.06) in Figure 59(a). Theoretically, instead, one would have expected the coincidence peak grows quadratically with the input pump power [72]. This is due to parasitic effects in the resonator, most likely due to both two-photon absorption (TPA) and associated free-carrier absorption (FCA) which broaden the cavity linewidth, consequently decreasing the field enhancement factor. Moreover, there is also to consider the thermo-optic effect induced by two-photon absorption, which slightly red-shift the resonances with increasing pump power, inhibiting an optimal cou-

pling of pump energy into the resonator. Eventually, at powers higher than 2.5 mW, the curve starts to saturate. Following Ref. [162], by increasing the pump power, there is also surely the onset of multi-pair emission effects. In this case the approximated expression in Equation 91 is not any more valid to represent the generated state and higher order terms must be included in the description. It is well known in literature that multi-pair emission by spontaneous parametric processes has a detrimental effect on coincidence measurements [161].

The CAR, shown in Figure 59(b), exhibits a maximum value of (5 ± 1) at low pump powers ($\sim 1\,mW$), and then monotonically decreases as the power increases. Ideally, in the absence of background noise, CAR is expected to decrease as the inverse of the generation rate, that is to say quadratically with the pump power [161, 163]. At low pump powers, however, the generated photon flux becomes comparable with the background count rate, determining an overestimation of the accidental counts that decrease the value of the CAR. At high pump powers, instead, we already pointed out that we faced non-negligible thermal effects within the resonator. As a matter of fact, the pump level is high enough to activate thermal effects, experimentally observed in a bistable behaviour of the device, which degrades the generation efficiency.

To summarize, let us compare in Table 7 the results here presented with the current state of the art for the on-chip generation of photon pairs using silicon-based microring resonator.

Parameter	Thesis work	[164]	[72]	[165]
Quality factor	13500	92000	7900	95000
Coupling losses (dB)	7	3.5	3.5	3
Filtering losses (dB)	8.5	6	13	5.5
Detection efficiency	5%	90%	10%	15%
Dark count rate (Hz or cps)	6000	1	100	100
Generation rate ($MHz\,mW^{-2}$)	1	150	5	100
CAR	5	12000	250	60

Table 7: Summary and comparison of the performances of the experiment reported in this Chapter with respect to the state of the art for the on-chip generation and detection of photon pairs using silicon-based micro-ring resonator.

We see that the total quality factor of the Add-Drop resonator used here is typically lower with respect to the ones reported in literature. We already discussed that we did not exploit the maximum achievable field enhancement of the ring, as we operated it in a symmetrical under-coupling regime.

For what concerns the coupling losse of the device, we experienced higher losses with respect to the other works. Our waveguide presents

a direct tapering from a waveguide width of 2 µm to the nominal waveguide width of 0.5 µm in 0.6 mm. The experienced 7 dB of coupling loss is consistent with the overlap integral calculation between the waveguide mode profile and the Gaussian spot size of the tapered fiber, placed at the correct working distance. At the time the chip was designed, it was not necessary to further engineered the the fiber to waveguide coupling. In this direction one possibility is to design an inverse tapering geometry. For example in [72], the authors reported a 300 µm long silicon inverse tapers ending in a 20 nm tip width covered by $1.5 \times 2\,\mu m^2$ polymer waveguides, which resulted in 3.5 dB coupling loss. Another possible coupling strategy makes use of grating couplers, which relies on a completely different working principle [22]. Coupling losses of few dBs were reported in literature with this kind of couplers, which have also the advantage to reduce Fabry-Perot oscillations within the waveguide, which can be a big issue in high-index material such as silicon [166, 167].

For what concerns the filtering stage, instead, the overall loss associated with the presented thesis work is comparable to the ones reported in literature. The values reported in Table 7 were taken as the average value between the signal and idler losses.

What really makes the difference between the various approaches is the detection stage. We used two InGaAs single-photon counters. Their maximum detection efficiency can be set to 25%. At the maximuum efficiency however also the dark count rate of the device considerably increases. For this reason we found the optimal configuration to be 5% of detection efficiency, 40 µm of dead time, with an associated dark count rate of 6 kHz. Better performances of InGaAs based single-photon counters were reported in [165]. However, these parameters are orders of magnitude different with respect to the superconducting nanowire single photon detectors (SNSPD), used in [72, 164] and also operated in free-running mode. They have performances close to the one of an ideal detector at telecom wavelength. Their main limitation is that they have to be operate at 0.8 K, in contrast to the relatively easy internal cooling system of the InGaAs SPADs at about −50 °C.

To the best of our knowledge, the detection efficiency of SNSPD can be as high as 90%, dark count rate of 1 Hz and reset time of 40 ns [82]. These values make the difference, because in coincidence measurements loss scales quadratically, as can be seen from Equation 96. Having low losses is crucial, since this lets the pump excitation be less intense (of the order of 0.01 mW in Ref. [164]), with the important advantage to be far below the threshold value to activate nonlinear absorption mechanisms and thermal effects within the silicon microring, as well as multi-pair emission effects.

As a net result the maximum achievable CAR resulted to be more than three orders of magnitude higher in [164]. Still, with a reduced

dark count rate of one order of magnitude and a factor 2-3 of better detection efficiency lead to a CAR ~ 100 in [72, 165].
Further comparison between recent results of photon pair generation using silicon microring resonators ca be found in [165].

To conclude, we demonstrated the occurrence of spontaneous four wave mixing in integrated SOI microring resonators. The results are in good agreement with the theoretical predictions. For effectively dealing with more complex quantum optical circuits, better performances in terms of signal to noise ratio are needed. At telecom wavelength, superior detection performances are provided by the superconducting based technology at the cost to being forced to work at cryogenic temperature.
We will see in Chapter 7, that this is not the case in the mid-infrared (MIR) spectral range. Indeed, at higher wavelengths, the SNSPD performance substantially degrades, letting a detection approach based on the spectral translation of MIR photons into the visible range to show better detection performances.

Part III

MANIPULATION AND DETECTION SCHEMES OF ENTANGLED PHOTON PAIRS

Part III is dedicated to discuss different ways to manipulate and detect quantum state of light produced by nonlinear optical processes. In Chapter 6 quantum interference effects in an asymmetric free space Mach-Zehnder interferometer are presented and theoretically confirmed. In Chapter 7 the detection of MIR correlated photons by means of coincidence measurement is addressed. This is based on a highly efficient up-converter module, which translates the detection of the MIR photon pairs into the visible, where efficient single-photon detectors do exist. Finally in Chapter 8 the manipulation of the internal degrees of freedom of a photonic molecule composed by two coupled silicon microring resonators enables to enhance or to suppress FWM. This is demonstrated both theoretically and experimentally as a function of the interresonator phase and their relative eigenfrequency detuning.

6

HIDDEN QUANTUM INTERFERENCE PATHS IN AN ASYMMETRIC MACH-ZEHNDER INTERFEROMETER

In this Chapter the behaviour of the SPDC generated photon pairs discussed in Chapter 2 injected in the same input port of a free-space Mach-Zehnder interferometer (MZI) is discussed.
We consider the situation of an amplitude unbalanced interferometer, asymmetrically excited, where differences in the arms impede perfect cancellation of otherwise closed quantum channels. We experimentally and theoretically prove the coexistence of single, two-photon and Hong-Ou-Mandel like interference at the output of the MZI. We experimentally demonstrate oscillation in the coincidence rate outside the SPDC coherence time, which is a clear manifestation of the color-entangled nature of the two-photon state created in the down conversion process [168]. It will be shown that the tuning of arbitrarily small unbalance in the arm transmittance, leads to sharp changes in the coincidence detections, revealing beatings between one particle and two particle interference patterns. Surprisingly, the common assumption used in amplitude division experiments of lossless beamsplitter, does not allow us to theoretically predict the obtained experimental result. We found that the role of losses in the beamsplitter is actually not trivial and does affect the visibility of quantum interference.
The experiment described in this Chapter was done in collaboration with Dr. Massimo Borghi and Dr. Mattia Mancinelli. The theoretical analysis in Section 6.4 was developed in collaboration with Dr. Massimo Borghi. Dr. Hannah Price gave an important contribution through helpful discussions in Section 6.4.2.

6.1 COINCIDENCE MEASUREMENT ON SPDC PHOTON PAIRS GENERATED FROM PPLN

In this Section coincidence measurements performed on the NIR generated SPDC photon pairs are presented. With reference to Chapter 2, the SPDC photons are emitted from a periodically poled $LiNbO_3$ crystal region with a poling period of 19.1 µm when the operating temperature was set to T = 80 °C. This configuration corresponds to a broadband degenerate emission around $\lambda = 1.55\,\mu m$. After the collimator placed in position 10 in Figure 13, the SPDC photon pairs are fibre coupled and divided with a 50:50 fibre splitter. As is sketched

in Figure 60, a photon pair (red and black circles) can actually follow different paths after the beamsplitter:

- (A, D) One photon in each arm, the pair is divided. Each SPAD generates an impulse at the same time. These paths contribute to the coincidence measure giving a peak in the cross-correlation measure.
- (B, C) Two photons in one arm, the pair is not divided. Only one SPAD generates an impulse. These paths generate the spurious coincidences and add an offset in the cross correlation curve.

Since only 2 paths of 4 can generate coincidence detections, half of the total flux is wasted and generates spurious coincidences. This will add 3 dB of loss to the 7.8 dB that have been estimated in Chapter 2 from the output facet of the PPLN to the fibre. We will see in Chapter 7 that dealing with non-degenerate SPDC process allows to avoid the 3 dB beamsplitter loss, by a colour-dependent division of the photon pairs with a dichroic mirror.
The detection stage used is equal to the one presented in Chapter 5, which is composed of two InGaAs single-photon counting detectors (Id210 and Id201). Here we exploit the same detection scheme, already discussed in Chapter 5, sketched in Figure 55. Id210 works in free running mode (40 µs of dead-time) and has the task to detect one photon of the pair (in this case either signal or idler). Id201 is triggered by Id210 and is enabled for a gate width of 100 ns with 25% detection efficiency. An optical delay line, sketched in Figure 60 by a yellow rectangle, is needed to compensate the electronic delay accumulated in the triggering operation between the two SPADs.

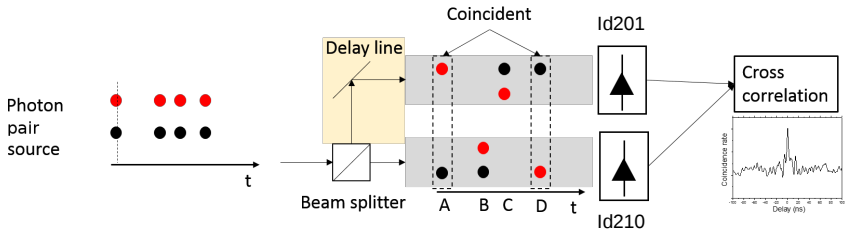

Figure 60: Sketch of the coincidence scheme. (A,B,C,D) All the possible paths that a photon pair can take after the beam-splitter.

After the detection, the two output voltage traces from the SPADs are fed into a field programmable gate array digital correlator that provides the coincidence rate. The coincidence window is 5 ns.
The coincidence measurement after 100 s of integration time is reported in Figure 61. A clear coincidence peak appears at 25 ns time

delay over an almost constant background, constituted by the accidental counts. The 25 ns time delay is the excess optical delay of the signal photon to be safely detected by Id210 within its gate width of 100 ns. The coincidence peak is (48 ± 1)Hz, with a background of spurious coincidences of (3.4 ± 0.1)Hz. This leads to a CAR of (13.1 ± 0.7). The pump power has been set to 2 mW, where the maximum CAR was observed. The rate of observed coincidences is consistent with the one expected through Equation 96. At higher pump power we experimentally observe that the CAR decreases, most likely due to the growing onset of multi-pair emission events [96].
We already commented in Table 7 that the performances in coincidence measurements that we can obtain with our instrumentations are far from the state of the art. In the case for example of PPLN waveguides, CAR > 10000 was already reported in literature [169]. As we said, in our implementation the main limiting factor is the poor efficiency of our InGaAs SPADs and the huge dark count rate with respect to superconducting-based technology detectors. A substantial improvement in the CAR can be obtained by reducing the coincidence window till the SPAD jitter, which is typically about 200 ps in our case [32]. Actually, we were able to program our FPGA digital correlator (Atlys Spartan 6 circuit board) to reduce the coincidence window till 1.33 ns for the experiments reported in Chapter 5 and Chapter 7. Lower coincidence window was found not feasible with our circuit board, which has a limited native clock of 100 MHz. As a matter of fact, lower coincidence window would lead to unreliable logic operations in our digital correlator.

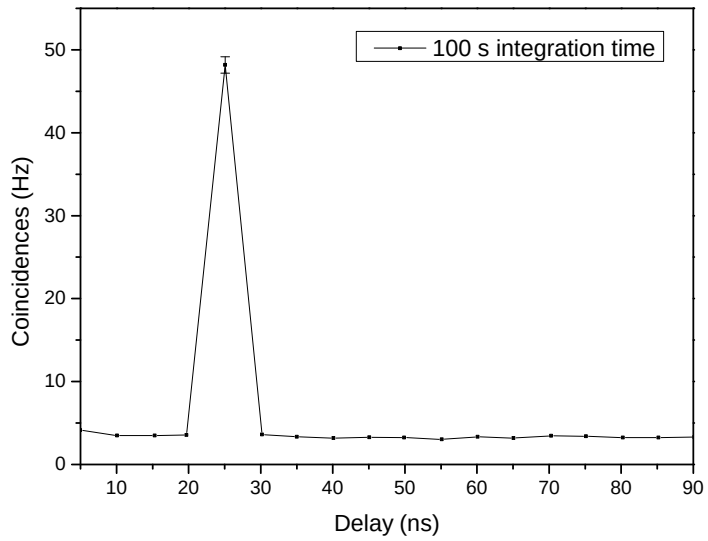

Figure 61: Coincidence rate as a function of the relative time delay. The integration time is 100 s

Nevertheless, we will see in Section 6.6 that, by an efficient averaging procedure in the coincidence counts as a function of the time-delay in the Mach-Zehnder interferometer, we are still able to resolve with a sufficient signal-to-noise ratio quantum interference fringes.

6.2 THE BIPHOTON WAVEFUNCTION

Considering a collinear process where pump, signal and idler propagate along the PPLN crystal's x-axis, the two-photon state produced by SPDC, in the low pump approximation can be written as [170]:

$$\left|\psi_{gen}\right\rangle = NL \int_0^\infty \int_0^\infty d_{eff}(\lambda_s, \lambda_i)\alpha(\lambda_p)\eta(\lambda_s, \lambda_i)\hat{a}_s^\dagger \hat{a}_i^\dagger \left|0\right\rangle d\lambda_s d\lambda_i \quad (97)$$

where N is a normalization constant, L is the length of the crystal and $d_{eff}(\lambda_s, \lambda_i)$ is the nonlinear coefficient introduced in Chapter 2 which in general depends on the wavelength. $\hat{a}_j^\dagger$ with $(j = s, i)$ is the usual creation operator, whose action when it is applied to the vacuum state ($\hat{a}_j^\dagger \left|0\right\rangle = \left|1\right\rangle_j$), is to create a photon at wavelength λ_j [23]. The function $\alpha(\lambda_p)$ is the pump envelope amplitude, which for a Gaussian distribution is given by:

$$\alpha(\lambda_p) = e^{-\frac{(\lambda_p - \lambda_{p0})^2}{2\gamma^2}} \quad (98)$$

where λ_{p0} is the central pump wavelength and λ_p is fixed by the conservation energy as $1/\lambda_p = 1/\lambda_s + 1/\lambda_i$.
The function $\eta(\lambda_s, \lambda_i)$ which appears in Equation 97 is the *quasi-phase matching amplitude*, which is given by:

$$\eta(\lambda_s, \lambda_i) = e^{i\Delta k_m L/2}\,\mathrm{sinc}\left[\frac{\Delta k_m L}{2}\right] \quad (99)$$

The function $\eta(\lambda_s, \lambda_i)$ can be easily derived from Equation 24.
The quantity Δk_m is the phase mismatch, which in a periodically poled structure with poling period Λ is given by:

$$\Delta k_m = \Delta k - m\frac{2\pi}{\Lambda} = 2\pi\left[\frac{n(\lambda_p)}{\lambda_p} - \frac{n(\lambda_s)}{\lambda_s} - \frac{n(\lambda_i)}{\lambda_i} - \frac{m}{\Lambda}\right] \quad (100)$$

where m is an odd integer (positive or negative), referred to as the QPM order. Quasi-phase-matching is when $\Delta k_m = 0$, i.e. when the quasi-phase matching amplitude is maximized. This fixes the condition for the poling period to be $\Lambda = m2\pi/\Delta k$ (Equation 30).
With reference to Equation 90, we can define the *biphoton wavefunction*, in the literature also called Joint Spectral Amplitude JSA, for the

type-o collinear process in PPLN, as the product of pump and phase-matching envelope amplitude:

$$\phi(\lambda_s, \lambda_i) = \alpha(\lambda_p)\eta(\lambda_s, \lambda_i) = e^{-\frac{(\lambda_p - \lambda_{p0})^2}{2\gamma^2}} e^{i\Delta k_m L/2} \operatorname{sinc}\left[\frac{\Delta k_m L}{2}\right] \quad (101)$$

The modulus square of the biphoton wavefunction, which is called Joint Spectral Intensity (JSI), is the probability distribution function of specific signal and idler wavelength pairs being emitted.
A simulation for the SPDC biphoton wavefunction, with the experimental parameters discussed in Chapter 2 is reported in Figure 62. As is possible to note from Figure 62(b), signal and idler frequen-

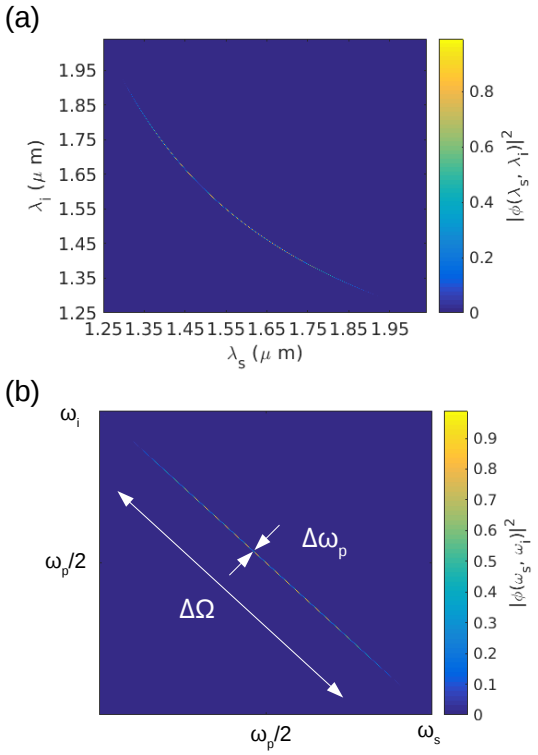

Figure 62: (a) Modulus square of the biphoton wavefunction as a function of the signal and idler wavelengths (λ_s, λ_i). (b) Modulus square of the biphoton wavefunction as a function of the signal and idler frequencies (ω_s, ω_i). $\Delta\Omega$ is the average spectral bandwidth of the SPDC photons, while $\Delta\omega_p$ is the bandwidth of the pump photons. The simulation parameters are: $\Lambda = 19.10\,\mu m$, T = 80 °C, the Sellmeier relation in Equation 20, $\gamma = 0.5\,nm$, $\lambda_{p0} = 775\,nm$, L = 1 mm.

cies are negatively correlated, oriented exactly at −45° due to energy conservation $\omega_p = \omega_s + \omega_i$. In Figure 62 we indicate the average spectral bandwidth of the SPDC photons with $\Delta\Omega$. This has been experimentally characterized in Figure 20 to be ∼ 300 nm in wavelength.

In Section 6.4 the SPDC bandwidth will be modelled with a Gaussian distribution for the ease of calculation. We will see in Section 6.6 that this description is accurate enough to theoretically predict the quantum interference effects observed at the output of the Mach-Zehnder interferometer. The quantity $\Delta\omega_p$ represents the pump bandwidth which is inversely proportional to the parameter γ in Equation 98. The pump bandwidth defines a finite extension of JSI along the direction which is transverse with respect to the spectral bandwidth. This seems to violate energy conservation. However, any pump field has always a finite *coherence time*, which is inversely proportional to the spectral linewidth of $\Delta\omega_p$. This uncertainty in the energy of the pump reflects in the spectral properties of the down converted radiation. In particular, the effect is to broaden the signal/idler spectral distribution. In Figure 62(b), the elongated shape of the JSI qualitatively manifests the time-energy entanglement of the generated photon pairs. The amount of spectral correlations can be quantified in terms of the *Schmidt decomposition*, which is expressed as a linear combination:

$$\phi(\omega_s, \omega_i) = \sum_n \sqrt{c_n} f_n(\omega_s) g_n(\omega_i) \tag{102}$$

where f_n and g_n both represent a complete set of orthonormal functions [171]. The coefficients c_n are positive real numbers known as the Schmidt coefficients, satisfying $\sum_n c_n = 1$ [45]. The Schmidt decomposition can be used to quantify the degree of entanglement in the system via the Schmidt number [172]:

$$K = \frac{1}{\sum_n c_n^2} \tag{103}$$

For a non-entangled state, the biphoton wavefunction is a factorable state, i.e. the Schmidt coefficients are $c_{n=1} = 1$ and $c_{n\neq 1} = 0$ so that the Schmidt number is $K = 1$. For a correlated system, as the one reported in Figure 62, multiple Schmidt coefficients are non-zero, so that $K > 1$. The bigger the Schmidt number, the more entangled the two-photon quantum state. The Schmidt coefficients can be obtained numerically by a singular-value decomposition of the biphoton wavefunction [173]. Experimentally, instead, the smartest way to retrieve the biphoton wavefunction is by means of stimulated measurement (DFG measurements in the case of SPDC). Tuning the wavelength of a seed input signal allows mapping the biphoton wavefunction with high fidelity. This method, called stimulated emission tomography (SET), outperforms the quantum state tomography approach, which aims to reconstruct the density matrix of a quantum state [156][20][174].

However, since photon detection is proportional to the light intensity, experimentally one has a direct access only to the JSI and not to the biphoton wavefunction, with an inherent loss of phase informa-

tion. In this case the metric used to quantify the entanglement is the Schmidt number lower bound (SNLB) [175].
We did not retrieve experimentally the JSI simulated in Figure 62, as it was not the goal of the experiment reported in this Chapter. Nonetheless, we will see in Section 6.6, we were still able to experimentally demonstrate the color-entangled nature of the photon pairs. Indeed, we experimentally demonstrate oscillation in the coincidence rate outside the SPDC coherence time, which is a clear manifestation of the color-entangled nature of the two-photons state created in the down conversion process [168].

To conclude the section let us discuss why separable state, the ones yielding minimal entanglement, are also interesting. Generally, separable states are highly sought after for heralded single-photon sources based on spontaneous parametric processes, where the detection of one photon of the pair should not influence the quantum mechanical state of the other one [176][177]. Such separable states are typically obtained with pulsed laser source and narrow-band phase matching function, which should have a parallel or orthogonal direction [20, 178]. The figure of merit for single-photon sources is called *purity*, which is defined as $\gamma = \mathrm{Tr}(\hat{\rho}^2)$, where $\hat{\rho}$ is the density matrix of the quantum state. The purity defines a measure on quantum states, giving information on how much a state is mixed [30]. It is actually equal to the inverse of the Schmidt number (Equation 103).
It is important to bear in mind that, unlike other physical system which can generate single photons, such as colour-centers in diamond or quantum dots [54, 179], heralded single-photon sources are not real single-photon source. This is due to the fact that Equation 97 is only an approximated formula and there are always some higher order terms.
On the other hand, the time-correlation property of the emitted pairs in spontaneous parametric processes, allows one to exploit the heralding process to reveal the presence of a single photon, once the other photon of the pair has been detected.

6.3 CLASSICAL MACH-ZEHNDER INTERFEROMETER

In this section the physics of a Mach-Zehnder interferometer (MZI) is introduced from a classical point of view.
In Section 6.4 the corresponding quantum mechanical formalism is developed, which is needed to provide a full description of the interference effects generated by the two-photon quantum mechanical state. In general, an interferometer is a device used to determine the relative phase shift variations between two collimated beams, derived by splitting light from a single source. The basic component of an interferometer is the *beamsplitter*. Let us consider the beamsplitter model sketched in Figure 63. Light is incident from the a, b input

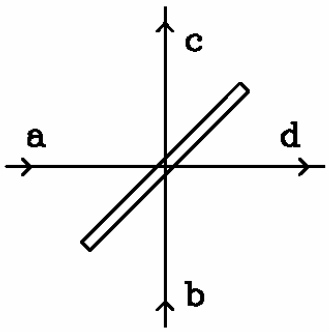

Figure 63: Scheme of a beam-splitter. *a*, *b* are input arms, while *c*, *d* are output arms.

arms and is transmitted/reflected into the *c*, *d* output arms. In a classical framework, the beamsplitter operation can be modelled by the scattering matrix $S(\omega)$, which connects the output fields to the input ones as follows:

$$\begin{pmatrix} E_c(\omega) \\ E_d(\omega) \end{pmatrix} = S(\omega) \begin{pmatrix} E_a(\omega) \\ E_b(\omega) \end{pmatrix} \tag{104}$$

For a lossless beam-splitter, energy conservation arguments allow writing *S* in the form [180]:

$$S(\omega) = \begin{pmatrix} r(\omega) & it(\omega) \\ it(\omega) & r(\omega) \end{pmatrix} \tag{105}$$

where *r*, *t* are real functions of ω and due to energy conservation they satisfy the relation $t(\omega)^2 + r(\omega)^2 = 1$.
We recognize that *r* is the amplitude reflection coefficient and *t* is the amplitude transmission coefficient. In the case of a balanced beam splitter, *r* and *t* are equal with amplitude $r = t = 1\sqrt{2}$. Remarkably, we will see in Section 6.4 that for a *lossy* beam-splitter, the phase relation between the amplitude and reflection coefficient (r,t) in Equation 105 is not a priori fixed to $\pi/2$ [181].
Let us discuss in the following the physics of the Mach-Zehnder interferometer (MZI). MZI is a device for demonstrating interference by division of amplitude. A light beam is first split into two parts by a beamsplitter and then recombined by a second beamsplitter. In Figure 64 a sketch of a MZI is reported. Classically it can be demonstrated that the light intensity at the output ports of *BS2* follows an harmonic law as a function of the relative phase $\Delta\Phi$, introduced between the two arms of the interferometer. Let us consider for example the case of a monochromatic plane wave of intensity I_0, propagating in the *z* direction at the input port of a MZI, say port *a*. Let us sup-

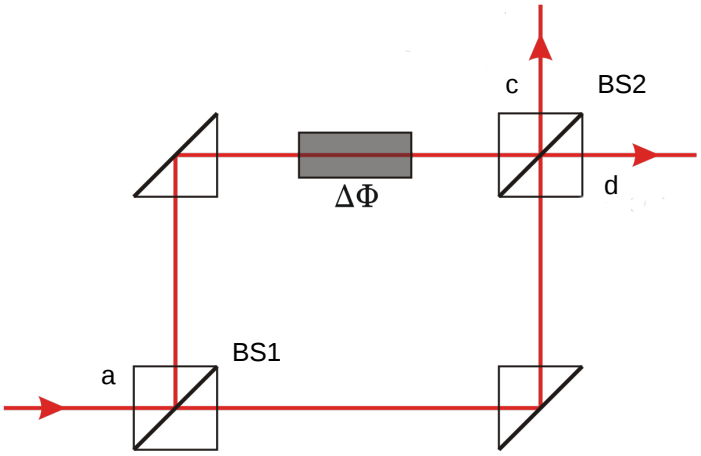

Figure 64: Basic scheme of a Mach-Zehnder interferometer. A collimated beam is split by *BS1*. The two resulting beams are each reflected by a mirror. In one arm is present a de-phaser which imparts a phase-shift $\Delta\Phi$ between the two waves. The two beams then interferes on *BS2*. The result of interference can be recorded at both the interferometer output ports *c*,*d*.

pose also for simplicity that the MZI beamsplitters are balanced and lossless. After *BS1* the intensity is equally split between the two arms of the interferometer. Assume then that one wave is delayed by an optical path length d with respect to the other. The term optical path length is used to underline that $d = nl$ where n is the refractive index and l the distance: d can be varied by changing n, l or both at the same time. The complex amplitudes for the two waves right before *BS2* are given by $U_1 = \sqrt{I_0/2}\, e^{ik(z+d)}$, $U_2 = i\sqrt{I_0/2}\, e^{ikz}$, where k is the wavevector. The intensity I at the output of the interferometer, say c port is given by:

$$I = \left|r\,U_1 + it\,U_2\right|^2 = \frac{1}{2}\left[\left|U_1\right|^2 + \left|U_2\right|^2 + iU_1^* U_2 - iU_1 U_2^*\right] \tag{106}$$

By substituting U_1 and U_2 in Equation 106, it gives:

$$I = \frac{I_0}{2}\left[1 - \cos(\Delta\Phi)\right] = \frac{I_0}{2}\left[1 - \cos\left(\frac{2\pi d}{\lambda}\right)\right] \tag{107}$$

where λ is the wavelength of the plane waves considered in the calculus. From Equation 107 it can be noted that, when the delay d is an integer multiple of λ, complete destructive interference occurs and the total intensity vanishes. On the other hand, when d in an odd integer multiple of $\lambda/2$, complete constructing interference occurs and $I = I_0$. For the d port of the interferometer, in the case of lossless beam-

splitter, the intensity is π-shifted with respect to the one reported in Equation 107.

6.3.1 *Coherence functions*

More formally, amplitude interference fringes arising from an interferometric system based on amplitude division, are linked to the first order correlation function.
The first order correlation $G^{(1)}(\Delta\tau)$ in the case of stationary states, such as the case of a plane wave, is given by [182]:

$$G^{(1)}(\Delta\tau) = \langle E^*(t)E(t+\Delta\tau)\rangle \tag{108}$$

where <> denotes an average over time. The first order correlation is actually the amplitude-amplitude correlation function. First order interference effects are classical phenomena: the result derived in Equation 107 would have been found equal even in a full quantum mechanical approach, with the the electric field which appears in Equation 108 quantized [24]. Considering a source with a finite coherence time τ_c, the function $G^{(1)}(\Delta\tau)$ is different from zero only if $|\Delta\tau| \lesssim \tau_c$. As we see in Equation 107, the result is an harmonic oscillation as a function of the relative time delay $\Delta\tau$. The general definition of coherence time is [182]:

$$\tau_c = \frac{1}{|G^{(1)}(0)|^2}\int_{-\infty}^{\infty}|G^{(1)}(\Delta\tau)|^2 d\Delta\tau \tag{109}$$

It is thus evident that the knowledge of the coherence time of the radiation injected in an interferometric structure is a key parameter. In particular, in order to be able to show non-classical interference fringes, the interferometer must be able to span a time delay which greatly exceeds the coherence time of the injected radiation.
In the case of a box-like spectrum, which approximates the spectrum reported in Figure 20(a) for the poling period $\Lambda = 19.10\,\mu m$ at T = 80 °C, the time bandwidth relation is given by [182]:

$$\tau_c = \frac{1}{\Delta\nu} = \frac{\lambda^2}{c\Delta\lambda} \tag{110}$$

The fact that the coherence time of an optical signal is inversely proportional to its bandwidth is a consequence of the Fourier relationship between the two. In general, as the width of the pulse increases in the time domain, the spectral width decreases in the frequency domain and vice-versa. With the SPDC generation set-up reported in Figure 13, the effective spectral bandwidth is $\Delta\lambda = 150\,nm$, shaped by the 1500 nm long-wave pass filter and by the InGaAs responsivity. It is true that with such a filter we are cutting the spectrum of Figure 20 below 1500 nm, but such photons would not have their long

wavelength counterpart due to the sharp decrease of the detector efficiency of the InGaAs-based SPAD for $\lambda > 1600\,nm$, see Figure 15(a). The theoretical estimation of the coherence time of the SPDC emitted radiation results to be $\tau_c = 53\,fs$, which will result consistent with the experimental observation reported in Section 6.6.

Let us introduce the second-order correlation function, as a first step in a classical framework. This function measures the intensity-intensity fluctuation of an optical field. The normalized second order coherence function $g^{(2)}(\Delta\tau)$, in the simple case of a plane wave in a stationary state, is given by:

$$g^{(2)}(\Delta\tau) = \frac{\langle I(t)I(t+\Delta\tau)\rangle}{\langle I(t)\rangle^2} \tag{111}$$

It is worth commenting on some properties related to the intensity of classical fields. The intensity of a classical field should have positive variance, i.e. $Var(I) = \langle I^2\rangle - \langle I\rangle^2 \geqslant 0$, where the equality holds for an ideal monochromatic source of radiation. The positive variance property leads to the following inequality:

$$Var(I) = \langle I^2\rangle - \langle I\rangle^2 \geqslant 0 \implies 1 \leqslant g^{(2)}(0) < \infty \tag{112}$$

Moreover, if one applies Cauchy-Schwarz-inequality for random variables to Equation 111, it is possible to derive the following properties [106]:

$$|\langle I_1 I_2\rangle|^2 \leqslant \langle I_1^2\rangle\langle I_2^2\rangle \implies g^{(2)}(\Delta\tau) < g^{(2)}(0) \tag{113}$$

Figure 65 reports the $g^{(2)}$ functions for laser light and thermal light. As is possible to see from the graph, such classical sources of radiation fulfil relations Equation 112-113.
In particular, thermal light is said to be *super-Poissonian*, as it exhibits a statistical distribution which has a variance larger than the one of Poissonian light. The intensity of thermal light fluctuates randomly, giving rise to super-Poissonian statistics with $g^{(2)}(0) = 2$.

Any light source that violates the inequalities 112-113 is inherently *non-classical*. Within the framework of second quantization, it is possible to derive the $g^{(2)}(0)$ expression for a Fock state composed by n photons as [23]:

$$g^{(2)}(0) = \frac{\langle n(n-1)\rangle}{\langle n\rangle} \tag{114}$$

which for $n = 0$ gives $g^{(2)}(0) = 0$. In a quantized fashion, we can think about the $g^{(2)}$ function as the joint probability to have coincidence detections as a function of the relative time delay between two signals. Antibunching in the $g^{(2)}$ function indicates sub-Poissonian photon statistics. The second-order correlation function is the quantity measured to characterize a single-photon source. This is typically performed in a Hanbury Brown–Twiss interferometer set-up, where the emitted light is split with a 50/50 beamsplitter onto two single-

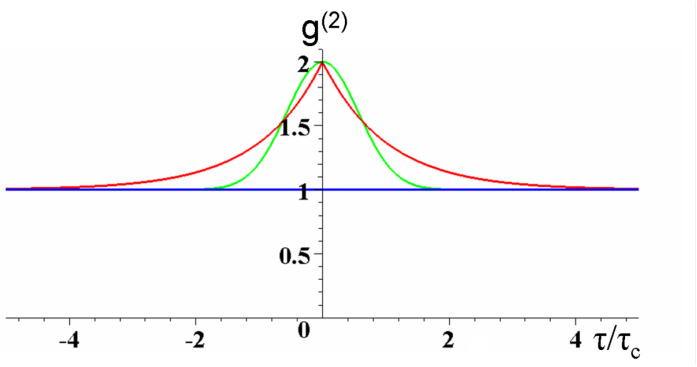

Figure 65: $g^{(2)}$ as a function of the delay normalized to the coherence time τ/τ_c. The blue curve is for a coherent state (an ideal laser or a single frequency). The red curve is for Lorentzian chaotic light (e.g. collision broadened). The green curve is for Gaussian chaotic light (e.g. Doppler broadened). The chaotic light is super-Poissonian and bunched. Image taken from [183].

photon detectors [184]. The observation of a dip in the coincidence count around relative zero delay, reveals that the source dominantly emits single photons.

6.4 QUANTUM MACH-ZEHNDER INTERFEROMETER

In a quantum description of light, the matrix S introduced in Equation 104 has the meaning of the scattering S-matrix connecting the amplitude of the single-photon eigenfunction of energy $\omega = ck$ at the input ports $[\psi_a(\omega), \psi_b(\omega)]$ to the amplitude of the same wavefunction at the output ports of the beamsplitter $[\psi_c(\omega), \psi_d(\omega)]$:

$$\begin{pmatrix} \psi_c(\omega) \\ \psi_d(\omega) \end{pmatrix} = S(\omega) \begin{pmatrix} \psi_{a,in}(\omega) \\ \psi_{b,in}(\omega) \end{pmatrix} \tag{115}$$

A sketch of the Mach-Zehnder interferometer under analysis is reported in Figure 66.
The Mach-Zehnder interferometer is characterized by the presence of two beamsplitters, which actions are modelled as:

$$\begin{aligned} \text{BS1} \rightarrow & \quad \begin{pmatrix} r_1 e^{-i\delta} & t_1 \\ t_1 & r_1 e^{-i\delta} \end{pmatrix} \\ \text{BS2} \rightarrow & \quad \begin{pmatrix} r_{2c} e^{-i\delta} & t_{2c} \\ t_{2d} & r_{2d} e^{-i\delta} \end{pmatrix} \end{aligned} \tag{116}$$

where all coefficients r_i and t_i are real, and hence r_i^2 and t_i^2 are the reflectivity and transmittivity respectively.
Here we have assumed that the reflection and transmission coeffi-

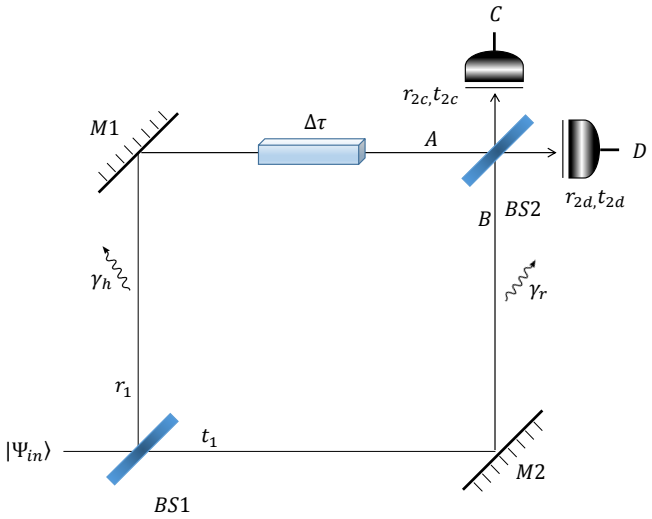

Figure 66: Sketch of the Mach-Zehnder interferometer under study, with parameters defined in the text.

cients are independent from the frequency for simplicity. We also have taken the operation of *BS1* to be symmetric, while that of *BS2* may be different for the light collected by detector C or D, as indicated by the second subscript c, d. As described in Section 6.5, experimentally we introduce such an asymmetry by tuning the position of detector *D* with respect to the output of *BS2*, thus reducing t_{2d} and r_{2d} relative to r_{2c} and t_{2c}. As we shall show, these coefficients control the amplitude of various photon interference effects and so this controlled asymmetry can be used to tune between different regimes. In the beamsplitter relation (116), we have also explicitly kept the relative phase δ between the reflection and transmission coefficients. For an ideal lossless beamsplitter, the relative phase must be equal to $\pi/2$ as required by energy conservation [185]. However, as derived by Barnett et. al. [181], this stringent phase condition may be relaxed when a beamsplitter is intrinsically lossy. This will be discussed in further detail at the end of this Section. Note that we assume for simplicity that the relative phase is identical and symmetric for both beamsplitters. We will come back to this in Section 6.6.

The goal of this analysis is to study the joint probability to have coincidence detections at t and $t+\tau$ between the two output ports of the interferometer (*C* and *D*) when the SPDC photon pairs enter in the same input port of the interferometer. Therefore, to study photon interference, we calculate the coincidence rate of photons arriving at the two photodetectors, which operate with a resolving time T_R and efficiency *K*. With reference to Figure 66, the probability per unit time of coincidence detections at the output ports *C* and *D* of the MZI at times t and $t+\tau$ is given by [186]:

$$P(\tau) = K\langle \hat{E}_D^-(t)\hat{E}_C^-(t+\tau)\hat{E}_C^+(t+\tau)\hat{E}_D^+(t)\rangle \tag{117}$$

where $\hat{E}_C^+$ and $\hat{E}_D^+$ are respectively the positive frequency parts of the electric field operator at the output ports *C* and *D* of the interferometer [23]. Equation 117 can be viewed as the non-normalized quantum-mechanical expression of the classical second-order coherence function which appears in Equation 111.
The expectation values of Equation 117 is calculated on the following quantum-mechanical state:

$$|\psi_{in}\rangle = |0\rangle + \frac{\beta}{\sqrt{2}} \int d\omega_s d\omega_i \, \phi(\omega_s, \omega_i) \, \hat{a}^\dagger_{\omega_s} \hat{a}^\dagger_{\omega_i} |0\rangle \tag{118}$$

which represents the two-photon state produced by the SPDC in low pump approximation. The simulation of the modulus square of the biphoton wavefunction $\phi(\omega_s, \omega_i)$ under analysis is reported in Figure 62.
In what follows, we will consider the pump field as monochromatic, since its coherence time is assumed to greatly exceed the one of the down converted photons. As a consequence of this approximation, we can use the energy conservation relation $\omega_p = \omega_s + \omega_i$ to express the frequency of one photon of the pair as ω, and the frequency of the twin photon as $\omega_p - \omega$. In this way, the biphoton wavefunction, which we approximate to be Gaussian, can be written as:

$$\phi(\omega_s, \omega_i) \simeq \phi(\omega) = \frac{1}{\sqrt[4]{\pi}\sqrt{\sigma}} e^{-\frac{(\omega - \omega_p/2)^2}{2\sigma^2}} \tag{119}$$

in which σ is the bandwidth of the generated photons.
We can distinguish between two-photon and single-photon-like interference effects by studying Equation 117 as a function of the relative time delay $\Delta\tau$ between the two MZI arms. Experimentally, we use a heater to vary $\Delta\tau$, and hence we indicate the upper arm with the subscript *h* (heater) and the lower arm with *r* (reference). The propagation losses along the two arms are given by γ_h^2 and γ_r^2 respectively. Combining this with the beamsplitter relations (116), we can write the electric fields E_C and E_D as:

$$\begin{aligned} E_C^-(t) &= r_1 \gamma_h r_{2c} e^{-i2\delta} E_{in}^-(t - \Delta\tau) + t_1 \gamma_r t_{2c} E_{in}^-(t) \\ E_D^-(t) &= t_1 \gamma_r r_{2d} e^{-i\delta} E_{in}^-(t) + r_1 \gamma_h t_{2d} e^{-i\delta} E_{in}^-(t - \Delta\tau) \end{aligned} \tag{120}$$

where E_{in}^- is the negative frequency part of the input electric field operator at *BS1*. From these expressions for the electric fields, we can calculate the photon coincidence rate, provided that we also specify the input radiation state $|\Psi_{in}\rangle$. By inserting a completeness relation

between $E_C^-(t+\tau)$ and $E_C^+(t+\tau)$ in Equation 117, and by using Equation 120 we find:

$$\begin{aligned} P(\tau,\Delta\tau) = K \Big| & \gamma_{hc}\gamma_{rd} e^{-i3\delta} \langle E_{in}^-(t) E_{in}^-(t+\tau-\Delta\tau)\rangle + \\ & + \gamma_{rd}\gamma_{rc} e^{-i\delta} \langle E_{in}^-(t) E_{in}^-(t+\tau)\rangle + \\ & + \gamma_{hc}\gamma_{hd} e^{-i3\delta} \langle E_{in}^-(t-\Delta\tau) E_{in}^-(t+\tau-\Delta\tau)\rangle + \\ & + \gamma_{hd}\gamma_{rc} e^{-i\delta} \langle E_{in}^-(t-\Delta\tau) E_{in}^-(t+\tau)\rangle \Big|^2 \end{aligned} \tag{121}$$

where the expectation values are now evaluated between the initial state $|\Psi_{in}\rangle$ and the vacuum state $|0\rangle$:

$$\langle E_{in}^-(t) E_{in}^-(t')\rangle = \langle \Psi_{in}| E_{in}^-(t) E_{in}^-(t') |0\rangle \tag{122}$$

In Equation 121 we have introduced the parameters:

$$\begin{aligned} \gamma_{hc} &= r_1 \gamma_h r_{2c} \quad & \gamma_{hd} &= r_1 \gamma_h t_{2d} \\ \gamma_{rc} &= t_1 \gamma_r t_{2c} \quad & \gamma_{rd} &= t_1 \gamma_r r_{2d} \end{aligned} \tag{123}$$

where the subscript h, r refers to the path along the upper or lower arm of the interferometer respectively, while subscript c, d denotes whether the photon arrives at detector *C* or *D*. The expectation values in Equation 121 can be evaluated by using the Fourier representation of the negative frequency part of the input electric field [23]:

$$E_{in}^-(t) = \int a_\omega^\dagger e^{i\omega t} d\omega \tag{124}$$

and hence that:

$$\langle E_{in}^-(t) E_{in}^-(t')\rangle = 2\phi(t-t') e^{i\omega_p t'} \tag{125}$$

where $\phi(t)$ is the Fourier transform of $\phi(\omega)$. Substituting Equation 125 into Equation 121, we obtain that $P(\tau) \propto |p_{h,h} + p_{r,r} + p_{h,r}^{(R)} + p_{h,r}^{(T)}|^2$, where:

$$p_{h,h} = 2\gamma_{hc}\gamma_{hd}\, e^{-i(\omega_p \Delta\tau + 3\delta)} e^{-\frac{\sigma^2\tau^2}{2}} \tag{126}$$

$$p_{r,r} = 2\gamma_{rc}\gamma_{rd}\, e^{-\frac{\sigma^2\tau^2}{2}} e^{-i\delta} \tag{127}$$

$$p_{h,r}^{(R)} = 2\gamma_{hc}\gamma_{rd}\, e^{-i\left(\frac{\omega_p \Delta\tau}{2} + 3\delta\right)} e^{-\frac{\sigma^2(\tau-\Delta\tau)^2}{2}} \tag{128}$$

$$p_{h,r}^{(T)} = 2\gamma_{hd}\gamma_{rc}\, e^{-i\left(\frac{\omega_p \Delta\tau}{2} + \delta\right)} e^{-\frac{\sigma^2(\tau+\Delta\tau)^2}{2}} \tag{129}$$

Equation 126-129 are the transition amplitudes associated with the indistinguishable paths through which the photon pair can travel from the input of *BS1* to the photodetectors. With reference to Figure 67, the amplitudes $p_{h,h}$ and $p_{r,r}$ refer to *bunching*, when both photons

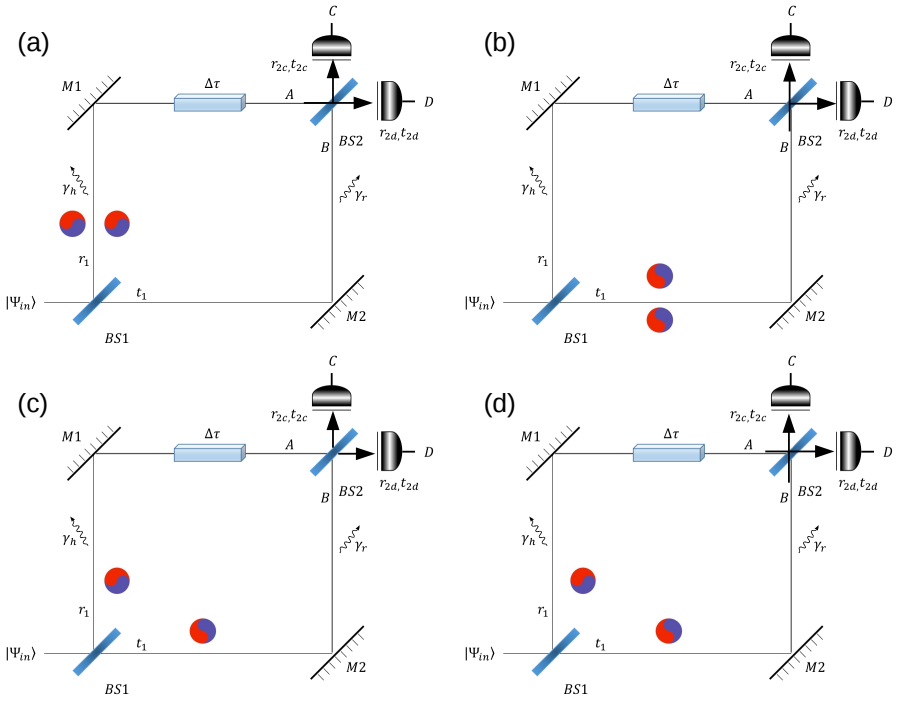

Figure 67: Panels (a,b,c,d) sketch the possible paths that a photon pair can take after *BS1*, to the output ports *C*,*D*. (a,b) refer to *bunching* states, or *NooN* states with $N = 2$. Here the pair is not split after *BS1*. (c,d) refer to *antibunching* states since the pair is split by BS1. In case (c), both the photons are reflected at *BS2*, while in (d) both the photons are transmitted at *BS2*.

are either reflected or transmitted by *BS1*. On the other hand, the amplitudes $p_{h,r}^{(R)}$ and $p_{h,r}^{(T)}$ describe *antibunching*, when the photon pair is split at *BS1*. In these cases, the superscript R, T denotes respectively when the photons are both either reflected or transmitted at *BS2*. We emphasise that the anti-bunching paths ($p_{h,r}^{(T,R)}$) are not generally allowed when both input ports of *BS1* are excited, due to the Hong-Ou-Mandel effect at the first beamsplitter [187]. By using only a single input port, we therefore explore a richer interplay of interference effects where the photon pair can travel along both anti-bunching and bunching paths.

To calculate the coincidence rate, we have to square the sum of all the transition amplitudes in Equation 126-129, and integrate τ over the coincidence resolving time of the photo-detectors T_R. In Equation 126-129, each amplitude vanishes when τ is much greater than the photon coherence time $\tau_c = 1/\sigma$, while for all practical experiments $T_R \gg \tau_c$. Hence, we can effectively extend the integration over τ from $-\infty$ to ∞, to finally obtain the coincidence rate:

$$N_c(\Delta\tau) = K'(C_1 + C_2 + C_3) \tag{130}$$

where K' is a constant and the three terms on the right hand side are defined as follows:

$$C_1 = \gamma_{hc}^2\gamma_{rd}^2 + \gamma_{hd}^2\gamma_{rc}^2 + 2A_{\omega_p}\, e^{-\sigma^2\Delta\tau^2}\cos(2\delta) \tag{131}$$

$$C_2 = \gamma_{hc}^2\gamma_{hd}^2 + \gamma_{rc}^2\gamma_{rd}^2 + 2A_{\omega_p}\cos(\omega_p\Delta\tau - 2\delta) \tag{132}$$

$$C_3 = 2e^{-\frac{\sigma^2\Delta\tau^2}{4}}\left[A^{(1)}_{\omega_p/2}\cos\left(\frac{\omega_p\Delta\tau}{2} + 2\delta\right) + A^{(2)}_{\omega_p/2}\cos\left(\frac{\omega_p\Delta\tau}{2}\right)\right] \tag{133}$$

where we have introduced the following parameters:

$$A_{\omega_p} = \gamma_{rc}\gamma_{rd}\gamma_{hc}\gamma_{hd} \tag{134}$$

$$A^{(1)}_{\omega_p/2} = \gamma_{hc}\gamma_{rc}(\gamma_{rd}^2 + \gamma_{hd}^2) \tag{135}$$

$$A^{(2)}_{\omega_p/2} = \gamma_{hd}\gamma_{rd}(\gamma_{hc}^2 + \gamma_{rc}^2) \tag{136}$$

It is also convenient to introduce the power-amplitude coefficient $A_{\omega_p/2}$ associated with the frequency component at $\omega_p/2$:

$$A^2_{\omega_p/2} = \left(A^{(1)}_{\omega_p/2}\right)^2 + \left(A^{(2)}_{\omega_p/2}\right)^2 + 2A^{(1)}_{\omega_p/2}A^{(2)}_{\omega_p/2}\cos(2\delta) \tag{137}$$

Let us comment and give a physical interpretation to the various terms which appear in Equation 130:

- The C_1 term, Equation 131, represents the antibunching-antibunching interaction between the paths (c) and (d) in Figure 67, resulting in the well known HOM dip at the optical contact of the MZI ($\Delta\tau = 0$);
- the C_2 term, Equation 132, describes the bunching-bunching interaction between the paths (a) and (b) in Figure 67, which is mediated by the coupling strength A_{ω_p}. This term oscillates at frequency ω_p which is two times the average single photon frequency ($\omega_p/2$) and is responsible of two-photon interference.
- the C_3 term, Equation 133, comes from the interference between the bunching cases and the anti-bunching ones, and is mediated by the interaction parameter $A_{\omega_p/2}$.

It is worth noting that the interference channel described by Equation 133 is actually missing in a balanced MZI or in a MZI which is fed symmetrically at the two input ports, due to a completely destructive quantum interference [168, 188, 189]. This term shows fringes at $\omega_p/2$, which creates a single-photon interference pattern. The origin of the single-photon interference channel described by Equation 133, can be seen from the fact that the phase difference between the bunching and the antibunching cases is always $(\omega_p/2)\Delta\tau$. In fact, from the comparison of the paths (a-b) in Figure 67 with the ones in Figure 67(c-d), one can notice that there is always one arm of the interferometer which

carries one more photon with respect to the other.
This is analogous to the situation when a single-photon enters at the input of *BS1*: it can take either the lower arm or the upper one, giving rise to a relative phase difference of $(\omega_p/2)\Delta\tau$ between the two paths.
In general, the coincidence pattern calculated in Equation 130 will exhibit competing effects between single and two-particle interference, where their relative visibility can be evaluated by the magnitude of an *unbalancing* parameter:

$$\xi = A_{\omega_p/2}/A_{\omega_p} \tag{138}$$

6.4.1 *Lossless beamsplitter*

Let us discuss the theoretical expectation of the coincidence rates at the output of the MZI, assuming both the beam-splitters lossless. In the lossless case the phase that appears in Equation 116 is fixed by the energy conservation and is given by $\delta = \frac{\pi}{2}$ [185].
In this case Equation 138 simplifies to:

$$\xi = \frac{A_{\omega_p/2}}{A_{\omega_p}} = \frac{(\gamma_{hc}\gamma_{rd} - \gamma_{rc}\gamma_{hd})(\gamma_{hc}\gamma_{hd} - \gamma_{rc}\gamma_{rd})}{\gamma_{rc}\gamma_{rd}\gamma_{hc}\gamma_{hd}} \tag{139}$$

and we can straightforwardly consider the two limits for $\xi \to 0$ and $\xi \to \infty$. In the limit when $\xi \to 0$, antibunching-bunching interactions undergo complete destructive interference, and the single-particle-like features disappear from the coincidence pattern.
This happens if we impose some symmetries losses along each arm, or on the beamsplitter coefficients. The simplest case that we can consider is when both the beam-splitters are 50/50 devices and the two arms have identical loss rates. This condition implies to have $\gamma_{hc} = \gamma_{hd} = \gamma_{rc} = \gamma_{rd}$ (see Equation 123) and the power-amplitude coefficient defined in Equation 137 $A_{\omega_p/2} = 0$.
This means that, only one frequency is observed when the device is ideally symmetric, which is consistent with what was found in previous works [168, 186, 188]. We also note that there are actually three other configurations for which $\xi = 0$, which with reference to Figure 64 are given by:

1. If *BS2* is balanced, so that $\gamma_{hc} = \gamma_{hd}$ and $\gamma_{rd} = \gamma_{rc}$.
2. If *BS1* is balanced while the arm losses γ_r and γ_h are also equal, so that $\gamma_{hc} = \gamma_{rc}$ and $\gamma_{rd} = \gamma_{hd}$.
3. If the transmittance from the input to port C along the upper arm is equal to the transmittance to port D along the lower arm (i.e. $\gamma_{rd} = \gamma_{hc}$) or vice-versa ($\gamma_{hd} = \gamma_{rc}$).

In the limiting case where $\xi \to \infty$, instead, the coincidence rate shows no signs of two-photon correlations. This happens when one of the

four loss factors in Equation 123 is equal to zero.
If we consider for example the ideal extreme case $\gamma_{hc} = 0$, then the photon which fires the detector at port C is forced to come from the lower arm, providing a *which-path* information. The remaining uncertainty between the paths which the other photon of the pair may take to fire the other detector, gives rise to pure single-photon interference. The lack of two-photon correlations can be also explained from the fact that when $\gamma_{hc} = 0$, the bunching path in Figure 67(a) is suppressed, so bunching-bunching interactions (which are the source of two photon correlations) cancel.
In general, the presence of beamsplitter loss impedes a complete cancellation of the antibunching-bunching term (Equation 133). However, it is again the transmittance balanced configuration which minimizes this interference effect. Intermediate values of ξ can be realized by changing the relative arm transmittance.

6.4.2 *Lossy beamsplitter*

Let us comment here in details the physical implications of a lossy beamsplitter. In the lossless case, the input/output equations can be written explicitly from Equation 115:

$$\begin{aligned} \psi_d(\omega) &= t(\omega)\psi_a(\omega) + r(\omega)\psi_b(\omega) \\ \psi_c(\omega) &= t(\omega)\psi_b(\omega) + r(\omega)\psi_a(\omega) \end{aligned} \tag{140}$$

Note that in Equation 140, the parameters $r(\omega), t(\omega)$ are in general complex and an explicit phase relation has been not already fixed. The relations which appear in Equation 140 are subjected to the constraints imposed by unitarity:

$$\begin{aligned} |t(\omega)|^2 + |r(\omega)|^2 &= 1 \\ t(\omega)r^*(\omega) + t^*(\omega)r(\omega) &= 0 \end{aligned} \tag{141}$$

for all frequencies ω, ensuring the conservation of energy and the orthogonality of the two outgoing modes. What happens instead for a lossy beamsplitter is the following. The conditions reported in Equation 141 no longer hold exactly, but instead, they change to the following two inequalities [181]:

$$\begin{aligned} |t(\omega)|^2 + |r(\omega)|^2 &\leqslant 1 \\ |t(\omega)r^*(\omega) + t^*(\omega)r(\omega)| &\leqslant 1 - |r(\omega)|^2 - |t(\omega)|^2 \end{aligned} \tag{142}$$

The first inequality appearing in Equation 142, is the probability of survival for a single photon incident on the beam splitter. The second inequality arises by considering the input fields with classical or coherent amplitudes and requiring that the total output intensity

should be less than or equal to that at the input.
Hereafter, we will drop the dependence on frequency for simplicity, assuming that these coefficients are approximately constant over the considered spectral range. Now, as stated above, in a lossless beamsplitter, unitarity requires that the two outgoing modes are orthogonal. Choosing the transmission coefficient to be real, this can be written as:

$$t(\omega) = t, \qquad r(\omega) = te^{\pm i\pi/2} = \pm it \tag{143}$$

for a symmetric beamsplitter. If we have losses, the constraint on the phase can be relaxed. In Equation 142, we substitute $r = te^{i\phi}$, to write the two inequalities as:

$$\begin{aligned} 2t^2 &\leqslant 1 \\ 2t^2(1+|\cos\phi|) &\leqslant 1 \end{aligned} \tag{144}$$

So we can deduce the possible values of ϕ, provided that we know t. For example, if the probability of a single photon passing through the beamsplitter without being absorbed is γ, then $t = \sqrt{\gamma/2}$; the second inequality can then be written as:

$$|\cos\phi| \leqslant (1/\gamma - 1) \tag{145}$$

Of course in the limit that $\gamma = 1$ (i.e. a lossless beamsplitter), this constrains $\phi = \pm\pi/2$ as expected. When $\gamma < 1$, the phase δ can also be higher or lower than $\pi/2$, with important consequences. Firstly, we notice from Equation 131 that if $\delta \neq \pi/2$, the magnitude of the HOM dip will be smaller as the antibunching paths acquire different phases upon exiting *BS2*. Therefore they no longer completely destructively interfere. This is the reduction in the visibility of the Hong-Ou-Mandel effect for a lossy beamsplitter with non-orthogonal reflection and transmission coefficients, predicted also in [181].
The experimental characterization of the beamsplitter losses is reported in Figure 68. The beamsplitter losses have been measured for both *S* and *P* polarized waves in the wavelength range [1510;1570] nm, which almost covers the spectral bandwidth of the SPDC photons injected in the MZI. In the experimental set-up described in Section 6.5 we worked with S polarized photons. This corresponds to an average loss of $(21.9 \pm 0.4)\%$ for each BS.
With respect to the formalism previously introduced, this leads to $\gamma = (0.781 \pm 0.004)$. Then, assuming the beamsplitter to be balanced (i.e. $|r| = |t|$), the range of δ becomes:

$$0.82\,\frac{\pi}{2} \lesssim |\delta| \lesssim 1.12\,\frac{\pi}{2} \tag{146}$$

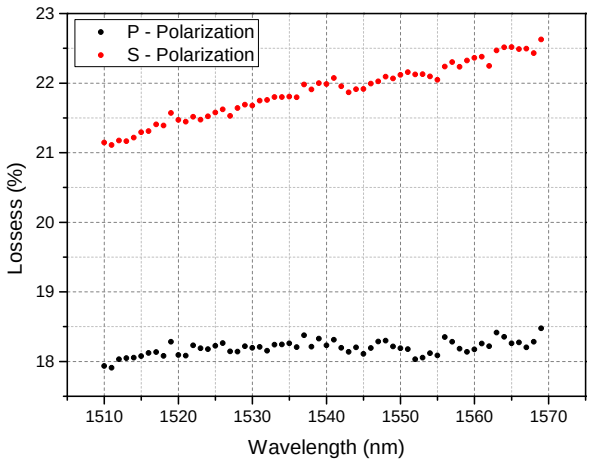

Figure 68: Beamsplitter losses for P and S polarized waves as a function of the wavelength.

While this may at first seem a small difference from $\delta = \pi/2$, it is enough to dramatically affect the appearance of the coincidence pattern, as it can be appreciated in Figure 69. We change the phase here

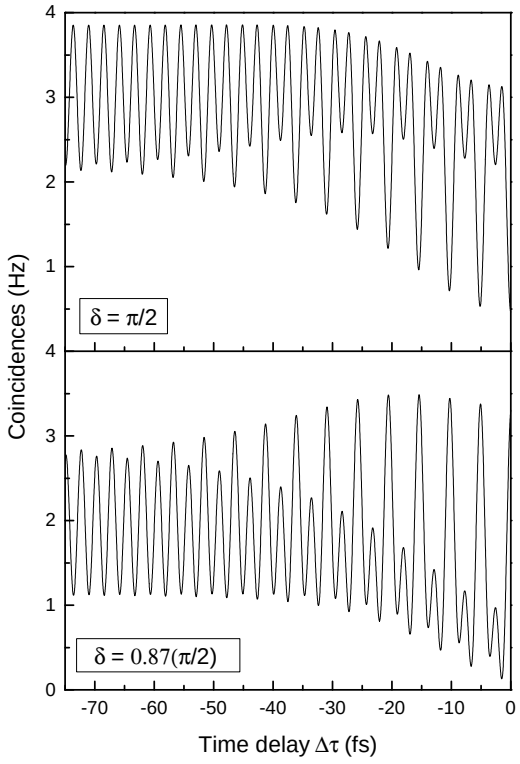

Figure 69: Theoretical coincidence rate in Equation 130 as a function of the interferometer time delay $\Delta\tau$, for different values of the beamsplitter phase δ. The parameters of the simulation are the same used for the solid red curve in Figure 73 for $\xi, = 1.34$ and are reported in Table 8. Image taken from [190].

from $\delta = \pi/2$ to $\delta = (0.87)\pi/2$, which corresponds to the phase found

from our fit to the experimental results reported in Section 6.6 and it is compatible with the measured beam-splitter losses in Figure 68.
Furthermore we can see that while the condition for $\xi_c \to \infty$ is not affected by the beamsplitter phase, in the limit of $\xi_c \to 0$ it is. We can understand this directly from Equation 137, by noting that if $\delta \neq \pi/2$, there will never be a complete cancellation of the antibunching-bunching term. However, it can be shown that this term is still minimised by the ideal symmetric configuration where $\gamma_{hc} = \gamma_{hd} = \gamma_{rc} = \gamma_{rd}$. As we can see, this phase change affects many of the qualitative features in the coincidence patterns, including the envelope behaviour around the optical contact and the fringe pattern. Again, we emphasise that this remarkable phase sensitivity arises from the rich interplay of multiple interference terms, going beyond previously reported experiments [168, 188].
Recently, the lossy beamsplitter phase effect has been observed also in other physical systems [73, 191–193]. For example, in [73] the authors reported a quantum interference experiment in silicon-on-insulator wire waveguide. Here, the beamsplitter-like operation is realized by a 2x2 multi-mode interference coupler (MMI). The integrated Mach-Zehnder interferometer therefore was formed by two multi-mode interference coupler thermo-optic phase shifter, connected by two waveguides, one of which with a voltage controlled phase shifter. The authors actually found a discrepancy between the measured beamsplitter visibility in a HOM measurement and the nominal MMI visibility. They attribute the discrepancy to the intrinsic losses within the MMI device. In [193], instead, a plasmonic version of the HOM effect was reported. Here is the case of another integrated version a beamsplitter-like operation, which is formed by a directional coupler. The directional coupler is composed by dielectric-loaded surface plasmon polariton waveguides directly integrated into silicon nitride waveguides. They observed high HOM visibility, consistent with the predictions of the case of a lossy directional coupler. More recently, in [191, 192] a study on two-photon quantum interference in an opaque scattering medium was reported. In the experiment the authors sent photon pairs generated in a bulk nonlinear crystal, through an opaque scattering medium. The authors investigated two-photon quantum interference in a programmable 2x2 beamsplitter made of a multiple-scattering medium and a liquid-crystal-based spatial light modulator. Again, the programmed beamsplitter does not need to fulfil energy conservation over the two selected output channels and hence could be nonunitary. Differently from the work here reported and the previously discussed works [73, 193], here the authors have the freedom to tune the beamsplitter phase via a spatial modulator. They were able to tune the quantum interference between the photon pair from "the classical" bunching (Hong-Ou-Mandel-like) to the

opposite case, where the two photons are antibunched after the beam-splitter.

6.5 EXPERIMENTAL SET-UP

Quantum interference effects have been experimentally investigated in the free-space Mach-Zehnder reported in Figure 70. Type-0 SPDC co-polarized and collinear signal and idler photons around the degenerate wavelength 1550 nm, are injected in the MZI through the same input port. The details of the SPDC generation of photon pairs is discussed in Chapter 2. The effective SPDC bandwidth is $\Delta\lambda = 150\,\text{nm}$. As it is possible to see from the Figure 70, in order to introduce

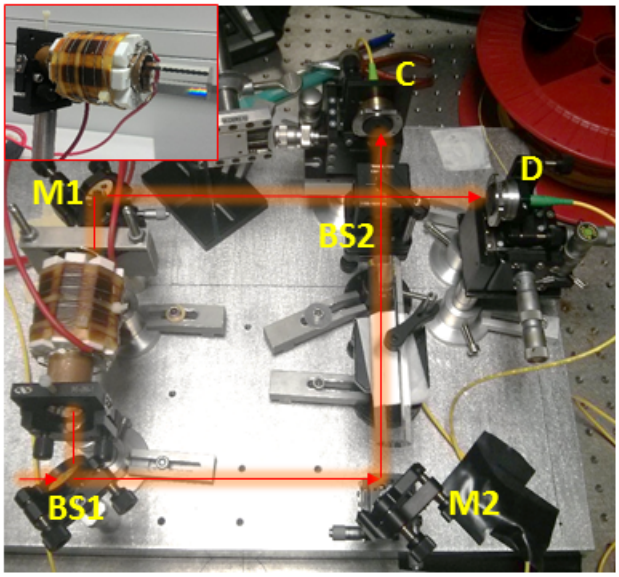

Figure 70: Photo of the free-space Mach-Zehnder interferometer. The inset shows the system used to change the delay on the upper interferometer arm.

a variable time delay between the two arms of the interferometer, an $l = 12\,\text{cm}$ long cylinder of Borosilicate Crown glass (NbK_7) was placed in both MZI arms [194]. We inserted the same NbK_7 cylinder in each arm of the MZI, otherwise the optical path difference would have been be too far from the balanced situation ($\Delta\tau = 0$). As it is possible to see from the inset of Figure 70, in one arm, the NbK_7 was inserted into an electric heater. The home-made electric heater is composed by 8 ceramic resistors of R = 10 Ω connected in parallel around a hollow copper cylinder within which the glass cylinder is placed.

The resistors are connected to a DC power supply that delivers the current to vary the temperature of the NbK_7. In this way it is possible to exploit the thermo-optic coefficient of the NbK_7 to smoothly vary the refractive index. The induced time delay can be calculated as follows:

$$\Delta\tau = \frac{l\Delta n}{c} = \frac{l}{c}\frac{dn}{dT}\Delta T \tag{147}$$

where $dn/dT = 2.45 \times 10^{-6}\,1/K$ is the NbK_7 thermo-optic coefficient [194] and ΔT is the temperature variation of the glass. Experimentally it is actually not easy to estimate the effective temperature variation of the glass material. The NbK7 is not really inserted for its entire length in the heater and therefore the temperature is not constant along the length of the glass cylinder. Moreover, even if the glass cylinder were inserted completely in the heater, the temperature would not be the same along its entire length due to an inherent temperature gradient within the cylinder. Therefore, the time delay was more accurately characterized by injecting in the MZI a CW laser, tuned to the central wavelength of the SPDC radiation at 1550 nm. By looking at the classical interference fringes, a fringe period of 5.16 fs was estimated. By delivering 40 W of electrical power, we were able to induce a variable time delay between the arms as high as almost 130 fs with an electric current of 5 A (see Figure 71).

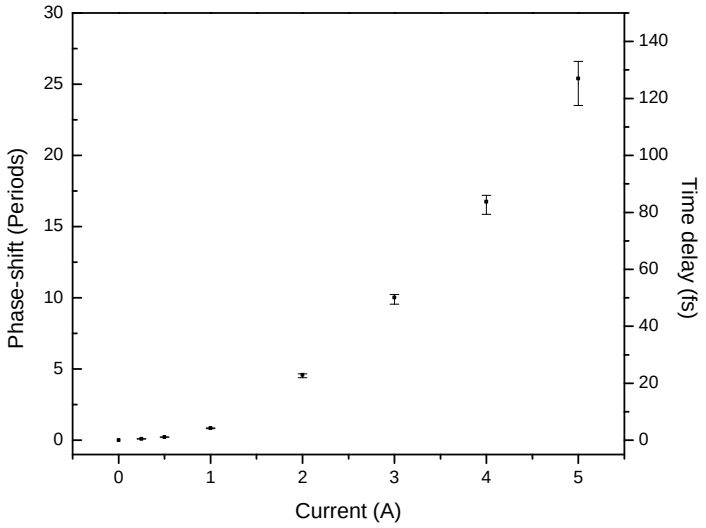

Figure 71: Phase-shift reported in periods and time delay induced as a function of the applied electrical current through the heater.

Considering the theoretically derived coherence time $\tau_c \sim 53$ fs, the time delays are sufficiently larger than τ_c and therefore all the various interference effects theoretically predicted by Equation 130 can be investigated. In particular, time delays larger than τ_c are needed in order to show pure quantum two-photon interference effects. We ac-

tually programmed the current generator with a LabVIEW software to provide electrical current through the heater, in order to have a slow, linear, increasing time delay between the two arms of the interferometer. It will be shown in Section 6.6 that the time delay between the MZI arms can be as long as 180 fs in a 4-h measurement. The smoothness of the refractive index change and the long duration of the measurement allows reducing the overall noise of the system and to produce high quality coincidence fringes with relatively low counts (< 10 Hz).
With reference to Figure 70, the photons at the output ports of the MZI are then focused by two lenses onto two InGaAs single-photon counting detectors (Id210 and Id201). One detector was used in free running mode (40 µs of deadtime) to detect one photon of the pair. When the other detector was triggered, it was enabled for a gate width of 100 ns. The detection scheme is the same shown in Chapter 5. The outputs of the two SPADs are then fed into a FPGA digital correlator that provides the coincidence rate over a coincidence window of 5 ns in real time. As introduced above, the parameters in Equation 123 are tuned by inducing controllable losses by slightly misaligning the lenses in front of the photon counters.

6.6 EXPERIMENTAL MEASUREMENTS

The single port (in this case port D) measured count rate as a function of the time delay $\Delta\tau$ is shown inFigure 72. Since the curve is symmetric with respect to $\Delta\tau = 0$, we report only the measured values for negative time delays.

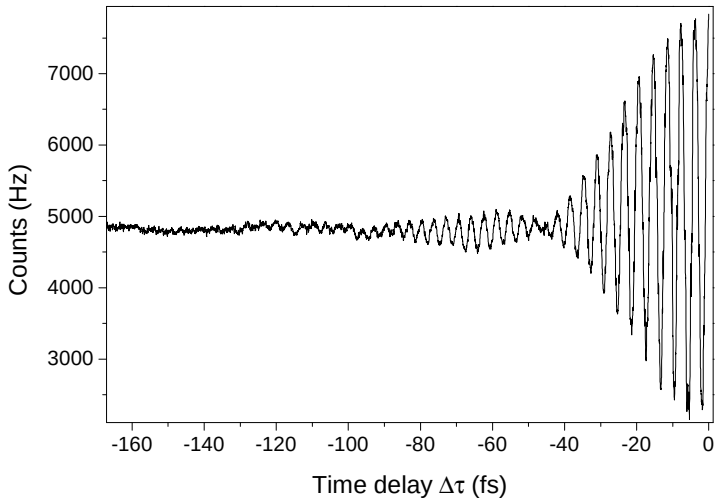

Figure 72: Single-photon interference fringes measured at the D output port as a function of the time delay $\Delta\tau$. Image taken from [195].

Following a similar approach to the one discussed in Section 6.4, it is possible to show that the D port count rate C_D is given by:

$$C_D(\Delta\tau) \propto \langle \hat{E}_D^-(t)\hat{E}_D^+(t)\rangle \propto \gamma_{hd}^2 + \gamma_{rd}^2 + 2\gamma_{hd}\gamma_{rd} e^{-\frac{\Delta\tau^2\sigma^2}{4}} \cos\left(\frac{\omega_p \Delta\tau}{2}\right) \tag{148}$$

We see from Equation 148 that the single port count rate should exhibit oscillations with a period equal to $\frac{2\pi}{\omega_p/2}$, modulated by a slowly varying envelope due to the finite coherence time τ_c of the photons. This is experimentally confirmed in Figure 72, where the SPDC coherence time has been estimated from the FWHM of a Gaussian fit to be $\tau_c^{FWHM} = (48 \pm 1)\,fs$. The experimental coherence time is actually close to the theoretical estimation derived in Section 6.3 from the SPDC spectrum, which was $\sim 53\,fs$. In the discussion which follows we will consider the coherence time to be $\tau_c = \tau_c^{FWHM}/2$, as the experimental data are reported only for $\Delta\tau < 0$. The oscillations in Figure 72 are not quantum interference effects, since they come from single-particle interference. It would have been possible to derive Equation 148 also from a classical point of view, as it was done in Section 6.3. In particular, since the function $C_D(\Delta\tau)$ is *symmetric* with respect to $\Delta\tau = 0$, within the experimental data uncertainty, this legitimises the simplified choice to consider the relative phase identical and symmetric for both beamsplitters in Equation 116. However, in general the two phases are not necessarily equal. In this case, the oscillations reported in Figure 72 would not have been symmetric with respect to $\Delta\tau = 0$.

We note in Figure 72 that the oscillations do not damp immediately to zero for $\Delta\tau \gg \tau_c$, but exhibit ripples. This is due to the box-like spectral distribution of the photons entering the MZI, shaped by the presence of the 1500 nm long-pass filter and by the roll-off of the InGaAs-based SPAD for $\lambda > 1600\,nm$, see Figure 15(a). As a result, it is expected that the single port count rate shows an autocorrelation which resembles a sinc function. However, the Gaussian distribution introduced in Equation 119 is a good enough approximation for our theoretical description, as we see in Figure 73. It lets us predict all the interesting physical features experimentally observed.

The coincidence rate obtained for different values of the unbalancing parameter ξ, defined in Equation 138, is shown in Figure 73. To change the value of ξ, we simply independently tune the position of the focusing lenses in front of the detectors C and D. The values of ξ reported in Figure 73 are taken from simulation, which are the red curves in Figure 73 obtained from Equation 130. By programming the current generator to provide a smooth, linearly increasing time delay, this gives us the freedom to average over substantial stretches of experimental data to improve the signal-to-noise ratio of the measurement.

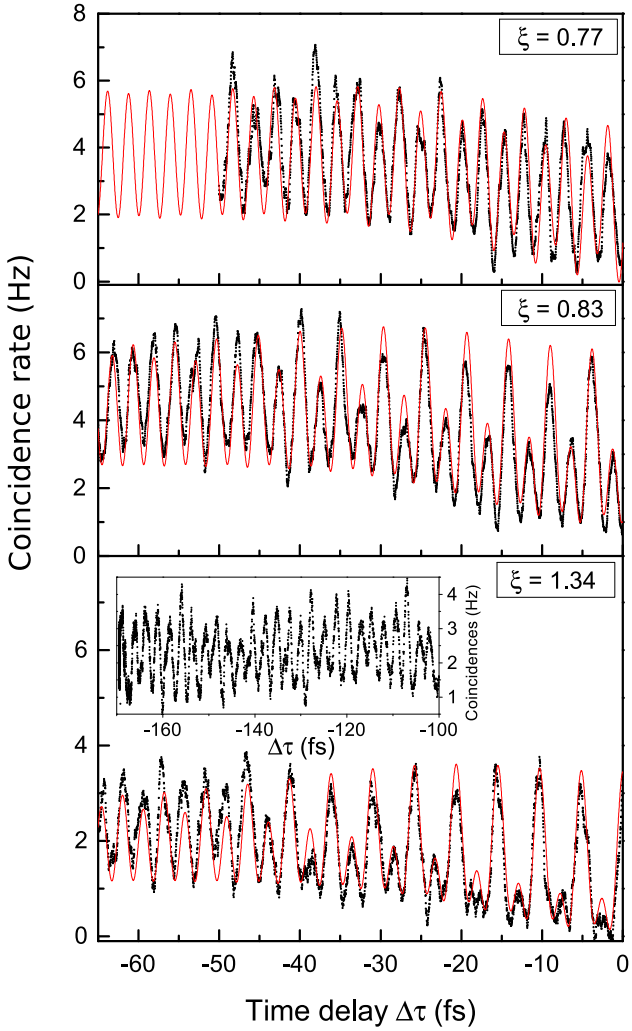

Figure 73: Coincidence rates averaged over different values of the unbalance parameter ξ (Equation 138), as a function of the time delay $\Delta\tau$. The solid red curves are fits from Equation 130, while black scatter points are experimental data. The inset shown in the panel $\xi = 1.34$ shows the coincidence rate for time delays larger than the single photon coherence time. A value of $\delta = 0.87\pi/2$ has been used which is compatible with a measured beam-splitter loss of 22%. The reported value of ξ is taken from the fit. Values of the other fit parameters are reported in Table 8.

In particular we under-sampled our data points by a factor of 40 for averaging, still having a high density of experimental points (dots in Figure 73). This is the main reason why we do not have huge error bars with such little counts per second. As already said, typically a complete scan took approximately 4 hours.

Three exemplary values of the unbalancing parameter ξ were considered, showing different regimes in the coincidence interference patterns of Figure 73. They are the following:

- In the case $\xi = 0.77$ in Figure 73, we balanced the interferometer in order to suppress antibunching-bunching interactions, C_3 term in Equation 130. The residual component at $\omega_p/2$ is only due to the beam splitter losses (approximately 22%). The coincidence rate exhibits practically the same oscillating behaviour at frequency ω_p within and outside the coherence time of the single photons. Within the coherence time, $|\Delta\tau| < \tau_c$, the observed pattern becomes a mixture between bunching-bunching (see Figure 67) and HOM-like interference. The latter manifests itself as a decrease in the average value of the coincidence counts as we approach $\Delta\tau = 0$, as expected. We can see that the oscillation in the coincidence rate for $|\Delta\tau| > \tau_c$ is a clear manifestation of the colour-entangled nature of the two-photons state created in the down conversion process [168]. To clearly show that the oscillation at frequency ω_p is due to purely second order interference effects, we plot in the inset of Figure 73 (panel $\xi = 1.34$) the coincidence rate for time delays greatly exceeding the single photon coherence time ($|\Delta\tau| > 100fs$). As we can see from Figure 72, for such time delays any possible contribution arising from first order interference to the coincidence pattern vanishes. Even if not reported in Figure 73, the very same oscillations outside τ_c are observed regardless of the value of ξ.

- As ξ is increased, the pattern changes significantly with respect to the balanced situation, due to the enabling of new interference paths. The case at $\xi = 0.83$ in Figure 73 *includes two-photon, one-photon and HOM interference effects all in a single coincidence pattern*. Indeed, outside the coherence time, the antibunching terms in Figure 67(c-d) have vanishing probability, so the interference fringes at ω_p are due to purely two-photon correlation effects. For $|\Delta\tau| < \tau_c$, instead, the paths (c) and (d) in Figure 67 are allowed to interfere with the ones in (a) and (b), creating a mixed pattern in which single-particle interference at $\omega_p/2$ and two-particle one at ω_p coexist. The HOM effect again can be seen as the decrease of the average coincidences within the coherence time.

- We see from Figure 73 that it is sufficient to induce a value of $\xi = 1.34$ to practically cancel the oscillations at ω_p within the coherence time. In general the higher the unbalance between the arms is, the higher is the suppression of the two-photon contribution at ω_p and, at the same time, the higher the visibility of the single-photon component at $\omega_p/2$.

In Figure 73, the simulations (solid red curves) match the experiment well only if the phase δ slightly deviates from $\frac{\pi}{2}$ ($\delta = 0.87\frac{\pi}{2}$).
The fit procedure is based on a differential evolution genetic algorithm [196], which minimizes the cost function reported in Equa-

tion 130. The free parameters are $(\gamma_{hd}, \gamma_{hc}, \gamma_{rd}, \gamma_{rc}, \sigma, \delta, K')$. The frequency ω_p was fixed to $\omega_p = 2.448\,fs^{-1}$. The algorithm was run 15 times in order to improve the accuracy of the parameters. Each run was stopped after a fixed number of iterations (600). Further iterations were seen to not significantly improve the goodness of the fit (fit quality increases only by 0.001% by doubling the number of iterations). The fit parameters are indicated in Table 8.

Parameters	$\xi = 0.77$	$\xi = 0.83$	$\xi = 1.34$
$K'[s^{-1}]$	1.8 ± 0.1	3.6 ± 0.4	12 ± 1
$\sigma^{-1}[fs]$	24.1 ± 0.7		
$\delta[rad]$	1.37 ± 0.04		
γ_{hd}	0.47 ± 0.01	0.300 ± 0.001	0.124 ± 0.005
γ_{hc}	0.65 ± 0.02	0.66 ± 0.04	0.55 ± 0.02
γ_{rd}	0.64 ± 0.02	0.500 ± 0.001	0.36 ± 0.01
γ_{rc}	0.65 ± 0.02	0.66 ± 0.03	0.35 ± 0.01
$A_{\omega_p/2}$	$(9.7 \pm 0.7) \cdot 10^{-2}$	$(5.41 \pm 0.3) \cdot 10^{-2}$	$(1.14 \pm 0.04) \cdot 10^{-2}$
A_{ω_p}	(0.125 ± 0.002)	$(6.5 \pm 0.2) \cdot 10^{-2}$	$(8 \pm 1) \cdot 10^{-3}$
ξ	0.77 ± 0.05	0.83 ± 0.04	1.34 ± 0.05

Table 8: List of the coefficients minimizing the discrepancy between the data in Figure 73 and the curve generated by Equation 130.

The unbalancing parameters ξ reported in Figure 73 was estimated with the fit. The fit parameters found in this way were consistent with the controlled losses introduced in the experiment. Since the value of σ does not depend on ξ, we computed it only for $\xi = 1.34$ and then kept it fixed during the optimization of the cases $\xi = 0.77$ and $\xi = 0.83$. The minimum loss measured from the input port of the MZI to the two detectors is ~ -7 dB, which is comparable to the value found in the simulation (minimum lossess of ~ -9 dB).
Importantly, the experimental data could not be fit with a phase $\delta = \pi/2$, i.e. assuming a lossless beamsplitters. This can be seen at a glance in Figure 69 by noting the key qualitative differences between the theoretical pattern obtained for $\delta = \pi/2$ and the one used to fit the experimental data in Figure 73, $\delta = (0.87 \pm 0.04)\pi/2$.

To conclude, for all three values of the unbalancing parameter in Figure 73, a very good agreement between the experimental results and the theoretical model is observed.

7

MID INFRARED COINCIDENCE MEASUREMENTS AT ROOM TEMPERATURE

In this Chapter an experimental demonstration of single-photon counting in the mid infrared (MIR) spectral range is presented.
The MIR is emerging as an interesting field in photonics for several applications, such as gas analysis and medical diagnostics [197, 198]. Modern quantum cascade lasers have been recently developed as ideal coherent MIR excitation sources, but simple, low-noise, room-temperature detectors and imaging systems lag behind [85, 199]. In this framework, the Denmark Technical University (DTU) developed a high-efficiency up-conversion system for sensitive, two dimensional mid-infrared single-photon spectral imaging [200]. It will be shown in this Chapter, how this powerful device can be used to break the wall of single-photon detection in the MIR. In particular, room temperature coincidence measurements with non-degenerate twin photons at about 3.1 µm, produced by SPDC in a PPLN nonlinear crystal, were demonstrated. To the best of our knowledge, the obtained result is the first successful attempt towards the extension of quantum optics experiments into the MIR spectral region.
This work was done with the collaboration of Dr. Mattia Mancinelli and Mrs Sara Piccione. The Fotonik group in DTU designed and fabricated the up-converter module.

7.1 MIR DETECTION: AN OPEN ISSUE

What really makes MIR single-photon experiments elusive is the lack of high sensitivity detectors. MIR detectors face many limitations, mainly due to their inherent sensitivity to the *black body radiation* and to the *dark current* induced by the finite temperature of the detector itself [104].
We have already seen in Equation 31 that the probability to thermally promote an electron-hole pair in a semiconductor material follows a Boltzmann distribution. This will give rise to dark count events $\propto e^{-\frac{\Delta E}{k_B T}}$, where ΔE is the semiconductor energy band-gap, k_B is the Boltzmann constant and T is the temperature, see Figure 74(a).
Visible semiconductor-based detectors, where silicon is the most efficient material, show an intrinsically higher energy band-gap ($\Delta E \sim 1.17\,eV$) compared to NIR and MIR semiconductor detectors.
For instance, one can see that at room temperature the probability to thermally promote an electron-hole pair, is 15 orders of magnitude

higher in a MIR alloy compound such as HgCdTe, than in silicon [201].

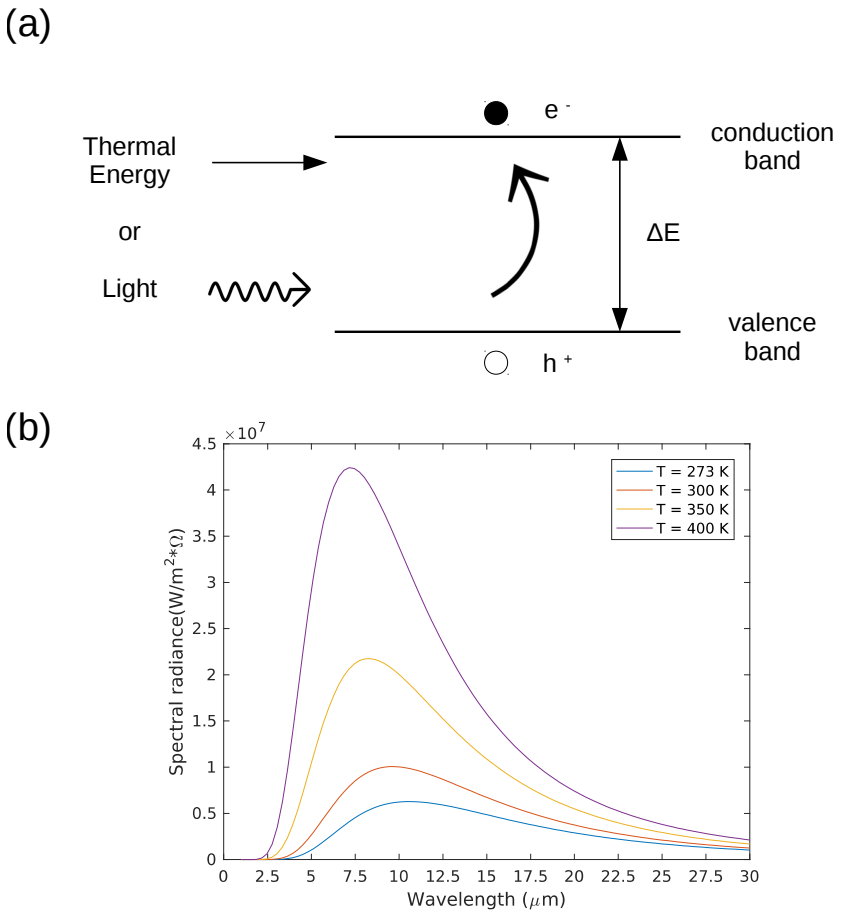

Figure 74: (a) Electron promotion from the valence band to the conduction band as a consequence of a thermal or optical excitation. (b) Spectral radiance of black-body radiation for different temperatures.

The other major source of noise in MIR detectors is associated with the detection process itself, due to the inherent sensitivity to black body radiation. If the thermal generation is reduced much below the background level, the performance of the device is typically determined by the background radiation. This regime is known as the Background Limited Infrared Photodetector, BLIP conditions [104].
Black body radiation is the thermal electromagnetic radiation which is absorbed and re-radiated by an ideal body in thermodynamic equilibrium with its environment. All objects are continually emitting radiation, which can in most cases be by black body radiation. The black

body radiation spectral radiance $B(\lambda, T)$ is described by the Planck's law, which is given by [202]:

$$B(\lambda, T) = \frac{2hc^2}{\lambda^5} \frac{1}{e^{\frac{hc}{\lambda k_B T}} - 1} \tag{149}$$

where h is the Planck constant. In Figure 74(b) black body spectral radiances at different temperatures are reported. The integral of Equation 149 over wavelength gives the total radiant flux, known as *Stefan-Boltzmann law*:

$$L = \frac{\sigma}{\pi} T^4 \tag{150}$$

where σ is the Stefan-Boltzmann constant. Therefore as it is possible to see from Figure 74(b), the higher is the temperature the higher is the radiant flux, with its strong $\propto T^4$ dependence. Moreover, the higher the temperature, the lower the wavelength at which the spectral radiance is peaked, with the following relation:

$$\lambda_{max} = b/T \tag{151}$$

where b is a proportionality constant, called Wien's displacement constant. Equation 151 is known as *Wien's law*.
Typically the spectral operational bandwidth of a semiconductor-based detector is not narrow, and the integrated black body radiation due to Equation 150-151 increases with T resulting in a non negligible source of noise. At the end of the day, this influences and limits the performance of the detector. In principle, the noise could be reduced by cooling the detector. MIR detectors are typically cooled down to the liquid nitrogen temperature (77 K), but still the detector signal-to-noise ratio remains poor compared to NIR and visible light detectors. Eventually, the small MIR semiconductor-based detector sensitivity will prevent any useful single-photon counting capability.
A possible solution could be the use of Superconducting Nanowire Single-photon Detectors (SNSPDs). SNSPDs exploit superconductivity for achieving single-photon detection capability. Their operation can be briefly summarized as follows [203]:

- the SNSPD is maintained well below its superconducting critical temperature, typically with a liquid helium cryostat at 4.2 K and direct current biased just below its critical current;
- in this regime, an infrared photon impinging on the SNSPD has enough energy to disrupt hundreds of Cooper pairs, thereby forming a so-called *hotspot*;
- the hotspot region acts as a resistive region, forcing the supercurrent to flow around it;

- the local current density on the sides increases beyond the critical current density, forming a resistive barrier across the width of the SNSPD;
- the sudden increase in resistance from zero to a finite value, generates a measurable output voltage pulse across the nanowire width, which eventually reveals the detection of a photon.

We already discussed in Table 7 that this kind of detector shows *system detection efficiency* at telecom wavelengths (around 1.55 µm) as high as 93%, with a system dark count rate of about 1 Hz [82].
The system detection efficiency is defined as:

$$\eta_{sde} = \eta_{de} \times \eta_{coupling} \tag{152}$$

where η_{de} is the intrinsic device detection efficiency and $\eta_{coupling}$ takes into account the coupling efficiency of the signal with the detector itself. Therefore, η_{sde} and η_{de} are only equal for perfect optical coupling, i.e. when $\eta_{coupling} = 1$. Basically, the system detection efficiency takes into account the overall probability that a single photon incident upon the detector is successfully detected. As a matter of fact, until now we have always implicitly considered detector system detection efficiency, as the ones reported in Figure 15(a) and Figure 54. We will see in Section 7.5 that it important for the sake of clarity to bear in mind the distinction between η_{sde} and η_{de}.

Now the question: are SNSPDs really able to detect MIR single-photons? Well, it has been shown recently that by reducing the nanowire width the sensitivity can be extended into the MIR. However, the system detection efficiency drops dramatically to a value of about 2%, while the dark count rate increases considerably [204]. This negative trend adds to the always present stringent requirement dealing with SNSPDs, that is that they are forced to inherently work at cryogenic temperatures. We will come back to SNSPDs at the end of the Chapter in Table 9, where we compare their performances with what we are going to present as a MIR up-conversion scheme for achieving single-photon counting. To the best of our knowledge, MIR single-photon counting in transition-edge sensors (TES) [205], which are also based on superconductivity, has never been reported in the literature.

7.1.1 *MIR up-conversion*

The basic idea for enabling single-photon detection in the MIR spectral range relies on the $\chi^{(2)}$ process called Sum Frequency Generation (SFG), which is sketched in Figure 75. SFG is a three-wave mixing process which can be described as the annihilation of two input photons at angular frequencies ω_p and ω_s, which generates an idler photon at frequency $\omega_i = \omega_p + \omega_s$. As for any nonlinear wave-mixing phe-

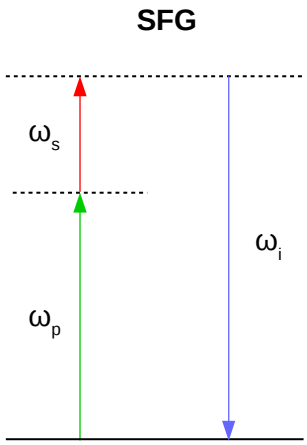

Figure 75: Sketch of the energy diagram for the $\chi^{(2)}$ process Sum Frequency Generation (SFG). The frequency of the pump photon is denoted as ω_p and the signal photon by ω_s. The generated photon is called idler and it is indicated by ω_i.

nomenon, this can only occur if the energy and momentum are conserved in the process. In what follows we will consider the case of three collinear plane waves propagating in a periodically poled nonlinear material (PPLN) along the z-axis, such that $\mathbf{k} = k\hat{z}$. In this situation the energy and momentum relation for the SFG process are given by [18]:

$$\omega_i = \omega_p + \omega_s \tag{153}$$

$$2\pi\frac{n(\lambda_p, T)}{\lambda_p} = 2\pi\left[\frac{n(\lambda_s, T)}{\lambda_s} + \frac{n(\lambda_i, T)}{\lambda_i} + \frac{1}{\Lambda}\right] \tag{154}$$

where $n(\lambda, T)$ is the refractive index of $LiNbO_3$ given by the Sellmeier relation, reported in Equation 20[100]. Λ is the poling period, which we have seen in Equation 61 that counter-acts the dispersion between the interacting wavelengths: Equation 154 is satisfied thanks to the last term that is inversely proportional to Λ.

The process in which we are interested in is the up-conversion of MIR single-photons into the visible, where efficient and low noise rooom temperature silicon-based SPAD can detect the up-converted photons. If we consider for example $\lambda_s = 3\,\mu m$ and $\lambda_p = 1.064\,\mu m$, from Equation 153 one immediately realizes that the up-converted photon wavelength will be $\lambda_i = [1/\lambda_p + 1/\lambda_s]^{-1} \sim 0.785\,\mu m$, which falls within the detection bandwidth of commercially available efficient silicon SPADs [206]. Thus, instead of performing a direct single-photon detection in the MIR, we approached the problem differently

by using the concept of spectral translation.
We will see that this approach is feasible thanks to the use of an efficient up-converter module, which is used in combination with a silicon SPAD in the detection.

7.2 THE UP-CONVERTER MODULE

The concept of up-conversion is not new and it was already investigated in the '60 [207], but what has limited the applicability of the process was the extremely low experienced quantum efficiency. Some attempts of frequency up-conversion schemes have been reported so far, which however exhibited limited SFG efficiencies, of the order of $\sim 10^{-5}$ [208].
The scenario changed when a group from the Denmark Technical University (DTU) in 2012 demonstrated that the efficiency of the up-conversion process can be dramatically enhanced, by placing the non-linear crystal inside a resonant cavity [200]. A measured conversion quantum efficiency (QE) of 20% was demonstrated, due to the high circulating power within the cavity resulting from the low-loss cavity design. This is at least three orders of magnitude higher than the one reported in similar up-conversion schemes [208]. A sketch of the up-converter module is reported in Figure 76.
Here, the QE of the SFG process is boosted at the maximum efficiency by $\sim 100\,W$ of continuous-wave intracavity circulating pump power. The QE scales linearly with the mixing power, so the high circulating power leads to an increase in QE by a factor of ~ 100 over a corresponding single-pass configuration [208].
Let us give a closer look to the up-converter module reported in Figure 76. The module comprises of two distinct parts.
First, the up-conversion crystal is placed inside a high-finesse 1.064 µm laser cavity in order to enhance the up-conversion probability (QE). The module consists of a $Nd : YVO_4$ laser cavity, optically pumped by a $4\,W$ Broad Area diode Laser (BAL) at 880 nm, designed to generate an intense, continuous, TEM_{00}, intra-cavity laser beam. The laser cavity optical pumping power can be adjusted as a function of the supplied electrical current in the range [0;4] A. The optimal $4\,W$ pump power is obtained at $3.6\,A$. Higher pump powers introduce thermal instabilities within the cavity, which in the end degrade the up-converter module performances. The laser cavity is a folded Fabry-Perot cavity, where the initial mirror is indicated as M1, while the end mirror is labelled by M7 (see Figure 76). All mirrors are covered with a high reflection coating for 1064 nm, in order to reduce the cavity losses. Mirror M7 is constructed on a substrate of undoped YAG substrate, which, together with anti-reflective coating, allows high transparency in the range [2;4] µm. M4 and M5 act as a filtering stage for the 880 nm light and are placed in a separated black

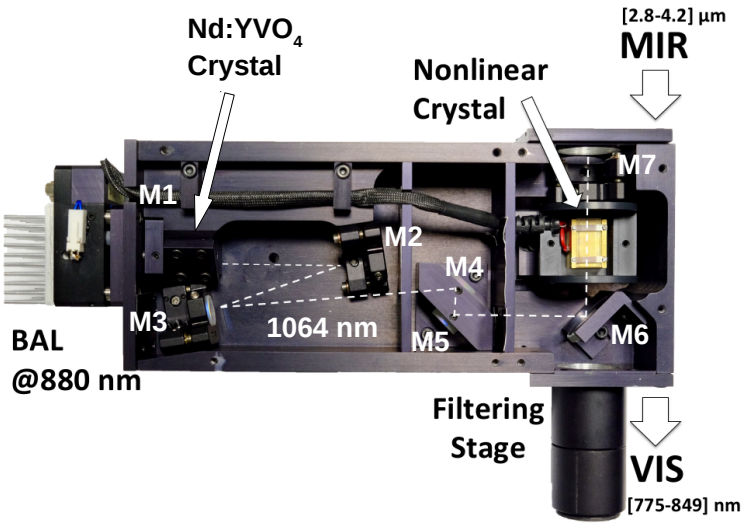

Figure 76: Photograph of the up-converter module. The description of the different parts is reported in the main text.

chamber. Also M7 along with M6, through which the up-converted radiation exits from the cavity, are located in a separate compartment to avoid the presence of scattered radiation from possible residual 880 nm BAL pump power. All the mirrors are plane, except M3 which is concave (radius of curvature 200 mm) and is the one which determines the appropriate beam waist within the PPLN nonlinear crystal. Daily alignment is performed on cavity mirrors M3 and M7, which are easily accessible and can be tuned with appropriate screws from outside.

Second, there is the the up-conversion crystal, which is a 20 mm (5 mm) long PPLN fabricated for SFG generation between a 1.064 µm pump laser beam and incident radiation in the range [2.8;4.2] µm.

The wavelength upper limit is set by the PPLN, which is transparent up to 5 µm [100]. The lower spectral limit is set by the available poling periods in our nonlinear crystal. The PPLN is from Covesion Ltd. [31] and has five poling periods ranging from 21 to 23 µm in steps of 0.5 µm. Each poling channel has a $1 \times 1\,\mathrm{mm}^2$ aperture. In order to reduce Fresnel reflection losses, the PPLN crystal is AR-coated for 1.064 µm and 3 µm radiation, respectively. As for the NIR PPLN discussed in Chapter 2, by using a temperature controller (TEC), fine tuning of the phase-match condition can be achieved.

7.3 UP-CONVERTER MODULE EXPERIMENTAL CHARACTERIZATION

In this Section the experimental characterization of the module is presented. Actually the experimental characterization was done for two up-converter modules. Indeed, we will see in Section 7.5 that to perform coincidence measurement on MIR photon pairs we need two separate up-converter modules. Section 7.3.1 reports the experimental characterization of the laser cavity, while Section 7.3.2 considers the module spectral response characterization.

7.3.1 *Up-converter module laser cavity*

The first sets of measurements were performed in order to test the behaviour of the laser cavity inside the module. In particular, for monitoring the intra-cavity power and the beam waist, which are the two main parameters that characterize the functionality of the conversion system. The characterization was performed on both the available modules, using two different PPLN crystals, whose lengths are $L_1 = 20\,mm$ and $L_2 = 5\,mm$. Figure 77 shows the fluctuations of the intra-cavity power as a function of time.
The measurements were taken by setting the current of the pump diode equal to 3.2 A. From Figure 77 we see that the intra-cavity power actually fluctuates by about $\pm 0.02\%$ compared to its average value. We repeated the same measurement without the PPLN crsytal placed within the laser cavity path, which gave a more stable average power in time. A possible explanation of these observations lies in the temperature dependence of the $LiNbO_3$ refractive index, which slightly changes in time due to a weak absorption of the strong pump field which circulates within the module. The PPLN temperature variations causes a modulation in the cavity optical path, which eventually lets the pump power fluctuates in time. Indeed, note that the temperature of the nonlinear crystal is not really fixed, but it is rather controlled with a PID (Proportional Integral Derivative) control loop feedback mechanism within $\pm 0.1\,^{\circ}C$ accuracy in the range [30;200] $^{\circ}C$.
We have already seen in Equation 25, that the efficiency of a nonlinear process is proportional to the intensity of the interacting waves. Therefore, in order to fully characterize the up-conversion efficiency of our modules, it is essential to measure the pump beam waist within the PPLN crystal. It is not actually possible to directly measure the pump beam waist in the middle of the PPLN crystal, therefore a 4-f system has been exploited. The 4-f lens system utilizes two lenses of equal focal length, in our case f = 75 mm, positioned in such a way that the distance between the object and the image is equal to $4 \times f$. By using standard ray optics, it can be shown that the object plane is imaged at a distance $4 \times f$, therefore allowing direct access to the field inside the

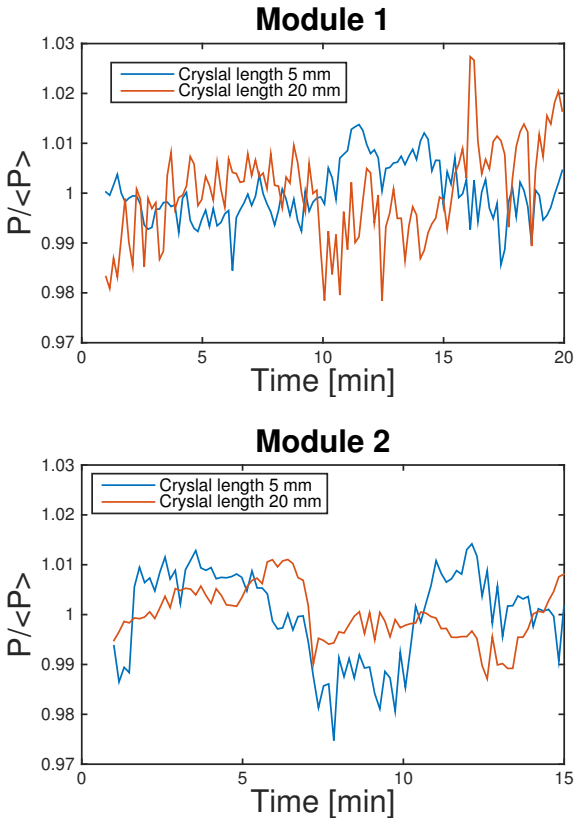

Figure 77: Fluctuations of the module intra-cavity power normalized with respect to the mean value, for both the modules, and for both the two crystals. The injected current was set equal to 3.2 A, which corresponds to a cavity power of P = 41 W.

crystal [22]. A beam profiler (Thorlabs BP209-IR/M - Dual Scanning Slit Beam Profiler) was then placed in the image plane to measure the pump waist. The obtained results are reported in Figure 78.
The dependence of the beam waist on the cavity power can be again attributed to the temperature variations caused by the laser itself. The temperature fluctuations cause changes in the refractive index of the gain medium, which can act as a thermal lens for the beam, causing some variations of the beam dimension. The average different beam waist dimension between the two modules likely arises from unavoidable fabrication differences between the two.
From now on for the sake of avoiding redundancy, we will report on the characterization of a single module.
In Figure 79, the output spectrum from the up-converter module is reported. It was collected at the output of mirror M6 (see Figure 76). The measurement was taken for the poling period equal to 21.5 µm at 100 °C. In Figure 79 the different curves refer to different values of the injected current intensity in the diode laser, which pumps the up-converter module.

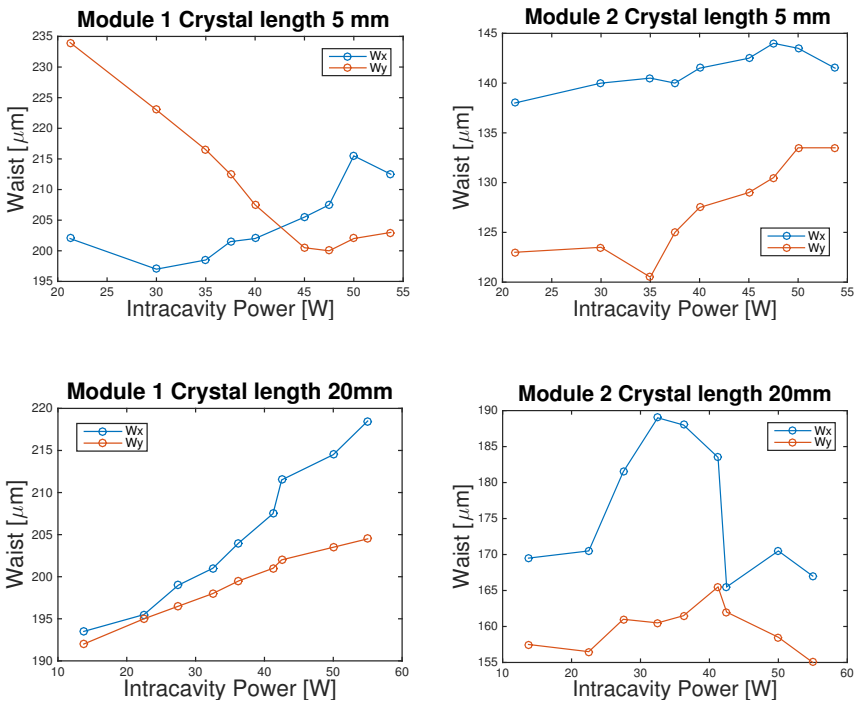

Figure 78: Beam Waist along the x and y directions as a function of the cavity power for the 20 mm and 5 mm crystal and both the two modules.

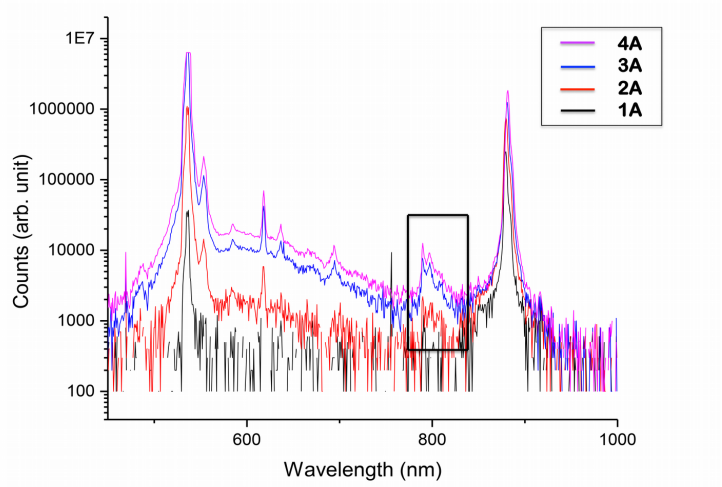

Figure 79: Spectra at the output of the up-converter module for different values of the injected currents to the Broad Area diode Laser (BAL). The measure was taken for a poling period $\Lambda = 21.5\,\mu$m, at a temperature of 100 °C. The black box highlights the spectral region where the black body up-conversion is likely to occur. The measure was taken with only a filter to cut off the pump at 1064 nm placed in front of a visible monochromator.

The higher the injected current, the higher the intensity of the 1064 nm laser light that circulates within the module and, so the higher the conversion efficiency. But, at the same time, the higher the current, the higher also the noise that comes from the up-converted black body radiation from the environment, as is highlighted by the black box in Figure 79. A trade-off was found, in term of signal to noise ratio, at a current value of 3.6 A. The measurements were performed using a filter in front of a visible monochromator (Ocean Optics USB2000) to cut off the pump at 1064 nm. In Figure 79 it is clearly possible to see both the contributions of the residual of the diode laser pump at 880 nm and of the result of the Second Harmonic Generation in the PPLN crystal of the 1064 nm pump, at 532 nm. In the region, which goes from 600 nm to 700 nm, the spectral lines that appear are due to stray-light from the room illumination.
Another interesting part of the spectrum lies in the range which goes from 790 nm to 810 nm, which in Figure 79 is highlighted by a rectangle. Here, the appearance of this spectral band is associated to the up-conversion of the black body radiation emitted by the environment. The band is wider than expected, and the reason lies in the fact that the black body radiation is isotropically emitted at every angle and the phase matching is angle dependent [202].

7.3.2 *Up-converter phase matching property*

Here the spectral characterization of the up-converter module is presented. Since we were not equipped with a tunable MIR laser source, we decided to approach the problem from the other end. We investigated the phase matching capabilities of the up-converter module by exploiting DFG from a tunable visible laser source which, after the interaction with the strong laser field at 1064 nm, generates MIR light around 3 µm. DFG can be seen as the inverse process of SFG and it is characterized by the same phase matching relation reported in Equation 154. A scheme of the experimental set-up used is reported in Figure 80.

The light source is a a Ti:sapphire (Tsunami) visible laser, whose wavelength can be tuned from 700 nm to 1000 nm. It can reach an average maximum power of 1 *W* and is equipped with an acousto-optic modulator that can switch the laser operation from a quasi-CW (not mode locked) to a mode locked regime. During the experiment, the laser was set to work in the quasi-CW mode. The laser source passes through a variable attenuation stage, used to tune the power. After it, light is 99:1 split. The 1% is sent to a monochromator, which monitors the beam wavelength. The rest is directed to a converging lens of focal lenght 18.5 cm, which is needed to reduce the beam waist and make it comparable with the one of the up-conversion module.

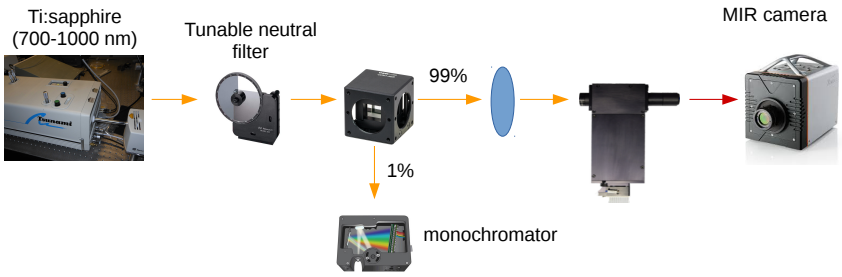

Figure 80: Sketch of the optical set-up used for the spectral characterization of the up-converter module.

Note that, in order to achieve efficient nonlinear conversion, it is necessary that the two interacting fields spatially overlap within the PPLN crystal. The waist of the beam before passing the lens was measured with the beam profiler. This was found to be equal to $w_x = 595\,\mu m$ and $w_y = 525\,\mu m$. After the lens, the Ti:sapphire beam waist in the center of the PPLN crystal was measured to be $w_x = 125\,\mu m$ and $w_y = 115\,\mu m$, therefore optimal for a good spatial overlap with the pump beam waist (see Figure 78).
Both the pump and the Ti:sapphire laser were filtered out by a germanium window, which allows only the generated MIR photon to exit the up-converter module. The alignment of the up-converter module with respect to the external incident beam is controlled with a custom 6 axis positioning system, three linear axes and three rotational axes. Since we do not have at our disposal a MIR Optical Spectrum Analyser, we used a MIR camera (Onca-MWIR-InSb) as a detector. The camera is based on a 320x256 array of InSb pixels, which is cooled by a Stirling cycle refrigerator. The camera covers the spectral band from $1\,\mu m$ to $5.5\,\mu m$ [209]. We actually used the camera as a large area detector: the pixel intensity was characterized as a function of the incident reference $1.55\,\mu m$ power. A linear relation was found between the integrated image frame and the incident power, which was then normalized for the InSb responsivity as a function of the wavelength. With a Labview program, specifically realized for the the measurement, it was possible to collect the frames taken from the ONCA camera as a function of the wavelength, monitored by the Ocean Optics 2000+ spectrometer, for different values of temperature. We aligned the incoming Ti:sapphire laser collinear with the intracavity laser field. The measurement was done for all the PPLN poling periods, which ranges from 21 to $23\,\mu m$ in steps of $0.5\,\mu m$, both for the $5\,mm$ and $20\,mm$ crystal long. The oven which heats the PPLN crystal can cover in principle the temperature range of [20;200]°C. However, the feasible starting temperature was found to be about T = 60 °C. This is due to the fact that the crystal, as a consequence of a little

but non negligible absorption, warms up, and the oven is not able to maintain the crystal temperature at values close to room temperature. The Ti:sapphire wavelength was tuned in the range [770;850] nm at a fixed step of 0.1 nm, which covers the spectral region in which we expect to find the phase-matched MIR radiation. Figure 81(a) shows the obtained results as a function of temperature and wavelength, for the 5 mm long PPLN crystal. As it is possible to see from Figure 81(a), the phase-matched wavelengths of the modules can be effectively tuned as a function of the PPLN crystal temperature. With the available poling periods it is actually possible to phase match MIR wavelengths in the range [2.9;4.2] µm.

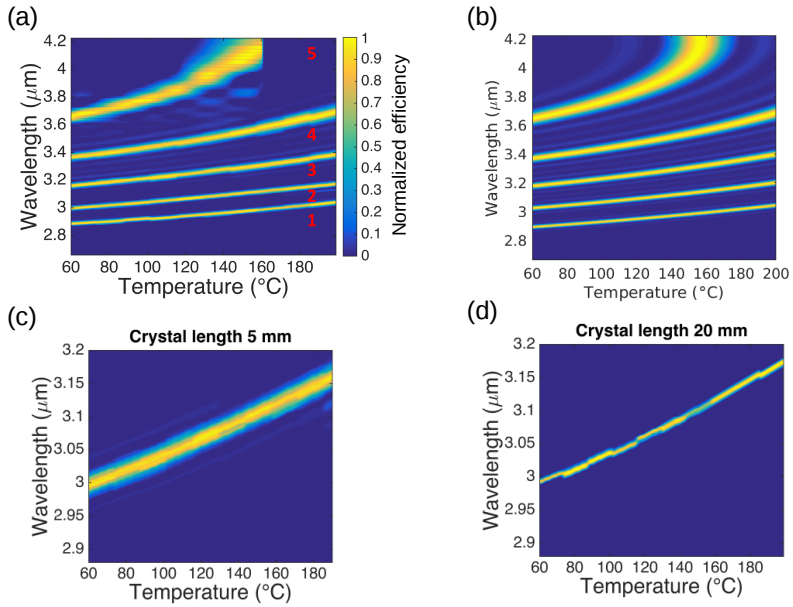

Figure 81: (a) Experimental normalized DFG efficiency as a function of the converted wavelength and the crystal temperature for the 5 mm PPLN long crystal. The curves were collected for all the five different poling periods which are: 21 µm (1), 21.5 µm (2), 22 µm (3), 22.5 µm (4), 23 µm (5). (b) Simulated DFG efficiency as a function of the crystal temperature and the poling period in (a) for the 5 mm PPLN long crystal. The simulation assumes collinear DFG between 2 monochromatic wavelengths, one at 1064 nm and the other one in the range [770;850] nm. (c-d) Comparison of the experimental bandwidth for the 5 mm long and 20 mm long crystals for the 21.5 µm.

Figure 81(b) simulates, with the same experimental parameters, the characterization reported in Figure 81(a). The simulation assumes collinear DFG between 2 monochromatic wavelengths, one at 1064 nm and the other one in the range [770;850]nm.
We see that the theoretical simulation matches the experimental re-

sult very well. In particular, both show the general trend that longer phase matched wavelengths exhibit broader conversion bandwidths, as expected. Even though the general trend of the experimental phase matching curves is well predicted by the theory, with a fitting procedure we found a slight mismatch from the nominal poling period.
For example, in the case of the nominal 21.5 µm poling period, we experimentally found that the poling period which fits the experimental data is equal to $(21.41 \pm 0.01)\mu m$. This corresponds to a difference of about 100 nm with respect to the nominal value provided by the company which fabricated the PPLN crystals [31]. However, this mismatch implies an offset of only few nm in the phase-matched wavelength with respect to the nominal expected behaviour, therefore in the following, for simplicity, we will continue to consider the nominal poling period values.
In Figure 81(c-d) the spectral response of the up-converter module for the 21.5 µm poling period for the two different crystal lengths are reported for comparison. In Chapter 2 the generated intensity for DFG was explicitly derived, which resulted to be:

$$I_i = \frac{2 d_{eff} \omega_i^2 I_p I_s}{n(\omega_p) n(\omega_s) n(\omega_i) \epsilon_0 c_0^3} L^2 \, \mathrm{sinc}^2\left(\frac{\Delta k L}{2}\right) \tag{155}$$

It can be shown with a Taylor expansion of Equation 155 that, at the lowest order, the phase matching bandwidth is proportional to $1/L$. This is also evident from the experimental measurements reported in Figure 81(c-d). The measured phase-matching bandwidth, calculated as the FWHM, is found to be (21.9 ± 0.2) nm for the smaller crystal, while it is equal to (7.7 ± 0.2)nm for the longer one. The experimental result matches with the theoretical $1/L$ expected dependence, which predicts a factor 4 difference between the bandwidths, which is almost equal to what was found also experimentally.

Let us discuss now the module *conversion efficiency* characterization of the module. We proceeded as follows: first we monitored the generated MIR radiation as a function of the incident Ti:sapphire laser, keeping the intra-cavity power of the module fixed. Then, we fixed the Ti:sapphire incident power and we monitored the generation efficiency as a function of the intra-cavity power, determined by the injected BAL current. Figure 82(a-b) shows the converted power as a function of the incident power. The measurement was done both for the 20 mm and for the 5 mm long crystal. The operation current of the module was set equal to the optimal value of 3.6 A, which corresponds to an intra-cavity power of approximately 62 *W* using the 20 mm crystal long and of 68 *W* for the smallest crystal.
The beam waists, along the x and y direction were equal to ($w_x = 225\,\mu m$, $w_y = 196\,\mu m$), for L = 20 mm, and ($w_x = 210\,\mu m$, $w_y = 200\,\mu m$) for L = 5 mm. The poling period was 21 µm, while the crys-

tal temperature was set to T = 100 °C, in order to phase-match the visible wavelength of $\lambda = 780\,nm$ (see Figure 81).

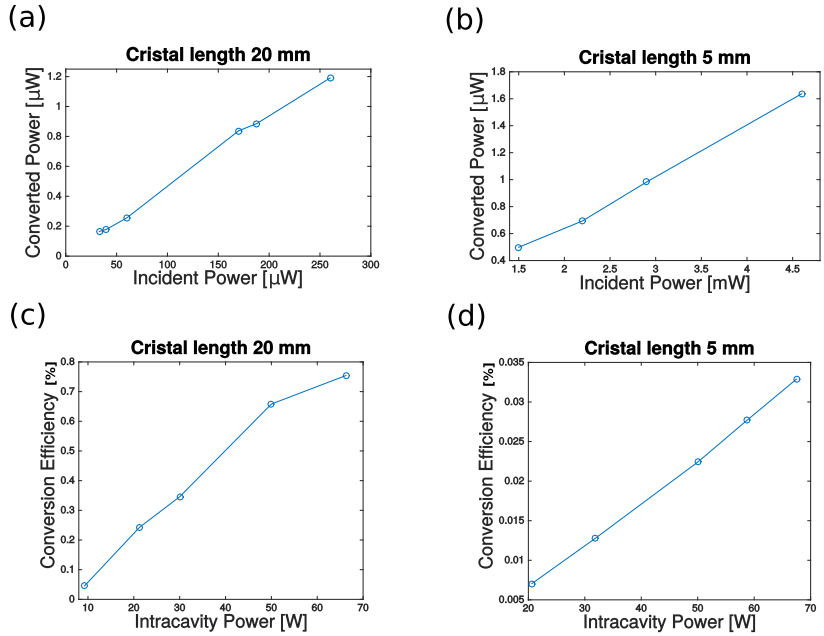

Figure 82: (a) MIR generated power through DFG as a function of the incident Ti:sapphire power at the PPLN facet, for the 20 mm long crystal. The diode current was set to 3.6 A. (b) The same of (a) for the 5 mm long crystal. (c) Conversion efficiency as a function of the intra-cavity power for the 20 mm long crystal. The incident power of the Ti:sapphire laser was 100 μW. (d) Conversion efficiency as a function of the intra-cavity power for the 5 mm long crystal. The incident power of the Ti:sapphire laser was 6.4 mW. The conversion efficiency is referred in percentage.

The generated MIR power scales linearly with the Ti:sapphire laser power, as expected from Equation 155. In particular the conversion efficiency was found to be equal to $\eta_{DFG}^{20mm} = (0.65 \pm 0.02)\%$ for the longer crystal, and $\eta_{DFG}^{5mm} = (0.033 \pm 0.002)\%$ for the shorter crystal. The efficiency was estimated as the mean value of all the collected data, while the associated error is the standard deviation. We see from Equation 155 that the generated intensity scales as L^2, where L is the crystal length. In our case, the expected efficiency is reduced by a factor 16 for the shorter crystal, which agrees with what was found experimentally.
Now, this is for the DFG nonlinear process. What about the efficiency of SFG, which is actually the process which we are interested in?
By developing an analogous calculus for SFG with respect to the one done for DFG in Chapter 2, it is possible to derive a relation which links the efficiency of the two processes as [18]:

$$\eta_{SFG} = \left[\frac{\lambda_{MIR}}{\lambda_{VIS}}\right]^2 \eta_{DFG} \tag{156}$$

If we consider the particular case where $\lambda_{MIR} = 3.1\,\mu m$ and $\lambda_{VIS} = 0.792\,\mu m$, it is possible to derive $\eta_{SFG} = (10.0 \pm 0.3)\%$, for the for L = 20 mm long crystal. We will see in Section 7.4, that the chosen λ_{MIR} actually corresponds to the degenerate SPDC generated MIR wavelength.

Another set of measurements was performed to experimentally confirm the linear dependence of the generated power with respect to the power of the interacting fields, see Equation 155. The data were collected as a function of the operational current of the module, i.e. the intra-cavity power, and are shown in Figure 82(c-d). In particular, in Figure 82(c) the conversion efficiency as a function of the intra-cavity power for the 20 mm long crystal is reported. The incident power of the Ti:sapphire laser was 100 μW. Figure 82(d) reports the conversion efficiency as a function of the intra-cavity power for the 5 mm long crystal, where the Ti:sapphire laser power was set to 6.4 mW.

As it is observed in Figure 82(c-d) for the shorter crystal, the variation of the injection current does not influence the stability of the laser cavity, while this is not really the case for the longer crystal. For this set of measurements the generated MIR power was easily measured with the help of a thermopile, which was placed at the output of the module, in correspondence to the mirror M7 (see Figure 76).

The Ti:sapphire power was set to an average value that led to a sufficiently high signal-to-noise ratio in the MIR detection with the power meter. Remember that mirror M7 is transparent only in the range [2;4] µm, which allows only the converted power to be measured. The reasons for the small deviations from the linearity in Figure 82 are instabilities within the module laser cavity, which can lead to fluctuations of the intra-cavity power and the beam waist during the measurement.

A further characterization of the module was performed in order to measure the angle dependence of the phase matching condition. Up to now we have always considered collinear interactions, but the momentum conservation is a vectorial relation. Let us consider the geometrical scheme reported in Figure 83, which shows a top view of the system under analysis.

We consider the incoming radiation from the Ti:sapphire laser to form an angle θ with respect to the normal of the crystal plane. Note that the interacting waves are supposed to be parallel in the direction orthogonal to the drawing reported in Figure 83. The phase matching relation reported in Equation 154 for the collinear case, is generalized for the non-collinear case as follows:

$$\begin{cases} \frac{n(\lambda_p)}{\lambda_p} \sin\theta_c = \frac{n(\lambda_i)}{\lambda_i} \sin\phi \\ \frac{n(\lambda_p)}{\lambda_p} \cos\theta_c = \frac{n(\lambda_s)}{\lambda_s} + \frac{n(\lambda_i)}{\lambda_i} \cos\phi + \frac{1}{\Lambda} \end{cases} \tag{157}$$

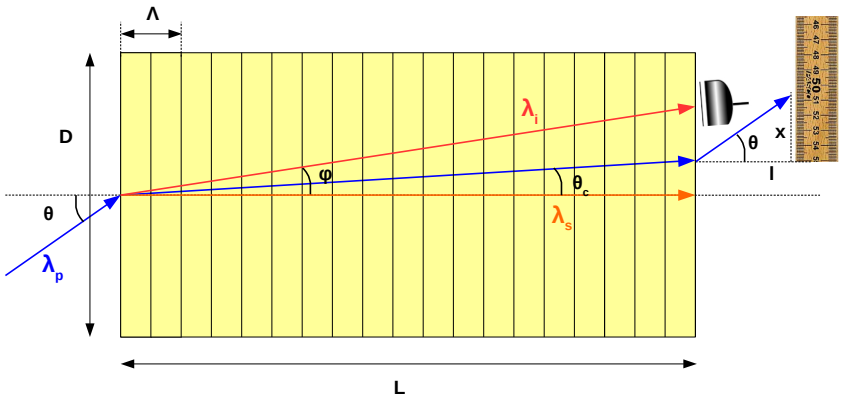

Figure 83: Sketch of the geometry under consideration for the non-collinear phase-matching study.

where we are still considering DFG. Here, λ_p is the Ti:sapphire wavelength, $\lambda_s = 1064\,nm$ is the intra-cavity field wavelength and λ_i is the MIR generated wavelength. The angle inside the crystal θ_c was evaluated through Snell's law from the external angle θ: $\sin\theta = n(\lambda_p, T)\sin\theta_c$. The angle ϕ is the angle between the generated MIR light and the normal to the crystal, i.e. with respect the intra-cavity beam.

The spectrum of the down-converted light was collected, for different values of θ as reported in Figure 84(a). The measurement was done by varying the Ti:sapphire wavelength in the range [780;815] nm, for the nominal poling period $\Lambda = 21.5\,\mu m$, at a fixed crystal temperature T = 130 °C for the 5 mm long crystal. From the measurements it is evident that by increasing θ, the phase-matched wavelength red-shifts and the bandwidth increases. For being up-converted, it is necessary that the radiation which enters in module, overlaps with the Gaussian beam inside the nonlinear crystal. This is the reason why there exists a maximum acceptance angle, beyond which light cannot be efficiently up-converted.

With reference to Figure 83, the maximum angle within the PPLN crystal θ_c^{max} can be determined as:

$$\theta_c^{max} = \arctan\left[\frac{w}{L}\right] \tag{158}$$

where w is the intra-cavity beam waist, experimentally characterized in Figure 78. In the case under analysis L = 5 mm and if we consider in a first approximation a constant average beam waist of <w> = 150 µm, the maximum internal angle is $\theta_c^{max} = 1.72°$. Therefore, the maximum acceptance angle can be estimated from the Snell law to be $\theta \sim 3.8°$, which indicates a conservative upper limit in the considered approximation limit. This is is actually greater than the experi-

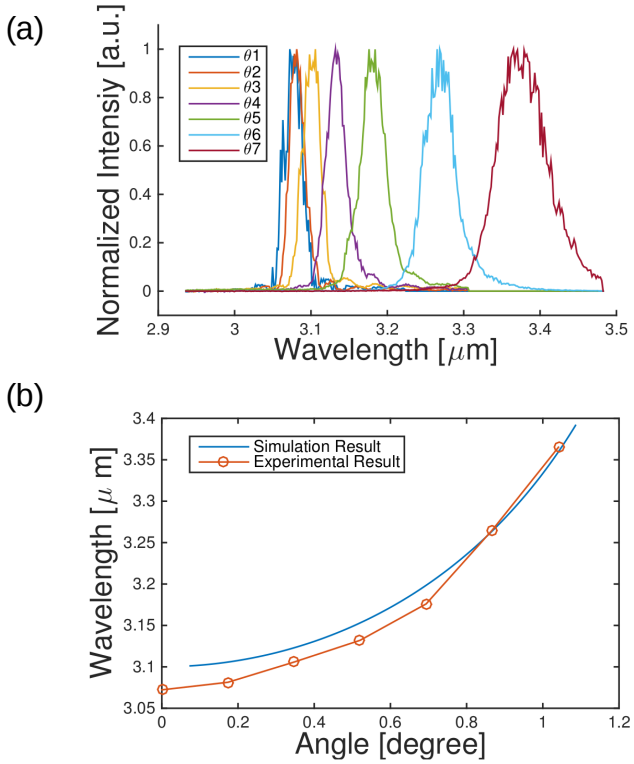

Figure 84: (a) Normalized spectra collected as a function of the relative angle θ between the incident Ti:sapphire laser and the intra-cavity beam. $\theta_1 = 0°$, $\theta_2 = 0.17°$, $\theta_3 = 0.35°$, $\theta_4 = 0.52°$, $\theta_5 = 0.69°$, $\theta_6 = 0.87°$, $\theta_7 = 1.04°$. (b) Phase-matched wavelength as a function of the angle θ. The red dots represent the experimental data, while the blue curve refers to the expected behaviour from Equation 157.

mentally measured angles to which the experimental curves in Figure 84(a) refer. Experimentally the angle was varied by a rotational stage, mounted in the mechanical support, which holds the conversion module. With respect to Figure 83, the θ angle was evaluated from the relation $\theta = \text{atan}(x/l)$, where l defines the optical lever from the output of the crystal. In the experiment we chose $l = 75\,\text{cm}$, which is long enough to let us resolve the different angles.

Figure 84(b) shows the phase-matched wavelength, experimentally measured in Figure 84(a), as a function of the relative angle between the intra-cavity field and the incoming visible light, compared with the expected behaviour from Equation 157. The experimental result agrees with the theoretical expectation.

Thus, another degree of freedom to tune the phase-matched wavelength of an incoming MIR radiation (in the case of SFG) can be the variation of the relative angle between the light and the up-converter module. However, it is not easy to guarantee the optimal overlap between the Gaussian profiles of both the intra-cavity field and the one

of the incoming beam. It is actually experimentally easier to tune the phase matched wavelength with the PPLN crystal temperature in a collinear geometry, as it is shown in Figure 81(a).
For this reason, in the experimental measurements reported in Section 7.5, the temperature phase-matching tuning will be only exploited in a collinear three-wave mixing geometry.

7.4 MID INFRARED COINCIDENCE MEASUREMENT SET-UP

In this Section the experimental set-up used to detect MIR photon pairs is presented. This is sketched in Figure 85(a).
A fibre-coupled, continuous-wave laser with tuning range [1.52;1.565] μm and maximum output power of 70 mW (PPCL300 Pure Photonics) is amplified using an erbium-doped fibre amplifier with maximum output power of 800 mW. We controlled the polarization of the light from the laser with a free-space polarization controller stage composed of two quarter-wave plates and one half-wave plate. The pump beam at 1.55 μm is focused by L1 into a PPLN crystal pumping the SPDC process. Lens L1 has a focal length of 150 mm and focuses the beam, whose waist before L1 is 2.25 mm, to a beam waist of 35 μm in the PPLN crystal. We found that the optimum condition in term of SPDC generation efficiency was achieved when the Rayleigh range is approximatively half the length of the crystal [31].
Note that, the overall efficiency in collecting the generated MIR photons is strictly determined by the dimension of the beam waist. Hence, the various focal lengths and the relative distances between the lenses and the nonlinear crystals have to be carefully selected. For this reason a numerical simulation, based on the evaluation of the beam along the optical path with standard Gaussian optics, was performed in order to achieve the optimum condition. This is reported in Figure 85(b). The colours refer to: pump beam at 1.55 μm (black), SPDC-generated beam at around 3.1 μm (red), up-converted beam 792 nm (blue). This is particularly important for the up-conversion stage. Indeed, let us remember that the incoming MIR beam waist should be comparable to the beam waist of the module laser to be efficiently up-converted.

The SPDC PPLN crystal contains 16 different poled regions each with a transverse cross section of $500 \times 500\ \mu m^2$. The nominal poling period used is 34.48 μm. The fine-tuning of the phase-matching condition is performed by changing the crystal temperature. The degenerate SPDC emission at 3.1 μm was experimentally phase-matched when the SPDC PPLN was set to $T_{deg}^{exp} = 135\,^{\circ}C$, which, compared to the nominal one $T_{deg}^{sim} = 187\,^{\circ}C$, leads to a real poling period of $\Lambda_{MIR}^{real} = 34.68\,\mu m$. The oven housing with the nonlinear crystal can be translated, allowing for selection of the required poling period. After the SPDC PPLN crystal, the generated MIR photon pairs and the

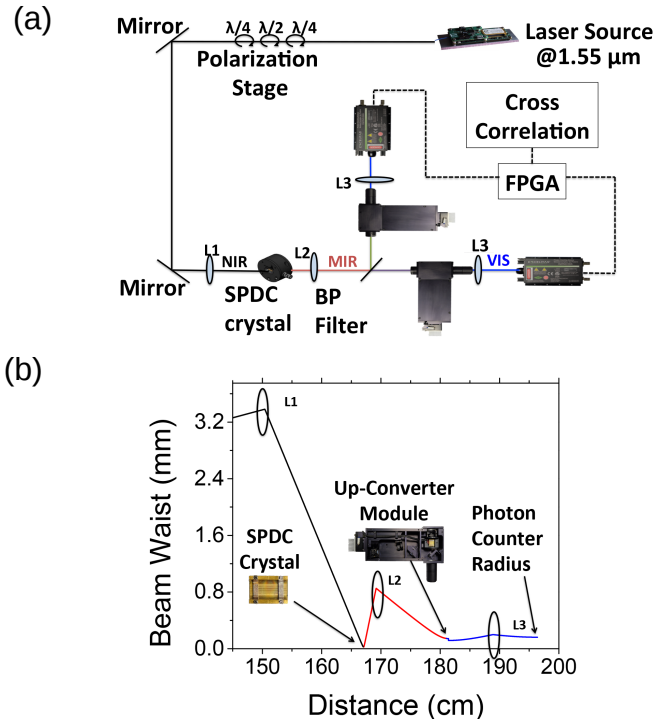

Figure 85: (a) Experimental set-up used for coincidence measurements on SPDC generated MIR photon pairs. (b) Simulation of the beam waist as a function of the distance along the optical axis of the system from the laser to the silicon-based SPAD detector. The colours refer to: pump beam at 1.55 µm (black), SPDC-generated beam at about 3.1 µm (red), up-converted beam at about 792 nm (blue).

residual 1.55 µm pump are collimated by a CaF_2 converging lens L2, whose focal length is 18 mm.

In the case of the coincidence measurement, reported in Figure 89, the generated photon pairs are non-degenerate and they can be spectrally separated thanks to an optical bandpass filter centred at 3 µm, with a measured bandwidth of 500 nm. The idler wavelength at 3.343 µm is reflected and sent to one up-conversion detection module, while the signal photon at 2.89 µm is transmitted through the bandpass filter to the second up-conversion detection module. Residual pump photons at 1.55 µm are eliminated by Germanium windows, placed at the entrance of each of the up-conversion modules. After the up-conversion process, the generated visible light is collimated and focused to match the small sensitive area of the silicon-based SPAD (SPCM-AQRH Excelitas) by lens L3. L3 has a focal length of 75 mm and it is placed at a distance of 73.8 mm from the photon counter. The up-converted beam waist is about 300 µm. The SPCM-AQRH is based on a silicon avalanche photodiode with a circular active area. It achieves a peak

photon detection efficiency of about 65% at 792 nm over a 180 µm diameter with unmatched uniformity over the full active area.
The visible SPAD detection efficiency is reported in Figure 86(a). The detector works in free running mode with a dead time of 20 ns and a linear dynamic range of 36 dB. The typical maximum count rate before 100% saturation is 40 MHz. In the experiment the SPAD is operated at a maximum count rate $\sim$ 100 kHz $\ll$ 40 MHz, where the detector responds in a linear fashion and we do not have to really worry about nonlinear correction. We saw in Figure 54, instead, that this is not often the case for the InGaAs SPAD modules.
Better visible SPADs are available on the market if improved performances are needed [32]. The output TTL voltage of the Si SPADs is fed into a Field Programmable Gate Array (FPGA) digital correlator that provides the coincidence rate. The FPGA is programmed to make a real-time cross-correlation between the TTL signals of the two Si SPADs. The coincidence window is 1.33 ns.

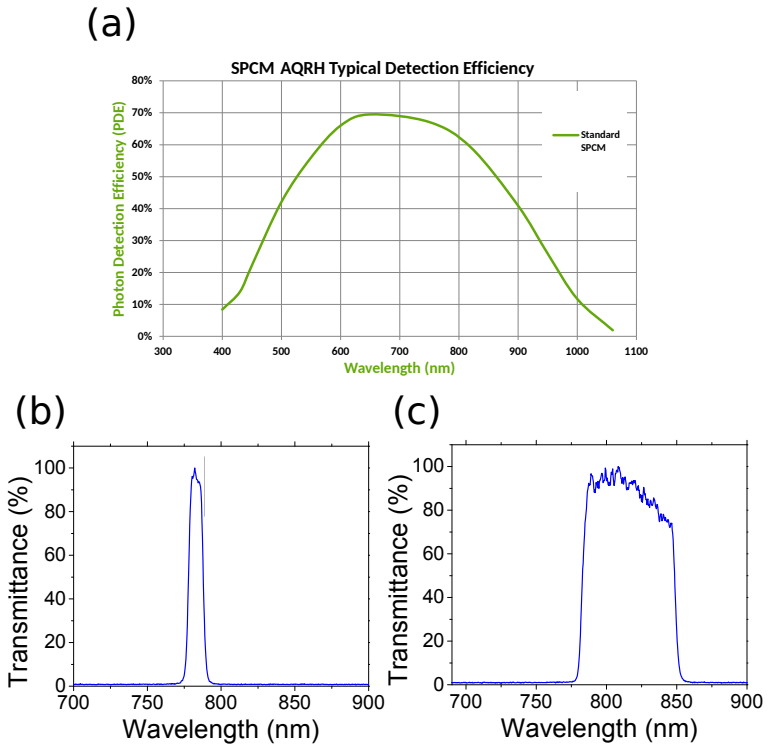

Figure 86: (a) Detection Efficiency of the silicon-based Excelitas SPAD. Image taken from the device datasheet [206]. (b) Transmittance of the set of filters placed after the up-converter module, used for the signal photons (centred at 778 nm) (c) Transmittance of the set of filters placed after the up-converter module, used for the idler photons (centred at 807 nm).

We will show in Section 7.5 that the up-converter module coupled to the visible SPAD actually constitutes an efficient MIR single-photon detector. Now, what about the noise?

In Section 7.1 we commented that MIR detector performances are typically limited by black body radiation, see Figure 74(b). This is also the case of our MIR single-photon detector, therefore the right filtering of unwanted background radiation is crucial. To reduce the noise when the up-converter module is coupled to the SPAD, a pinhole has been used to spatially filter out the noise. Moreover, since the up-converted photon pairs are actually generated in a very narrow band, bandpass filters have been used at the output of the up-converter module. In this way the noise presents at the output of the up-converter module (see for example Figure 79), is spectrally filtered, thus reducing the associated system background rate and increasing the signal to noise ratio. The filter transmittance for each set of filters used is reported in Figure 86(b-c). The set of filters is composed by: short pass (cut-off at 1000 nm), short pass (cut-off at 850 nm), long pass (cut-off at 600 nm). For the signal photons it was also possible to insert an additional short pass (cut-off at 800 nm), with the advantage to further narrow the transmittance bandwidth.
The total loss from the output facet of the SPDC PPLN to the single-photon detector was estimated to be about 25 dB. The various contributions are:

- 10 dB comes from the module up-conversion efficiency (10% of efficiency);
- 0.45 dB comes from the transmission losses of L2;
- 0.5 dB comes from the transmission losses of the filtering stage between the module and the SPAD (~90% transmittance);
- 1.9 dB comes from the SPAD detection efficiency (65% DE according to the datasheet);
- the remaining 12.15 dB are due to a non-optimized overlap between the up-converted photons and the SPAD circular active area.

Let us comment in the following the loss that comes from the non-optimized overlap between the up-converted photons and the SPAD circular active area. The effective up-converted beam radius was measured to be 300 µm. This was measured by varying the detector position within the plane of the beam. With this procedure, the beam-detector overlap is mapped for different relative position and the effective beam radius can be derived.
As a matter of fact, in our implementation, a tighter focus was not feasible. More in details, actually we tried to use lenses with shorter focal lengths in place of L3, whose focal length is 7.5 cm. However, it was not possible to increase the signal to noise ratio. There are some technical issues that led this result. On one hand a tighter focus decreases the up-converted spot size, while on the other hand it also

reduces the Rayleigh range making the alignment procedure more and more sensitive.
To better understand this, it is worth explaining how the alignment procedure works in the experimental set-up sketched in Figure 85(a). The alignment on the correct poled region of the SPDC PPLN was done by looking at the radiation generated by the random errors in the poling periods. Indeed, during the experiment it was noticed that the nonlinear crystal was able to phase-match different nonlinear processes, e.g. SHG at 775 nm. Moreover, another nonlinear process arises from the interaction between the light generated by the SHG and the pump beam at 1.55 µm. The two beams, via the process of SFG, generate radiation at a wavelength equal to 516 nm, which, by the way, contributes to increase the external noise associated with the measurements.
Also the up-converter module itself generates as a side effect radiation at 532 nm, by means of SHG of the 1064 nm intra-cavity pump beam (see Figure 79). We exploited actually these higher order effects of the two PPLN crystals, to perform a first rough alignment of the up-converter module with respect to the optical axis of the incoming 1.55 µm pump photons. In particular, the alignment was done by removing the Germanium windows at the entrance of the up-conversion modules and by matching the overlap between the two greenish signals. Then the SPAD is aligned with respect to the up-converter 532 nm signal. As a second step, the detector alignment is optimized by maximizing the counts of the SPDC up-converted photons (at this point, the filter stage and the Ge window are in place).
We experienced that the alignment of the 532 nm signal was slightly different from to the up-converted radiation, due to chromatic aberration of the lens L3. Since these higher order effects are generated from random poling imperfections, it is not certain that they are collinear with the nonlinear processes of SPDC and SFG of interest.
The alignment issue is actually amplified by using shorter focal lengths, as the alignment is more sensitive in that case. Moreover, spherical aberrations are also present, and they are amplified by shorter focal lengths as well. In light of these reasons, we think that in order to reduce the optical coupling losses it would be easier the use of a larger area detector instead of a tighter focus.
At the same time, we are currently working to couple both the input and the output of the up-converter module with optical fibres. This will significantly ease the input-output manipulation of the light to and from the module, as well as, at the same time, drastically reduce the coupling losses with the detector.
We will come back to this at the end of the Chapter, when in Table 9 we will compare our MIR single-photon detection method with the one of Superconducting Nanowire Single Photon Detectors (SNSPDs).

7.5 EXPERIMENTAL MEASUREMENTS

In this Section MIR single-photon experimental measurements are presented.
To summarize, the up-converter module experimental characterization described in Section 7.3 shows that the proposed system can be tuned to any MIR wavelength within the transparency range of the nonlinear material. Furthermore, the up-conversion process inherently acts as a spectral and spatial filter for the incoming light radiation. For example, in the case of the 5 mm long crystal at 3.1 µm, the spectral and angular acceptance bandwidths are 24 nm and 3.8°. Therefore, it allows both spectrally and spatially resolved measurements at the single-photon level. This is in strong contrast with common direct MIR detection systems.
On the other hand, the fact that a detector has a limited bandwidth has also drawbacks. Working with a broad- band MIR source, it is not possible to get the entire source spectrum in a single measurement. In this case, it is required to scan the phase-matching condition in order to reconstruct the entire source spectrum.
In Figure 87(a) an illustrative sketch of the experiment under analysis is reported. In correspondence, in Figure 87(b) the simulated SPDC generated spectra with the up-converter module bandwidth are reported.

In the SPDC case, the calculation assumes collinear interaction using pump photons at 1.55 µm in a 10 mm long PPLN crystal, with an experimentally determined real poling period of $\Lambda_{MIR}^{real} = 34.68\,\mu m$.
In particular, the degenerate process, where the signal and idler photons have the same wavelength of 3.1 µm, is achieved at a nonlinear crystal temperature of $T_{deg} = 135\,^{\circ}C$ (solid blue curve in Figure 87). By tuning the PPLN crystal temperature to 68 °C, two side lobes appear symmetrically distributed in energy around the degenerate wavelength 3.1 µm. This is due to energy conservation. The spectral bandwidths of the two SPDC peaks, defined as their FWHM, are 50 nm for the 2.89 µm peak and 66 nm for the 3.34 µm peak, respectively. In the case of degenerate SPDC, the bandwidth is 200 nm.
The bandwidths of the two up-converter modules are reported also in Figure 87, along with the SPDC spectra.
In order to phase-match the degenerate SPDC photons, the two up-converter modules were set to T = 145 °C with a poling period of 21.5 µm (solid green curve in Figure 87). The spectral acceptance bandwidth of the two modules is 7 nm, using 20 mm long PPLN crystals, see Figure 81.
For the coincidence measurements, the non-degenerate SPDC emission configuration was exploited. Here, one module is tuned to phase-match the signal wavelength at 2.89 µm using a poling period of

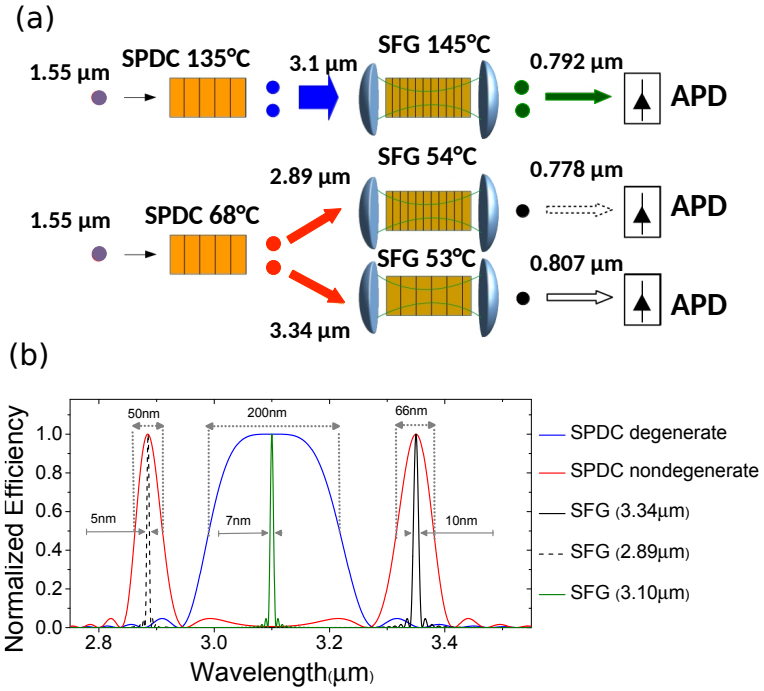

Figure 87: (a) Sketch of the generation and detection stages. (b) Simulated down-conversion spectra and module bandwidth as a function of the temperature. Image taken from [88].

21 µm and a crystal temperature of T = 54 °C (dashed black curve in Figure 87 b). The other module is set to phase-match the idler photon at a wavelength of 3.34 µm, using a poling period of 22.5 µm and a PPLN temperature of 53 °C (solid black curve in Figure 87(b)). The bandwidths of the up-conversion modules are 5 nm for the shorter 2.89 µm, and 10 nm for the longer 3.34 µm wavelength.

Comparing the SPDC bandwidths with the bandwidths of the up-conversion modules, it is clear that the detection system is more efficient for the non-degenerate process with respect to the degenerate case. Considering the spectral overlap of the degenerate SPDC spectrum and of the module bandwidth, each module is only able to up-convert about 3% of the emitted photons.

In the non-degenerate case, instead, we estimated 11% up-conversion efficiency from the signal band, centred at 2.89 µm, and 16% up-conversion efficiency from the idler band, centred at 3.34 µm. The wavelength dependece of the spectral overlap arises from the fact that longer phase matched wavelength exhibit broader conversion bandwidths, as expected [200].

The difference in the up-conversion efficiency between the degenerate and non-degenerate case is the main reason to exploit the non-degenerate SPDC process. In addition, there are also other experimental issues favouring the non-degenerate process.

By spectrally separating the photon pairs with a simple dichroic filter,

we avoid losing 3 dB as it would be the case with a 50:50 beam-splitter (see Figure 60). Also, the non-degenerate configuration permits to operate the SPDC and intra-cavity PPLN crystals at lower temperatures, which significantly reduces the noise due to black body radiation.
Figure 88 shows the SPDC signals while temperature scanning the SPDC crystal and keeping fixed the module, with the constant parameters at 21.5 µm poling period at 145 °C.

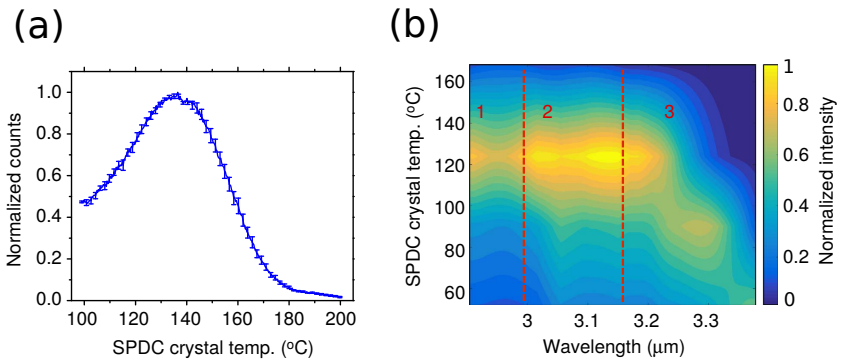

Figure 88: (a) Collected photons at 3.1 µm as a function of the SPDC crystal temperature. The module settings were constant during the measurement (21.5 µm poling period, 145 °C crystal temperature). Error bars: ± 1 standard deviation due to Poissonian statistics. (b) Experimental spectrum of the SPDC nonlinear process as a function of the SPDC crystal temperature measured by the module. Different poling periods (labelled as 1, 2, 3 regions in the figure) of the SFG crystal in the module were used to scan the phase-matched wavelength. The SFG phase-matched wavelength was also tuned as a function of the crystal temperature.

According to the simulation reported in Figure 81, in Figure 87 the maximum signal was found at a nonlinear SPDC crystal temperature of $T_{deg} = 135\,°C$. Tuning the SPDC crystal to different temperatures the detected signal drops, as expected (see Figure 87).
In Figure 88(b) the experimental SPDC spectrum is reported. The data were collected as a function of the SPDC crystal temperature, in order to show the degenerate and non-degenerate processes. To cover a wide spectral region, we used three different poling periods in the up-converter module: (1) 21 µm, (2) 21.5 µm and (3) 22 µm. For each poling period, we scan the phase-matched wavelength with the SFG crystal temperature, according to the experimental characterization reported in Figure 81. The discrepancies with the simulated SPDC spectrum reported in Figure 12, have to be primarily attributed to the difficulties encountered in the alignment of the laser cavity for the different poled regions by scanning the crystal temperature.

Let us discuss in the following the coincidence measurements performed on non-degenerate SPDC MIR photon pairs. In Figure 89(a) a photograph of the real MIR coincidence set-up is reported. In both modules the longer L = 20 mm crystals were used, which guarantees

an up-conversion efficiency of about 10%. One module is tuned to phase-match the signal wavelength at 2.89 µm using a poling period of 21 µm at T = 54 °C. The other module is set to phase-match the idler photon at a wavelength of 3.34 µm, using a poling period of 22.5 µm at T = 53 °C.

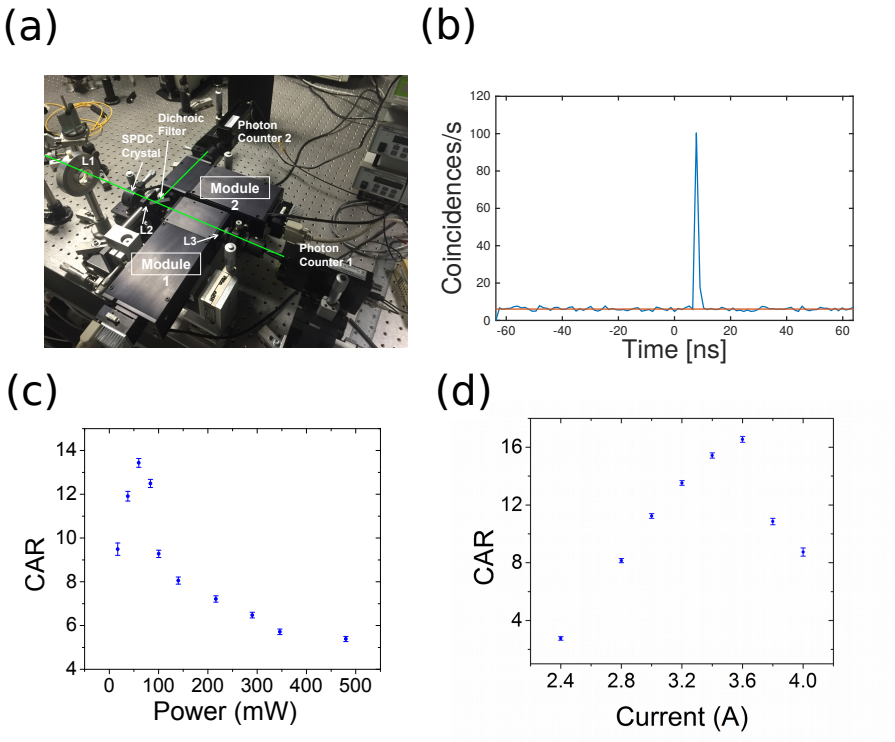

Figure 89: (a) Photograph of the MIR coincidence set-up. (b) Coincidence rate after 10 s of integration with a pump power of 70 mW, incident on the SPDC crystal. The coincidence window is 1.33 ns. The coincidence peak rate is 105 ± 1 Hz. (c) CAR as a function of the pump power on the SPDC crystal. The data were collected for 50 s of integration time to reduce the errors in the high-power regime. (d) CAR as a function of the injected current for the optical pumping of the module laser cavity. The data were collected for 50 s of integration time. Error bars are derived from the standard deviation of the coincidence peak and the standard error of the mean accidental background rate.

A clear peak of coincidences in time between the signal and idler photons is observed in Figure 89(b). This coincidence peak demonstrates the time-correlated nature of the MIR generated photon pairs and the capability of our systems to perform this kind of measurement. Ideally, the coincidence peak should have appeared at a zero delay, but due to differences in the propagation delays of the electrical signals between detectors and the correlation unit, it appears at 8 ns. The coincidence background rate is dominated by background noise photons, which are uncorrelated in contrast to the time correlated nature of the SPDC photon pairs.

The coincidence to accidental ratio (CAR) is calculated as the number of coincidences within the coincidence window of 1.33 ns, divided by the average of the background counts on the same time window taken apart from the peak, which is represented as an horizontal red line in Figure 89(b). It is enough to integrate for 10 s to have a CAR of 15.7 ± 0.4, with a coincidence rate of (105 ± 1) Hz and an accidental mean rate of coincidence of (6.7 ± 0.1) Hz. Clearly, the longer the integration time, the smaller is the error in the final measure. The experimental coincidence measurement was performed with an incident pump power set to an optimal value of 70 mW. After optimization of the PPLN crystal temperatures, the count rate for Module 1 was 153 kHz (signal photons), with a background rate of 9 kHz. The count rate for Module 2 was 150 kHz (idler photons), with a background rate of 14 kHz. The main contribution to the background count rate in both up-converter modules originates from spurious signals at the output of the module itself. The average dark count rate of the silicon SPAD is ~ 100 Hz which is 2 orders of magnitude lower than the black-body back-ground noise, which is still integrated after the filters, see Figure 79 and Figure 86(c-d).
From the measured count rate it is possible to estimate the conversion efficiency of the SPDC process. The conversion efficiency of the SPDC process is $\eta_{SPDC} \sim -92$ dB. The estimation takes into account the spectral acceptance of the modules, which actually reduces the overall number of SPDC detected photon pairs. As was shown in Equation 96, from $\eta_{SPDC} \sim -92$ dB it is possible to calculate the generation rate and then estimate the expected coincidence rate by knowing the total losses. The estimated coincidence rate is comparable to the experimental result. The CAR was characterized as a function of the pump power, as reported in Figure 89(c). We experimentally observed that above 70 mW the CAR decreases. The reason for that is the increasing probability of multi-pair emission which has a detrimental effect on the coincidence measurement [96, 161]. Moreover, the high power regime actually considerably increases the level of the accidental background noise, which eventually contributes to the effective CAR decrease at high pump powers.
Finally, in Figure 89(d) an experimental characterization of the CAR as a function of the intra-cavity pump power is reported. This measurement supports the choice of working with an injected current value of 3.6 A, as it gives the best CAR. We already commented in Section 7.3 that, at higher laser cavity optical pumping, thermal effects determines instabilities within the module. This leads to a CAR drop due to an effective decrease in the up-conversion efficiency.

Let us now compare the presented MIR single-photon capabilities with the other currently available technology, which is based on superconductivity. A one to one comparison is reported in Table 9. We

Parameter	Module + SPAD	SNSPDs
Quantum efficiency	6.5%	2%
Coupling efficiency	5.5%	~100%
System detection efficiency	0.35%	2%
System dark count rate (kHz)	1	>10
Dead time (ns)	20	<10
Working temperature (K)	300	1.5
Reference	This work	[204]

Table 9: Summary and comparison of the performances between the two MIR single photon-photon counting technologies.

already introduced in Section 7.1 that, by moving from telecom wavelengths to the MIR, the SNSPDs performances decrease drastically.
To the best of our knowledge, we found only one reference work which deals with 30-nm-wide SNSPDs in the MIR, by Marsili et. al (2012) ref [204]. Compared to these SNSPDs, the quantum efficiency (QE) of our MIR single-photon detector composed by the up-converter module + SPAD is more than three times higher. The QE of the module + SPAD is given by the product between the up-conversion efficiency of the module (10%) and the SPAD quantum efficiency (65%). Even though our detection system effectively shows an higher QE with respect to SNSPDs, the overall system detection efficiency remains lower. This is due to the non-negligible coupling losses that we experienced between the up-converter module and the SPAD active area.
We are currently working on to improve the detection method. In more details, it was demonstrated previously that the SFG QE can be pushed as high as 20% [200] (in the present work, instead, it was measured to be about 10%). Moreover, commercially available Si SPAD can reach a detection efficiency as high as 80% (ID 120) [32]. Id120 has also the advantage to have 500 µm of diameter which defines the active area (it was 180 µm in the experimental set-up in Figure 89(a)). The use of this SPAD, together with an optimized design of the up-converted visible photon waist at the detector, will allow reducing the ~ 12 dB of coupling losses and, eventually, substantially eliminating them. Therefore, in the optimized system the system detection efficiency η_{sde} would be given by:

$$\eta_{sde} = \eta_{de} \times \eta_{coupling} = (20\% \times 80\%) \times 90\% = 15\% \qquad (159)$$

Furthermore, we are currently working to couple the input and the output of the up-converter module with optical fibres. This will significantly ease input-output manipulation of light, as well as, at the same time, drastically reduce the coupling losses with the detector.

Let us comment on the system dark count rate which appears in Table 9. The system dark count rate reported in [204] is 100 Hz, at T = 1.5 K. However, this measure was done by blocking the optical coupling between the input optical fibres and the devices with a metal shutter kept at T = 1.5 K. Since black body radiation is the main source of noise in the MIR, we reported in Table 9 the dark count rate measured with a room temperature shutter, for the sake of a fair comparison of the two technologies.
However, what is evident between the two technologies is the huge gap between the device operational temperature. Since SNSPDs rely on the superconductivity phenomenon, they are forced to work at cryogenic temperature, while our detection system works at room temperature. Furthermore, the timing properties of our method (response time and timing jitter), is primarily determined by the electronics of the silicon SPAD and not by the up-conversion process itself, which can be considered instantaneous at most time scales employed. We point out that with pulsed upconversion schemes, instead, by triggering the SPADs with the pulsed source (as it was done in Chapter 3), one can actually obtain a very fast detector, whose timing properties are eventually limited by the detector jitter (about 350 ps in our case [206]).

To conclude, we were able for the first time to demonstrate that it is possible to extend quantum optics experiments in the MIR spectral region. The current experiment can be considered as a proof of concept demonstration for correlation experiments, suggesting a proper set-up that exploits the benefits that the up-conversion technology can offer. To the best of our knowledge, no further works have followed ref [204] concerning MIR single-photon capabilities based on SNSPDs in the MIR spectral region.
Instead, a follow-up of our work was recently published in [210]. Here, the authors report on generation and detection of highly non-degenerate photon pairs at room temperature, one at 780 nm and the other at 3950 nm. The 780 nm photons are directly measured with a silicon SPAD, while the MIR photons are up-converted by using a PPLN waveguide, which attains 34% internal conversion efficiency. They demonstrated with this approach a CAR as high as (54 ± 7).

8

FOUR WAVE MIXING CONTROL IN A PHOTONIC MOLECULE

In this Chapter the generation properties of FWM in a system composed by two side coupled microring resonators will be discussed both from a theoretical and experimental point of view. We can think this physical system as a photonic molecule [211].
Through the manipulation of the inter-resonator phase and their relative eigenfrequency detuning, we will show that coherent collective excitations, analogous to sub-radiance and super-radiance of diatomic systems, can be activated. The increased photon lifetime associated to the sub-radiant state is exploited to enhance the internal field of the constituents of the molecule, thus boosting the FWM signal. On the other hand, we can reconfigure the state to have energy equipartition among the resonators, and, consequently, suppress FWM by making the two signal waves to interfere destructively in the bus waveguides.
The work described in this Chapter was done in collaboration with Dr. Massimo Borghi. Dr. Jean-Marc Fedeli of CEA-LETI fabricated the sample.

8.1 THEORETICAL DESCRIPTION OF TWO SIDE-COUPLED MICRORING RESONATORS

A sketch of the structure under analysis is reported in Figure 90.

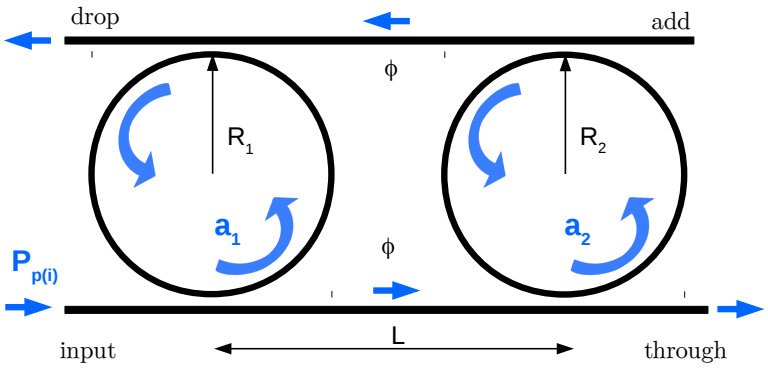

Figure 90: Sketch of two side coupled Add-Drop filter micro-resonators.

The two microrings are in the Add-Drop filter configuration, i.e. with two common bus waveguides evanescently coupled to them. The

physical properties of the microrings are similar to the one discussed in Chapter 5, but with the advantage of an additional degree of freedom. This is provided by the tuning of the relative phase $\phi = \beta(\omega)L = \frac{\omega n_{eff}(\omega)L}{c}$ between the two rings which actually mediates their coupling. Here, $\beta(\omega) = \frac{\omega n_{eff}(\omega)}{c}$ is the mode propagation constant and n_{eff} its effective index, as usual.
Another degree of freedom which is going to be exploited, is the eigenfrequency difference δ between the two rings. As it is possible to see from Figure 90, the two rings have similar radius, i.e. spectrally close eigenfrequencies. It will be shown in Section 8.2 how it is possible to independently thermally tune the inter-resonator phase ϕ and the resonator eigenfrequency detuning δ.
The inter-resonator phase ϕ and their eigenfrequency difference δ actually set the internal state of the molecule. Through the control of these parameters, coherent collective excitations, analogous to sub-radiance and super-radiance of diatomic systems, can be activated.
The increased photon lifetime associated with the sub-radiant state is exploited to enhance the internal field of the constituents of the molecule, thus boosting the FWM signal. On the other hand, we can reconfigure the state to have energy equipartition among the resonators, and consequently suppress FWM by making the two signal waves to interfere destructively in the bus waveguides. Moreover, we show that the same control can be applied to spontaneous FWM.

In the following the theoretical formalism which describes stimulated FWM in the photonic molecule is presented. It will be assumed that the two rings posses equal intrinsic photon lifetime τ_i and equal energy decay rates $\gamma_e = 1/\tau_e$ into the bus waveguides. The set of pump, signal and idler resonances involved in the FWM process will be labelled as $\omega_{1(2),j}$, with $j = p, s, i$ and $1(2)$ refers to the ring. The structure is excited at the input port with two continuous wave lasers, with frequency ω_p and ω_i, which can be slightly detuned from the two resonators eigenfrequencies by the quantities $\Delta\omega_{1(2),p}$ and $\Delta\omega_{1(2),i}$ respectively. The two lasers carry a power $P_p = |p_p|^2$ and $P_i = |p_i|^2$ respectively.
The FWM coupled mode equations for the slowly varying energy envelopes $a_{i,p,s}$ in the two resonators are given by [136]:

$$\begin{aligned}
\frac{da_{1,p(i)}}{dt} &= i\left(\omega_{1,p(i)} - \omega_{p(i)} + \frac{i}{\tau_{tot}}\right)a_{1,p(i)} - \mu a_{2,p(i)} + i\sqrt{\frac{2}{\tau_e}}p_{p(i)} \\
\frac{da_{2,p(i)}}{dt} &= i\left(\omega_{2,p(i)} - \omega_{p(i)} + \frac{i}{\tau_{tot}}\right)a_{2,p(i)} - \mu a_{1,p(i)} + i\sqrt{\frac{2}{\tau_e}}e^{-i\phi_{p(i)}}p_{p(i)} \\
\frac{da_{1,s}}{dt} &= i\left(\omega_{1,s} - \omega_s + \frac{i}{\tau_{tot}}\right)a_{1,s} - \mu a_{2,s} + \Gamma a_{1,p}^2 a_{1,i}^* \\
\frac{da_{2,s}}{dt} &= i\left(\omega_{2,s} - \omega_s + \frac{i}{\tau_{tot}}\right)a_{2,s} - \mu a_{1,s} + \Gamma a_{2,p}^2 a_{2,i}^*
\end{aligned} \tag{160}$$

where $\tau_{tot} = \frac{\tau_e \tau_i}{\tau_e + 2\tau_i}$ is the total photon lifetime, $\mu = \frac{2}{\tau_e} e^{-i\phi}$ is the coupling constant and $|\Gamma|^2$ is the rate of energy conversion into the signal wave. In Equation 160, we neglect all the FWM terms except the one involved in signal generation, as well as thermal and free carrier induced resonance shifts, since their effect will be negligible in the experiment described in Section 8.2. Under the undepleted pump (and idler) approximation [18], the pump and idler amplitudes $a_{1(2),p(i)}$ are given by $a_{1(2),p(i)} = E_{1(2),p(i)} p_{p(i)}$, where:

$$\begin{aligned} E_{1,p(i)} &= \frac{\tau_{tot}\left(\tau_{tot}\left(i\mu^2\sqrt{\tau_e} - 2\Delta\omega_{2,p(i)}\sqrt{\frac{1}{\tau_e}}\right) - 2i\sqrt{\frac{1}{\tau_e}}\right)}{\sqrt{2}\left(\tau_{tot}^2\left(\Delta\omega_{1,p(i)}\Delta\omega_{2,p(i)} + \mu^2\right) + i(\Delta\omega_{1,p(i)} + \Delta\omega_{2,p(i)})\tau_{tot} - 1\right)} \\ E_{2,p(i)} &= \frac{i\mu\tau_{tot}\left(2\sqrt{\frac{1}{\tau_e}}\tau_{tot} + \sqrt{\tau_e}\left(i\Delta\omega_{1,p(i)}\tau_{tot} - 1\right)\right)}{\sqrt{2}\left(\tau_{tot}^2\left(\Delta\omega_{1,p(i)}\Delta\omega_{2,p(i)} + \mu^2\right) + i(\Delta\omega_{1,p(i)} + \Delta\omega_{2,p(i)})\tau_{tot} - 1\right)} \end{aligned} \tag{161}$$

are the Energy Enhancement factors (EE) for resonator 1 and 2, respectively, which have units of $\sqrt{s}$.
It is interesting to compare the expressions in Equation 161, to the on resonance EE of a single Add-Drop resonator. We will refer to it as the *isolated* resonator, in order to distinguish this configuration from the one in which the two rings are coupled. To simplify the analysis, we can set $\phi = 2m\pi$, with m integer, so that the coupling term μ is a real number. It is not difficult to show that this choice actually maximizes the modulus of Equation 161.
The EE of the isolated resonator is given by $|E_{iso}| = \frac{\sqrt{2}}{\tau_e}\tau_{tot}$, and we can evaluate the quantity $\frac{E_{1,p(i)}}{E_{iso}}$ as:

$$\frac{E_{1,p(i)}}{E_{iso}} = \frac{\tau_e^2\left((2 + i\Delta_{p(i)})\tau_{tot} - 1\right)}{4\tau_{tot}^2 + \tau_e^2\left(\Delta_{p(i)}\tau_{tot} + i\right)\left((\delta_{p(i)} + \Delta_{p(i)})\tau_{tot} + i\right)} \tag{162}$$

in which the quantities $\Delta_{p(i)} = (\omega_{2p(i)} - \omega_{p(i)})$ and $\delta_{p(i)} = (\omega_{1p(i)} - \omega_{2p(i)})$ have been introduced.
By differentiating the modulus of Equation 162 with respect to $\delta_{p(i)}$ and solving for $\frac{d\left|E_{1,p(i)}/E_{iso}\right|}{d\delta_{p(i)}} = 0$, we obtain the relation between $\delta_{p(i)}$ and $\Delta_{p(i)}$ which maximizes the EE ratio. This is given by:

$$\delta_{p(i)}^{max} = \frac{\Delta_{p(i)}\left(\tau_e^2 + \tau_{tot}^2\left(\Delta_{p(i)}2\tau_e^2 + 4\right)\right)}{\tau_e^2\left(\Delta_{p(i)}^2\tau_{tot}^2 + 1\right)} \tag{163}$$

which inserted into Equation 162, gives the maximum EE induced by the coupling of the two resonators:

$$\left|\frac{E_{1,p(i)}}{E_{iso}}\right|_{max} = \frac{\tau_e\sqrt{\left(\Delta_{p(i)}^2\tau_{tot}^2 + 1\right)\left(\tau_e^2 + \tau_{tot}^2\left(\Delta_{p(i)}^2\tau_e^2 + 4\right) - 4\tau_e\tau_{tot}\right)}}{\tau_e^2 + \tau_{tot}^2\left(\Delta_{p(i)}^2\tau_e^2 - 4\right)} \tag{164}$$

This quantity is plotted in Figure 91 for $\tau_e = 1\,ps$ and for different values of the total photon lifetime τ_{tot}. From Figure 91 we see that

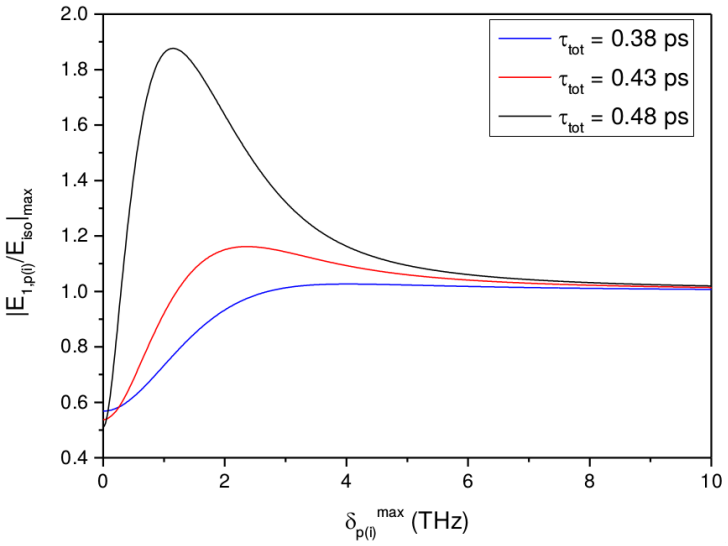

Figure 91: Modulus of the ratio of the energy enhancement (EE) factor of ring 1 coupled to ring 2 and of an on resonance isolated ring. The different curves refer to different value of τ_{tot}, where $\tau_e = 1\,ps$ have been set.

when $\delta_{p(i)}\tau_e \gg 1$, $|E_{1,p(i)}/E_{iso}| \to 1$.
This makes sense, as for large detuning ring 1 is not any more coupled to ring 2 and therefore the numerator tends to be equal to the denominator in Equation 164. In the opposite limit, i.e. when $\delta_{p(i)}\tau_e \ll 1$ (hence $\Delta_{p(i)} \to 0$ from Equation 163), the two rings have the same eigenfrequencies and are excited on resonance. In this regime the internal EE of ring 1 decreases. The physical interpretation of this parameter configuration will be discussed in detail in Section 8.4, where it will be shown that the supermode supported by the photonic molecule has the maximum photon lifetime, but it is strongly undercoupled to the bus waveguides, hence the internal field enhancement drops.
Between the two limits there exists an optimal value of resonator detuning $\delta_{p(i)}$, which maximizes the ratio of Equation 164. We see from Figure 91 that the ratio gets bigger and bigger as the total lifetime tends to $\tau_{tot} = 0.5\,ps$, which means for $\tau_e = 1\,ps$, to the critical coupling condition. We already commented in Chapter 5 that a real symmetric Add-Drop ring resonator cannot be excited in critical coupling condition, as it would be lossless in that case.
Here, we limit ourselves to note that the energy enhancement factor of ring 1 coupled to ring 2 gets higher with respect to the one of an on-resonance ring, as we approach the critical coupling condition. In this configuration, the energy stored by ring 1 within the molecule

exceeds the one of the isolated resonator, a condition that we denote as *Coupled Resonator Field Enhancement* (CRFE).
By inserting Equation 161 into Equation 160 and solving for the signal amplitude $a_{1(2),s}$, we have:

$$\begin{aligned} a_{1,s} &= \frac{\Gamma p_p^2 p_i^* \tau_{tot} \left(\mu E_{2,p}^2 E_{2,i}^* \tau_{tot} + E_{1,p}^2 E_{1,i}^* \left(i\Delta\omega_{2,s}\tau_{tot} - 1\right)\right)}{\tau_{tot}^2 \left(\Delta\omega_{1,s}\Delta\omega_{2,s} + \mu^2\right) + i(\Delta\omega_{1,s} + \Delta\omega_{2,s})\tau_{tot} - 1} \\ a_{2,s} &= \frac{\Gamma p_p^2 p_i^* \tau_{tot} \left(\mu E_{1,p}^2 E_{1,i}^* \tau_{tot} + E_{2,p}^2 E_{2,s}^* \left(i\Delta\omega_{1,s}\tau_{tot} - 1\right)\right)}{\tau_{tot}^2 \left(\Delta\omega_{1,s}\Delta\omega_{2,s} + \mu^2\right) + i(\Delta\omega_{1,s} + \Delta\omega_{2,s})\tau_{tot} - 1} \end{aligned} \tag{165}$$

The signal power in the drop port P_D is the coherent sum of the signals generated by the two resonators and coupled into the output waveguide, and is given by $P_D = \frac{2}{\tau_e}|a_{1,s} + e^{-i\phi(\omega_s)}a_{2,s}|^2$.
By using Equation 165, this expression reduces to the simple form $P_D = \Gamma^2 P_p^2 P_i(\gamma_1 + \gamma_2 + \gamma_{12})$, in which:

$$\begin{aligned} \gamma_1 &= |E_{1,p}|^4 |E_{1,i}|^2 |E_{1,s}|^2 \\ \gamma_2 &= |E_{2,p}|^4 |E_{2,i}|^2 |E_{2,s}|^2 \\ \gamma_{12} &= 2\,\mathrm{Re}(E_{1,p}^2 (E_{2,p}^*)^2 E_{1,s}^* E_{2,s} E_{1,i} E_{2,i}^*) \end{aligned} \tag{166}$$

In Equation 166, we identify the term γ_1 (γ_2) as the signal generated by ring 1 (ring 2) and coupled into the drop port. Since the two are coherent, the term γ_{12} takes into account the interference between them. From Equation 161-162, it is evident that it is possible to change the relative phase between the two signal waves by acting on the resonator detuning δ and the inter-resonator phase ϕ (for the pump, idler and signal). In this way, constructive or destructive interference can be realized. If no CRFE occurs, the EE factors in Equation 166 are lower than $|E_{iso}|$, so that the maximum level of generated signal will never exceed $4P_{Ds,iso}$, in which $P_{Ds,iso}$ is the signal generated for an isolated resonator coupled to the drop port. This simple check can be used to distinguish whether the increase of the FWM efficiency is due to the coherent interference of the signal waves generated by the two resonators, or if it is due to the CRFE effect.

8.2 DEVICE AND EXPERIMENTAL SET-UP

In this section the experimental set-up used to investigate FWM in the photonic molecule composed of two side-coupled ring resonators is presented. A sketch of the experimental set-up is reported in Figure 92(a). The set-up used for this experiment is similar to the one reported in Figure 43 in Chapter 4.

Two tunable CW C-band lasers are set on resonance to the pump and idler resonances of ring 2. The two lasers are both TE polarized, combined and injected to the input port of the system, see Figure 92(b). The pump and idler powers were set to 300 μW (within the

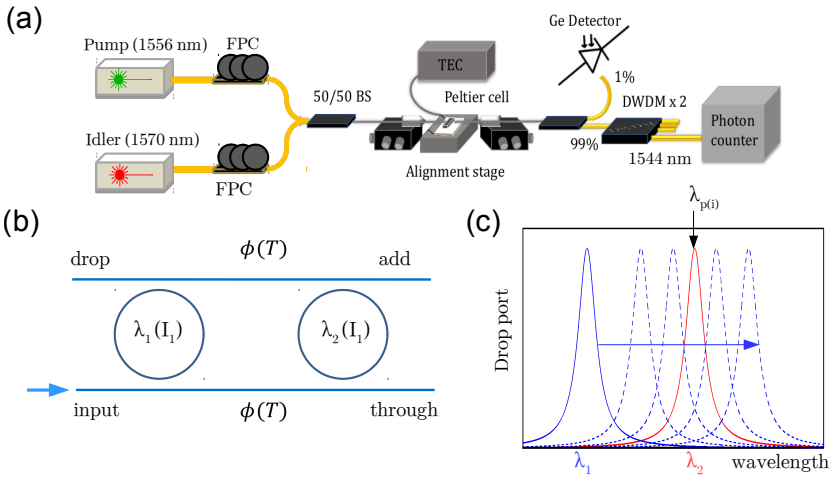

Figure 92: (a) Experimental set-up for studying stimulated FWM. FPC = Fiber Polarization Controller, BS = Beam Splitter, DWDM = Dense Wavelength Division Multiplexing Module, TEC = Thermo-electric Controller. (b) Sketch of the device under test. The resonance wavelength of ring 1(2) is tuned with the electrical current flowing into the micro-heater $I_{1(2)}$. The phase ϕ instead is varied as a function of the Peltier temperature, placed beneath the device. (c) Scheme of the measurement procedure: for different values of the inter-resonators phase ϕ, pump (idler) laser is kept fixed and resonant with ring 2. Ring 1 resonance wavelengths are then swept over the ones of ring 2. The generated signal is detected by the single-photon counter and the top-scattered light is acquired by the infrared camera.

input waveguide), which leads to a sufficient detectable signal without activating thermal or two-photon absorption effects within the two rings. The device presents nominally equal performances with respect to the ones discussed in Chapter 5, as it underwent the same fabrication process. Here the inner radii are respectively, $R_1 = 6.495\,\mu m$ and $R_2 = 6.505\,\mu m$. Ring 1 refers to the resonator with internal radius R_1, and ring 2 to the one with internal radius R_2. The center-to-center distance between the two rings is $L = 53.01\,\mu m$. Above each resonator, a micro-metallic heater is placed. In this way it is possible to tune separately, through the thermo-optic effect, the resonance wavelength of each resonator. The simulated external lifetime ($k^2 \sim 2\%$, k coupling coefficient) is $\tau_e = 50\,ps$, while by considering the measured value of $-3\,dB cm^{-1}$ for the linear propagation losses, the intrinsic lifetime is $\tau_i = 70\,ps$. This leads to a total quality factor of $Q_{tot} = 15\,000$, consistent with the measured one from the device spectrum, discussed in Chapter 5. The free spectral range of both the rings is about $13.5\,nm$. We estimated $-7\,dB$ of coupling losses per facet, which sum up to $\sim -15.5\,dB$ of total insertion losses (the sample is $0.5\,cm$ long).

The sample is in thermal contact with a Peltier cell, whose temperature can be controlled by an external Temperature Controller (TEC) in

the range of 25-75 °C, with an approximate accuracy of ± 1 °C. This provides the control of the relative phase ϕ between the two resonators. The temperature variation is translated into a phase change from the relation:

$$\Delta\phi = \frac{\partial n_{eff}}{\partial T}\frac{\omega L}{c}\Delta T \tag{167}$$

where $\frac{\partial n_{eff}}{\partial T}$ is the thermo-optic coefficient and ΔT the temperature increase with respect to a reference value ($T_{ref} = 25\,°C$).
The upper temperature limit of 70 °C is actually fixed by thermal instabilities of the whole chip which arise at high temperature. Due to this limitation, we are able to induce a maximum phase variation of $\Delta\phi = 0.7\pi$.
Light is collected at the output fibre and it is split: 1% goes to a germanium detector in order to monitor the level of the total transmitted signal and so to ensure that the pump and the idler lasers are set on resonance. The remaining is directed to an additional filtering stage. The generated signal inside the resonator is filtered from the co-propagating pump and idler beams by using two cascaded Dense Wavelength Division Multiplexing (DWDM) modules (~2.5 dB insertion loss), and directed to a photon counter (ID Quantique ID220) operating in Free Running mode, with a detection efficiency of 5% and a dead time of 40 µs. The DWMD modules achieve a signal isolation of more than 100 dB. Since the pump and idler wavelengths are always kept fixed and locked to ring 2 resonances, also the generated signal wavelength is fixed. Note that due to unwanted Fabry-Perot reflections between the waveguide end facets, this condition may be slightly detuned from a perfect on-resonance excitation.
In this way, we set the generated signal wavelength such that it fits within our Dense Wavelength Division Multiplexing (DWDM) module ($\lambda_s = 1544\,nm$). This allows us to perform an efficient and easier filtering of the generated signal photons with respect to the one reported in Chapter 5 for the coincidence measurement.
On top of the sample an infrared camera (Xenics Xeva-2.5-320) is placed. It actually has two tasks. On one side, it helped during the alignment procedure of the butt coupling of the light in and out of the device. On the other side, it was used to record the top-scattered light from the two rings during the FWM measurements. In Figure 92(c) an intuitive sketch of the measurement procedure is reported. Starting from room temperature (T = 25 °C), the Peltier temperature is increased, and the corresponding induced thermal red-shift of the ring 2 resonance is compensated with a controlled reduced current into the corresponding heater. In this way, the ring 2 signal resonance remains effectively locked within the chosen DWDM channel regardless of the Peltier temperature, and the net effect of the temperature increase is to change the value of ϕ.
Ring 1 resonance wavelengths are then swept over the ones of ring 2. During the ring 1 sweep, the generated signal is detected by the

single-photon counter and the top-scattered light is acquired by the infrared camera.

8.3 EXPERIMENTAL MEASUREMENTS

In this section the experimental results achieved will be presented and compared with the theoretical expectation. In Figure 93 the experimental normalized map of the stimulated FWM intensity as a function of the resonators wavelength detuning $\Delta\lambda = \lambda_1 - \lambda_2$ (called $\delta = -\frac{2\pi c \Delta\lambda}{\lambda^2}$ in Section 8.1) and the Peltier temperature T is reported.

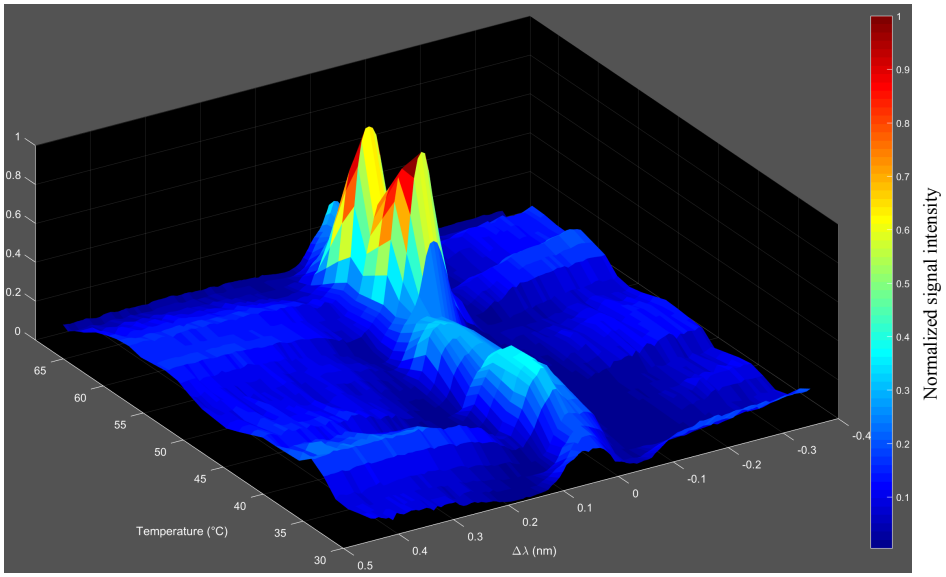

Figure 93: Normalized measured signal intensity in the parameter space defined by the resonance wavelength detuning $\Delta\lambda$ between the two rings and the Peltier temperature. In the measurement the pump and idler wavelengths are kept fixed and locked to ring 2 resonances.

As it is possible to appreciate from the 3D plot, there is actually a non trivial trend of the FWM efficiency in the parameter space ($\Delta\lambda$,T) and different regions of the parameter space reveal distinct regimes. It is possible to see that at $T \sim 60\,°C$, a steep generation enhancement is observed. Moreover, in general, when the detuning between the two rings is $> \pm 0.3\,nm$, which corresponds approximately to three times the ring resonance linewidth, the two rings become effectively decoupled and the generated signal is due to only ring 2. In this regime, as one would expect, the generated signal does not depend on the inter-resonator phase ϕ (in Figure 93 reported as the direct physical quantity T). As $|\Delta\lambda| \to 0$, the resonators coupling gets important, and the generated signal strongly depends on the the Peltier temperature. For a more direct comparison with the theory, the experimental map

is reported in Figure 94(a) as a function of $\Delta\lambda$ and the inter-resonator phase ϕ, which is derived from Equation 167. In order to validate the experimental result, the signal intensity has been simulated by using Equation 166. The result of the simulation is shown in Figure 94(b). A good agreement is found between theory and experiment.

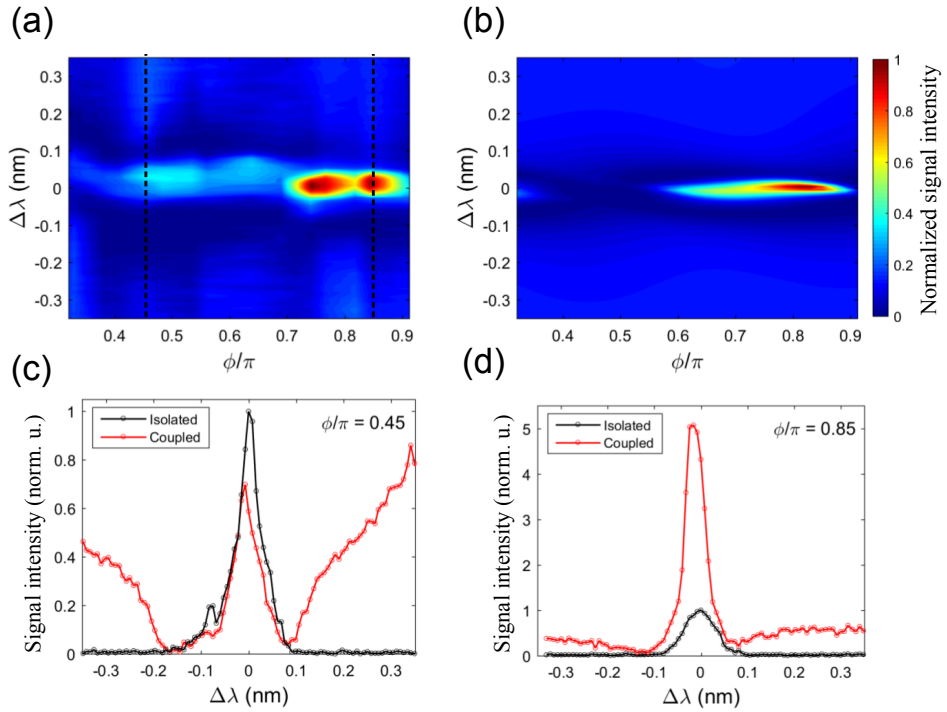

Figure 94: (a) Measured signal intensity in the parameter space defined by the resonance wavelength detuning $\Delta\lambda$ between the two rings and inter-resonator phase ϕ. The two dashed black lines refer to the cross section graphs (c)-(d). (b) Simulated signal intensity in the same parameter space defined in (a). (c) Signal intensity at the phase $\phi = 0.45\pi$ as a function of $\Delta\lambda$ for the coupled (red) and the isolated (black, only ring 1 excited) configuration. (d) Same as in (c), but for the enhancing phase $\phi = 0.85\pi$. The data in panels (c) and (d) have been normalized for the signal intensity relative to the isolated configuration at $\phi = 0.45\pi$.

The best match between simulation and experiment is found by setting the input pump and idler wavelengths slightly blue detuned ($-0.015\,\mathrm{nm}$ and $-0.025\,\mathrm{nm}$ respectively) with respect to the corresponding resonance wavelengths of ring 2. We already commented on this fact in Section 8.2, and attributed the wavelength mismatch to the Fabry-Perot reflections at the input-output facets of the sample. We point out that also the double enhancement spots at $\phi = 0.75\pi$ and $\phi = 0.85\pi$ in Figure 94(a) are due to these reflections which affect the pump and idler intensities. Indeed, as suggested by the simulation in Figure 94(b), the maximum enhancing phase should be unique and

placed approximately at $\phi = 0.8\pi$.
We excluded the possibility that the observed enhancement is due to the coherent interference of these reflections by averaging the signal generated by the isolated resonator over multiple temperatures. The same was done for the signal recorded in the coupled configuration, by varying the temperature across the enhancement point.
In Figure 94(c) a cross section of the colour-map of panel (a) at $\phi = 0.45\pi$, is reported. When the two rings are slightly detuned ($|\Delta\lambda| \lesssim 0.1\,\mathrm{nm}$), we observe a complete suppression of the FWM signal. This suppression ends when the resonance wavelengths of the two rings are almost overlapped ($\Delta\lambda \sim 0$). In this case, a narrow peak emerges in the generated signal. In order to compare the performance of the coupled configuration to the one of an isolated resonator, we tuned the resonance wavelength of ring 2 very far from the pump (idler) wavelength, so that the system reduces to a single cavity, where only ring 1 is effective. In this case, the detuning $\Delta\lambda$ which appears in Figure 94(c,d) for the isolated case has to be interpreted as the detuning of λ_1 with respect to the pump (idler) wavelength. As emerges from Figure 94(c), the signal intensity of the coupled system never exceeds the one of the isolated resonator, as expected also from the simulation.

In the interval defined by $0.7\pi < \phi < 0.9\pi$, FWM suppression is still observed for $|\Delta\lambda| \lesssim 0.1\,\mathrm{nm}$, but when the two resonators become almost overlapped, a clear enhancement of the generated signal occurs. In particular, in Figure 94(d) a cross section of the colourmap of panel (a) at $\phi = 0.85\pi$ is reported. As it is possible to see from the plot, when the two rings are almost overlapped the coupled configuration exceeds the ring 1 isolated emission by (7.0 ± 0.2) dB. As discussed in Section 8.1, since this value corresponds to an enhancement of more than a factor of 4, it has to be necessarily attributed to the CRFE effect.
We have seen that the experimental map, Figure 94(a), closely matches the simulated one in Figure 94(b). Let us look it into more details, by analyzing the various terms that appear in Equation 166 and linking them to the experimental observation of the top-scattering images.
In Figure 95(a), the terms γ_1, γ_2 and γ_{12} have been plot normalized with respect to $(\gamma_1 + \gamma_2)$ in the parameter space $(\Delta\lambda, \phi)$. As already stated, at large detunings, indicated with black and white stars in Figure 95(a), only ring 2 is excited, and FWM will only occur within this resonator, i.e., $\gamma_2/(\gamma_1 + \gamma_2) \to 1$. This is clearly seen in Figure 95(b), where the top-scattered light from the two rings were recorded for different resonators detuning $\Delta\lambda$ at the theoretical enhancing phase $\phi = 0.8\pi$. This measurement actually gives a qualitative description of the amount of energy stored inside the rings in different configurations. In particular, at large detunings the light is scattered only by ring 2, as expected.
As ring 1 is progressively tuned on resonance, the energy coupled inside the resonator increases accordingly. When the two rings are

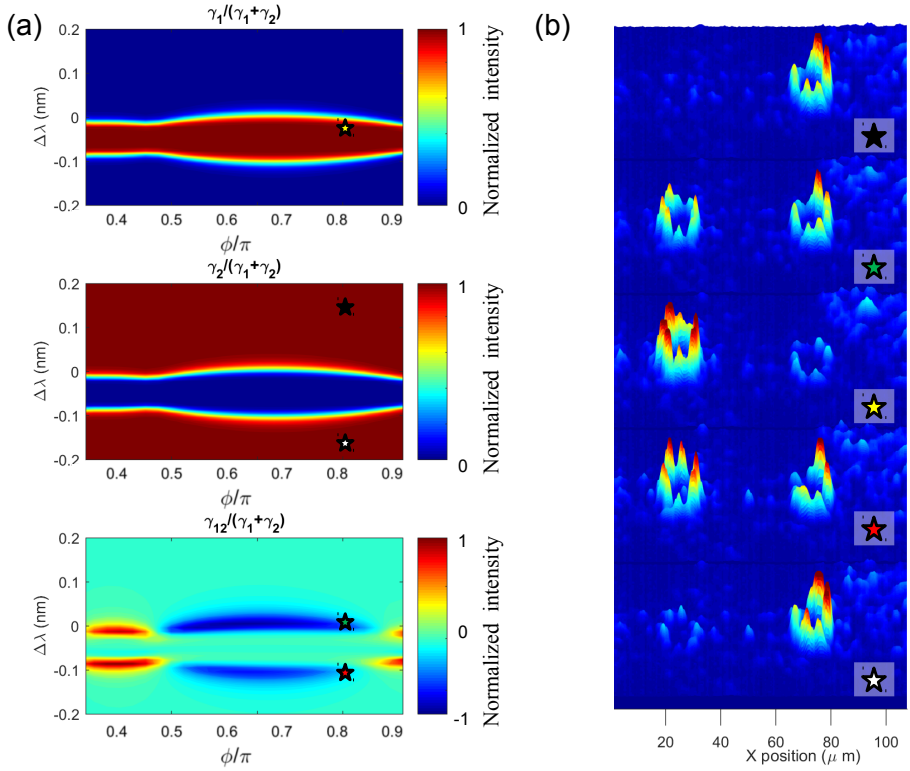

Figure 95: (a) From top to bottom: signal generated ring 1 (γ_1 in Equation 166), signal generated by ring 2 (γ_2 in Equation 166) and effect of mutual interference (γ_{12} in Equation 166). The coloured stars refer to the points in the parameter space defined by $\Delta\lambda$ and ϕ in which the top scattering patterns in panel (b) have been measured. (b) Elaborated top images of the light scattered by the two resonators at different detunings $\Delta\lambda$ and for a fixed value of the phase $\phi = 0.8\pi$ (enhancing phase of the simulation). The leftmost ring corresponds to ring 1. Peaks and valleys in the scattering patterns are due to the inhomogeneities of the scattering centres.

slightly detuned ($|\Delta\lambda| \lesssim 0.1$ nm), we see from Figure 95(b) that the two rings share almost the same energy. In this regime, the signal waves generated by FWM have equal amplitudes but they are out of phase, giving raise to destructive interference in the drop channel (red and green stars in Figure 95). This is the origin of FWM suppression observed in Figure 94, in particular at $\phi = 0.85\pi$.
Intriguingly, from Figure 95(a), we observe that at $\phi = 0.45\pi$, the interference between the two signal waves is constructive for ($|\Delta\lambda| \lesssim 0.1$ nm), but in Figure 94(c) we still observe signal suppression with respect to large detunings $\Delta\lambda$, i.e., when only ring 2 is excited. This ambiguity is solved by looking at the simulation shown in Figure 94(b). Here, we see that at $\phi = 0.45\pi$, the FWM signal is always very low when the two resonators are coupled ($|\Delta\lambda| \lesssim 0.1$ nm), meaning that the fields inside both rings are suppressed by mutual interference. Thus, even though

the interference of the signal waves is constructive, the overall intensity at $|\Delta\lambda| \lesssim 0.1\,\mathrm{nm}$ is still lower than the one at large detunings, thus appearing in Figure 94(c) as an effective suppression of the signal.
It is possible to see from Figure 95(b) that when the two rings are almost spectrally overlapped, the energy stored by ring 1 is increased, while ring 2 is inhibited. By looking at Figure 95(a), this feature seems to be independent on the value of ϕ, so one may wonder why enhancement occurs only for specific values of the inter-resonator phase ϕ. This fact will be explained in detail in Section 8.4 in terms of the excitation of a high-Q supermode (sub-radiant mode) in the photonic molecule, which is highly localized in phase space. At this stage, we limit ourselves to note that the strength of the localized energy in ring 1 should depend on the phase ϕ. Anyway, in general we see from Figure 95(b), that the field distribution between the two resonators closely follows the theoretical predictions shown in Figure 95(a). In particular, when signal suppression is observed, both resonators appear equally bright, and, when signal enhancement occurs, the fields are found mostly localized in ring 1.

We also tried to link the generated signal waves coupled into the drop channel in the various regimes quantitatively to the internal field enhancement inside the rings, evaluated by integrating the top-scattered light. Figure 96(a-b) reports the simulated internal field enhancement of ring 1 and ring 2 in the coupled and isolated (for ring 1) configurations as a function of the resonators detuning $\Delta\lambda$. Panel (a) refers to the experimental enhancing phase $\phi = 0.85\pi$ and panel (b) for the considered not-enhancing phase $\phi = 0.45\pi$. These quantities are proportional to the energy stored inside the rings. As a comparison, Figure 96(c-d) reports the corresponding experimental integrated top-scattered light. We see a good qualitative agreement between theory and experiment. At the experimental enhancing phase $\phi = 0.85\pi$ in Figure 96(a), it is possible to see that ring 1, in the coupled configuration, is brighter by almost a factor of 2 with respect to the isolated case, Figure 96(a). This is due to the CRFE effect. In contrast, at $\phi = 0.45\pi$, the coupling with ring 2 does not increase the field inside ring 1, Figure 96(b). These trends are also found from the experimental curves shown in Figure 96(c,d). Here the difference in brightness is less marked than in the simulation. This is an experimental limitation of the measurement due to the poor dynamic range of the image sensor. At $\phi = 0.45\pi$, CRFE is not effective, and we cannot resolve the difference between the coupled and the isolated configuration.

We obtained an additional evidence of the occurrence of the CRFE also from measurements of spontaneous FWM. In this case, the idler laser in Figure 92(a) was off and the spontaneously generated signal photons were acquired as a function of the resonators detuning $\Delta\lambda$ for

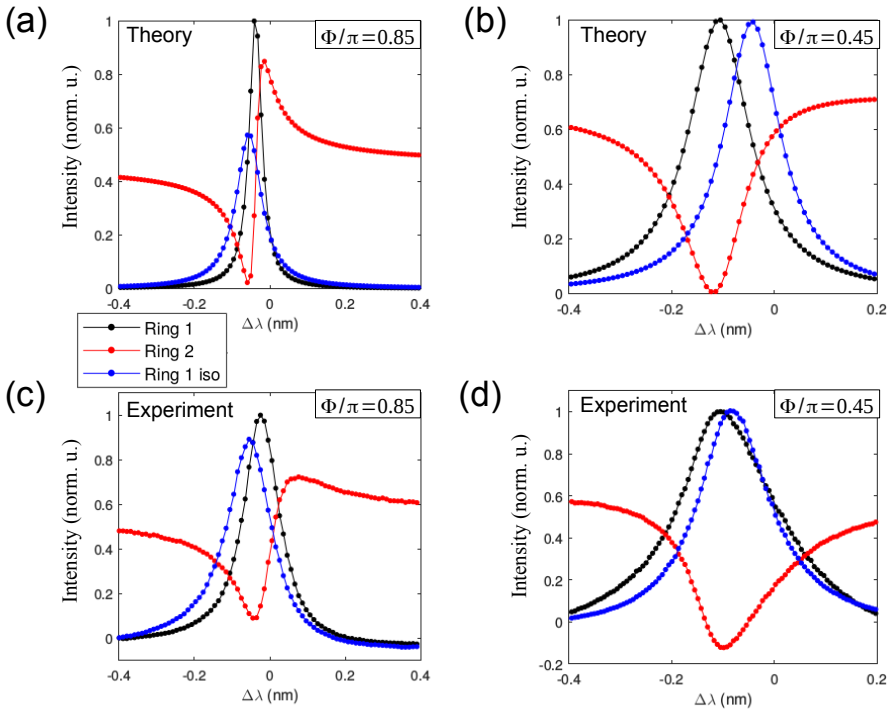

Figure 96: (a) Simulated internal field enhancement of ring 1 (black dotted line) and ring 2 (red dotted line) in the coupled configuration. The field enhancement of ring 1 when it is isolated from ring 2 is shown by the blue dotted line. Here, the detuning $\Delta\lambda$ in the isolated configuration has the same meaning as in Figure 94(c,d). This simulation assumes $\phi = 0.85\pi$. (b) Same as in (a) for $\phi = 0.45\pi$. (c) Top-scattering intensity integrated over the area of ring 1 and 2 when $\phi = 0.85\pi$. The colours have the same meaning as in (a). (d) Same as in (c) for $\phi = 0.45\pi$. Here, the intensity relative to ring 2 near zero detuning is negative because of the background subtraction. In all panels the field enhancement refers to the pump wave.

the experimental enhancing phase $\phi = 0.85\pi$.

In Figure 97 the spontaneous FWM generated signal is reported as a function of $\Delta\lambda$ for the coupled case (red curve) and isolated case (black curve). In order to have a sufficient signal-to-noise ratio in detection, the pump power within the input waveguide was increased from $300\,\mu W$ to $1\,mW$. As it is possible to see from the triangular-shaped resonance in the isolated case, the pump level is high enough to activate thermal effects within the resonator. The increase in the internal energy in the system in the coupled configuration is manifested by the onset of a bistability effect when the two rings are brought spectrally closed, which increases the signal counts. This clearly qualitatively shows that the energy stored inside the photonic molecule is higher in the coupled case with respect to the isolated one.

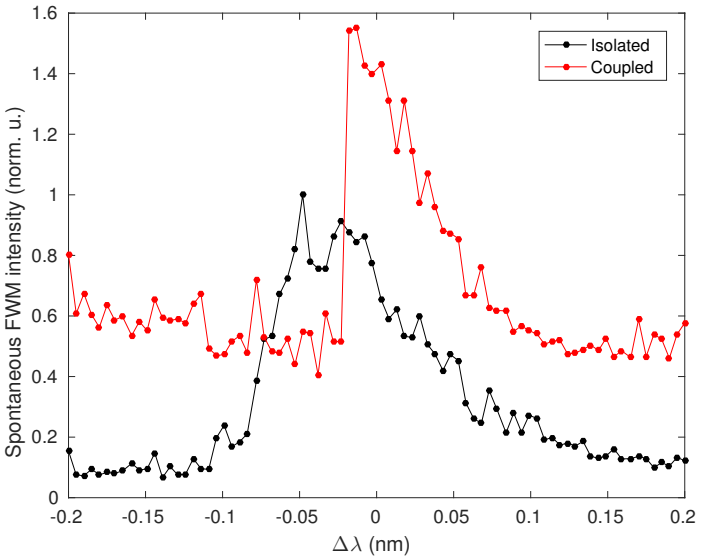

Figure 97: Spontaneous FWM intensity at the experimental enhancing phase $\phi = 0.85\pi$ for the coupled (red curve) and isolated configuration (black curve).

The enhancement is a factor of two, which is less than the 7 dB-enhancing effect experienced in the stimulated measurement, Figure 94(d). However, the signal detected in the spontaneous process is integrated over all the generation bandwidth of the coupled resonator system, while the corresponding stimulated process generates photons only at the signal frequency determined by $\omega_s = 2\omega_p - \omega_i$. Thus, the two efficiencies should not be directly proportional [212]. The two will progressively overlap if a narrow bandpass filter, whose bandwidth is much lower than the one of the coupled system, is applied to the spontaneous signal before detection.
Moreover, the activation of thermal effects modifies the effective detuning $\Delta\lambda$ between the two resonators through the thermo-optic effect, and losses induced by two-photon absorption decreases the quality factor of the individual resonators. These effects are detrimental for the observation of CRFE, and can lead to significant deviations from the predictions of Equation 166, in which thermal induced resonance shifts as well as nonlinear absorption phenomena have not been taken into account.

The impact of two-photon absorption can be considerably reduced by lowering the input pump power from 1 mW to a few hundred µW [164]. As already discussed at the end of Chapter 5 in Table 7, this is possible at telecom wavelength if superconducting nanowire single photon detectors are exploited, which show superior performance in terms of detection efficiency and dark counts. In our experiment, this

was not possible due to the very low signal-to-noise ratio imposed by the high dark counts of our single-photon detector ($> 6.5\,\mathrm{kHz}$).

8.4 SUPERMODE ANALYSIS

An alternative approach to solve the set of Equation 160 for the pump and the idler energy amplitudes $a_{1(2),p(i)}$ is to make a change of basis, such that the equations of motion becomes uncoupled. The physical meaning of this mathematical theoretical reformulation is to find the supermodes supported by the photonic molecule, looking for collective excitations considering the system as a whole. We rewrite the equation for the pump (or the idler) amplitude a of Equation 160, using the following compact matrix notation:

$$\mathbb{M}\bar{a} - i\omega_p \mathbb{1} + \bar{b} = 0 \tag{168}$$

where

$$\mathbb{M} = \begin{bmatrix} i\omega_1 - \frac{1}{\tau_{tot}} & -\mu \\ -\mu & i\omega_2 - \frac{1}{\tau_{tot}} \end{bmatrix} \qquad \mathbb{1} = \begin{bmatrix} 1 & 0 \\ 0 & 1 \end{bmatrix}$$

and

$$\bar{a} = \begin{bmatrix} \bar{a}_1 \\ \bar{a}_2 \end{bmatrix} \qquad \bar{b} = \begin{bmatrix} i\sqrt{\frac{2}{\tau_e}} \\ i\sqrt{\frac{2}{\tau_e}}\, e^{-i\phi} \end{bmatrix}$$

For simplicity, here we set the input power equal to one. We now look for a change of coordinates $\bar{a} \to \bar{a_s}$ described by $\bar{a} = \mathbb{P}\bar{a_s}$, such that $\mathbb{P}^{-1}\mathbb{M}\mathbb{P}$ is diagonal. The matrix $\mathbb{P}$ will then have on its columns the eigenvectors of $\mathbb{M}$, and the diagonal elements of $\mathbb{P}^{-1}\mathbb{M}\mathbb{P}$ will be the eigenvalues of $\mathbb{P}$. By solving the characteristic equation, the eigenvalues $\eta_{1,2}$ are given by:

$$\eta_{1,2} = -\frac{1}{\tau_{tot}} + \frac{i(\omega_1 + \omega_2)}{2} \pm \frac{1}{2}\sqrt{\frac{16}{\tau_e^2}\left(\cos 2\phi - i \sin 2\phi\right) - \delta^2} \tag{169}$$

where $\delta = \omega_1 - \omega_2$ is the eigenfrequency detuning between the two resonators. The matrix $\mathbb{P}$ has the following form:

$$\mathbb{P} = \begin{bmatrix} \frac{\sqrt{4\mu^2 - \delta^2} - i\delta}{2\mu} & \frac{-\sqrt{4\mu^2 - \delta^2} - i\delta}{2\mu} \\ 1 & 1 \end{bmatrix} \tag{170}$$

while its inverse $\mathbb{P}^{-\mathbb{1}}$ is given by:

$$\mathbb{P}^{-\mathbb{1}} = \frac{1}{\det(\mathbb{P})} \begin{bmatrix} 1 & \frac{\sqrt{4\mu^2 - \delta^2} + i\delta}{2\mu} \\ -1 & \frac{\sqrt{4\mu^2 - \delta^2} - i\delta}{2\mu} \end{bmatrix} \tag{171}$$

The real part of Equation 169 gives the photon lifetimes $\tau_{s1,s2}$ of the supermodes of the structure, while the imaginary part represents their

eigenfrequencies $\omega_{s1,s2}$. The supermode energy amplitudes a_{s1} and a_{s2} are given by:

$$a_{s1} = \frac{-i\sqrt{\frac{2}{\tau_{e,s1}^{down}}}}{i(\omega_{s1} - \omega_p) - 1/\tau_{s1}} \tag{172}$$

$$a_{s2} = \frac{-i\sqrt{\frac{2}{\tau_{e,s2}^{down}}}}{i(\omega_{s2} - \omega_p) - 1/\tau_{s2}} \tag{173}$$

where we have defined $\tau_{e,s1}^{down} = \tau_e/(P_{11}^{-1} + P_{12}^{-1}\, e^{-i\phi})^2$ and $\tau_{e,s2}^{down} = \tau_e/(P_{21}^{-1} + P_{22}^{-1}\, e^{-i\phi}))^2$.
The total energy amplitude coupled into the drop port is given by:

$$\begin{aligned} a_{drop} &= i\sqrt{\frac{2}{\tau_e}}a_1 + i\sqrt{\frac{2}{\tau_e}}\, e^{-i\phi} a_2 \\ &= \left[\frac{\sqrt{\frac{2}{\tau_{e,s1}^{down}}}\sqrt{\frac{2}{\tau_{e,s1}^{up}}}}{i(\omega_{s1} - \omega_p) - 1/\tau_{s1}} + \frac{\sqrt{\frac{2}{\tau_{e,s2}^{down}}}\sqrt{\frac{2}{\tau_{e,s2}^{up}}}}{i(\omega_{s2} - \omega_p) - 1/\tau_{s2}}\right] \end{aligned} \tag{174}$$

where we have defined $\tau_{e,s1}^{up} = \tau_e/(P_{11} + P_{21}\, e^{-i\phi})^2$ and $\tau_{e,s2}^{up} = \tau_e/(P_{12} + P_{22}\, e^{-i\phi}))^2$.
From Equation 174, it is possible to recognize that the system composed by two symmetrical side-coupled ring resonators can be equivalently described by a single photonic molecule sustaining two uncoupled modes $a_{s1(2)}$ which are *asymmetrically* coupled to the two bus waveguides.
Therefore, even though the symmetric coupling of the two cavities inherently forbids the critical coupling condition in presence of loss, the supermodes supported by the system do show an effective asymmetric coupling, hence they could be critically coupled by some combinations of the parameters δ and ϕ.

Some considerations about the validity of the supermode description of the system need to be discussed. The main stringent requirement is that the matrix $\mathbb{P}$ should be invertible:

$$\det(\mathbb{P}) = \frac{\tau_e}{2} e^{i\phi}\sqrt{\frac{16}{\tau_e^2}e^{-i2\phi} - \delta^2} \neq 0 \tag{175}$$

This is clearly not satisfied if $\delta^2 \to 16/\tau_e^2$ and $\phi = m\pi$ (where m is an integer), for which we have that $\tau_{e,s1}^{down}, \tau_{e,s2}^{down} \to 0$.
As we approach to this condition, the weak coupling approximation which underlies the validity of coupled mode equations $\tau_{e,s1(2)}^{down} \gg 2\tau_{rt}$, in which τ_{rt} is the roundtrip time of light in the cavity, does not hold any more [213].
It is worth to note that in the strong coupling regime, the inadequacy of Equation 172 and Equation 173 is reflected in the violation of energy conservation. The extreme condition $\delta = \frac{4}{\tau_e}$ corresponds to the onset of Coupled Resonator Induced Transparency (CRIT) in

the structure, since the supermode lifetimes become equal, and their eigenfrequecies start to be symmetrically split with respect to the center frequency $(\omega_1 + \omega_2)/2$ [214].
Figure 98(a,b) shows the photon lifetimes of the two supermodes, which have been normalized with respect to the total lifetime of the isolated cavity modes τ_{tot}.

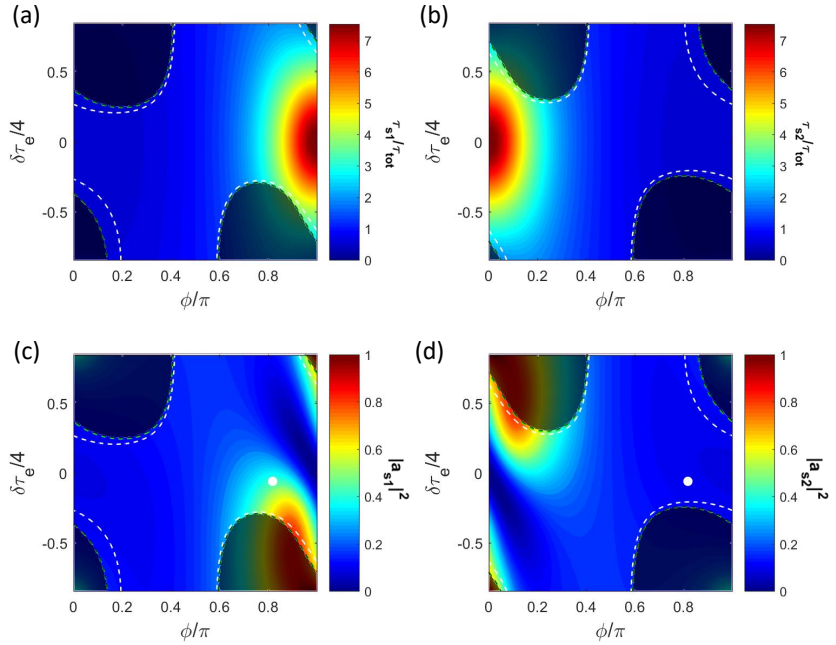

Figure 98: (a) Lifetime τ_{s1} of supermode 1 normalized with respect to the lifetime of the single cavity τ_{tot}. (b) Lifetime τ_{s2} of supermode 2 normalized with respect to the lifetime of the single cavity τ_{tot}. (c) Normalized energy carried by supermode 1 when excited with a laser at frequency ω_p (defined in Section 8.3). (d) Normalized energy carried by supermode 2 when excited with a laser at frequency ω_p. In all the panels, the dashed white lines indicate where the respective supermodes are critically coupled, while the shaded regions indicate where energy conservation is violated due to the lost of the weak coupling regime. The white dots in panels (c) and (d) are placed where FWM enhancement is observed (see Figure 94(a,b)).

The green contour lines are placed where the quantity $1/\tau_{s1(2)} - 1/\tau^{up}_{e,s1(2)} - 1/\tau^{down}_{e,s1(2)} = 0$, i.e. they define the boundaries where energy conservation is violated. The shaded regions in Figure 98, characterized by $1/\tau_{s1(2)} - 1/\tau^{up}_{e,s1(2)} - 1/\tau^{down}_{e,s1(2)} < 0$, have then no physical meaning. One can see that at $\phi = \pi$ and $\delta = 0$, the supermode 1 has the maximum lifetime, corresponding to $\tau_{s1} = \tau_i$. In contrast, at $\phi = 0$ and $\delta = 0$, its photon lifetime is minimized. Supermode 2 has the opposite behaviour.
The energy stored by the two supermodes $|a_{s1(2)}|^2$, evaluated at the

pump frequency ω_p of the experiment, is shown in Figure 98(c,d).
At the coordinate point in the parameter space (ϕ, δ) where FWM enhancement is experimentally observed, white dot in Figure 98(c,d), we can see that the total energy is essentially carried by supermode 1, which is a consequence of its increased photon lifetime. This high-Q supermode is actually a collective excitation of the photonic molecule, which shows sub-radiant property [215]. This is at the origin of the CRFE effect introduced in Section 8.1.

As it can be noticed from Figure 98(c,d), the highest energy is not localized where supermode 1 shows the maximum sub-radiance. This is due to the fact that when $\phi = \pi$ and $\delta \to 0$, from Equation 171 we have that $\tau_{e,s1}^{down} \to \infty$ (the same occurs for $\tau_{e,s1}^{up}$), which is equivalent to say that the supermode becomes completely decoupled from any external excitation. Consequently, as experimentally observed, the point where FWM is maximized will be located nearby the point of maximal sub-radiance, in a position determined by the pump (idler) exciting frequency and waveguide dispersion.
Indeed, at a fixed Peltier temperature and heater current, the phase ϕ and the detuning δ will be different for the pump, the signal and the idler field, since these quantities are all wavelength dependent. In general, the maximum of the field enhancement for these three frequencies will be reached in three different points of the parameter space (all nearby the maximal sub-radiance), and as shown by Equation 166, the overall enhancement of the FWM process will be reached where their product is maximized.

9

CONCLUSIONS

This thesis work was carried out within the framework of the *SiQuro* project, which was focused on the study of integrated devices for quantum optics applications.
I did concentrate on the generation, manipulation and detection of sources of quantum states of light. Even though the long-term goal of the project was the realization a silicon-based quantum photonics chip, at first I studied a bulk nonlinear crystal, called Lithium Niobate ($LiNbO_3$), which has a well-known sizeable $\chi^{(2)}$ nonlinearity, $\chi^{(2)} = 28\,pm/V$. The crystal is a domain-engineered material, named Periodically Poled Lithium Niobate (PPLN), which permits to obtain through the *quasi-phase-matching* technique, efficient nonlinear optical processes.
In particular, in Chapter 2 a suitable PPLN was used for achieving Spontaneous Parametric Down Conversion (SPDC). The photon pair source was characterized by means of coincidence measurements and by its tunable spectral emission property. For this goal, single-photon resolved spectra were investigated.
To further manipulate the generated photons, they were injected into an asymmetric Mach-Zehnder interferometer, to study quantum interference effects. This part is addressed in Chapter 6. In the experiment, a pair of 1550 nm colour-entangled photons enters in the same input port of the interferometer. Photon antibunching (split) and bunching (NooN) states are created after the first beamsplitter, and the strength of their self and mutual interaction is changed by tuning the asymmetry of the transmittance between the two arms. A theoretical description was developed, which demonstrates that the amplitude probabilities associated to the possible ways that the two photons can reach the two single-photon detectors at the output ports of the MZI, strongly depend on the arm losses, detector misalignment and beamsplitter loss. Surprisingly, some of these paths are forbidden by *destructive quantum interference*, and, thus, hidden in the ideal description.

The next step was to transfer the acquired know-how in quantum optics into integrated silicon photonics. The long-term goal is the demonstration of the generation of Mid-infrared (MIR) entangled photon pairs by SPDC in strained silicon waveguides. It is worth to remark that silicon has a centrosymmetric crystalline structure, that leads to a null second order nonlinear $\chi^{(2)}$ coefficient. However, recently it has been reported that by stressing a Si waveguide with a silicon nitride over-layer, a sizeable $\chi^{(2)}$ is induced. In 2012 Second Harmonic Generation (SHG) measurements were reported in large area

strained Si waveguides by our laboratory [114]. Actually, the SHG data were affected by different contributions caused by the interfaces, the free carrier induced internal electric fields, the inhomogeneous strain and the uncontrolled modal structure of the waveguides [19].
I built an optical set-up able to reveal at first the occurrence of SHG in strained silicon waveguides (Chapter 3), since it is orders of magnitude more efficient with respect to the opposite process, SPDC. The silicon waveguides were designed according to a nonlinear propagation model. The design maximizes the SHG efficiency by a detailed simulation of the waveguide modal structure to achieve *multimodal phase matching*. Waveguides of different widths were measured for different pump powers and wavelengths. SHG was observed and by quantifying the generation efficiency, I estimated the value of the strain induced second order nonlinearity to be $\chi^{(2)} \sim 1\,\mathrm{pm/V}$. While I was able to demonstrate consistently the occurrence of multimodal SHG, unfortunately, it is still not possible to clearly determine the physical origin of the observed $\chi^{(2)}$. There could still be parasitic charge effects within the sample playing a non-negligible role in the final estimation of the strain-induced second order nonlinearity.

Having been successful in the observation of SHG in strained silicon waveguides, the opposite process, SPDC, could be looked for as well. Considering a pump at telecom wavelength, entangled photon pairs in the MIR will be generated in that case. This is an intriguing process, especially due to recent interest to move quantum optics applications to the MIR. The experimental set-up in itself is challenging, since single-photon detection is mandatory and in the MIR it is really an issue. This is due to the fact that MIR detectors face many limitations, mainly due to the inherent sensitivity to unwanted incident black-body radiation and dark current, induced by the finite temperature of the detector itself. Cooling the detectors generally improves the signal to noise ratio, but the resulting sensitivity still is not enough to achieve single-photon counting capabilities in the MIR.
The proposed solution presented in this thesis work (Chapter 7), is to exploit the concept of *spectral translation*. The idea is to up-convert the infrared radiation into the visible domain by means of optical nonlinear effects. Thanks to a collaboration with the Danish Technical University, I developed two up-converter modules with single-photon capability in the MIR. In this way, I was able to demonstrate room temperature coincidence measurement with non-degenerate twin photons at about $3.1\,\mu\mathrm{m}$. Both the generation of MIR photon pairs and the nonlinear up-conversion are based on free-space PPLN crystals. To asses the single-photon capability of the detection unit, I performed coincidence measurements on the generated photon pairs by SPDC, with a coincidence to accidental ratio of 15.7 ± 0.4. The presented detection system outperforms single-photon detectors based on superconducting nanowires in the MIR, which are operated in the few Kelvin

regime, in terms of quantum efficiency, speed and noise. This was the first demonstration of coincidence measurement in the MIR and actually could pave the way for future quantum optical experiments in the MIR. The experiment is based on a free-space configuration, but fully integrated devices can be conceived with the up-conversion mechanism. For example, up-conversion capability can be obtained by the exploitation of third order nonlinear effects in the CMOS compatible SiN or SiON alloy. Then, the up-converted visible photons can be efficiently detected by integrated silicon SPADs, with the control electronics eventually also integrated on chip.
The SiON platform was specifically addressed and optically characterized in Chapter 4. SiON is an appealing material in photonics: it is transparent from the UV to the Mid-infrared (it does not suffer multi-photon absorption losses), it shows minimal insertion losses and it is CMOS compatible. Nonetheless, the SiON optical properties have not yet been fully characterized. In particular, very few studies on its linear and nonlinear optical properties have been reported so far. I studied the thermo-optic coefficient and the nonlinear refractive index n_2 of a relatively high refractive index ($n \sim 1.83$ at $1.55\,\mu m$) SiON. The device under test was an integrated racetrack resonator in the All-Pass filter configuration. The nonlinear characterization was performed by determining the efficiency of stimulated Four Wave Mixing (FWM). The results envisaged that SiON has thermal and nonlinear optical properties which are competing to the other silica or silicon based materials. This shows that SiON is an excellent trade-off platform for the design of nonlinear and quantum optical integrated photonic circuits, in which thermal reconfiguration and nonlinear parameteric processes constitutes fundamental operations.

In Chapter 5 I investigated the generation of correlated photon pairs from Silicon On Insulator (SOI) microring resonators coupled with single-mode waveguides. In this case the nonlinear process under study is spontaneous FWM and it relies on the strong silicon $\chi^{(3)}$. While $\chi^{(2)}$-based nonlinear optical phenomena in silicon still need to be fully characterized and developed, robust photon pair sources from silicon microring resonators at telecommunications wavelengths at room temperature have been already reported so far [165]. Comparing to the $\chi^{(2)}$-based SPDC, spontaneous FWM is more difficult to deal with, since one has to filter out the pump photons that are spectrally placed close to the generated photon pair. Due to the generally inherent poor efficiency of spontaneous parametric processes, the filtering of the pump photons in SFWM is actually a non trivial task to be accomplished. I performed a correlation measurement of the arrival times of the signal and idler photons to verify the time-correlated nature of the pair. The results are in good agreement with the theoretical predictions. From this work, it is clear that to deal with more complex quantum optical circuits, better performances in

terms of signal to noise ratio in the detection are needed. At telecom wavelength, superior detection performances are provided by the superconducting-based technology, at the cost to work at cryogenic temperature.

In Chapter 8 I investigated a photonic molecule made by two coupled silicon microring resonators. I demonstrated, both theoretically and experimentally, that the photonic molecule possesses sufficient degrees of freedom for a FWM control which goes beyond the standard enhancement regime, including also the possibility to suppress the FWM output. Only two parameters are required to set the internal state of the molecule: the inter-resonator phase and their relative eigenfrequency detuning. Through their manipulation, coherent collective excitations, analogous to sub-radiance and super-radiance of diatomic systems, can be activated. The increased photon lifetime associated to the sub-radiant state is exploited to enhance the internal field of the constituents of the molecule, thus boosting the FWM signal. On the other hand, the state can be reconfigured to have energy equipartition among the resonators, and consequently suppress FWM by making the two signal waves to interfere destructively in the bus waveguides. Moreover, I showed that the same control can be applied to spontaneous FWM. The device is then also appealing for the realization of bright sources of correlated photon pairs. Beside the increased brightness with respect to isolated resonators enabled by sub-radiance, the coherent control of the amplitude probabilities of the photons generated in the two resonators, and scattered in a common output channel, could be used to reconfigure the quantum state.

The performance of the molecule, considered as a whole, is superior with respect to its internal constituents. In particular, it was experimentally confirmed that through sub-radiance, it is possible to overcome the maximum field enhancement of each isolated resonator, which is unavoidably fixed by the critical coupling condition.

[1] M Mitchell Waldrop. "More than moore." In: *Nature* 530.7589 (2016), pp. 144–148.

[2] Deji Akinwande, Nicholas Petrone, and James Hone. "Two-dimensional flexible nanoelectronics." In: *Nature communications* 5 (2014), p. 5678.

[3] Govind P Agrawal. *Nonlinear fiber optics*. Academic press, 2007.

[4] Richard A Soref. "Silicon-based optoelectronics." In: *Proceedings of the IEEE* 81.12 (1993), pp. 1687–1706.

[5] Massimo Borghi. "Linear, nonlinear and quantum optics in Silicon Photonics." PhD thesis. University of Trento, 2016.

[6] Rolf Horn, Payam Abolghasem, Bhavin J Bijlani, Dongpeng Kang, AS Helmy, and Gregor Weihs. "Monolithic source of photon pairs." In: *Physical review letters* 108.15 (2012), p. 153605.

[7] Lorenzo Pavesi and David J Lockwood. *Silicon photonics iii*. Springer, 2016.

[8] URL: https://refractiveindex.info/.

[9] Francesco Testa, Claudio J Oton, Christophe Kopp, Jong-Moo Lee, Rubén Ortuño, Reinhard Enne, Stefano Tondini, Guido Chiaretti, Alberto Bianchi, Paolo Pintus, et al. "Design and implementation of an integrated reconfigurable silicon photonics switch matrix in IRIS project." In: *IEEE Journal of Selected Topics in Quantum Electronics* 22.6 (2016), pp. 155–168.

[10] Q Lin, Oskar J Painter, and Govind P Agrawal. "Nonlinear optical phenomena in silicon waveguides: modeling and applications." In: *Optics express* 15.25 (2007), pp. 16604–16644.

[11] Cesar Jauregui, Jens Limpert, and Andreas Tünnermann. "High-power fibre lasers." In: *Nature photonics* 7.11 (2013), p. 861.

[12] M Borghi, C Castellan, S Signorini, A Trenti, and L Pavesi. "Nonlinear silicon photonics." In: *Journal of Optics* 19.9 (2017), p. 093002.

[13] D Gandolfi, R Guider, T Chalyan, L Pavesi, L Pasquardini, C Pederzolli, A Samusenko, and G Pucker. "Sensitivity and Limit of detection of biosensors based on ring resonators." In: *AISEM Annual Conference, 2015 XVIII*. IEEE. 2015, pp. 1–4.

[14] Rayleigh John William Strutt. *The theory of sound*. London, Macmillan and co., 1877.

[15] Wim Bogaerts, Peter De Heyn, Thomas Van Vaerenbergh, Katrien De Vos, Shankar Kumar Selvaraja, Tom Claes, Pieter Dumon, Peter Bienstman, Dries Van Thourhout, and Roel Baets. "Silicon microring resonators." In: *Laser & Photonics Reviews* 6.1 (2012), pp. 47–73.

[16] Chen Sun, Mark T Wade, Yunsup Lee, Jason S Orcutt, Luca Alloatti, Michael S Georgas, Andrew S Waterman, Jeffrey M Shainline, Rimas R Avizienis, Sen Lin, et al. "Single-chip microprocessor that communicates directly using light." In: *Nature* 528.7583 (2015), p. 534.

[17] John McCalpin. *STREAM: Sustainable Memory Bandwidth in High Performance Computers*. Sept. 1991.

[18] Robert W Boyd. *Nonlinear optics*. Academic press, 2003.

[19] Clemens Schriever, Federica Bianco, Massimo Cazzanelli, Mher Ghulinyan, Christian Eisenschmidt, Johannes de Boor, Alexander Schmid, Johannes Heitmann, Lorenzo Pavesi, and Jörg Schilling. "Second-Order Optical Nonlinearity in Silicon Waveguides: Inhomogeneous Stress and Interfaces." In: *Advanced Optical Materials* 3.1 (2015), pp. 129–136.

[20] Davide Grassani, Angelica Simbula, Stefano Pirotta, Matteo Galli, Matteo Menotti, Nicholas C Harris, Tom Baehr-Jones, Michael Hochberg, Christophe Galland, Marco Liscidini, et al. "Energy correlations of photon pairs generated by a silicon microring resonator probed by Stimulated Four Wave Mixing." In: *Scientific reports* 6 (2016), p. 23564.

[21] Juerg Leuthold, C Koos, and W Freude. "Nonlinear silicon photonics." In: *Nature Photonics* 4.8 (2010), p. 535.

[22] Bahaa EA Saleh, Malvin Carl Teich, and Bahaa E Saleh. *Fundamentals of photonics*. Vol. 22. Wiley New York, 1991.

[23] Rodney Loudon. *The quantum theory of light*. OUP Oxford, 2000.

[24] Claude Cohen-Tannoudji, Jacques Dupont-Roc, Gilbert Grynberg, and Patricia Thickstun. *Atom-photon interactions: basic processes and applications*. Wiley Online Library, 1992.

[25] Jan Faye. "Copenhagen Interpretation of Quantum Mechanics." In: *Stanford Encyclopedia of Philosophy*. Ed. by Edward Zalta. 2008.

[26] Max F Riedel, Daniele Binosi, Rob Thew, and Tommaso Calarco. "The European quantum technologies flagship programme." In: *Quantum Science and Technology* 2.3 (2017), p. 030501.

[27] Elizabeth Gibney. *Billion-euro quantum project takes shape*. 2017.

[28] Erwin Schrödinger. "An undulatory theory of the mechanics of atoms and molecules." In: *Physical review* 28.6 (1926), p. 1049.

[29] Werner Heisenberg. "Über den anschaulichen Inhalt der quantentheoretischen Kinematik und Mechanik." In: *Original Scientific Papers Wissenschaftliche Originalarbeiten*. Springer, 1985, pp. 478–504.

[30] Michael A Nielsen and Isaac Chuang. *Quantum computation and quantum information*. 2002.

[31] URL: https://www.covesion.com.

[32] URL: http://www.idquantique.com.

[33] Masoud Mohseni, Peter Read, Hartmut Neven, Sergio Boixo, Vasil Denchev, Ryan Babbush, Austin Fowler, Vadim Smelyanskiy, and John Martinis. "Commercialize quantum technologies in five years." In: *Nature News* 543.7644 (2017), p. 171.

[34] Emanuel Knill, Raymond Laflamme, and Gerald J Milburn. "A scheme for efficient quantum computation with linear optics." In: *nature* 409.6816 (2001), p. 46.

[35] URL: http://qubitekk.com/.

[36] Jacques Carolan, Christopher Harrold, Chris Sparrow, Enrique Martín-López, Nicholas J Russell, Joshua W Silverstone, Peter J Shadbolt, Nobuyuki Matsuda, Manabu Oguma, Mikitaka Itoh, et al. "Universal linear optics." In: *Science* 349.6249 (2015), pp. 711–716.

[37] Ronald L Rivest, Adi Shamir, and Leonard Adleman. "A method for obtaining digital signatures and public-key cryptosystems." In: *Communications of the ACM* 21.2 (1978), pp. 120–126.

[38] IA Walmsley. "Quantum optics: Science and technology in a new light." In: *Science* 348.6234 (2015), pp. 525–530.

[39] Anne Broadbent and Christian Schaffner. "Quantum cryptography beyond quantum key distribution." In: *Designs, Codes and Cryptography* 78.1 (2016), pp. 351–382.

[40] Charles H Bennet. "Quantum cryptography: Public key distribution and coin tossing." In: *Proc. of IEEE Int. Conf. on Comp., Syst. and Signal Proc., Bangalore, India, Dec. 10-12, 1984*. 1984.

[41] Charles H Bennett. "Quantum cryptography using any two nonorthogonal states." In: *Physical review letters* 68.21 (1992), p. 3121.

[42] Dagmar Bruß. "Optimal eavesdropping in quantum cryptography with six states." In: *Physical Review Letters* 81.14 (1998), p. 3018.

[43] Valerio Scarani, Antonio Acin, Grégoire Ribordy, and Nicolas Gisin. "Quantum cryptography protocols robust against photon number splitting attacks for weak laser pulse implementations." In: *Physical review letters* 92.5 (2004), p. 057901.

[44] Artur K Ekert. "Quantum cryptography based on Bell's theorem." In: *Physical review letters* 67.6 (1991), p. 661.

[45] Artur Ekert and Peter L Knight. "Entangled quantum systems and the Schmidt decomposition." In: *American Journal of Physics* 63.5 (1995), pp. 415–423.

[46] Lev Davidovich Landau and Evgenii Mikhailovich Lifshitz. *Quantum mechanics: non-relativistic theory*. Vol. 3. Elsevier, 2013.

[47] Marlan O Scully and M Suhail Zubairy. *Quantum optics*. Cambridge university press, 1997.

[48] N Bergamasco, M Menotti, JE Sipe, and M Liscidini. "Generation of path-encoded GHZ states in an integrated platform." In: *arXiv preprint arXiv:1704.03213* (2017).

[49] Boris Korzh, Charles Ci Wen Lim, Raphael Houlmann, Nicolas Gisin, Ming Jun Li, Daniel Nolan, Bruno Sanguinetti, Rob Thew, and Hugo Zbinden. "Provably secure and practical quantum key distribution over 307 km of optical fibre." In: *Nature Photonics* 9.3 (2015), p. 163.

[50] Louis Salvail, Momtchil Peev, Eleni Diamanti, Romain Alléaume, Norbert Lütkenhaus, and Thomas Länger. "Security of trusted repeater quantum key distribution networks." In: *Journal of Computer Security* 18.1 (2010), pp. 61–87.

[51] Momtchil Peev, Christoph Pacher, Romain Alléaume, Claudio Barreiro, Jan Bouda, W Boxleitner, Thierry Debuisschert, Eleni Diamanti, M Dianati, JF Dynes, et al. "The SECOQC quantum key distribution network in Vienna." In: *New Journal of Physics* 11.7 (2009), p. 075001.

[52] Juan Yin, Yuan Cao, Yu-Huai Li, Sheng-Kai Liao, Liang Zhang, Ji-Gang Ren, Wen-Qi Cai, Wei-Yue Liu, Bo Li, Hui Dai, et al. "Satellite-based entanglement distribution over 1200 kilometers." In: *Science* 356.6343 (2017), pp. 1140–1144.

[53] John S. Bell. "On the Einstein-Podolsky-Rosen paradox." In: *Physics* 1 (1964), pp. 195–200.

[54] Bas Hensen, Hannes Bernien, Anaïs E Dréau, Andreas Reiserer, Norbert Kalb, Machiel S Blok, Just Ruitenberg, Raymond FL Vermeulen, Raymond N Schouten, Carlos Abellán, et al. "Loophole-free Bell inequality violation using electron spins separated by 1.3 kilometres." In: *Nature* 526.7575 (2015), pp. 682–686.

[55] David C Burnham and Donald L Weinberg. "Observation of simultaneity in parametric production of optical photon pairs." In: *Physical Review Letters* 25.2 (1970), p. 84.

[56] John F Clauser, Michael A Horne, Abner Shimony, and Richard A Holt. "Proposed experiment to test local hidden-variable theories." In: *Physical review letters* 23.15 (1969), p. 880.

[57] Juan Yin, Ji-Gang Ren, He Lu, Yuan Cao, Hai-Lin Yong, Yu-Ping Wu, Chang Liu, Sheng-Kai Liao, Fei Zhou, Yan Jiang, et al. "Quantum teleportation and entanglement distribution over 100-kilometre free-space channels." In: *Nature* 488.7410 (2012), p. 185.

[58] Jeremy L O'Brien, Geoffrey J Pryde, Andrew G White, Timothy C Ralph, and David Branning. "Demonstration of an all-optical quantum controlled-NOT gate." In: *Nature* 426.6964 (2003), p. 264.

[59] Hannes Hübel, Deny R Hamel, Alessandro Fedrizzi, Sven Ramelow, Kevin J Resch, and Thomas Jennewein. "Direct generation of photon triplets using cascaded photon-pair sources." In: *Nature* 466.7306 (2010), p. 601.

[60] Philip Walther, Kevin J Resch, Terry Rudolph, Emmanuel Schenck, Harald Weinfurter, Vlatko Vedral, Markus Aspelmeyer, and Anton Zeilinger. "Experimental one-way quantum computing." In: *Nature* 434.7030 (2005), p. 169.

[61] Lucia Caspani, Chunle Xiong, Benjamin J Eggleton, Daniele Bajoni, Marco Liscidini, Matteo Galli, Roberto Morandotti, and David J Moss. "Integrated sources of photon quantum states based on nonlinear optics." In: *Light: Science & Applications* 6.11 (2017), e17100.

[62] Jeremy O'Brien, Brian Patton, Masahide Sasaki, and Jelena Vučković. "Focus on integrated quantum optics." In: *New Journal of Physics* 15.3 (2013), p. 035016.

[63] Alberto Politi, Martin J Cryan, John G Rarity, Siyuan Yu, and Jeremy L O'brien. "Silica-on-silicon waveguide quantum circuits." In: *Science* 320.5876 (2008), pp. 646–649.

[64] Alberto Peruzzo, Mirko Lobino, Jonathan CF Matthews, Nobuyuki Matsuda, Alberto Politi, Konstantinos Poulios, Xiao-Qi Zhou, Yoav Lahini, Nur Ismail, Kerstin Wörhoff, et al. "Quantum walks of correlated photons." In: *Science* 329.5998 (2010), pp. 1500–1503.

[65] Andrea Crespi, Roberto Osellame, Roberta Ramponi, Daniel J Brod, Ernesto F Galvao, Nicolo Spagnolo, Chiara Vitelli, Enrico Maiorino, Paolo Mataloni, and Fabio Sciarrino. "Integrated multimode interferometers with arbitrary designs for photonic boson sampling." In: *Nature Photonics* 7.7 (2013), p. 545.

[66] Jonathan CF Matthews, Alberto Politi, André Stefanov, and Jeremy L O'brien. "Manipulation of multiphoton entanglement in waveguide quantum circuits." In: *Nature Photonics* 3.6 (2009), p. 346.

[67] Michael Kues, Christian Reimer, Piotr Roztocki, Luis Romero Cortés, Stefania Sciara, Benjamin Wetzel, Yanbing Zhang, Alfonso Cino, Sai T Chu, Brent E Little, et al. "On-chip generation of high-dimensional entangled quantum states and their coherent control." In: *Nature* 546.7660 (2017), p. 622.

[68] Nicolò Spagnolo, Chiara Vitelli, Marco Bentivegna, Daniel J Brod, Andrea Crespi, Fulvio Flamini, Sandro Giacomini, Giorgio Milani, Roberta Ramponi, Paolo Mataloni, et al. "Experimental validation of photonic boson sampling." In: *Nature Photonics* 8.8 (2014), p. 615.

[69] Alberto Politi, Jonathan CF Matthews, and Jeremy L O'brien. "Shor's quantum factoring algorithm on a photonic chip." In: *Science* 325.5945 (2009), pp. 1221–1221.

[70] Akihiro Tanaka, Mikio Fujiwara, Ken-ichiro Yoshino, Seigo Takahashi, Yoshihiro Nambu, Akihisa Tomita, Shigehito Miki, Taro Yamashita, Zhen Wang, Masahide Sasaki, et al. "High-speed quantum key distribution system for 1-Mbps real-time key generation." In: *IEEE Journal of Quantum Electronics* 48.4 (2012), pp. 542–550.

[71] Joshua W Silverstone, Damien Bonneau, Kazuya Ohira, Nob Suzuki, Haruhiko Yoshida, Norio Iizuka, Mizunori Ezaki, Chandra M Natarajan, Michael G Tanner, Robert H Hadfield, et al. "On-chip quantum interference between silicon photon-pair sources." In: *Nature Photonics* 8.2 (2014), p. 104.

[72] Stefano Azzini, Davide Grassani, Michael J Strain, Marc Sorel, LG Helt, JE Sipe, Marco Liscidini, Matteo Galli, and Daniele Bajoni. "Ultra-low power generation of twin photons in a compact silicon ring resonator." In: *Optics express* 20.21 (2012), pp. 23100–23107.

[73] Damien Bonneau, Erman Engin, Kazuya Ohira, Nob Suzuki, Haruhiko Yoshida, Norio Iizuka, Mizunori Ezaki, Chandra M Natarajan, Michael G Tanner, Robert H Hadfield, et al. "Quantum interference and manipulation of entanglement in silicon wire waveguide quantum circuits." In: *New Journal of Physics* 14.4 (2012), p. 045003.

[74] Davide Grassani, Stefano Azzini, Marco Liscidini, Matteo Galli, Michael J Strain, Marc Sorel, JE Sipe, and Daniele Bajoni. "Micrometer-scale integrated silicon source of time-energy entangled photons." In: *Optica* 2.2 (2015), pp. 88–94.

[75] Jay E Sharping, Kim Fook Lee, Mark A Foster, Amy C Turner, Bradley S Schmidt, Michal Lipson, Alexander L Gaeta, and Prem Kumar. "Generation of correlated photons in nanoscale silicon waveguides." In: *Optics express* 14.25 (2006), pp. 12388–12393.

[76] Marcelo Davanco, Jun Rong Ong, Andrea Bahgat Shehata, Alberto Tosi, Imad Agha, Solomon Assefa, Fengnian Xia, William MJ Green, Shayan Mookherjea, and Kartik Srinivasan. "Telecommunications-band heralded single photons from a silicon nanophotonic chip." In: *Applied Physics Letters* 100.26 (2012), p. 261104.

[77] Joshua W Silverstone, Raffaele Santagati, Damien Bonneau, Michael J Strain, Marc Sorel, Jeremy L O'Brien, and Mark G Thompson. "Qubit entanglement between ring-resonator photon-pair sources on a silicon chip." In: *Nature communications* 6 (2015), p. 7948.

[78] Philip Sibson, Chris Erven, Mark Godfrey, Shigehito Miki, Taro Yamashita, Mikio Fujiwara, Masahide Sasaki, Hirotaka Terai, Michael G Tanner, Chandra M Natarajan, et al. "Chip-based quantum key distribution." In: *Nature communications* 8 (2017), p. 13984.

[79] Damien Stucki, Nicolas Brunner, Nicolas Gisin, Valerio Scarani, and Hugo Zbinden. "Fast and simple one-way quantum key distribution." In: *Applied Physics Letters* 87.19 (2005), p. 194108.

[80] Kyo Inoue, Edo Waks, and Yoshihisa Yamamoto. "Differential phase shift quantum key distribution." In: *Physical Review Letters* 89.3 (2002), p. 037902.

[81] Robert H Hadfield. "Single-photon detectors for optical quantum information applications." In: *Nature photonics* 3.12 (2009), p. 696.

[82] F Marsili, Varun B Verma, Jeffrey A Stern, S Harrington, Adriana E Lita, Thomas Gerrits, Igor Vayshenker, Burm Baek, Matthew D Shaw, Richard P Mirin, et al. "Detecting single infrared photons with 93% system efficiency." In: *Nature Photonics* 7.3 (2013), pp. 210–214.

[83] Faraz Najafi, Jacob Mower, Nicholas C Harris, Francesco Bellei, Andrew Dane, Catherine Lee, Xiaolong Hu, Prashanta Kharel, Francesco Marsili, Solomon Assefa, et al. "On-chip detection of non-classical light by scalable integration of single-photon detectors." In: *Nature communications* 6 (2015), p. 5873.

[84] Joshua W Silverstone, Damien Bonneau, Jeremy L O'Brien, and Mark G Thompson. "Silicon quantum photonics." In: *IEEE Journal of Selected Topics in Quantum Electronics* 22.6 (2016), pp. 390–402.

[85] Yu Yao, Anthony J Hoffman, and Claire F Gmachl. "Mid-infrared quantum cascade lasers." In: *Nature Photonics* 6.7 (2012), pp. 432–439.

[86] Austin G Griffith, Ryan KW Lau, Jaime Cardenas, Yoshitomo Okawachi, Aseema Mohanty, Romy Fain, Yoon Ho Daniel Lee, Mengjie Yu, Christopher T Phare, Carl B Poitras, et al. "Silicon-chip mid-infrared frequency comb generation." In: *Nature communications* 6 (2015), p. 6299.

[87] Bahram Jalali. "Silicon photonics: Nonlinear optics in the mid-infrared." In: *Nature Photonics* 4.8 (2010), p. 506.

[88] M Mancinelli, A Trenti, S Piccione, G Fontana, Jeppe Seidelin Dam, Peter Tidemand-Lichtenberg, Christian Pedersen, and L Pavesi. "Mid-infrared coincidence measurements on twin photons at room temperature." In: *Nature communications* 8 (2017), p. 15184.

[89] Andreas Reinhard, Thomas Volz, Martin Winger, Antonio Badolato, Kevin J Hennessy, Evelyn L Hu, and Ataç Imamoğlu. "Strongly correlated photons on a chip." In: *Nature Photonics* 6.2 (2012), p. 93.

[90] Thibault Peyronel, Ofer Firstenberg, Qi-Yu Liang, Sebastian Hofferberth, Alexey V Gorshkov, Thomas Pohl, Mikhail D Lukin, and Vladan Vuletić. "Quantum nonlinear optics with single photons enabled by strongly interacting atoms." In: *Nature* 488.7409 (2012), p. 57.

[91] Rainer Blatt and David Wineland. "Entangled states of trapped atomic ions." In: *Nature* 453.7198 (2008), p. 1008.

[92] Birgit JM Hausmann, Brendan Shields, Qimin Quan, Patrick Maletinsky, Murray McCutcheon, Jennifer T Choy, Tom M Babinec, Alexander Kubanek, Amir Yacoby, Mikhail D Lukin, et al. "Integrated diamond networks for quantum nanophotonics." In: *Nano letters* 12.3 (2012), pp. 1578–1582.

[93] S Kumar, R Trotta, E Zallo, JD Plumhof, P Atkinson, A Rastelli, and OG Schmidt. "Strain-induced tuning of the emission wavelength of high quality GaAs/AlGaAs quantum dots in the spectral range of the 87Rb D2 lines." In: *Applied Physics Letters* 99.16 (2011), p. 161118.

[94] Katharina D Zeuner, Matthias Paul, Thomas Lettner, Carl Reuterskiöld Hedlund, Lucas Schweickert, Stephan Steinhauer, Lily Yang, Julien Zichi, Mattias Hammar, Klaus D Jöns, et al. "A stable wavelength-tunable triggered source of single photons and cascaded photon pairs at the telecom C-band." In: *arXiv preprint arXiv:1801.01518* (2018).

[95] Wolfgang Mauerer, Malte Avenhaus, Wolfram Helwig, and Christine Silberhorn. "How colors influence numbers: Photon statistics of parametric down-conversion." In: *Physical Review A* 80.5 (2009), p. 053815.

[96] Felix Bussieres, Joshua A Slater, Nicolas Godbout, and W Tittel. "Fast and simple characterization of a photon pair source." In: *Optics express* 16.21 (2008), pp. 17060–17069.

[97] URL: http://events.unitn.it/en/siquro.

[98] Toshiaki Suhara and Hiroki Kintaka. "Quantum theory analysis of twin-photon beams generated by parametric fluorescence." In: *IEEE journal of quantum electronics* 41.9 (2005), pp. 1203–1212.

[99] Lukas G Helt, Marco Liscidini, and John E Sipe. "How does it scale? Comparing quantum and classical nonlinear optical processes in integrated devices." In: *JOSA B* 29.8 (2012), pp. 2199–2212.

[100] U Schlarb and K Betzler. "Influence of the defect structure on the refractive indices of undoped and Mg-doped lithium niobate." In: *Physical Review B* 50.2 (1994), p. 751.

[101] O Gayer, Z Sacks, E Galun, and A Arie. "Temperature and wavelength dependent refractive index equations for MgO-doped congruent and stoichiometric LiNbO 3." In: *Applied Physics B: Lasers and Optics* 91.2 (2008), pp. 343–348.

[102] GD Miller, RG Batchko, WM Tulloch, DR Weise, MM Fejer, and RL Byer. "42%-efficient single-pass cw second-harmonic generation in periodically poled lithium niobate." In: *Optics letters* 22.24 (1997), pp. 1834–1836.

[103] Peter Seitz and Albert JP Theuwissen. *Single-photon imaging*. Vol. 160. Springer Science & Business Media, 2011.

[104] Antonio Rogalski. *Infrared detectors*. CRC press, 2010.

[105] Fabio Acerbi, Adriano Della Frera, Alberto Tosi, and Franco Zappa. "Fast active quenching circuit for reducing avalanche charge and afterpulsing in InGaAs/InP single-photon avalanche diode." In: *IEEE Journal of Quantum Electronics* 49.7 (2013), pp. 563–569.

[106] Leonard Mandel and Emil Wolf. *Optical coherence and quantum optics*. Cambridge university press, 1995.

[107] URL: https://www.idquantique.com/wordpress/wp-content/uploads/ID350-Datasheet.pdf.

[108] Marco Fiorentino, Sean M Spillane, Raymond G Beausoleil, Tony D Roberts, Philip Battle, and Mark W Munro. "Spontaneous parametric down-conversion in periodically poled KTP waveguides and bulk crystals." In: *Optics Express* 15.12 (2007), pp. 7479–7488.

[109] DA Kleinman. "Theory of optical parametric noise." In: *Physical Review* 174.3 (1968), p. 1027.

[110] S Tanzilli, W Tittel, H De Riedmatten, H Zbinden, P Baldi, M DeMicheli, Da B Ostrowsky, and N Gisin. "PPLN waveguide for quantum communication." In: *The European Physical Journal D-Atomic, Molecular, Optical and Plasma Physics* 18.2 (2002), pp. 155–160.

[111] Go Fujii, Naoto Namekata, Masayuki Motoya, Sunao Kurimura, and Shuichiro Inoue. "Bright narrowband source of photon pairs at optical telecommunication wavelengths using a type-II periodically poled lithium niobate waveguide." In: *Optics express* 15.20 (2007), pp. 12769–12776.

[112] Matthäus Halder, Alexios Beveratos, Robert T Thew, Corentin Jorel, Hugo Zbinden, and Nicolas Gisin. "High coherence photon pair source for quantum communication." In: *New Journal of Physics* 10.2 (2008), p. 023027.

[113] Rune S Jacobsen, Karin N Andersen, Peter I Borel, Jacob Fage-Pedersen, Lars H Frandsen, Ole Hansen, Martin Kristensen, Andrei V Lavrinenko, Gaid Moulin, Haiyan Ou, et al. "Strained silicon as a new electro-optic material." In: *Nature* 441.7090 (2006), p. 199.

[114] M Cazzanelli, F Bianco, E Borga, G Pucker, M Ghulinyan, E Degoli, E Luppi, V Véniard, S Ossicini, D Modotto, et al. "Second-harmonic generation in silicon waveguides strained by silicon nitride." In: *Nature materials* 11.2 (2012), p. 148.

[115] N.W. Ashcroft and N.D. Mermin. *Solid State Physics*. Cengage Learning, 2011. ISBN: 9788131500521. URL: https://books.google.it/books?id=x_s_YAAACAAJ.

[116] Massimo Cazzanelli and Joerg Schilling. "Second order optical nonlinearity in silicon by symmetry breaking." In: *Applied Physics Reviews* 3.1 (2016), p. 011104.

[117] Pedro Damas, Xavier Le Roux, David Le Bourdais, Eric Cassan, Delphine Marris-Morini, Nicolas Izard, Thomas Maroutian, Philippe Lecoeur, and Laurent Vivien. "Wavelength dependence of Pockels effect in strained silicon waveguides." In: *Optics express* 22.18 (2014), pp. 22095–22100.

[118] S Sharif Azadeh, F Merget, MP Nezhad, and J Witzens. "On the measurement of the Pockels effect in strained silicon." In: *Optics letters* 40.8 (2015), pp. 1877–1880.

[119] M Borghi, M Mancinelli, F Merget, J Witzens, M Bernard, M Ghulinyan, G Pucker, and L Pavesi. "High-frequency electro-optic measurement of strained silicon racetrack resonators." In: *Optics letters* 40.22 (2015), pp. 5287–5290.

[120] Massimo Borghi, Mattia Mancinelli, Martino Bernard, Mher Ghulinyan, Georg Pucker, and Lorenzo Pavesi. "Homodyne detection of free carrier induced electro-optic modulation in strained silicon resonators." In: *Journal of Lightwave Technology* 34.24 (2016), pp. 5657–5668.

[121] Irene Olivares, Todora Angelova, and Pablo Sanchis. "On the influence of interface charging dynamics and stressing conditions in strained silicon devices." In: *Scientific Reports* 7.1 (2017), p. 7241.

[122] Francesco De Leonardis, Richard A Soref, and Vittorio MN Passaro. "Investigation of Electric Field Induced Mixing in Silicon Micro Ring Resonators." In: *Scientific Reports* 7.1 (2017), p. 3401.

[123] Chin-Lin Chen. *Foundations for guided-wave optics*. John Wiley & Sons, 2006.

[124] RM Osgood, NC Panoiu, JI Dadap, Xiaoping Liu, Xiaogang Chen, I-Wei Hsieh, E Dulkeith, WMJ Green, and YA Vlasov. "Engineering nonlinearities in nanoscale optical systems: physics and applications in dispersion-engineered silicon nanophotonic wires." In: *Advances in Optics and Photonics* 1.1 (2009), pp. 162–235.

[125] Allan W Snyder and John Love. *Optical waveguide theory*. Springer Science & Business Media, 2012.

[126] Shiming Gao, Zhiqiang Li, En-Kuang Tien, Sailing He, and Ozdal Boyraz. "Performance evaluation of nondegenerate wavelength conversion in a silicon nanowire waveguide." In: *Journal of Lightwave Technology* 28.21 (2010), pp. 3079–3085.

[127] Pedro Damas, Delphine Marris-Morini, Eric Cassan, and Laurent Vivien. "Bond orbital description of the strain-induced second-order optical susceptibility in silicon." In: *Physical Review B* 93.16 (2016), p. 165208.

[128] Costanza Lucia Manganelli, Paolo Pintus, and Claudio Bonati. "Modeling of strain-induced Pockels effect in Silicon." In: *Optics express* 23.22 (2015), pp. 28649–28666.

[129] et al. Castellan Claudio. "Tuning the strain-induced resonance shift in silicon racetrack resonators by their orientation." In: *Optics express* In press (2018).

[130] E Timurdogan, Christopher V Poulton, MJ Byrd, and MR Watts. "Electric field-induced second-order nonlinear optical effects in silicon waveguides." In: *Nature Photonics* 11.3 (2017), p. 200.

[131] Lei Zhong and Fumio Shimura. "Investigation of charge trapping centers in silicon nitride films with a laser-microwave photoconductive method." In: *Applied physics letters* 62.6 (1993), pp. 615–617.

[132] KR Hiremath, R Stoffer, and M Hammer. "Coupled mode theory and FDTD simulations of the coupling between bent and straight optical waveguides." In: IEEE Lasers and Electro-Optics Society. 2003.

[133] Matthew Borselli, Thomas J Johnson, and Oskar Painter. "Beyond the Rayleigh scattering limit in high-Q silicon microdisks: theory and experiment." In: *Optics express* 13.5 (2005), pp. 1515–1530.

[134] Christina Manolatou and Michal Lipson. "All-optical silicon modulators based on carrier injection by two-photon absorption." In: *Journal of lightwave technology* 24.3 (2006), p. 1433.

[135] Wonjoo Suh, Zheng Wang, and Shanhui Fan. "Temporal coupled-mode theory and the presence of non-orthogonal modes in lossless multimode cavities." In: *IEEE Journal of Quantum Electronics* 40.10 (2004), pp. 1511–1518.

[136] M Mancinelli, M Borghi, F Ramiro-Manzano, JM Fedeli, and L Pavesi. "Chaotic dynamics in coupled resonator sequences." In: *Optics express* 22.12 (2014), pp. 14505–14516.

[137] A Trenti, M Borghi, S Biasi, M Ghulinyan, F Ramiro-Manzano, G Pucker, and L Pavesi. "Thermo-optic coefficient and nonlinear refractive index of silicon oxynitride waveguides." In: *AIP Advances* 8.2 (2018), p. 025311.

[138] Marco Masi, Régis Orobtchouk, Guofang Fan, Jean-Marc Fedeli, and Lorenzo Pavesi. "Towards a realistic modelling of ultracompact racetrack resonators." In: *Journal of Lightwave Technology* 28.22 (2010), pp. 3233–3242.

[139] M.J. Deen et. al. "Integrated Optoelectronics: Proceedings of the First International Symposium." In: *Proceedings (Electrochemical Society)*. Electrochemical Society. 2002.

[140] Fabio Turri. "Experiments and modelling of vertically coupled Microresonators." PhD thesis. University of Trento, 2017.

[141] Pierre-Élie Larré, Stefano Biasi, Fernando Ramiro-Manzano, Lorenzo Pavesi, and Iacopo Carusotto. "Pump-and-probe optical transmission phase shift as a quantitative probe of the Bogoliubov dispersion relation in a nonlinear channel waveguide." In: *The European Physical Journal D* 71.6 (2017), p. 146.

[142] David Milam. "Review and assessment of measured values of the nonlinear refractive-index coefficient of fused silica." In: *Applied optics* 37.3 (1998), pp. 546–550.

[143] Sarvagya Dwivedi, Alfonso Ruocco, Michael Vanslembrouck, Thijs Spuesens, Peter Bienstman, Pieter Dumon, Thomas Van Vaerenbergh, and Wim Bogaerts. "Experimental extraction of effective refractive index and thermo-optic coefficients of silicon-on-insulator waveguides using interferometers." In: *Journal of Lightwave Technology* 33.21 (2015), pp. 4471–4477.

[144] Amir Arbabi and Lynford L Goddard. "Measurements of the refractive indices and thermo-optic coefficients of Si 3 N 4 and SiO x using microring resonances." In: *Optics letters* 38.19 (2013), pp. 3878–3881.

[145] Donald E Bossi, Jacob M Hammer, and Joseph M Shaw. "Optical properties of silicon oxynitride dielectric waveguides." In: *Applied optics* 26.4 (1987), pp. 609–611.

[146] Winnie N Ye, D-X Xu, Siegfried Janz, Pavel Cheben, M-J Picard, Boris Lamontagne, and N Garry Tarr. "Birefringence control using stress engineering in silicon-on-insulator (SOI) waveguides." In: *Journal of Lightwave Technology* 23.3 (2005), pp. 1308–1318.

[147] Thibault Capelle, Yeghishe Tsaturyan, Andreas Barg, and Albert Schliesser. "Polarimetric analysis of stress anisotropy in nanomechanical silicon nitride resonators." In: *Applied Physics Letters* 110.18 (2017), p. 181106.

[148] Tobias Jan August Kippenberg. *Nonlinear optics in ultra-high-Q whispering-gallery optical microcavities*. California Institute of Technology, 2004.

[149] Kazuhiro Ikeda, Robert E Saperstein, Nikola Alic, and Yeshaiahu Fainman. "Thermal and Kerr nonlinear properties of plasma-deposited silicon nitride/silicon dioxide waveguides." In: *Optics express* 16.17 (2008), pp. 12987–12994.

[150] David J Moss, Roberto Morandotti, Alexander L Gaeta, and Michal Lipson. "New CMOS-compatible platforms based on silicon nitride and Hydex for nonlinear optics." In: *Nature photonics* 7.8 (2013), p. 597.

[151] Sven Ramelow, Alessandro Farsi, Stéphane Clemmen, Daniel Orquiza, Kevin Luke, Michal Lipson, and Alexander L Gaeta. "Silicon-nitride platform for narrowband entangled photon generation." In: *arXiv preprint arXiv:1508.04358* (2015).

[152] Roel Baets, Ananth Z Subramanian, Stéphane Clemmen, Bart Kuyken, Peter Bienstman, Nicolas Le Thomas, Günther Roelkens, Dries Van Thourhout, Philippe Helin, and Simone Severi. "Silicon Photonics: silicon nitride versus silicon-on-insulator." In: *Optical Fiber Communications Conference and Exhibition (OFC), 2016*. IEEE. 2016, pp. 1–3.

[153] Kevin Luke, Avik Dutt, Carl B Poitras, and Michal Lipson. "Overcoming Si 3 N 4 film stress limitations for high quality factor ring resonators." In: *Optics Express* 21.19 (2013), pp. 22829–22833.

[154] L Stefan, M Bernard, R Guider, G Pucker, L Pavesi, and M Ghulinyan. "Ultra-high-Q thin-silicon nitride strip-loaded ring resonators." In: *Optics letters* 40.14 (2015), pp. 3316–3319.

[155] Thomas J Johnson, Matthew Borselli, and Oskar Painter. "Self-induced optical modulation of the transmission through a high-Q silicon microdisk resonator." In: *Optics express* 14.2 (2006), pp. 817–831.

[156] Iman Jizan, LG Helt, Chunle Xiong, Matthew J Collins, Duk-Yong Choi, Chang Joon Chae, Marco Liscidini, MJ Steel, Benjamin J Eggleton, and Alex S Clark. "Bi-photon spectral correlation measurements from a silicon nanowire in the quantum and classical regimes." In: *Scientific reports* 5 (2015).

[157] LG Helt, Zhenshan Yang, Marco Liscidini, and JE Sipe. "Spontaneous four-wave mixing in microring resonators." In: *Optics letters* 35.18 (2010), pp. 3006–3008.

[158] Giuseppe Cantarella, Charalambos Klitis, Marc Sorel, and Michael J Strain. "Silicon photonic filters with high rejection of both TE and TM modes for on-chip four wave mixing applications." In: *Optics Express* 25.17 (2017), pp. 19711–19720.

[159] Bradley J Frey, Douglas B Leviton, and Timothy J Madison. "Temperature dependent refractive index of silicon and germanium." In: *arXiv preprint physics/0606168* (2006).

[160] Malvin Carl Teich and B Saleh. "Fundamentals of photonics." In: *Canada, Wiley Interscience* 3 (1991).

[161] Rui-Bo Jin, Ryosuke Shimizu, Isao Morohashi, Kentaro Wakui, Masahiro Takeoka, Shuro Izumi, Takahide Sakamoto, Mikio Fujiwara, Taro Yamashita, Shigehito Miki, et al. "Efficient generation of twin photons at telecom wavelengths with 2.5 GHz repetition-rate-tunable comb laser." In: *Scientific reports* 4 (2014), p. 7468.

[162] LG Helt, MJ Steel, and JE Sipe. "Parasitic nonlinearities in photon pair generation via integrated spontaneous four-wave mixing: critical problem or distraction?" In: *Applied Physics Letters* 102.20 (2013), p. 201106.

[163] Hiroki Takesue and Kaoru Shimizu. "Effects of multiple pairs on visibility measurements of entangled photons generated by spontaneous parametric processes." In: *Optics Communications* 283.2 (2010), pp. 276–287.

[164] Chaoxuan Ma, Xiaoxi Wang, Vikas Anant, Andrew D Beyer, Matthew D Shaw, and Shayan Mookherjea. "Silicon Photonic Entangled Photon-Pair and Heralded Single Photon Generation with CAR >12,000 and $g^{(2)}(0) < 0.006$." In: *arXiv preprint arXiv:1710.01001* (2017).

[165] Marc Savanier, Ranjeet Kumar, and Shayan Mookherjea. "Photon pair generation from compact silicon microring resonators using microwatt-level pump powers." In: *Optics express* 24.4 (2016), pp. 3313–3328.

[166] Dirk Taillaert, Peter Bienstman, and Roel Baets. "Compact efficient broadband grating coupler for silicon-on-insulator waveguides." In: *Optics letters* 29.23 (2004), pp. 2749–2751.

[167] Yun Wang, Xu Wang, Jonas Flueckiger, Han Yun, Wei Shi, Richard Bojko, Nicolas AF Jaeger, and Lukas Chrostowski. "Focusing sub-wavelength grating couplers with low back reflections for rapid prototyping of silicon photonic circuits." In: *Optics express* 22.17 (2014), pp. 20652–20662.

[168] Richard A Campos, Bahaa EA Saleh, and Malvin C Teich. "Fourth-order interference of joint single-photon wave packets in lossless optical systems." In: *Physical Review A* 42.7 (1990), p. 4127.

[169] Takahiro Inagaki, Nobuyuki Matsuda, Osamu Tadanaga, Masaki Asobe, and Hiroki Takesue. "Entanglement distribution over 300 km of fiber." In: *Optics express* 21.20 (2013), pp. 23241–23249.

[170] Fabian Laudenbach, Sebastian Kalista, Michael Hentschel, Philip Walther, and Hannes Hübel. "A novel single-crystal & single-pass source for polarisation-and colour-entangled photon pairs." In: *arXiv preprint arXiv:1612.06579* (2016).

[171] CK Law, IA Walmsley, and JH Eberly. "Continuous frequency entanglement: effective finite Hilbert space and entropy control." In: *Physical Review Letters* 84.23 (2000), p. 5304.

[172] CK Law and JH Eberly. "Analysis and interpretation of high transverse entanglement in optical parametric down conversion." In: *Physical review letters* 92.12 (2004), p. 127903.

[173] Peter J Mosley, Jeff S Lundeen, Brian J Smith, and Ian A Walmsley. "Conditional preparation of single photons using parametric downconversion: a recipe for purity." In: *New Journal of Physics* 10.9 (2008), p. 093011.

[174] Marco Liscidini and JE Sipe. "Stimulated emission tomography." In: *Physical review letters* 111.19 (2013), p. 193602.

[175] Andreas Eckstein, Guillaume Boucher, Aristide Lemaître, Pascal Filloux, Ivan Favero, Giuseppe Leo, John E Sipe, Marco Liscidini, and Sara Ducci. "High-resolution spectral characterization of two photon states via classical measurements." In: *Laser & Photonics Reviews* 8.5 (2014).

[176] J Belhassen, F Baboux, Q Yao, M Amanti, A Lemaître, SW Kolthammer, IA Walmsley, and S Ducci. "On-chip III-V monolithic integration of heralded single photon sources and beamsplitters." In: *arXiv preprint arXiv:1710.08710* (2017).

[177] Z Vernon, M Liscidini, and JE Sipe. "No free lunch: the trade-off between heralding rate and efficiency in microresonator-based heralded single photon sources." In: *Optics letters* 41.4 (2016), pp. 788–791.

[178] Fabian Laudenbach, Hannes Hübel, Michael Hentschel, Philip Walther, and Andreas Poppe. "Modelling parametric down-conversion yielding spectrally pure photon pairs." In: *Optics Express* 24.3 (2016), pp. 2712–2727.

[179] Xing Ding, Yu He, Z-C Duan, Niels Gregersen, M-C Chen, S Unsleber, Sebastian Maier, Christian Schneider, Martin Kamp, Sven Höfling, et al. "On-demand single photons with high extraction efficiency and near-unity indistinguishability from a resonantly driven quantum dot in a micropillar." In: *Physical review letters* 116.2 (2016), p. 020401.

[180] Hermann A Haus. "Waves and fields in optoelectronics. 1984." In: *isbn* 139460535 (), p. 402.

[181] Stephen M Barnett, John Jeffers, Alessandra Gatti, and Rodney Loudon. "Quantum optics of lossy beam splitters." In: *Physical Review A* 57.3 (1998), p. 2134.

[182] Joseph W Goodman. *Statistical optics*. John Wiley & Sons, 2015.

[183] URL: https://en.wikipedia.org.

[184] R Hanbury Brown and R Q_ Twiss. "A test of a new type of stellar interferometer on Sirius." In: *Nature* 178.4541 (1956), pp. 1046–1048.

[185] Anton Zeilinger. "General properties of lossless beam splitters in interferometry." In: *American Journal of Physics* 49.9 (1981), pp. 882–883.

[186] John G Rarity and PR Tapster. "Fourth-order interference in parametric downconversion." In: *JOSA B* 6.6 (1989), pp. 1221–1226.

[187] Chong-Ki Hong, Zhe-Yu Ou, and Leonard Mandel. "Measurement of subpicosecond time intervals between two photons by interference." In: *Physical review letters* 59.18 (1987), p. 2044.

[188] JG Rarity, PR Tapster, E Jakeman, T Larchuk, RA Campos, MC Teich, and BEA Saleh. "Two-photon interference in a Mach-Zehnder interferometer." In: *Physical review letters* 65.11 (1990), p. 1348.

[189] Matteo GA Paris. "Entanglement and visibility at the output of a Mach-Zehnder interferometer." In: *Physical Review A* 59.2 (1999), p. 1615.

[190] A Trenti, M Borghi, M Mancinelli, HM Price, G Fontana, and L Pavesi. "One and two-photon quantum interference in a Mach-Zehnder interferometer." In: *Nonlinear Optics and its Applications IV*. Vol. 9894. International Society for Optics and Photonics. 2016, 98940W.

[191] Ravitej Uppu, Tom AW Wolterink, Tristan BH Tentrup, and Pepijn WH Pinkse. "Quantum optics of lossy asymmetric beam splitters." In: *Optics express* 24.15 (2016), pp. 16440–16449.

[192] Tom AW Wolterink, Ravitej Uppu, Georgios Ctistis, Willem L Vos, Klaus-J Boller, and Pepijn WH Pinkse. "Programmable two-photon quantum interference in 10 3 channels in opaque scattering media." In: *Physical Review A* 93.5 (2016), p. 053817.

[193] James S Fakonas, Hyunseok Lee, Yousif A Kelaita, and Harry A Atwater. "Two-plasmon quantum interference." In: *Nature Photonics* 8.4 (2014), pp. 317–320.

[194] URL: http://www.schott.com/.

[195] A Trenti, M Borghi, M Mancinelli, HM Price, G Fontana, and L Pavesi. "Quantum interference in an asymmetric Mach-Zehnder interferometer." In: *Journal of Optics* 18.8 (2016), p. 085201.

[196] Rainer Storn and Kenneth Price. "Differential evolution–a simple and efficient heuristic for global optimization over continuous spaces." In: *Journal of global optimization* 11.4 (1997), pp. 341–359.

[197] Lasse Høgstedt, Jeppe Seidelin Dam, Anna-Lena Sahlberg, Zhongshan Li, Marcus Aldén, Christian Pedersen, and Peter Tidemand-Lichtenberg. "Low-noise mid-IR upconversion detector for improved IR-degenerate four-wave mixing gas sensing." In: *Optics letters* 39.18 (2014), pp. 5321–5324.

[198] Geng Song, Tao Qin, Hu Liu, Guo-Bing Xu, Yue-Yin Pan, Fu-Xing Xiong, Kang-Sheng Gu, Guo-Ping Sun, and Zhen-Dong Chen. "Quantitative breath analysis of volatile organic compounds of lung cancer patients." In: *Lung Cancer* 67.2 (2010), pp. 227–231.

[199] Albert Schliesser, Nathalie Picqué, and Theodor W Hänsch. "Mid-infrared frequency combs." In: *Nature Photonics* 6.7 (2012), pp. 440–449.

[200] Jeppe Seidelin Dam, Peter Tidemand-Lichtenberg, and Christian Pedersen. "Room-temperature mid-infrared single-photon spectral imaging." In: *Nature photonics* 6.11 (2012), pp. 788–793.

[201] URL: http://www.thorlabs.com.

[202] John David Jackson. *Classical electrodynamics*. 1999.

[203] Chandra M Natarajan, Michael G Tanner, and Robert H Hadfield. "Superconducting nanowire single-photon detectors: physics and applications." In: *Superconductor science and technology* 25.6 (2012), p. 063001.

[204] Francesco Marsili, Francesco Bellei, Faraz Najafi, Andrew E Dane, Eric A Dauler, Richard J Molnar, and Karl K Berggren. "Efficient single photon detection from 500 nm to 5 μm wavelength." In: *Nano letters* 12.9 (2012), pp. 4799–4804.

[205] Adriana E Lita, Aaron J Miller, and Sae Woo Nam. "Counting near-infrared single-photons with 95% efficiency." In: *Optics express* 16.5 (2008), pp. 3032–3040.

[206] URL: http://www.excelitas.com/Pages/Product/Single-Photon-Counting-Modules-SPCM.aspx.

[207] R Andrews. "IR image parametric up-conversion." In: *IEEE Journal of Quantum Electronics* 6.1 (1970), pp. 68–80.

[208] Guilherme Temporão, Sébastien Tanzilli, Hugo Zbinden, Nicolas Gisin, Thierry Aellen, Marcella Giovannini, and Jérome Faist. "Mid-infrared single-photon counting." In: *Optics letters* 31.8 (2006), pp. 1094–1096.

[209] URL: http://www.xenics.com.

[210] Yong Meng Sua, Heng Fan, Amin Shahverdi, Jia-Yang Chen, and Yu-Ping Huang. "Direct Generation and Detection of Quantum Correlated Photons with 3.2 um Wavelength Spacing." In: *Scientific reports* 7.1 (2017), p. 17494.

[211] Svetlana V Boriskina. "Photonic molecules and spectral engineering." In: *Photonic microresonator research and applications*. Springer, 2010, pp. 393–421.

[212] Stefano Azzini, Davide Grassani, Matteo Galli, Lucio Claudio Andreani, Marc Sorel, Michael J Strain, LG Helt, JE Sipe, Marco Liscidini, and Daniele Bajoni. "From classical four-wave mixing to parametric fluorescence in silicon microring resonators." In: *Optics letters* 37.18 (2012), pp. 3807–3809.

[213] Hermann A Haus. *Waves and fields in optoelectronics*. Prentice-Hall, 1984.

[214] M Mancinelli, R Guider, P Bettotti, M Masi, M Rao Vanacharla, and L Pavesi. "Coupled-resonator-induced-transparency concept for wavelength routing applications." In: *Optics express* 19.13 (2011), pp. 12227–12240.

[215] Jun Pan, Sunil Sandhu, Yijie Huo, Norbert Stuhrmann, Michelle L Povinelli, James S Harris, MM Fejer, and Shanhui Fan. "Experimental demonstration of an all-optical analogue to the superradiance effect in an on-chip photonic crystal resonator system." In: *Physical Review B* 81.4 (2010), p. 041101.